# Experimental Imaging of a Vertical Vein using Controlled-Source Seismic Interferometry

by

© **Kriselle Dias**

A thesis submitted to the
School of Graduate Studies
in partial fulfillment of the requirements
for the degree of
**Master of Science**


**Department of Earth Sciences (Geophysics)**
Memorial University of Newfoundland

**February 2018**

St. John's Newfoundland and Labrador

# Abstract

Seismic methods are desirably implemented in the imaging of economically viable hard rock mineral deposits, due to the technique's intrinsic higher resolution in comparison to traditionally used geophysical methods. Conventional surface seismic methods are inadequate in the imaging of steeply dipping targets, due to unfavourable geometrical relationships between the surface sources, surface receivers, and the target. There is poor recovery of data when geological features have a dip approximately equal to, or greater than 65°, as the reflected wave propagates at an angle that reaches the surface outside the aperture of the receiver array, or does not reach the surface at all. Steep dips also cause the overall travel path to be much longer than the depth of the target, causing a loss of energy and associated amplitude and high frequency attenuation which results in a low signal to noise ratio and associated processing issues.

This study investigates the viability of using a Vertical Seismic Profile (VSP) in combination with seismic interferometry as a new method of imaging thin and nearly-vertical veins, and develops techniques for the same, and for which a thin, nearly vertical barite vein at the Collier Point Barite property serves as a well constrained target for study. Seismic interferometry is a technique in which, a signal pair is cross-correlated to reproduce a virtual source-receiver pair and reconstruct the impulse response of a given medium. In using these methods, a source is virtually moved into a downhole location, which avoids issues associated with surface-seismic methods. The parameters of the experiment are optimized using ray-tracing analysis, finite-difference modelling and a study of the physical properties to ensure reflection detectability. The unprocessed dataset is highly contaminated by tube-waves which are removed using spiking deconvolution and F-K filtering. The pre-processed dataset is then subjected to seismic interferometry methods which theoretically results in the source and receiver placed in the same location, and is hence processed using standard CMP processing flows. It is noted that the seismic response to the barite target varies significantly through the profile. A 1-D synthetic seismogram modelling program is used to study the variations in the seismic response, and propose a geological interpretation for the same. The final processed image of the target is consistent with descriptions in prior geological reports.

This thesis has demonstrated that with the appropriate experiment optimization and processing parameters, VSPs in combination with the seismic interferometry procedure has proven to be an appropriate tool towards detecting and imaging vertical to near-vertical subsurface bodies of economic importance which may otherwise not be imaged appropriately using surface-seismic methods.

# Acknowledgments

I am greatly indebted to my supervisor, **Dr. Charles Hurich**, for providing me this research topic to continue my studies at Memorial University, and enabling me with all aspects of his supervision and advice. I would also like to thank my supervisory committee member, **Dr. Alison Malcolm** for her suggestions towards the betterment of my thesis.

I am also thankful to **Dr. Sharon Deemer** for providing me with invaluable technical advice and support during the processing of my data, **Mr. Peter Bruce** for technical assistance, and **Dr. Yingjian Xiao** for his help in conducting seismic velocity measurements. I would also like to thank **Dr. Alison Leitch** for her support through my undergraduate years, and her belief in me, which led to me taking on this project.

I acknowledge Landmark Solutions for providing the SeisSpace®/ProMAX® Seismic Processing Software, Schlumberger for providing the VISTA™ Seismic Processing software, the Centre for Wave Phenomena (CWP) at the Colorado School of Mines for providing the Seismic Unix utilities package, and the **Hibernia Management and Development Company (HMDC) Geophysics Fund** for field and salary support.

On a personal note, I would like to thank my orange-eyed companion, **Bandit Granter** for his sometimes reluctant company during the writing period. Finally, I am especially thankful to **Mr. Colin Granter** for his physical assistance during the recording of seismic data at the Collier Point Barite Property, and for always supporting me in my endeavours, both personally and professionally.

# Table of Contents

*Abstract* . . . . . i

*Acknowledgments* . . . . . ii

*List of Tables* . . . . . viii

*List of Figures* . . . . . xii

*List of Abbreviations and Symbols* . . . . . xii

*1.* Introduction . . . . . 1
1.1 Barite in Newfoundland . . . . . 5
1.2 Field Location . . . . . 6
1.2.1 Geology . . . . . 7
1.2.2 Barite Veins . . . . . 8
1.2.3 Alteration and Breccia Zones . . . . . 8

*2.* Theory and Method . . . . . 11
2.1 Virtual Source Method in Seismic Interferometry . . . . . 12
2.2 Interferometry Application at Collier Point . . . . . 14

*3.* Physical Rock Properties and Reflection Detectability . . . . . 15
3.1 Introduction . . . . . 15
3.2 Method . . . . . 16
3.3 Arkosic Bedrock . . . . . 18
3.3.1 Density of Arkosic Bedrock . . . . . 18
3.3.2 Porosity of Arkosic Bedrock . . . . . 18
3.3.3 Acoustic Velocity of Arkosic Bedrock . . . . . 19
3.4 Barite . . . . . 22
3.4.1 Density of Barite . . . . . 23
3.4.2 Acoustic Velocity of Barite . . . . . 23
3.4.3 Porosity of Barite . . . . . 24
3.5 Anisotropy Study on Barite . . . . . 25
3.6 Discussion of Reflectivity . . . . . 27
3.6.1 Reflectivity changes due to macro-porosity . . . . . 27

3.6.2 Reflectivity changes based on average data . . . 33
3.6.3 Resolution and detectability due to geometry of target . . . 34
3.7 Summary of Rock Properties and Detectability . . . 35

*4.* Experiment Optimization . . . 38
4.1 Ray-tracing analysis . . . 38
4.1.1 Physical Constraints and Ray-tracing Parameters . . . 39
4.1.2 Ray-path Diagrams . . . 41
4.1.3 Distance-time Graphs . . . 43
4.1.4 CMP Plots . . . 45
4.1.5 Summary of Ray-tracing Analysis . . . 48
4.2 Finite Difference Modelling . . . 49
4.2.1 2D Velocity Model . . . 50
4.2.2 Processing Parameters in Finite Difference Modelling . . . 53
4.3 Data Processing . . . 55
4.3.1 Virtual Source Gather . . . 64
4.3.2 Assignment of Polarities . . . 68
4.3.3 CDP Stack . . . 68
4.3.4 Migration . . . 74
4.3.5 Analysis of Synthetic Data . . . 78

*5.* Interferometry Experiment . . . 80
5.1 Drilling Procedure . . . 80
5.2 Walk-Away Seismic Experiment . . . 80
5.3 Equipment . . . 81

*6.* Seismic Data Processing . . . 84
6.1 Pre-processing . . . 84
6.1.1 Combining separate Vertical Seismic Profiles . . . 86
6.1.2 Identification of noise in Collier Point Dataset . . . 87
6.1.3 Deconvolution . . . 96
6.1.4 F-K Filtering . . . 106
6.2 Interferometry . . . 112
6.2.1 Correlation Gather . . . 113
6.2.2 Virtual Source Gather . . . 118
6.3 Assignment of Polarities . . . 124
6.4 CDP Stack . . . 124
6.5 Depth Migration . . . 131
6.6 Summary of Processing . . . 133

*7.* Discussion . . . 135
7.1 Identification of Vein in Dataset . . . 135
7.2 Examination of Reflection Events . . . 139

7.3 1-D synthetic modelling . . . 139
7.3.1 Single Boundary Response . . . 141
7.3.2 Three-layer response . . . 144
7.3.3 Characterizing Wavelets . . . 147
7.3.4 Summary of 1-D Modelling . . . 150
7.4 Proposed Geological Model . . . 156
7.4.1 Summary of Reflection Event 1 . . . 156
7.4.2 Summary of Reflection Event 2 - the barite vein . . . 159

*8.* Conclusion . . . 163
8.1 Summary of the thesis . . . 164
8.2 Limitations of Current Work . . . 166
8.3 Contribution of this thesis . . . 167

*Bibliography* . . . 167

*Appendices* . . . 171

*Appendix A. Creation of Velocity Model* . . . 172
A.1 Preparation of greyscale 2D graphic: . . . 172
A.2 Creation of Velocity Model in Seismic Unix . . . 173

*Appendix B. Seismic Unix Scripts* . . . 174
B.1 Create receiver locations . . . 174
B.2 Create shot gathers . . . 175
B.3 Concatenate individual shot files . . . 177
B.4 Concatenate cross-correlated filed with chosen channels . . . 178
B.5 Concatenate individual shot files to a multi-shot file . . . 180
B.6 Sort, trace-mix & trace taper cross-correlated files to create correlation gather 182

*Appendix C. Synthetic Modelling* . . . 184
C.1 Shots produced using Finite Difference Modelling Program . . . 184
C.2 Concatenating the shot records . . . 184
C.3 Cross-correlation of shot records . . . 185
C.4 Concatenation of cross-correlated shot records . . . 185

*Appendix D. ProMAX Processing Steps* . . . 186
D.1 Create dataset to be sorted in ProMax . . . 186
D.2 Create a virtual stack . . . 187
D.3 Specify Geometry for Creating a new CDP Stack . . . 189
D.4 Create a NMO-corrected CDP stack . . . 192
D.5 Perform Kirchoff Depth Migration . . . 194

*Appendix E. Interferometry Logs* . . . 197

*Appendix F. CDP Geometry* . . . . . 200

*Appendix G. 1-D Modelling Trials* . . . . . 204

# List of Tables


3.1 Densities of the arkosic bedrock from Collier Point, NL . . . . . 18
3.2 Porosities of the arkosic bedrock from Collier Point, NL . . . . . 19
3.3 Acoustic velocities of the arkosic bedrock from Collier Point, NL . . . . . 21
3.4 P-wave velocities and associated acoustic impedance of arkosic bedrock from Collier Point, NL . . . . . 21
3.5 Densities of the barite cores from Collier Point, NL . . . . . 23
3.6 Acoustic velocities of the barite cores from Collier Point, NL . . . . . 24
3.7 Porosities of the barite cores from Collier Point, NL . . . . . 25
3.9 P-wave velocities, densities and acoustic impedance of barite blocks . . . . . 26
3.8 Dimensions and Acoustic Velocities of barite blocks . . . . . 27
3.10 Recalculated densities of fluid-saturated barite (original density = 4.31 g/cc) 30
3.11 Summary of average physical properties for the arkosic sandstone and barite vein at Collier Point . . . . . 37

4.1 List of parameters and corresponding values used in Ray-tracing Program . . 41
4.2 Simulation Cases in the Ray-tracing Study . . . . . 41
4.3 2D Model Parameters applied to the Finite-Difference modelling program . . 54
4.4 List of parameters and experimental cases studied using the Finite-Difference modelling program . . . . . 54
4.5 2D Grid Parameters applied to the Finite-Difference modelling program . . . 54
4.6 Correlation scheme for creating virtual sources in finite-difference modelling . 59

6.1 Description & origin of major tube waves in the Collier Point dataset . . . . 92
6.2 Correlation scheme for creating virtual sources in Collier Point Dataset . . . 123

7.1 Properties of rocks used in 1-D synthetic modelling and resulting tuning thickness (or limit of resolution at 300 Hz) . . . . . 141
7.2 Layer thicknesses & resulting peak-to-trough amplitudes for 300 Hz Ricker wavelet . . . . . 146

E.1 Collier Point Interferometry Logs . . . . . 197
E.1 Collier Point Interferometry Logs . . . . . 198
E.1 Collier Point Interferometry Logs . . . . . 199

F.1 CDP Numbers with corresponding borehole depths and no. of traces in CDP bin . . . . . 200

F.1 CDP Numbers with corresponding borehole depths and no. of traces in CDP bin . . . . . 201
F.1 CDP Numbers with corresponding borehole depths and no. of traces in CDP bin . . . . . 202
F.1 CDP Numbers with corresponding borehole depths and no. of traces in CDP bin . . . . . 203

G.1 Log files used in Breccia Modelling . . . . . 204

# List of Figures


1.1 Schematic ray-paths for the shallow region of a seismic reflection from a steeply dipping target. Adapted from [Eaton et al., 1996] . . . 2
1.2 Borehole receivers are transformed to virtual borehole sources . . . 4
1.3 Simplified map showing the tectonostratigraphic zones and locations of significant barite occurrences in Newfoundland [Howse, 1992] . . . 6
1.4 Location of the Collier Point Barite property field area, within the municipality of Norman's Cove, Newfoundland (Department of Natural Resources, Newfoundland & Labrador) . . . 7
1.5 Collier Point Barite vein looking south along its strike, and demonstrating a pinch and swell structure along strike and down dip [Howse, 1992] . . . 10

2.1 Diagram representing creation of a virtual source at a receiver location . . . 13

3.1 Acoustic velocity testing on arkosic bedrock using ASTM standards . . . 20
3.2 Barite samples from the Collier Point Barite Property . . . 22
3.3 Visible porosities in barite samples . . . 25
3.4 Barite blocks used in anisotropy study . . . 26
3.5 Plots of fluid-saturated Porosities vs. Velocity . . . 31
3.6 Plots of fluid-saturated Porosities vs. Reflection Coefficient . . . 32

4.1 Physical constraints leading to borehole dipping angles and surface source array positioning not optimal for imaging . . . 40
4.2 Raypath diagrams demonstrating stationary phase rays at the 22nd virtual source . . . 42
4.3 Distance-time graph demonstrating the direct wave and reflection for the model geometry . . . 44
4.4 Plots of CMP depth along borehole for Case I, produced with the target dipping at 80° away from the borehole, and the borehole dipping at 75° towards the target . . . 46
4.5 Plots of CMP depth along borehole for Case II, produced with the target dipping at 80° away from the borehole, and the borehole dipping at 65° towards the target . . . 47
4.6 Diagram demonstrating the subsurface geometrical relation between drilled boreholes oriented at 75° and 65° towards the target, with respect to a dipping barite vein oriented at 80° from the surface (away from the target) . . . 52

4.7 2D model image file produced in Seismic Unix . . . . . 55
4.8 Shots produced in Seismic Unix using the finite-difference modelling program 57
4.9 Trace display for surface sources 1, 2 and 3 located closest to the borehole . 61
4.10 Trace display for surface sources 25, 26 and 27 . . . . . 62
4.11 Trace display for surface sources 29, 30, 31, which are furthest away from the borehole using a maximum offset of 60 m . . . . . 63
4.12 Virtual Source Gather for virtual shots 1, 2 and 3 located at the top of the borehole . . . . . 65
4.13 Virtual Source Gather for virtual shots 22, 23 and 24 located at the middle of the borehole . . . . . 66
4.14 Virtual Source Gather for virtual shots 40, 41 and 41 located at the end of the borehole . . . . . 67
4.15 CDP Stack of seismic section in Case I, with the borehole dipping at 75° towards the target, and 60 m Offset . . . . . 70
4.16 CDP Stack of seismic section in Case I, with the borehole dipping at 75° towards the target, and 100 m Offset . . . . . 71
4.17 CDP stack of seismic section in Case II, with the borehole dipping at 65° towards the target, and 60 m Offset . . . . . 72
4.18 CDP stack of seismic section in Case II, with the borehole dipping at 65° towards the target, and 100 m Offset . . . . . 73
4.19 Migrated Stack of seismic section in Case I, with the borehole dipping at 75° towards the target, and 60 m Offset . . . . . 75
4.20 Migrated Stack of seismic section in Case I, with the borehole dipping at 75° towards the target, and 100 m Offset . . . . . 76
4.21 Migrated stack of seismic section in Case II, with the borehole dipping at 65° towards the target, and 60 m Offset . . . . . 77
4.22 Migrated stack of seismic section in Case II, with the borehole dipping at 65° towards the target, and 100 m Offset . . . . . 78

5.1 Drillers creating a borehole at the Collier Point Barite Property . . . . . 81
5.2 A receiver on the bottom of hydrophone cable used in the experiment . . . . 82
5.3 Photo of trench dug for placing shot points during the Collier Point Interferometry Experiment . . . . . 82
5.4 Satellite photo of the Collier Point interferometry experiment site demonstrating location of shot points, borehole and shooting directions. . . . . 83

6.1 Pre-processing Flow . . . . . 85
6.2 Diagram demonstrating position of hydrophone and channels within the borehole 87
6.4 Unprocessed and raw seismograms . . . . . 91
6.5 Diagram demonstrating tube wave propagation in Shot 1 . . . . . 93
6.6 Fracturing around borehole walls as captured in borehole cameras . . . . . 94
6.7 Borehole camera log of inclined and vertical borehole at the Collier Point site 95
6.8 Spectral Analysis of Direct Wave in Shot 20 in the Collier Point Dataset . . 97

6.9 Spectral Analysis of a tube wave in Shot 20 in the Collier Point Dataset . . . 98
6.10 Spectral Analysis of Shot 20 in the Collier Point Dataset . . . 99
6.12 Autocorrelation of shots in the Collier Point Dataset . . . 101
6.13 Spectral Analysis of Shot 1 before Spiking Deconvolution . . . 102
6.14 Spectral Analysis of Shot 22 before Spiking Deconvolution . . . 103
6.15 Spectral Analysis after Spiking Deconvolution (60 ms) . . . 104
6.16 Seismic Dataset after Spiking Deconvolution (60 ms) . . . 105
6.17 Diagram representing downgoing and upgoing P and S-waves in the T-X domain and F-K domain (Adapted from [Hardage, 2000]) . . . 107
6.18 F-K Analysis of Shot 12 with waves within the F-K Spectrum labelled . . . 108
6.19 F-K Reject Filtering . . . 109
6.20 F-K Accept Filtering . . . 109
6.21 Seismic Dataset after F-K Reject Filtering and Spiking Deconvolution (60 ms) 110
6.22 Seismic Dataset after F-K Accept Filtering and Spiking Deconvolution (60 ms) 111
6.23 Interferometry processing flow . . . 112
6.24 Channel without trace-mixing or trace-tapering . . . 115
6.25 Channel after trace-tapering to 3 traces . . . 115
6.26 Channel after trace-mixing by a standard weighted-mix of 1,3,1 . . . 116
6.27 Channel after weighted trace-mix of 1,3,1 and trace-tapering to 3 traces . . . 116
6.28 Correlation gather for Live Source 1 (before summation) . . . 117
6.29 VSG creation flow . . . 118
6.30 Diagram demonstrating Generation of Virtual Source at Receiver 1 recorded at Receiver 2 . . . 119
6.31 Virtual Source Gathers from the Collier Point dataset without AGC . . . 121
6.32 Virtual Source Gathers from the Collier Point dataset with AGC . . . 122
6.33 CDP Fold . . . 125
6.34 CDP Geometry Spread . . . 126
6.35 CDP and Depth Migration creation flow . . . 127
6.36 CDP Stack for Collier Point Dataset . . . 128
6.37 CDP Stack for Collier Point Dataset . . . 129
6.38 CDP Stack for Collier Point Dataset . . . 130
6.39 Kirchhoff Depth Migrated Stack for Collier Point Dataset . . . 132
6.40 Differences in trace-mixing and trace-tapering . . . 134

7.1 Reflection events identified in pre-processed VSP . . . 136
7.2 Reflection Events identified in Virtual Source Gathers . . . 137
7.3 Timing of possible barite vein in pre-processed seismogram (before interferometry) . . . 138
7.4 Reflection Events viewed in CDP Stack . . . 139
7.5 Ricker Wavelet using in 1-D modelling . . . 140
7.6 Single boundary arkose-barite interface . . . 142
7.7 Single boundary barite-arkose interface . . . 143

7.8 Example of tuning when layer is bounded by reflection coefficients of the opposite sign [Hardage, 1987]. . . . . 145
7.9 Plot of peak-to-trough amplitudes for barite units of varying thicknesses . . . 147
7.10 Wavelet responses seen in the Collier Point Dataset . . . . . 148
7.11 Wavelet response for barite surrounded by high breccia . . . . . 149
7.12 Wavelet response for barite surrounded by low breccia . . . . . 150
7.13 Comparison of wavelet responses in Collier Point dataset with Breccia Model 1 152
7.14 Geological interpretation of synthetic wavelets from Breccia Model 1 . . . . . 153
7.15 Comparison of wavelet responses in Collier Point dataset with Breccia Model 4 154
7.16 Geological interpretation of synthetic wavelets from Breccia Model 4 . . . . . 155
7.17 Frequency content of Reflection Event 1 in Pre-Processed Gather . . . . . 157
7.18 Frequency content of Reflection Event 2 in Pre-Processed Gather . . . . . 158
7.19 Reflection Events and similarities in wavelet at depth . . . . . 159
7.20 Figure demonstrating a simulation of the CDP stack projected perpendicular to the borehole . . . . . 161

G.1 Scenarios produced for Breccia Model 1 . . . . . 208
G.2 Scenarios produced for Breccia Model 2 . . . . . 210
G.3 Scenarios produced for Breccia Model 3 . . . . . 212
G.4 Scenarios produced for Breccia Model 4 . . . . . 214
G.5 Scenarios produced for Breccia Model 5 . . . . . 216

# List of Abbreviations and Symbols

| | |
|---|---|
| $AGC$ | Automatic Gain Control |
| $CDP$ | Common Depth-Point |
| $CMP$ | Common Mid-Point |
| $\rho$ | Density |
| $F-K$ | Frequency-Wavenumber |
| $NMO$ | Normal Moveout |
| $\phi$ | Porosity |
| $rms$ | Root Mean Square |
| $V_P$ | P-wave Velocity |
| $V_S$ | S-wave Velocity |
| $VSP$ | Vertical Seismic Profile |

# Chapter 1

## Introduction

Conventional surface seismic methods are routinely applied in imaging horizontally oriented lithological targets. However, not all geological targets of interest are located horizontally, such as steeply dipping mineral bearing veins, or petroleum reserves trapped on the flanks of salt domes. The imaging of steeply dipping vertical targets through conventional surface seismic methods is largely inadequate due to unfavourable source-receiver geometries in relation to the target.

Generally speaking, any arbitrarily oriented subsurface target may be imaged adequately provided the reflected wavefield from the target is recorded by the receivers. In instances where the geological features have a dip approximately equal to, or greater than 65°, the reflected wave propagates at an angle that reaches the surface outside the aperture of a typical receiver array (i.e. aperture length appropriately scaled to experiment), and a large fraction of reflected energy is redirected horizontally or even downward, resulting in poor recovery of data.

Steep dips may also cause the overall travel path to be longer than the depth of the target which results in an attenuation of energy and a low signal to noise ratio which is undesirable in recovering data. If surface seismic methods are used to record deep target zones in steeply dipping targets, the receiver array would have to be placed at an impractically large distance

away from the seismic source. While turning-ray methods may be used in this situation, their application is presently limited to young sedimentary basins, which have sufficiently high vertical velocity gradients to return a diving wave within the recording aperture [Hale et al., 1992]. In these cases, a vertical seismic profiling (VSP) configuration may be more suitable for imaging the subsurface compared to surface seismic methods. In VSPs, downhole receivers in a borehole record the subsurface wavefield generated by surface seismic sources. This method can be used to intercept the horizontally propagating reflections generated by steep reflectors.

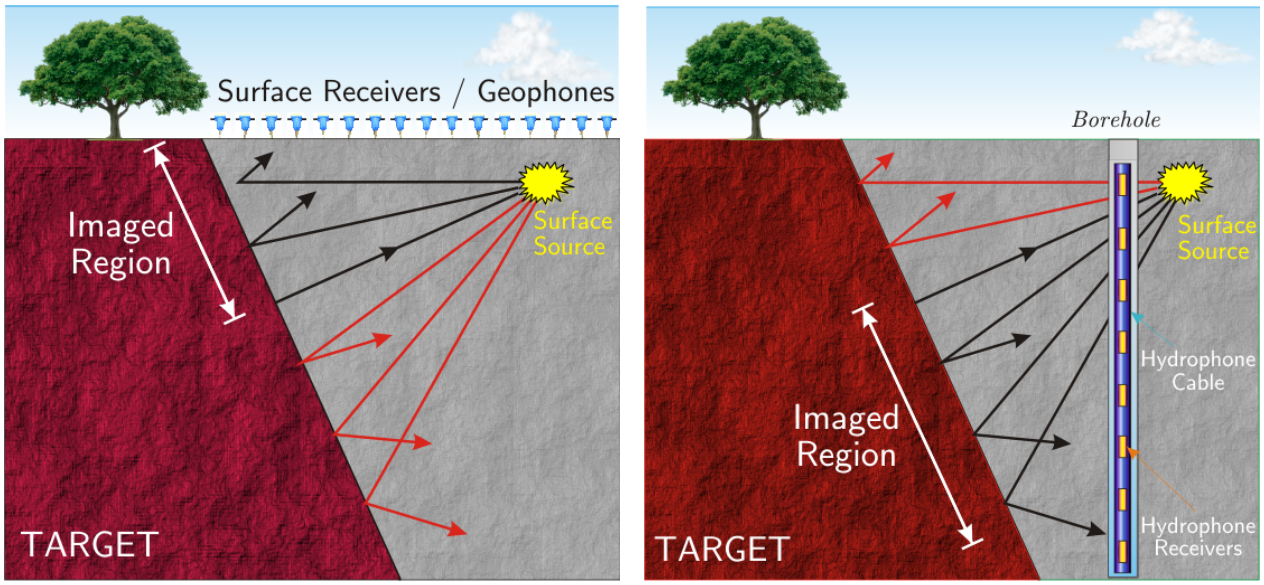


*(a)* Surface seismic survey *(b)* Vertical Seismic Profile (VSP)

*Fig. 1.1:* Schematic ray-paths for the shallow region of a seismic reflection from a steeply dipping target. Adapted from [Eaton et al., 1996]
In the surface seismic survey (1.1a), rays reflecting at deeper locations are directed away from the receiver array; however these are recorded in the VSP survey (1.1b)

Therefore, a VSP configuration is implemented in this thesis, as a means of imaging a thin, near-vertical target where surface seismic techniques may be inadequate. A simple VSP is shown in Figure 1.1b, where seismic sources are located on the horizontal surface at various offsets from a monitoring well (borehole filled with water) which is located adjacent to the target. A hydrophone cable (borehole receivers) is lowered into the monitoring well,

on which contributions from surface sources are recorded. The VSP is significantly more effective in imaging deeper regions of the target which are otherwise not adequately imaged using conventional surface seismic methods, such as in Figure 1.1a, where the majority of the reflected wave propagates at an angle that reaches the surface outside the aperture of the receiver array, or the wave does not reach the surface at all. The longer propagation distance in conventional surface seismic surveys also results in an attenuation of energy, causing a low signal to noise ratio and associated processing issues.

Although the VSP provides an improvement and deeper image recovery compared to conventional methods, some reflected waves still propagate at an angle outside the aperture of the receiver array. The VSP can be further enhanced by applying the seismic interferometry procedure to transform the borehole receivers to *virtual borehole sources* using the virtual source method (Figure 1.2). **Seismic interferometry** is a technique in which, a signal pair is cross-correlated to reproduce a virtual source-receiver pair and reconstruct the impulse response of a given media, in order to gain useful information about the subsurface. This method theoretically results in the source and receiver being placed in the same borehole, and can hence be treated in the same way as a conventional surface profile in which the sources and receivers are placed at the surface, and takes advantage of the signal to noise increase gained from standard common mid-point processing. As seismic interferometry methods can virtually move a source into a location within the borehole, they can image the subsurface adjacent to the borehole, with shorter propagation distances, and can also image below the overburden without prior knowledge of overburden velocities.

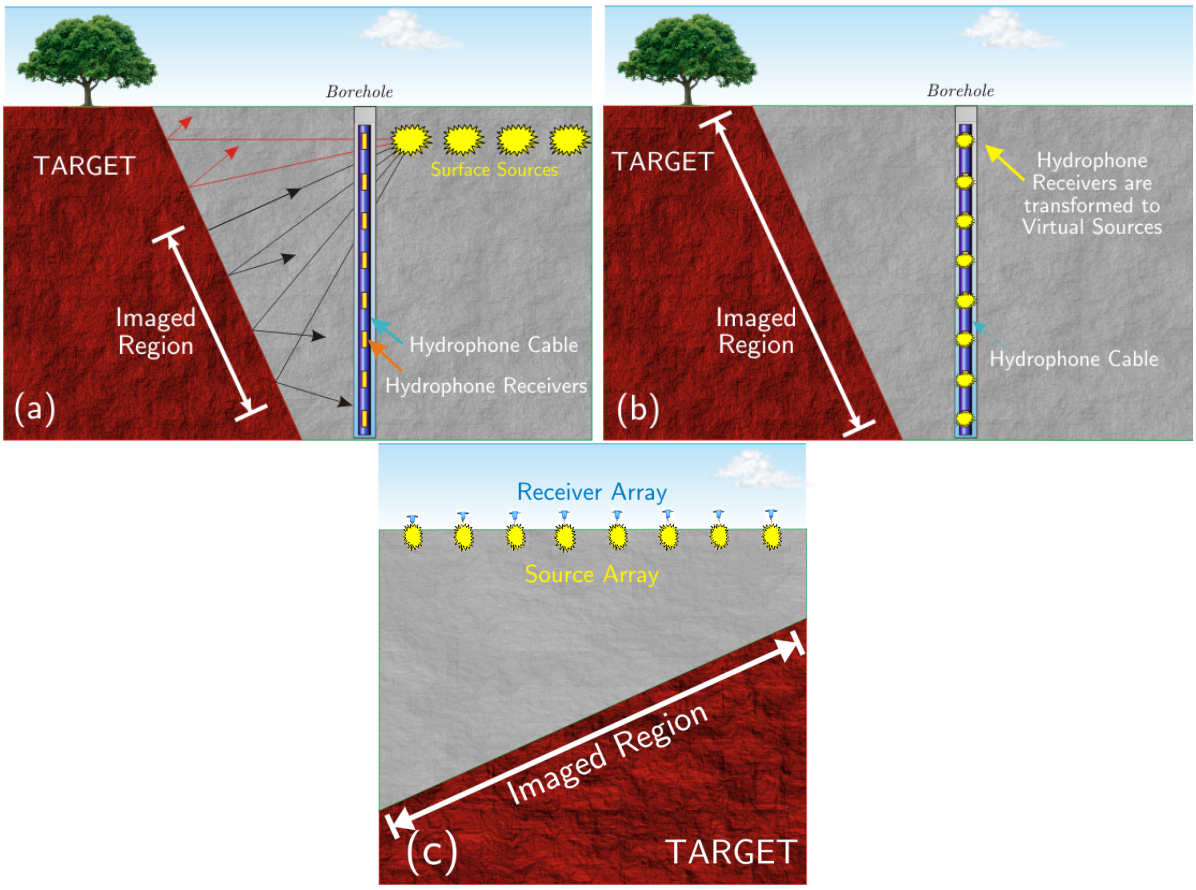


*Fig. 1.2:* Borehole receivers are transformed to virtual borehole sources
(a) - In a regular VSP survey, surface sources are placed at offsets from the borehole, which is filled with water and fitted with a hydrophone cable. (b) - In a VSP combined with seismic interferometry, the borehole receivers are transformed to virtual sources. (c) - This method theoretically results in the source and receiver being placed in the same borehole, and can be processed and interpreted in the same way as a conventional surface seismic profile in which the sources and receivers are placed on the surface.

Hence, a VSP in combination with the virtual source method using seismic interferometry is applied to experimentally image a nearly vertical, thin, sub-surface barite vein at the Collier Point Barite property in Eastern Newfoundland. The experiment is conducted primarily with the intention of technique development, as there are very few actual field examples of the use of seismic interferometry using VSPs for this type of imaging, and for which the Collier Point Barite vein serves as a well-constrained target for study.

## 1.1 Barite in Newfoundland

In Newfoundland, barite mostly occurs in the form of vein-type deposits on the Avalon Peninsula, notably around Placentia Bay and the St. Lawrence area of the Burin Peninsula (Figure 1.3). The origin of the veins is not well established, however field studies indicate a post-Cambrian and likely post-Silurian age. A prominent aeromagnetic anomaly on the granitic outcrop of the Placentia Bay's islands suggests that barite and other veins may be linked to the hydrothermal aureole of a granitic body largely hidden under Placentia Bay [Adams and Kerr, 2014]. Barite also occurs in the form of stratiform deposits in central Newfoundland. Elsewhere, it exists in the form of minor vein-type occurrences. The origin of barite deposits on the west coast of Newfoundland is unclear. Presently, significant barite deposits have not been recognized in Labrador [Adams and Kerr, 2014]. Barite is primarily used in the petroleum industry (roughly 85% of global consumption) as a weighing agent in drilling fluids or drilling mud, due to its high specific gravity (4.5 g/cc for pure $BaSO_4$), and low abrasivity. It is also non-corrosive, non-toxic, readily available and inexpensive, and is therefore preferable to synthetic alternatives. Barite used in drilling muds must have a minimum specific gravity of 4.2 g/cc. The barite at the Collier Point Property is of medical grade with $> 93\%$ purity.

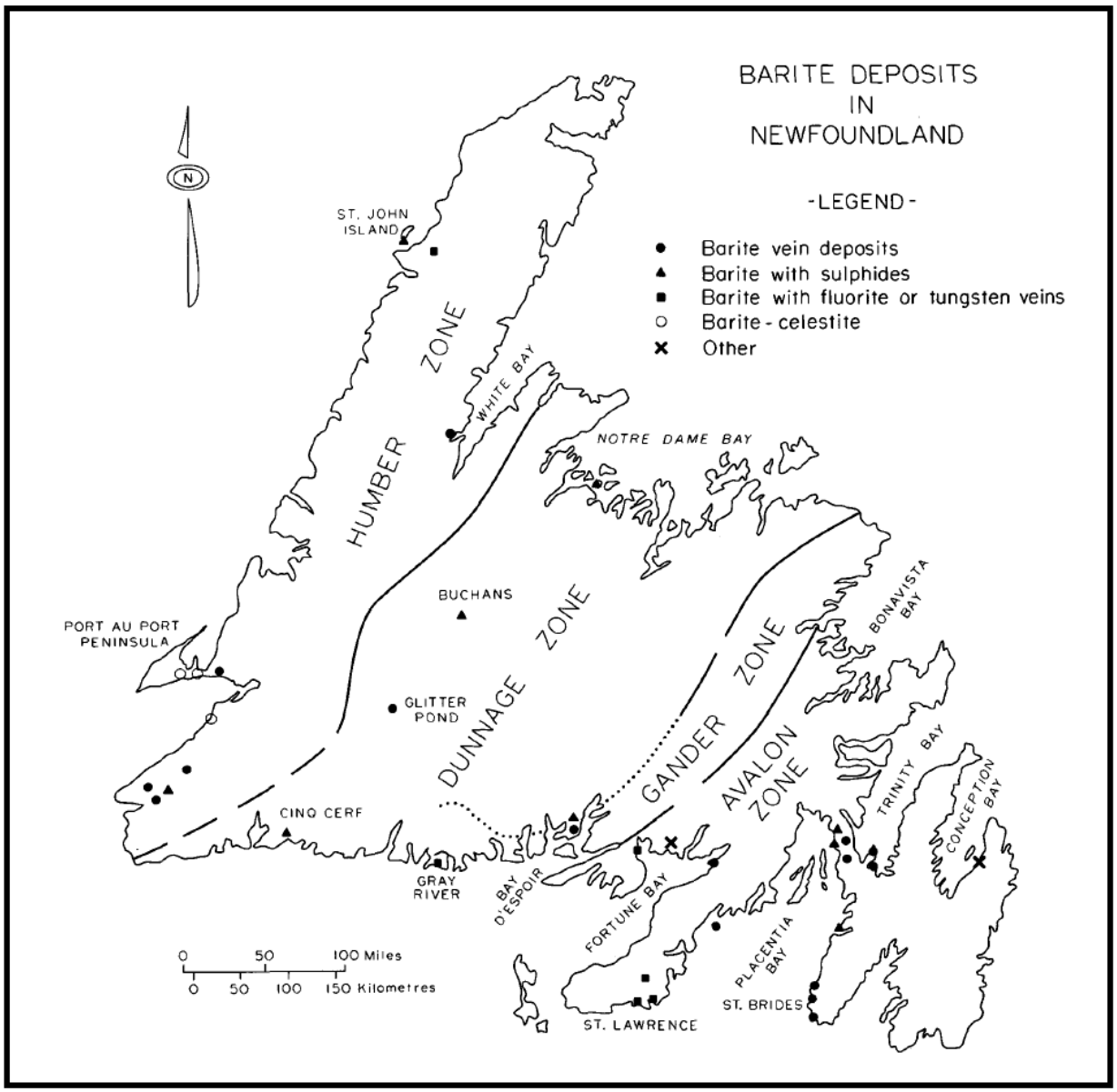


*Fig. 1.3:* Simplified map showing the tectonostratigraphic zones and locations of significant barite occurrences in Newfoundland [Howse, 1992]

## 1.2 Field Location

The Collier Point Barite property is located along the southern shore of Trinity Bay, within the municipality of Norman's Cove, Newfoundland, Canada. The site can be accessed

by a 3 km gravel road extending from paved highway no. 201. Barite veins were discovered at Collier Point and mined on a small scale from 1902 to 1904, and again in the 1980's. The Collier veins are hosted within the green arkose of the Neoproterozoic (Ediacaran) Heart's Desire Formation, and were considered to be the most significant barite producing location in Newfoundland and Labrador [Adams and Kerr, 2014].

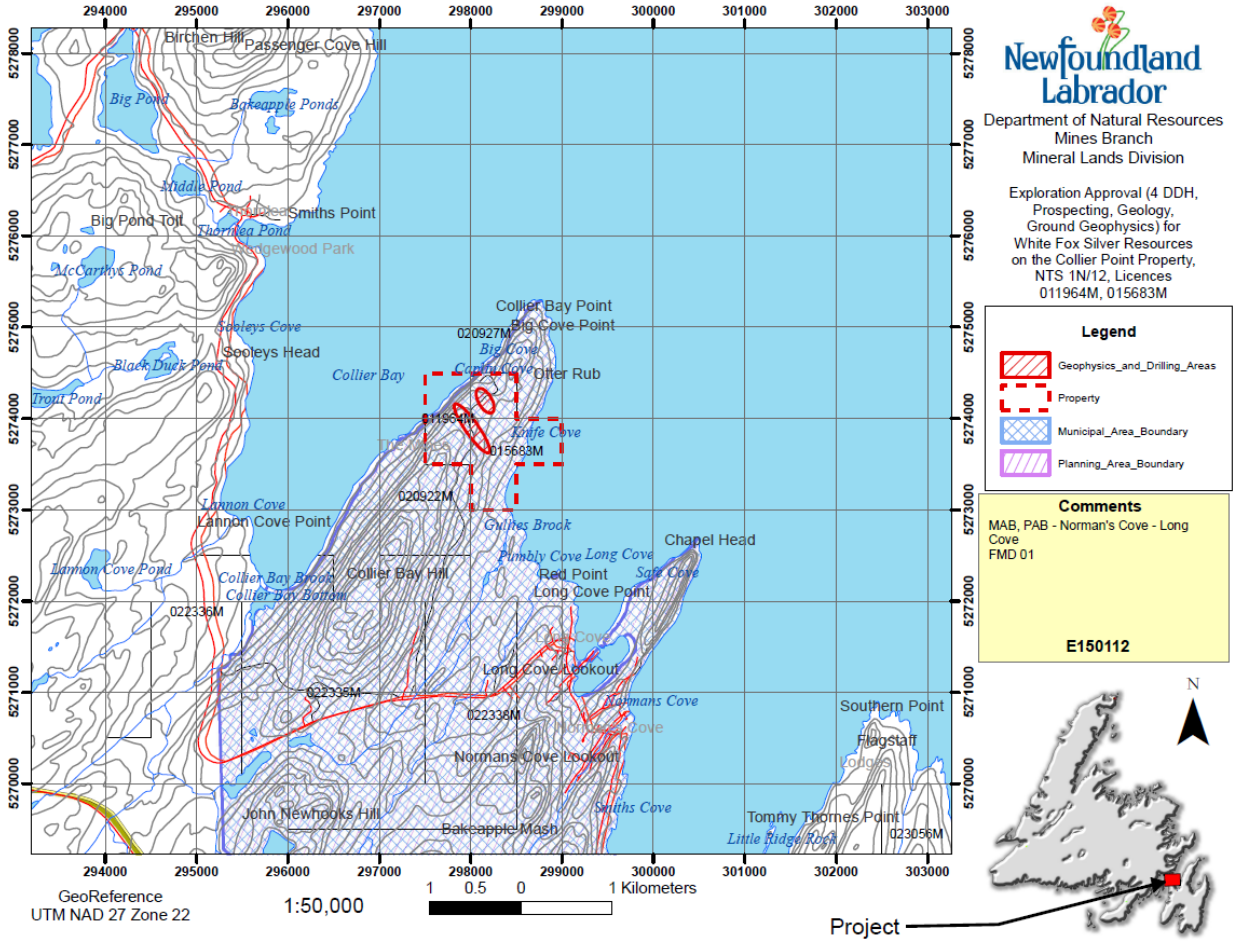


*Fig. 1.4:* Location of the Collier Point Barite property field area, within the municipality of Norman's Cove, Newfoundland (Department of Natural Resources, Newfoundland & Labrador)

### 1.2.1 Geology

The Collier Point property lies within the Avalon Tectonostratigraphic Zone of the Newfoundland Appalachians, and is underlain by the Late Proterozoic Musgravetown Group.

The southeastern part of the property is underlain by rocks of the Crown Hill Formation, which comprises of red pebble conglomerate and sandstone, with local red siltstone at the base and minor green conglomerate. The bedrock in the entire Collier Peninsula is a Precambrian arkosic sandstone and siltstone of the Hadrynian Heart's Desire Formation, which is interpreted to have formed in a shallow current swept submerged to deltaic environment. The arkose host is graded, shows evidence of cross bedding, and has been locally folded into a northeast trending asymmetric anticline of clastic sediments [McCartney, 1967]. The strike of the arkose varies from 035° to 070°E, and the dip varies from 10° to 40°.

### 1.2.2 Barite Veins

Barite is enclosed in the arkose host, in the form of massive and brecciated vein mineralization within an open fracture. The property hosts two veins. The main vein has a typical thickness of 1 m (maximum thickness of 3.6 m near the shoreline), and was exposed for more than 600 m along its strike. The strike of the barite veins varies from 330° to 360°, and the dip varies from 70°W to vertical across Collier Point. The barite mineralization demonstrates a primary "pinch and swell" structure both along strike and down dip. As a result of this structure, the barite vein varies in thickness from 0.30 m to 4 m, traced along a 40 m section of the vein [Hutchings, 1982]. The vein is assumed to have been emplaced as part of a regional scale hydrothermal plumbing system, which developed in a fault that transected the asymmetric anticline at Collier Point [Fracflow Consultants Inc., 1998].

### 1.2.3 Alteration and Breccia Zones

The barite is enclosed in an alteration zone within which the green-grey arkosic sandstone variably alters to a brown to yellowish friable condition, reflecting a loss of matrix cement. This alteration zone intensifies towards the barite vein mineralization, and forms a non-cohesive contact between the barite vein and the host rock [Hutchings, 1994]. The contacts

between the host arkosic sandstone and the barite vein are generally sharp, and the zones of alteration, mineralization, and brecciation have sharp contacts. Abrupt changes from massive to breccia zones, which consist of barite, calcite and fragmented sandstones were also observed. The white calcite occurring in breccia zones and on fractures, may or may not be associated with barite [Hutchings, 1994].

*Fig. 1.5:* Collier Point Barite vein looking south along its strike, and demonstrating a pinch and swell structure along strike and down dip [Howse, 1992]

# Chapter 2

## Theory and Method

This research is focused on borehole seismic interferometric experiments, where a barite vein below the surface is imaged using the virtual source method applied to walk-away vertical seismic profiles (VSPs). In this method, hydrophones are lowered down a monitoring well (borehole) filled with water, and seismic sources are located on the horizontal surface at various offsets from the well. The borehole receivers are transformed to virtual borehole sources via seismic interferometry and the contributions from surface sources are recorded on borehole receivers.

A virtual source is simulated at a borehole receiver at which the direct wave passes through, and is reflected off the target and back into adjacent borehole receivers. The virtual source method when applied to the dataset, theoretically results in the source and receiver being placed in the same borehole, and can hence be treated in the same way as a conventional surface profile in which the sources and receivers are placed at the surface. The data can then be processed using conventional seismic methods with standard CMP methods being used to produce the final image [Brand, 2010]. The positions of the receiver and source arrays address problems associated with surface profiling, such as minimal recovery of reflections and large angles of emergence.

## 2.1 Virtual Source Method in Seismic Interferometry

Claerbout proposed that "one side of the autocorrelation of the seismogram due to an impulsive source at depth is the seismogram due to an impulsive source on the surface" [Claerbout, 1968]. Essentially, he demonstrated that the cross-correlation of two traces recorded at two separate locations, results in a trace equivalent to the trace that would have been recorded at the second location, due to a source at the first location. **Seismic interferometry** is the process of cross-correlating a signal pair located at different receiver locations to reconstruct the impulse response of the medium between the receivers, and gain useful information about the subsurface. As seismic interferometry methods can virtually move a source into a location within the borehole, they can be applied in drilling operations to image the subsurface adjacent to the borehole in situations where conventional surface seismic methods are not feasible.

The virtual source method in seismic interferometry has been proposed to image the subsurface in such situations arising from complex, distorting subsurface geometries, and below associated heterogeneous overburdens without prior knowledge of overburden velocities and near surface changes. According to the **virtual source method**, if a given pair of receivers record waves excited by sources that populate a closed surface enclosing two receivers, the correlation of the wavefield recorded by the receivers when stacked over the physical sources should produce the true impulse response between the receivers [Bakulin and Calvert, 2006], i.e. the impulse response is obtained by cross-correlating the signal pair to reproduce a virtual source-receiver pair that is stacked over the physical sources. This results in imaging of the subsurface adjacent to the virtual source location. There is no 'real' source placed at the receiver location, hence it is called a 'virtual' source [Bakulin and Calvert, 2006] (Figure 2.1).

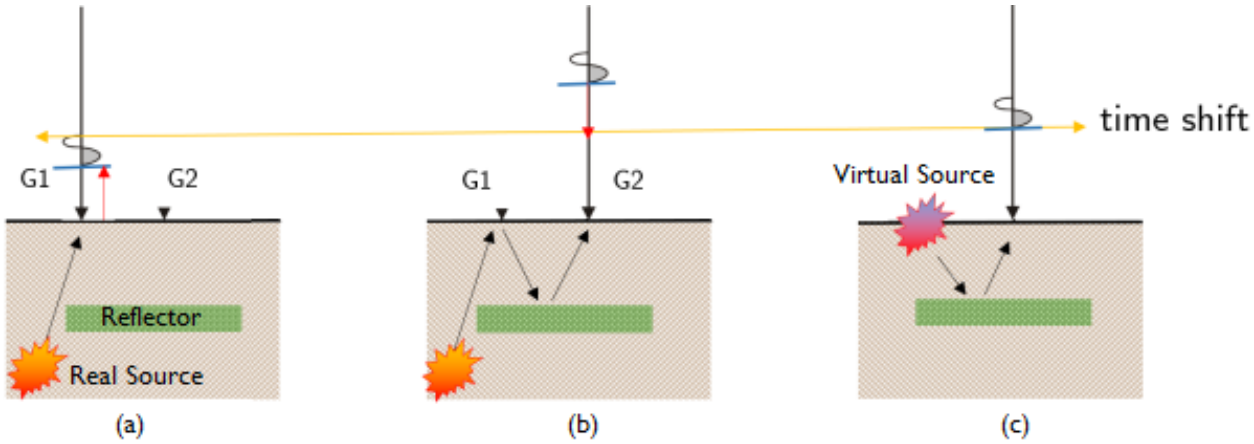


*Fig. 2.1:* Diagram representing creation of a virtual source at a receiver location Consider a theoretical situation comprising of a reflecting body in the subsurface, and a pair of recording devices, i.e. geophones located on the surface - G1 and G2. (a) - A subsurface source emits a wave to the surface that is received by geophone, G1. (b) - A second geophone, G2, receives a reflected wave from a reflector. (c) - The two signals recorded at G1 (Figure 2.1a) and G2 (Figure 2.1b) are cross-correlated. The procedure creates a time-shift due to which the travel path from the source to G1 is removed. (c) - Therefore, the resultant trace is theoretically the same as recording the contributions due to a source at G1, and is thereby a 'virtual source'. Adapted from [Schuster, 2009]

The resulting data can be treated as traditional CMP data, with an added advantage of an increased signal to noise ratio. Furthermore, re-datuming the surface sources into the borehole creates a more favourable source-receiver geometry for imaging steeply dipping targets, addressing problems such as minimal recovery of reflections and large angles of emergence. The relocation of the sources below the distorting effects of the overburden reduces the effect of complex and heterogeneous overburden velocity distributions which defocus the seismic energy and produces a poorly resolved final seismic image. Another advantage is that it can be utilized without prior knowledge of the time-varying subsurface velocities between the true surface sources and receivers [Hurich and Deemer, 2013]. This research will be focused on borehole seismic interferometric experiments at the Collier Point Barite property in Eastern Newfoundland, where a barite vein below the surface will be imaged using the virtual source method of seismic interferometry.

## 2.2 Interferometry Application at Collier Point

The interferometry experiment at Collier Point, NL, is conducted in the form of a walk -away seismic survey, using a series of live shot sources located on the surface at intervals of approximately 2 metres, resulting in a source array of 42 m in one direction/pass. The contribution due to the sources is recorded in the borehole using a hydrophone receiver cable. The sources were located in bedrock and charge sizes chosen to maximize high frequencies that enable higher quality imaging of the thin (1 - 4 m) barite vein. The field experiment at Collier Point yields a source frequency bandwidth of approximately 100 - 500 Hz.

Seismic methods study the changes in elastic rock properties (such as lithological or structural boundaries) as P and S-waves propagate through the Earth's subsurface, resulting in reflection, refraction and scattering of seismic waves. Interpretation of the seismic wavefield and creation of a wavefield model requires knowledge of elastic rock properties, such as P-wave velocity ($V_P$), S-wave velocity ($V_S$), and density of the medium the wave is propagating through, $\rho$. These elastic rock properties can be measured from borehole and laboratory measurements. The following chapter evaluates the elastic physical properties (acoustic velocities and densities) of the arkosic host and barite vein at the Collier Point barite property, with the objective of assessing the likelihood of imaging the barite target using the seismic reflection technique.

# Chapter 3

# Physical Rock Properties and Reflection Detectability

## 3.1 Introduction

To image a geological target using seismic methods, there must be a sufficiently high impedance contrast between the contrasting lithologies of the host and the target to produce detectable seismic reflections. Therefore, the **acoustic impedance** contrast between adjacent lithologies is one of the most important factors that determines the strength of the response from a seismic reflector. Other factors such as the geometry and size of the target also affect the strength of the response from a seismic reflector.

**Acoustic impedance** ($Z$) is defined as measure of opposition that a system presents to the acoustic flow, in response to an acoustic pressure applied to a system. It is described by the following relation:

$$Z = V_P \rho \tag{3.1}$$

Where $V_P$ is the velocity of the P-wave and $\rho$ is the density of the material the wave is propagating through. As the seismic wave interacts with the boundary separating the two

layers with differing acoustic impedences, some of the energy is reflected at the boundary, while some of the energy is transmitted through the boundary. The amplitude of the reflected wave is predicted by the product of the amplitude of the incident wave and the **seismic reflection coefficient,** $R$.

The reflection coefficient, R, for a normal incidence, planar P-wave modified for a simplified case of the Zoeppritz equations in a two-layer model is approximated by the following equation:

$$R = \frac{Z_2 - Z_1}{Z_2 + Z_1} = \frac{V_{P_2}\rho_2 - V_{P_1}\rho_1}{V_{P_2}\rho_2 + V_{P_1}\rho_1} \tag{3.2}$$

Where $V_{P_1}$, $V_{P_2}$ and $\rho_1$, $\rho_2$ are the P-wave velocities and densities for the first and second layers respectively. It is suggested [Salisbury et al., 1996] that in order to observe a reflection coefficient under ordinary field conditions, a minimum reflection coefficient of at least $\pm$ 0.06 is required.

Velocity and density measurements of the arkose and barite yield information about the acoustic impedance, and therefore the P-wave reflection coefficient between the arkose and the barite, giving an indication on how strong the reflection from the barite vein may be. Therefore, knowledge of the layer velocities ($V_P$, $V_S$) and densities ($\rho$) is required to ascertain reflectivity and assess the likelihood of observing an interpretable reflection signal.

This section discusses the acoustic velocities and densities of the arkosic bedrock and barite vein (and their resulting acoustic impedances and reflection coefficient), from samples obtained at the field site at Collier Point, NL.

## 3.2 Method

The **densities** of the arkose bedrock and the barite samples were measured at room temperature and pressure using the Archimedes Principle, where the density is calculated as:

$$\text{Density } (\rho) = \frac{\text{Mass of sample in air}}{\text{Mass of sample in air - Mass of sample in water}} \tag{3.3}$$

The **acoustic velocities** of the arkosic sandstone and barite were measured at room temperature and pressure using ASTM standards in the Geomechanics Laboratory. The rock samples were cored to diameters of 19 mm, and their ends were flattened. Shear couplant was applied to both ends of the core for better signal transmission between the transducer and the core. The transducers measure both P and S waves. A *pulser* was used to send a pulse through the *transducer*, which is transmitted through the core. The other transducer receives a transmitted signal which is amplified. Both channels of signals were synchronised and viewed through an Oscilloscope (Figure 3.1).

The **porosities** of the arkose sandstone and the barite vein are calculated from samples collected at the field site at Collier Point. The samples are saturated in water and placed into a vaccuumed container overnight to de-gass the samples and allow for the water to flow into the pore spaces. The porosity was measured by using the following formula:

$$\text{Porosity } (\phi) = \frac{\text{Pore Volume (mL)}}{\text{Total Volume (mL)}} = \frac{\text{Wt. of saturated core (g) - Wt. of dry core (g)}}{\text{Total Volume (mL)}} \tag{3.4}$$

As in the case of water, 1g = 1 mL, Equation 3.4 can be updated to:

$$\text{Porosity } (\phi) = \frac{\text{Pore Volume (mL)}}{\text{Total Volume (mL)}} = \frac{\text{Volume of water in pores (mL)}}{\text{Total Volume (mL)}} \tag{3.5}$$

The total volume of the samples is calculated from their masses and densities to determine the porosity.

## 3.3 Arkosic Bedrock

The host rock at the Collier Point Barite property is a Precambrian arkosic sandstone and siltstone of the Hadrynian Heart's Desire Formation. It varies in colour from green to gray. The arkose is graded and shows some evidence of cross bedding [Howse, 1992]. Minor white veins have been seen on the bedrock at the surface in some regions.

### 3.3.1 Density of Arkosic Bedrock

The density of the arkosic bedrock was measured by using the Archimedes Principle and resulted in an average density of 2.69 g/cc (Table 3.1).

*Tab. 3.1:* Densities of the arkosic bedrock from Collier Point, NL

| No. | Sample | Density g/cc |
|---|---|---|
| 1 | A1 | 2.68 |
| 2 | A2 | 2.67 |
| 3 | A3 | 2.68 |
| 4 | A4 | 2.69 |
| 5 | A5 | 2.71 |
| 6 | A6 | 2.7 |
| | Average | $2.69 \pm 0.014$ |

### 3.3.2 Porosity of Arkosic Bedrock

The porosity of the arkosic bedrock was measured and resulted in an average porosity of 1.26 % (Table 3.2).

*Tab. 3.2:* Porosities of the arkosic bedrock from Collier Point, NL

| No. | Sample | Porosity % |
|---|---|---|
| 1 | A1 | 1.39 |
| 2 | A2 | 1.81 |
| 3 | A3 | 1.76 |
| 4 | A4 | 0.95 |
| 5 | A5 | 0.78 |
| 6 | A6 | 0.84 |
| | Average | 1.26 ± 0.46 |

### 3.3.3 Acoustic Velocity of Arkosic Bedrock

The acoustic velocities of the arkosic sandstone were measured using cores from the field site, and conducted by Dr. Yingjian Xiao to determine the P-wave and S-wave velocities. The acoustic testing of the arkose cores indicated an average P-wave velocity of 5042 m/sec and an average S-wave velocity of 3059 m/sec (Table 3.3).

*(a)* Arkosic bedrock sample used for drilling cores

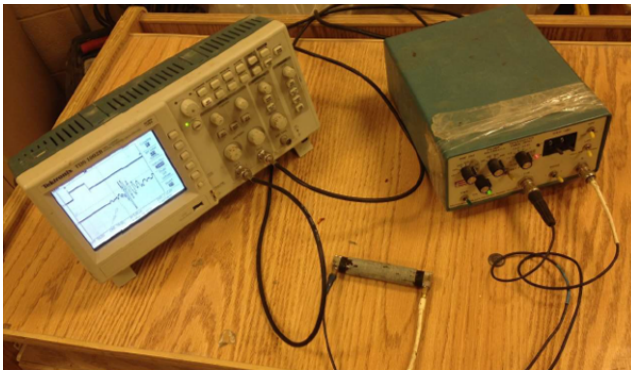

*(b)* Photograph demonstrating acoustic testing on arkosic bedrock core

*Fig. 3.1:* Acoustic velocity testing on arkosic bedrock using ASTM standards

*Tab. 3.3:* Acoustic velocities of the arkosic bedrock from Collier Point, NL

| No. | Sample | P-wave Velocity m/sec | S-wave Velocity m/sec |
|---|---|---|---|
| 1 | A1 | 5007 | 3017 |
| 2 | A2 | 4793 | 2945 |
| 3 | A3 | 4641 | 2852 |
| 4 | A4 | 4863 | 2944 |
| 5 | A5 | 5526 | 3265 |
| 6 | A6 | 5424 | 3330 |
| | Average | 5042 ± 356 | 3059 ± 193 |

*Tab. 3.4:* P-wave velocities and associated acoustic impedance of arkosic bedrock from Collier Point, NL

| Sample | Density g/cc | Velocity m/sec | Acoustic Impedance $kg\ sec^{-1}m^{-2}$ |
|---|---|---|---|
| 1 | 2.68 | 5007 | 13.4 |
| 2 | 2.67 | 4793 | 12.8 |
| 3 | 2.68 | 4641 | 12.4 |
| 4 | 2.69 | 4863 | 13.1 |
| 5 | 2.71 | 5526 | 15.1 |
| 6 | 2.7 | 5424 | 14.6 |
| | **avg. density** 2.69 ± 0.014 | **avg. velocity** 5042 ± 356 | **avg. impedance** 13.6 ± 10.2 |

## 3.4 Barite

The barite at Collier Point is in the form of a vein enclosed in the arkose host. The barite within the vein is massive, coarse bladed or banded, and the colour varies from pink to white, and occasionally a dark hue (Figure 3.2b). The colour variation is not associated with any obvious compositional variations. The barite ore has an average high purity value of 93% $BaSO_4$, which makes it of medical grade [Fracflow Consultants Inc., 1998].

*(a)* Barite hand samples - note large porosity

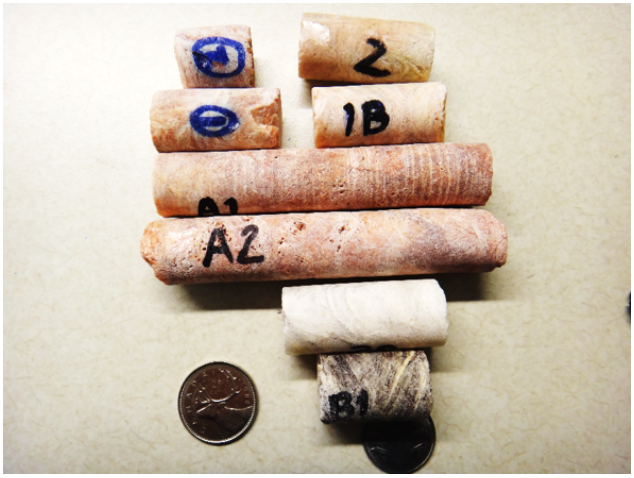


*(b)* Barite cores used for acoustic velocity testing - note wide variation in colour

*Fig. 3.2:* Barite samples from the Collier Point Barite Property

### 3.4.1 Density of Barite

The density of the barite cores was measured by using the Archimedes Principle and resulted in an average density of 4.26 g/cc (Table 3.5).

*Tab. 3.5:* Densities of the barite cores from Collier Point, NL

| No | Sample | Density g/cc |
|---|---|---|
| 1 | 1B | 4.25 |
| 2 | 2 | 4.27 |
| 3 | 3C | 4.39 |
| 4 | A1 | 4.13 |
| 5 | B1 | 4.26 |
| 6 | TB1 | 4.29 |
| 7 | TB2 | 4.24 |
| | Average | 4.26 ± 0.07 |

### 3.4.2 Acoustic Velocity of Barite

The acoustic velocities of the barite vein were measured using cores from the field site, and conducted by Dr. Yingjian Xiao and the author to determine the P-wave and S-wave velocities. The testing resulted in a P-wave velocity ranging between 1622 - 3388 m/sec and a S-wave velocity ranging between 920 - 2023 m/sec. There is a large variation in velocity and correspondingly high standard deviation within the barite samples.

*Tab. 3.6:* Acoustic velocities of the barite cores from Collier Point, NL

| No. | Sample | P-wave Velocity m/sec | S-wave Velocity m/sec |
|---|---|---|---|
| 1 | 1B | 1622 | 920 |
| 2 | 2 | 3388 | 2023 |
| 3 | 3C | 2421 | 1868 |
| 4 | A1 | 3225 | 2017 |
| 5 | B1 | 1684 | 949 |
| 6 | TB1 | 1989 | 1120 |
| 7 | TB2 | 2640 | 1746 |
| | Average | 2425 ± 706 | 1521 ± 503 |

### 3.4.3 Porosity of Barite

The porosities of the barite vein appear to be extremely low in the range of 0.31 - 1.91 %. The intergranular porosities in the tested samples are clearly very small and therefore do not account for the velocity variation in barite (Table 3.6). However, it should be noted that the measured porosities (Table 3.7) are not indicative of the overall bulk porosities because the samples although visibly porous may not be permeable enough to allow the flow of water into the pore spaces. Furthermore, measurements were conducted at room temperature and pressure, and the pore spaces shrink with increasing depth and increasing lithostatic pressure, further decreasing the porosity of the barite with increasing depth.

*Tab. 3.7:* Porosities of the barite cores from Collier Point, NL

| No. | Sample | Porosity % |
|---|---|---|
| 1 | 1B | 1.05 |
| 2 | 2 | 0.87 |
| 3 | 3C | 0.31 |
| 4 | A1 | 0.74 |
| 5 | B1 | 0.83 |
| 6 | TB1 | 1.62 |
| 7 | TB2 | 1.91 |
| | Average | $1.05 \pm 0.55$ |

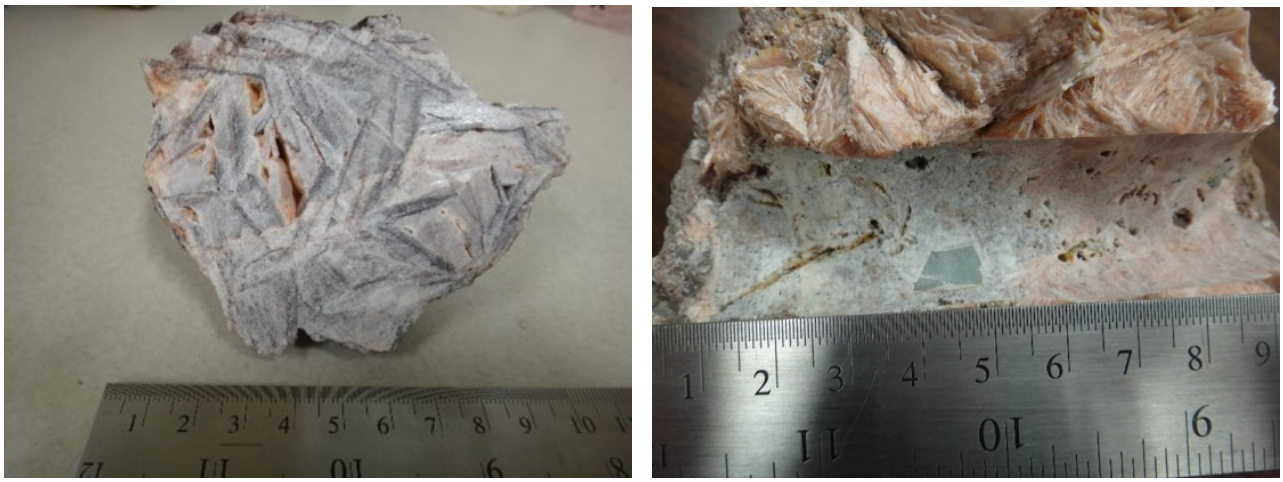

*(a)* Barite hand samples - note large porosity *(b)* Visible porosity through section of core

*Fig. 3.3:* Visible porosities in barite samples

## 3.5 Anisotropy Study on Barite

Anisotropy studies were conducted on the barite samples to investigate the cause of large variations in measured acoustic velocities which are independent of the density and porosity. The barite samples were cut into blocks and the acoustic velocity was measured in two directions perpendicular to each other, in each sample - along the crystallographic

c-axis (Figure 3.4a) and against the crystallographic c-axis in each block (Figure 3.4b). The anisotropy studies conducted on barite blocks demonstrate that the acoustic velocity is faster when measured along the c-axis and slower when measured against the c-axis (Table 3.8). Therefore, the anisotropy of the barite samples is likely the physical property resulting in the wide range of acoustic velocities on the barite core samples.

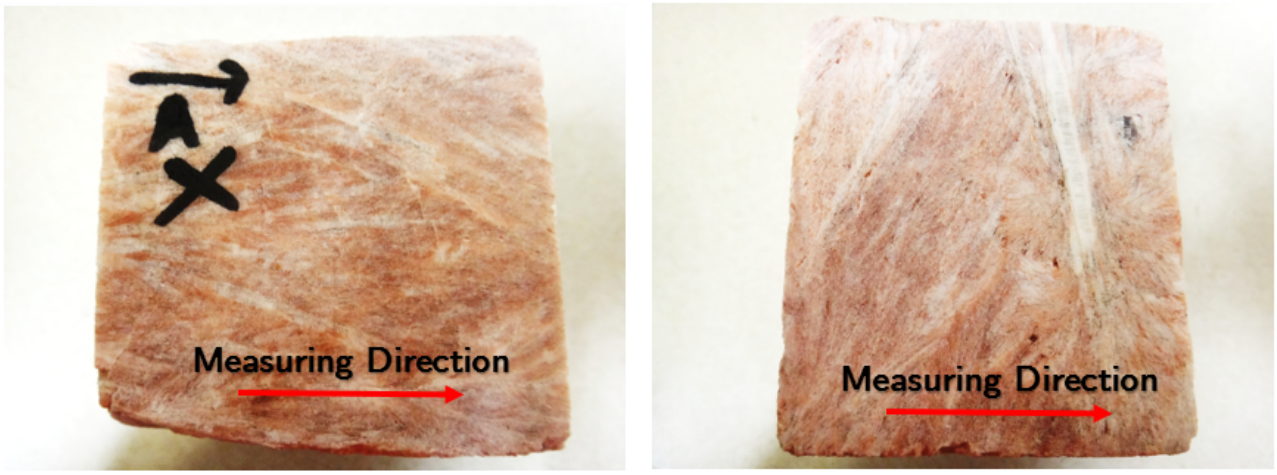


*(a)* Velocities measured along the c-axis *(b)* Velocities measured against the c-axis

*Fig. 3.4:* Barite blocks used in anisotropy study

*Tab. 3.9:* P-wave velocities, densities and acoustic impedance of barite blocks

| Sample | Density g/cc | Measuring Direction | Velocity m/sec | Acoustic Impedance $kg\ sec^{-1}m^{-2}$ |
|---|---|---|---|---|
| 1 | 4.30 | along c-axis | 3159 | 13.5 |
| | | against c-axis | 1468 | 6.3 |
| 2 | 4.31 | along c-axis | 4107 | 17.6 |
| | | against c-axis | 1380 | 5.9 |
| 4 | 4.66 | mixed orientation | 2265 | 12.2 |
| | | mixed orientation | 2847 | 15.3 |
| | **avg. density** | | **avg. velocity** | **avg. impedance** |
| | 4.43 | | 2538 | 11.2 |

*Tab. 3.8:* Dimensions and Acoustic Velocities of barite blocks

| Sample | Measuring Direction | Length mm | P-wave Velocity m/sec | S-wave m/sec |
|---|---|---|---|---|
| 1 | along c-axis | 63.18 | 3159 | 1981 |
| | against c-axis | 56.11 | 1468 | 863 |
| 2 | along c-axis | 81.99 | 4107 | 2247 |
| | against c-axis | 67.91 | 1380 | 720 |
| 4 | mixed orientation | 89.81 | 2265 | 1997 |
| | mixed orientation | 89.29 | 2847 | 1994 |
| | | | **avg. velocity** | **avg. velocity** |
| | along c-axis | | 3177 | 2075 |
| | against c-axis | | 1898 | 1193 |
| | | | **Overall avg. velocity** | **Overall avg. velocity** |
| | | | 2538 | 1634 |

## 3.6 Discussion of Reflectivity

As discussed in Section 3.1, the difference in acoustic impedance between successive rock layers dictates the reflection coefficient, and a large impedance mismatch results in a large reflection coefficient. The acoustic impedance is a function of the P-wave velocity ($V_P$) and the density ($\rho$). The geometry and size of the target also affects the resolution and detectability from a seismic reflector, as they affect the *reflection amplitude*.

### 3.6.1 Reflectivity changes due to macro-porosity

This section discusses the effect of macro-porosity on the reflection coefficient. The presence of macro-porosity would result in significant changes on the reflection coefficient, as the macro-porosity causes a reduction in the bulk density and P-wave velocity, thereby affecting the acoustic impedance and reflection coefficient.

There is an obvious presence of macro-porosity within the barite in some of the hand-

samples from Collier Point (Figure 3.2a) which is not addressed by the measured barite samples with no significant macro-porosity (Table 3.7), i.e. the laboratory-measured porosities ($\approx 1.05\%$) do not reflect the apparent porosities clearly visible in the samples. This may be due to two reasons:

1. The core samples do not have macro-porosity (which is the case in the samples), or
2. Very low permeability, which impedes flow of water into the pore spaces, thereby resulting in a low porosity measurement.

The **Wyllie time-average equation** [Wyllie et al., 1956] can be implemented to estimate the density and velocity variations associated with porosity, and therefore can be used to evaluate the potential affect of macro-porosity on the impedance of the barite and on the predicted reflection coefficient. For this evaluation, the **Wyllie time-average equation (1956)** is used to calculate the theoretical acoustic velocity of barite under a wide range of porosities (0% - 20%). It relates sonic velocities (in the form of slowness, 1/V) with the porosity of the rock and is based on the assumption that the total travel time recorded through a rock, is the sum of rock matrix travel time and pore fluid travel time. It is expressed as:

$$\frac{1}{V} = \frac{\phi}{V_f} + \frac{1-\phi}{V_m} \tag{3.6}$$

Where $\phi$: fractional porosity, V: velocity of the formation, $V_f$: velocity of the interstitial fluid, and $V_m$: velocity of the rock matrix. The associated density averaging equation is:

$$\rho = \phi\rho_f + (1-\phi)\rho_m \tag{3.7}$$

Where $\phi$ is the fractional porosity, $\rho_f$ is the density of the interstitial fluid (air or water), and $\rho_m$ is the density of the matrix (barite).

As the density of a rock decreases with increasing porosity, Equation 3.7 is used to calculate the theoretical density of a barite sample having a range of porosity ($\phi$) between 0% - 20%, and saturated with either air ($\rho_f = 0.001225$ g/cc) or water ($\rho_f = 1$ g/cc). The results are outlined in Table 3.10. Using Wyllie equations 3.6 and 3.7 and Table 3.10, theoretical plots of **porosity vs. P-wave velocity** for *air-saturated* (Figure 3.5a) and *water-saturated barite* (Figure 3.5b) are constructed for barite (average P-wave velocity 2477 of m/sec).

The **reflection coefficient** (Equation 3.2) is calculated for the model porosities (Plots 3.6a and 4.2b). While anisotropy accounts for the variation in seismic velocity measurements which ultimately affects reflectivity, it is noted that increasing porosity also results in a higher *theoretical reflection coefficient* due to an increased impedance difference. The reflection coefficient can increase from 0.1 at 0% *air-saturated* porosity to 0.56 at 20% *air-saturated* macro-porosity, similarly increasing from 0.1 at 0% *water-saturated* porosity to 0.26 at 20% *water-saturated* macro-porosity, which is a significant increase in reflection coefficient. Therefore, in effect, the true reflection coefficient from the arkose-barite contact at Collier Point may actually be higher than that projected by laboratory measurements which do not account for significant porosity.

*Tab. 3.10:* Recalculated densities of fluid-saturated barite (original density = 4.31 g/cc)

| Porosity (%) | Water Saturated Density | Air Saturated Density |
|---|---|---|
| 0% | 4.31 | 4.31 |
| 1% | 4.27 | 4.26 |
| 2% | 4.24 | 4.22 |
| 3% | 4.21 | 4.18 |
| 4% | 4.17 | 4.13 |
| 5% | 4.14 | 4.09 |
| 6% | 4.11 | 4.05 |
| 7% | 4.07 | 4.01 |
| 8% | 4.04 | 3.96 |
| 9% | 4.01 | 3.92 |
| 10% | 3.97 | 3.87 |
| 11% | 3.94 | 3.83 |
| 12% | 3.91 | 3.79 |
| 13% | 3.87 | 3.74 |
| 14% | 3.84 | 3.70 |
| 15% | 3.81 | 3.66 |
| 16% | 3.78 | 3.62 |
| 17% | 3.74 | 3.57 |
| 18% | 3.71 | 3.53 |
| 19% | 3.68 | 3.49 |
| 20% | 3.64 | 3.44 |

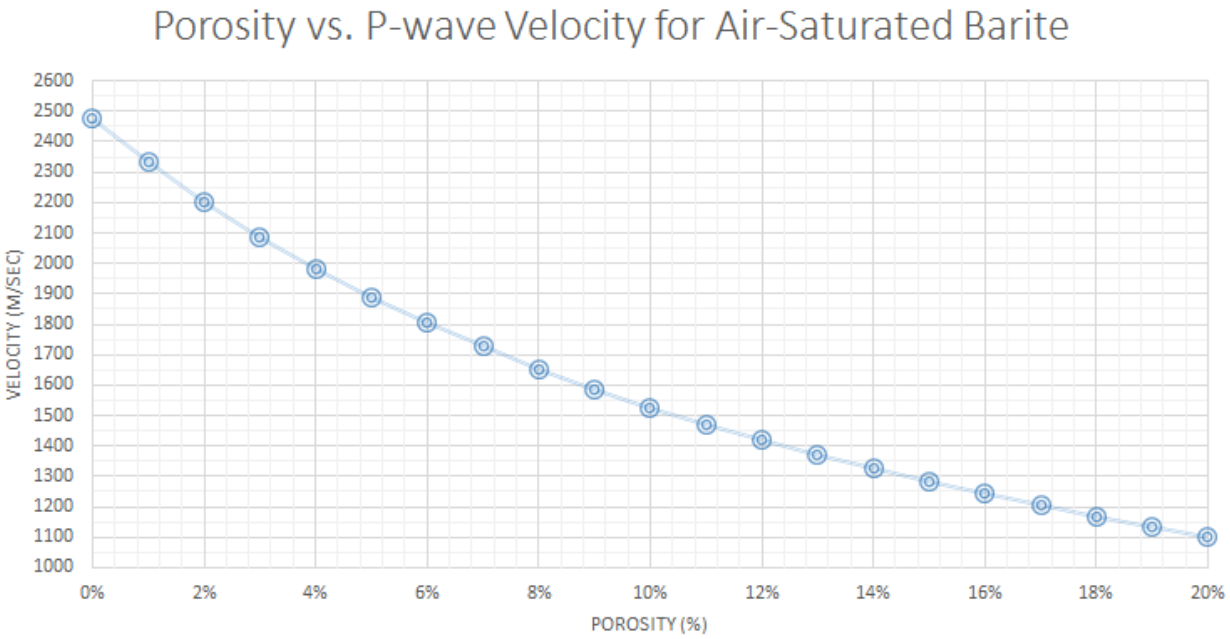


*(a)* Plot of air-saturated Porosity vs. Velocity for $V_m = 2477$ m/sec

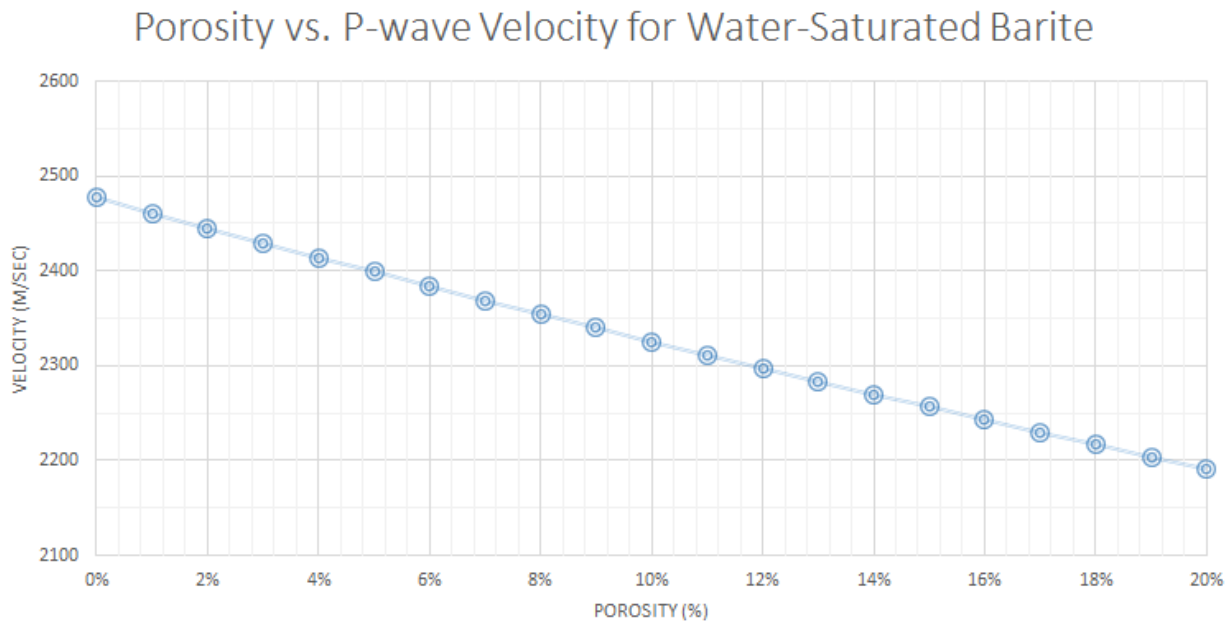


*(b)* Plot of water-saturated Porosity vs. Velocity for $V_m = 2477$ m/sec

*Fig. 3.5:* Plots of fluid-saturated Porosities vs. Velocity

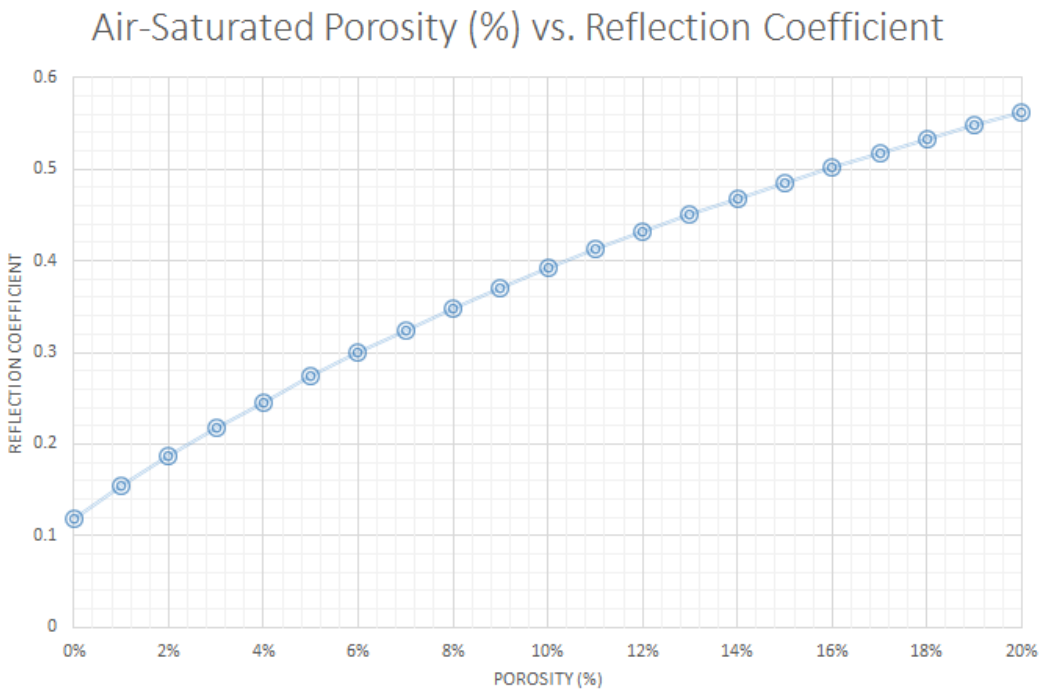


*(a)* Plot of air-saturated Porosity vs. Reflection Coefficient

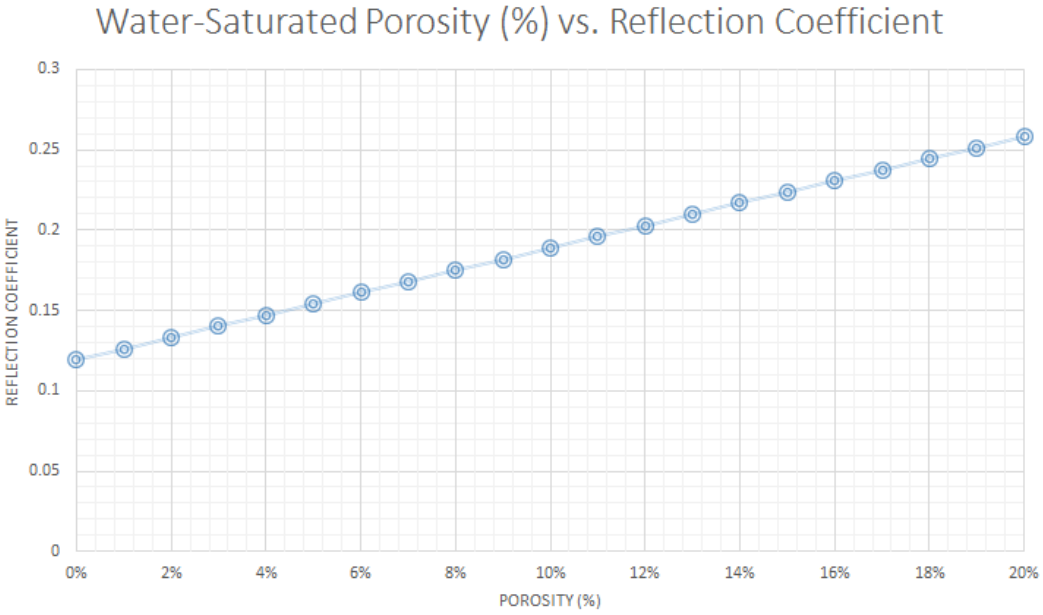


*(b)* Plot of water-saturated Porosity vs. Reflection Coefficient

*Fig. 3.6:* Plots of fluid-saturated Porosities vs. Reflection Coefficient

In summary, although some hand samples show significant macroporosity (Figure 3.3) (which could affect the seismic velocities), the large range in velocity (in the order of 1000 m/sec) in the measured samples (which do not show macroporosity) is largely due to anisotropy at the crystal level. Anisotropy and porosity are not linked. An increase in the porosity has the favourable effect of increasing the reflection coefficient by creating a larger impedance mismatch. By studying the Wyllie Equations for air-saturated (Figure 3.6a) and water-saturated (Figure 3.6b) barite, it is apparent that any inclusion of fluid within pores (at the field location) would result in a significantly higher reflection coefficient than values computed using straight averages. For example, **water-saturated barite with 5% porosity** would have a *P-wave Velocity of 2398 m/sec*, and a higher resultant reflection coefficient of - 0.15, compared to non-saturated barite which has an average *P-wave Velocity* of 2477 m/sec, and a smaller resultant reflection coefficient of - 0.11.

### 3.6.2 Reflectivity changes based on average data

Due to its anisotropic nature, and because the orientation of the barite crystals within the vein is unknown, we can assume random orientation in further calculations. Therefore, the P-wave and S-wave velocities of barite is the average of all measurements in all orientations. The reflection coefficient, R, was calculated as R = - 0.11 (which is greater than the minimum requirement of $\pm$ 0.06 [Salisbury et al., 1996]), therefore a detectable response could be expected from the arkose/barite interface based on average data (Table 3.11). However, it should be noted that the average acoustic velocities of the barite samples may not been indicative of the overall bulk elastic properties present in the subsurface due to certain regions of the barite vein being present in a fracture zone consisting of fragmented arkose, breccia and barite, which may decrease the impedance contrast, thereby reducing the reflection coefficient.

### 3.6.3 Resolution and detectability due to geometry of target

The geometry and size of the target plays an important role in the resolution and detectability of a response from the seismic target. The barite vein at Collier Point has a typical thickness of 1 m. Due to its 'pinch and swell' structure (Figure 1.5), it varies in thickness from 0.30 m to 4 m.

The **seismic resolution** is a function of the ability of the waveform to distinguish between adjacent layers i.e. the minimum distance between two adjacent layers for which they can be identified separately as two different interfaces instead of one. According to the *Rayleigh Criterion* for minimum resolvable detail, two nearby reflective interfaces should be about 1/4 wavelength ($\lambda$) in thickness to be distinguished separately. The wavelength ($\lambda$) is given by the formula:

$$\lambda = \frac{V}{f}, \tag{3.8}$$

$$\text{Therefore, the vertical seismic resolution, R} = \frac{\lambda}{4}, \tag{3.9}$$

where $V$ is the acoustic velocity of the layer and $f$ is the frequency. The seismic inteferometry experiment (Chapter 5) generates an average frequency ($f$) bandwidth of 100 - 500 Hz with a 300 Hz average, and the average velocity (V) of the barite vein is 2477 m/sec. Therefore the wavelength ($\lambda$) controlling the seismic resolution is between:

$$\lambda_1 = \frac{2477}{500} = 4.95 \text{ m} \tag{3.10}$$

and

$$\lambda_2 = \frac{2477}{100} = 24.8 \text{ m} \tag{3.11}$$

and the average wavelength is

$$\lambda_{avg} = \frac{2477}{300} = 8.26 \text{ m} \tag{3.12}$$

Using Eq. 3.9 the corresponding **seismic resolution** ($\lambda/4$) is:

- $R_1 = 1.23$ m for $\lambda_1$ at 500 Hz
- $R_2 = 6.2$ m for $\lambda_2$ at 100 Hz
- $R_{avg} = 2.1$ m for $\lambda_{avg}$ at 300 Hz

The seismic response to the thin barite vein results in both constructive and destructive interference as the seismic wavelet passes through the individual layers which modifies the peak-trough amplitude.The **maximum peak-trough amplitude** occurs at **1/4 $\lambda$ thickness** also known as the *tuning thickness* and is the *limit of resolution (R)*, i.e. it is the thinnest layer for which the front and back of the layer can be resolved. Therefore, the **highest amplitude response/limit of resolution** is at $\approx$ 1 m for 500 Hz frequency, $\approx$ 6 m for 100 Hz frequency, and similarly at $\approx$ 2 m for 300 Hz frequency.

As the target has a 'pinch and swell' structure and varies in thickness from 0.3 - 4 m, based on the above reasoning, the bandwidth of the dataset (100 - 500 Hz) is large enough to enable the tuning response in regions of the vein having a thickness between 1 m to 6 m. Therefore, the bandwidth of the dataset is optimal for creating a tuning response in the majority of the vein, except for regions where the thickness is less than 1 m. A more detailed investigation of the tuning response of the barite vein is given in Chapter 7.

## 3.7 Summary of Rock Properties and Detectability

Physical analysis of the rock types results in average P-wave values of 5042 m/sec for the arkosic bedrock and a range between 1622 - 3388 m/sec for the barite vein. The average density was 2.69 g/cc for the arkosic bedrock and 4.31 g/cc for the barite vein. The porosity

of the barite samples ranges between 0.31 - 1.05 % in the tested cores, which is not indicative of the bulk velocity as the barite vein in the field demonstrates a wide range of micro and macro-porosities (Figure 3.3).

By using the Wyllie Equation to calculate the theoretical acoustic velocity of barite under a wide range of porosities (0% - 20%), it is established that any macro-porosity within the barite causes a significant increase in the reflection coefficient (Section 3.6.1). Therefore, assuming macro-porosity in the Collier Point vein, the bulk reflection coefficient may be higher that that predicted from lab measurements (having a low porosity of $\approx$ 1.05 %), as increasing porosity causes a larger impedance contrast and therefore higher reflection coefficient. Furthermore, the frequency content of the data (100 Hz - 500 Hz) is adequate to allow $\mathbf{1/4}$ $\lambda$ frequency tuning in the majority of the vein, except for regions where the thickness is less than 1 m.

Therefore, the physical factors that affect the reflection coefficient and resolution are:

1. The interaction of the high P-wave velocity of the arkosic bedrock, along with the -
2. Lower P-wave velocity & higher density of the barite, which creates a large negative impedance contrast
3. The thickness and lateral variability of the barite target

The relationship between the velocity and density for the barite is not consistent with the directly proportional relationship generally demonstrated by normal silicates (i.e. increasing velocity with increasing density). Although density ($\rho$) of barite is very high, the velocity ($V_P$) does not show similar highs, and the two counter the value of the resultant acoustic impedance ($Z = V_p \ \rho$). Therefore, a significant reflection coefficient is produced mostly because of arkose's high velocity.

*Tab. 3.11:* Summary of average physical properties for the arkosic sandstone and barite vein at Collier Point

| Rock Type | $V_P$ m/sec | $V_s$ m/sec | Density g/cc | Porosity % | Acoustic Impedance $kg\ sec^{-1}m^{-2}$ | Reflection Coefficient |
|---|---|---|---|---|---|---|
| Arkose | 5042 | 3059 | 2.69 | 1.25 | 13.5 | |
| Barite | 2477 | 1573 | 4.31 | 1.05 | 10.6 | -0.11 |

# Chapter 4

## Experiment Optimization

This section studies the constraints imposed by the pre-existing geometry and setup of the experiment at Collier Point, NL and explores methods to optimize this particular experiment, through the use of ray-tracing analysis and creation of synthetic seismograms.

## 4.1 Ray-tracing analysis

Stationary phase rays (or image rays) are the raypaths that pass directly through a receiver (as a direct wave), and reflect off of the target and back to a secondary receiver. The travel-time from the receiver-target-secondary receiver is equivalent to a situation in which the source is present at one of the receivers. Stationary phase rays represent the kinematically correct raypaths that result in a stationary phase contribution during the summation of correlation gathers where only correctly located events constructively interfere. Not all potential raypaths result in stationary phase and under ideal conditions these contributions destructively interfere during summation. Raypath diagrams can be used to determine the feasibility of stationary phase in response to changing geometry of the VSP survey. The parameters of the survey (such as orientation of the borehole angle) can be adjusted to optimize the chances of producing maximum stationary phase contributions.

The ray-tracing program is implemented in MatLab using a script provided by Dr. Charles Hurich, and is used to study the interactions of stationary phase rays under the conditions of varying borehole and target dip angles. The script calculates the required source locations for downhole common mid-point gathers on a dipping target and dipping drill hole. It can be used to identify the surface source locations which produce a stationary phase contribution, and the location and fold of the common mid-point gathers resulting from the virtual sources. The ray-tracing program works by back-tracing the image ray from the reflection point on the target, through the receiver at which the virtual source is located and projects it back to the surface source location. One limitation of the ray-tracing solution is that it is an infinite bandwidth solution and doesn't provide the bandlimited response.

### 4.1.1 Physical Constraints and Ray-tracing Parameters

A optimal experimental setup would consist of a large source-receiver offset and the vein dipping in the direction of the borehole and surface source array (shot locations), which results in maximum stationary phase contributions, and therefore highest-quality imaging of the vein. Unfortunately physical constraints at the Collier Point Barite property exist in the form of sloping dug trenches and dense forest cover. These result in the only possible experimental setup to be conducted such that the vein is dipping away from the borehole and the surface source array (Figure 4.1) and a maximum source-surface offset of approximately 80 m at the field site, which is not optimal.

The parameters in the ray-tracing analysis are chosen to account for the physical constraints at the Collier Point field site, and resulting acquisition geometry. The borehole to target distance is set to 25 m. The initial depth of the virtual sources and receivers is set to 0.6 m. The total depth of the borehole is extended to 80 m. The number of receivers in the borehole is set to 42 with corresponding 42 virtual shots, having 2 m spacing. The maximum surface-source offset allowed is 60 m. The P-wave velocity was set to 5000 m/sec to simulate

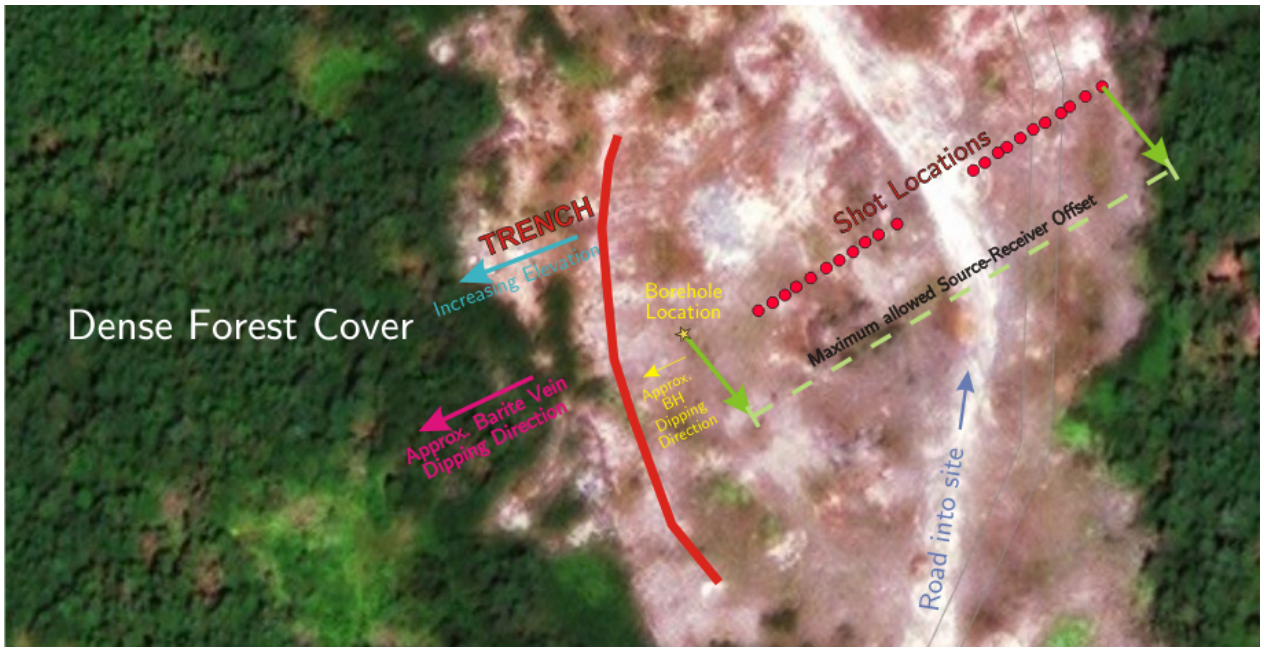


*Fig. 4.1:* Physical constraints leading to borehole dipping angles and surface source array positioning not optimal for imaging

velocities expected in the high-velocity hard bedrock of Collier Point, NL (Table 4.1).

Two simulation cases (Case I and Case II) were conducted to study the effect of varying borehole dip angles of 75° and 65°, on the final seismic image. The exact dip of the Collier Point vein is unknown and estimated from from 70°W to vertical across Collier Point (Subsection 1.2.2). Therefore, the dip of the near-vertical vein in the simulation cases were chosen to dip at 80°, i.e. at 100° from the surface, in a direction away from the borehole (Table 4.2).

*Tab. 4.1:* List of parameters and corresponding values used in Ray-tracing Program

| Parameter | Value |
|---|---|
| Borehole to target distance at surface | 25 m |
| P-wave Velocity | 5000 m/sec |
| Initial Depth of Virtual Sources and Receivers | 0.6 m |
| Depth Increment for Virtual Sources and Receivers | 2 m |
| Number of Receivers in Borehole | 42 m |
| Corresponding number of Virtual Sources | 42 m |
| Maximum Source Offset | 60 m |
| Maximum Depth of Borehole | 80 m |
| Maximum depth plotted in ray diagram | 100 m |

*Tab. 4.2:* Simulation Cases in the Ray-tracing Study

| Parameter | Case I | Case II |
|---|---|---|
| Dip of target with respect to surface | 100° | 100° |
| Dip of borehole with respect to surface | 75° | 65° |

### 4.1.2 Ray-path Diagrams

The ray-path diagrams demonstrate the stationary phase rays generated at the 22nd virtual source within the borehole, and maps the location of the true reflection points on the target for Cases I and II.

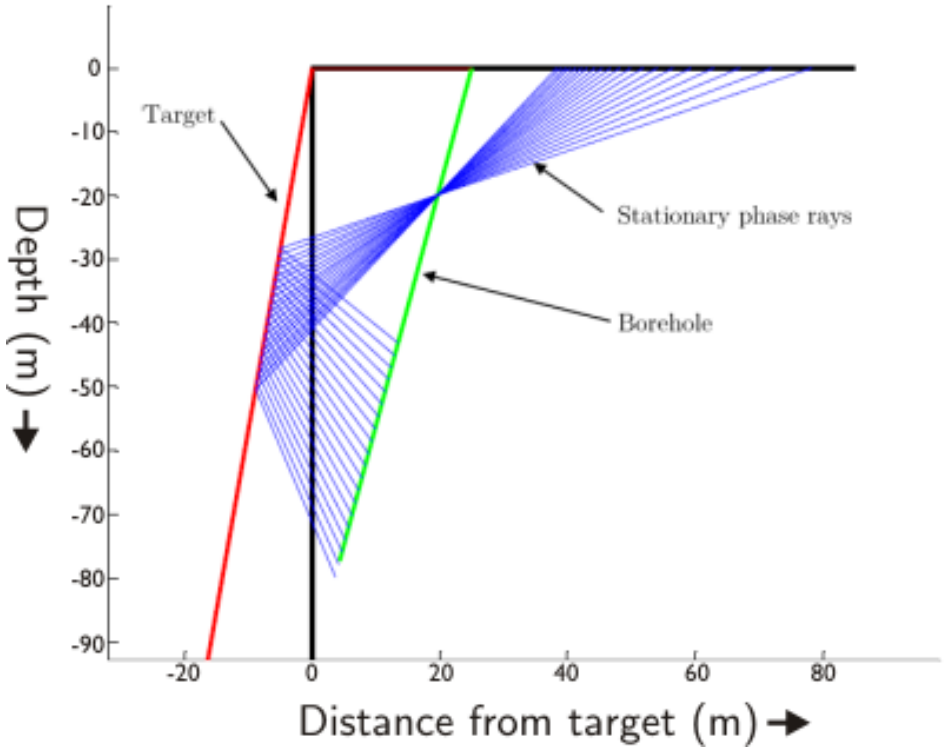


*(a)* Case I, produced with the target dipping at 80° away from the borehole, and the borehole dipping at 75° towards the target

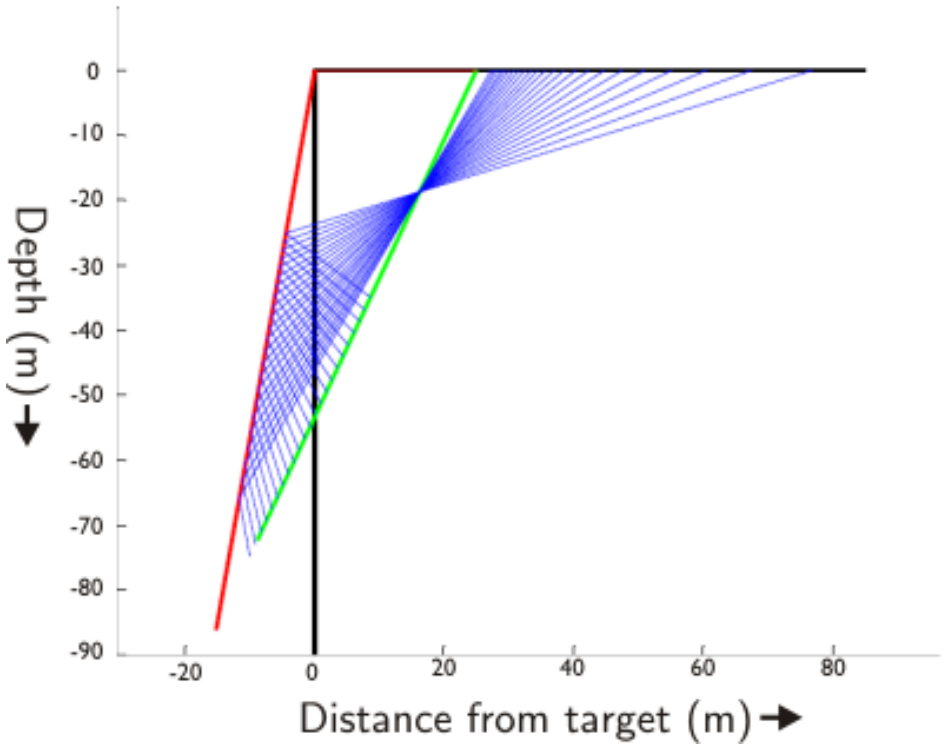


*(b)* Case II, produced with the target dipping at 80° away from the borehole, and the borehole dipping at 65° towards the target

*Fig. 4.2:* Raypath diagrams demonstrating stationary phase rays at the 22nd virtual source

### 4.1.3 Distance-time Graphs

The distance-time graphs demonstrate the direct wave and reflection for the model geometry, and help in assessing the time-separation between the direct wave and the reflection. A short time separation is undesirable as the resulting reflection would not be imageable. Additionally, studying the *moveout* of the reflections may provide some hints towards recognizing the reflection in the field records which can then be processed accordingly.

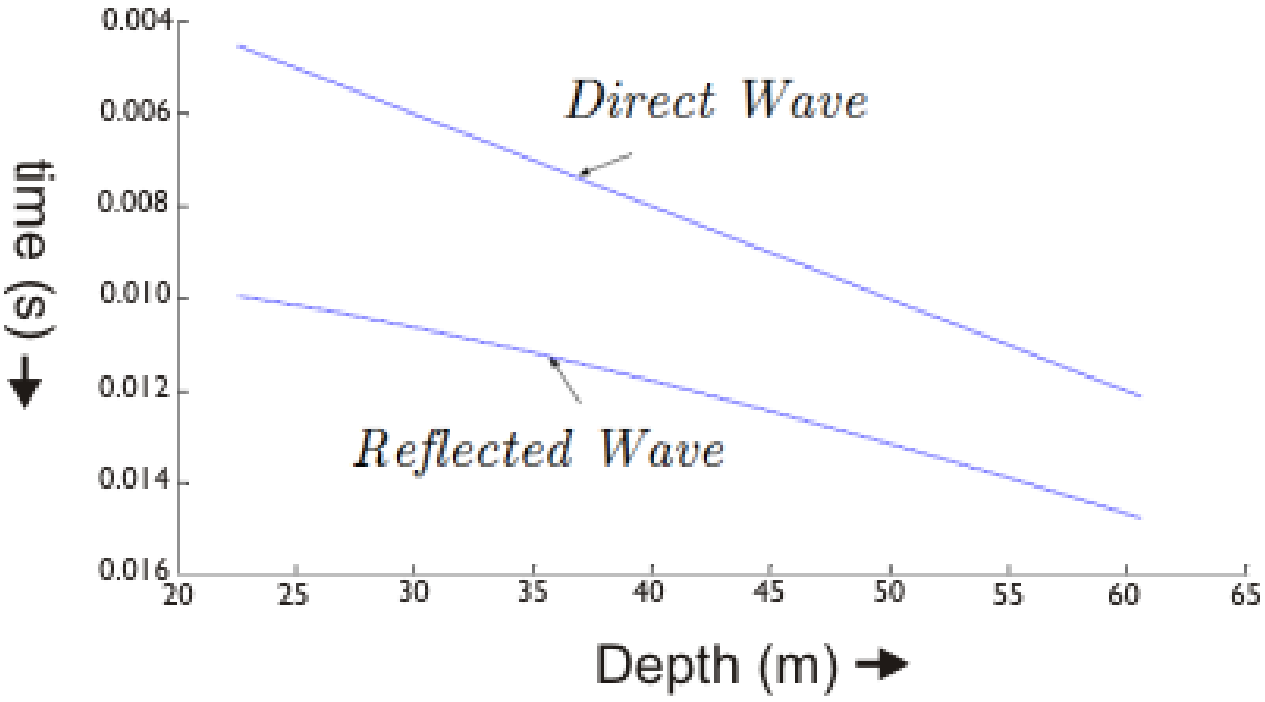


*(a)* Case I, produced with the target dipping at 80° away from the borehole, and the borehole dipping at 75° towards the target

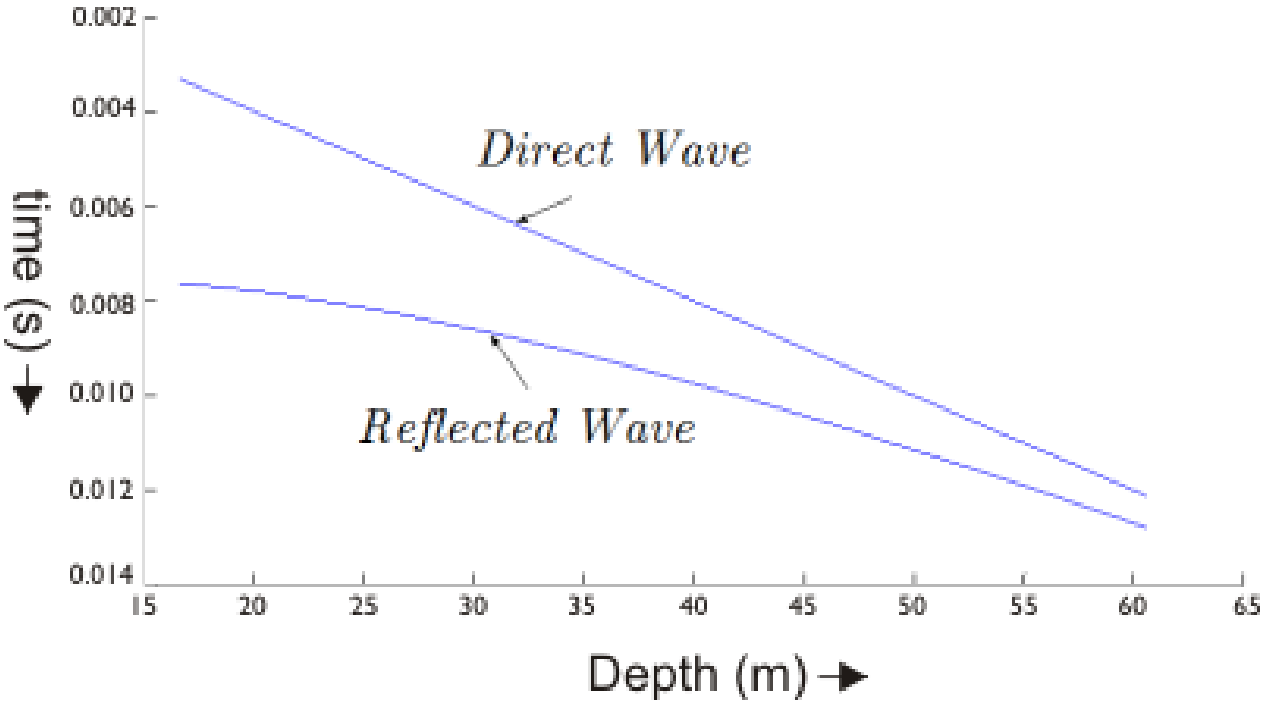


*(b)* Case II, produced with the target dipping at 80° away from the borehole, and the borehole dipping at 65° towards the target

*Fig. 4.3:* Distance-time graph demonstrating the direct wave and reflection for the model geometry

### 4.1.4 CMP Plots

The plots of CMP depth along borehole vs. Surface Source distance from the borehole demonstrate surface source locations required to satisfy stationary phase at corresponding CMP depth, and the plots of CMP depth along borehole vs. CMP Virtual Source-Receiver offset demonstrate the range of CMP source-receiver offsets which occur at different depths in the borehole. They help compare which orientation provides maximum stationary phase contributions in deeper regiona of the borehole, and the range of offsets available.

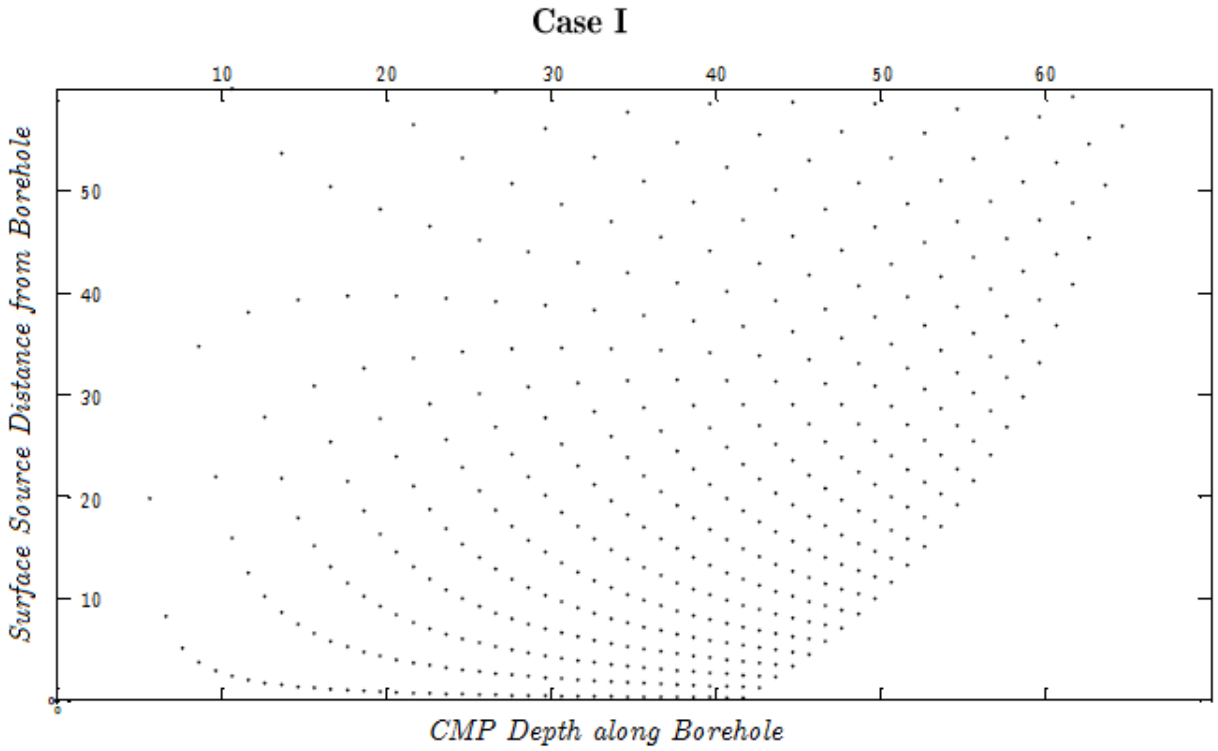


*(a)* Plot of CMP depth along the borehole vs. Surface Source Distance from the borehole

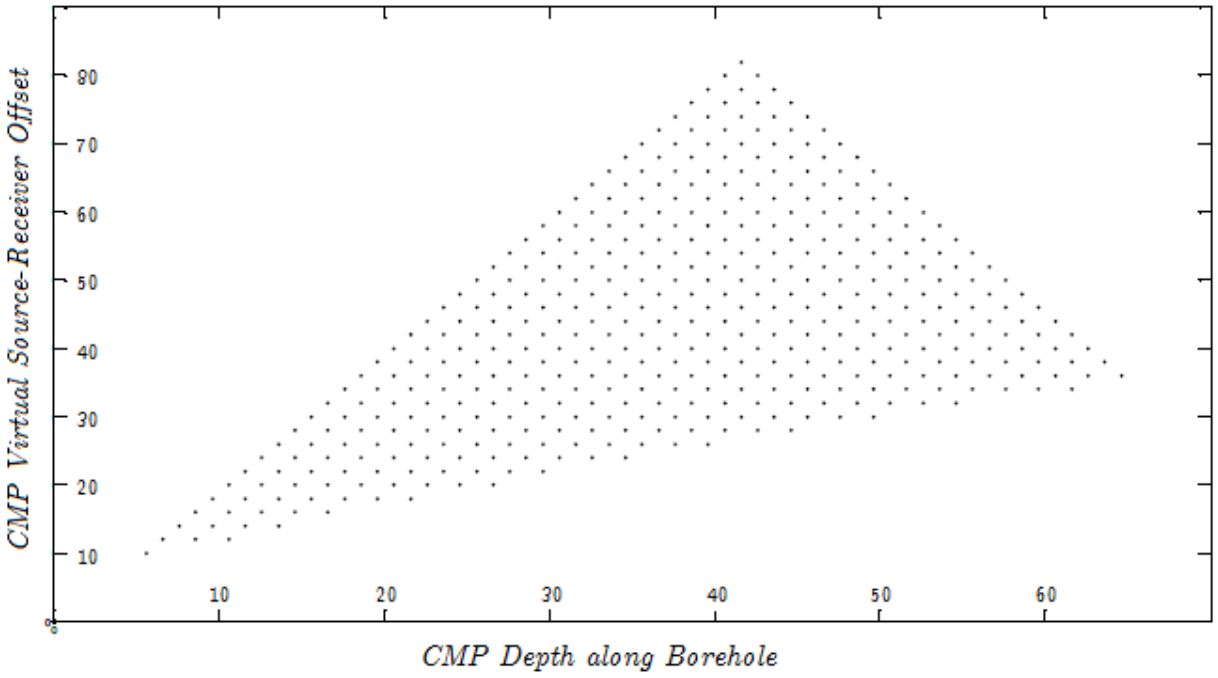


*(b)* Plot of CMP depth along borehole vs. CMP Virtual Source-Receiver offset

*Fig. 4.4:* Plots of CMP depth along borehole for Case I, produced with the target dipping at 80° away from the borehole, and the borehole dipping at 75° towards the target

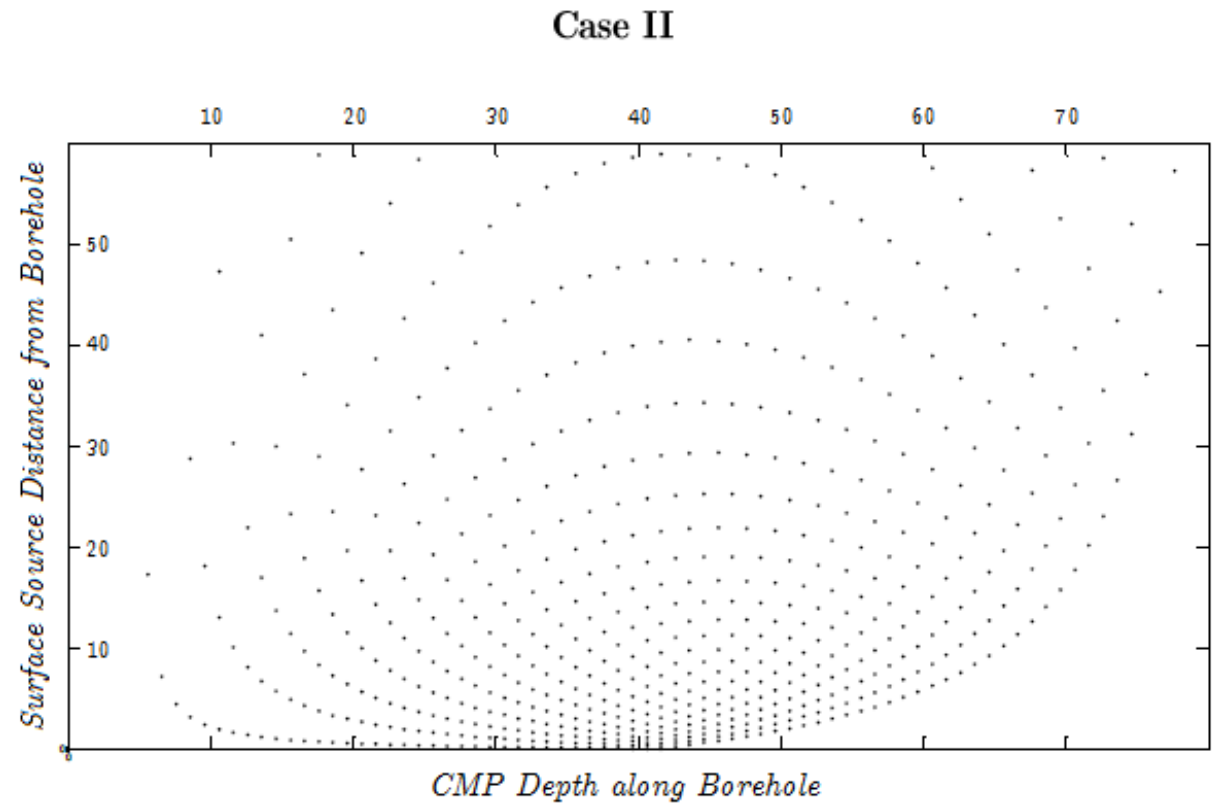


*(a)* Plot of CMP depth along the borehole vs. Surface Source Distance from the borehole

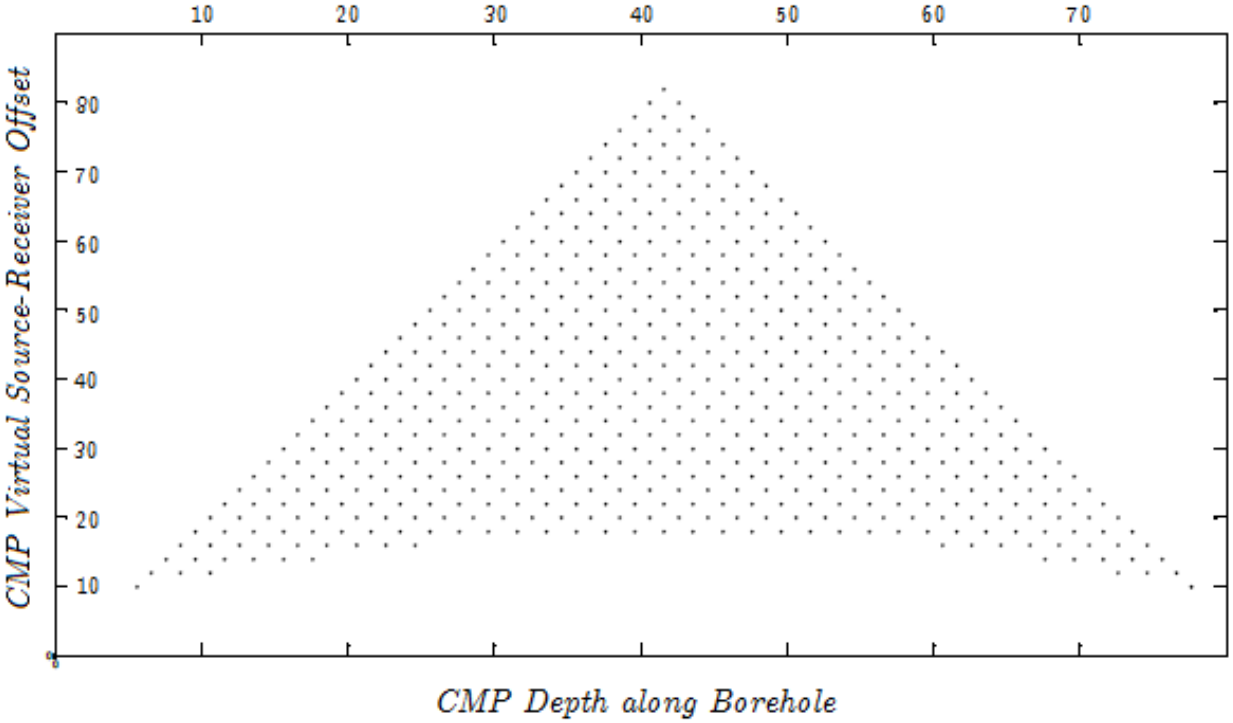


*(b)* Plot of CMP depth along borehole vs. CMP Virtual Source-Receiver offset

*Fig. 4.5:* Plots of CMP depth along borehole for Case II, produced with the target dipping at 80° away from the borehole, and the borehole dipping at 65° towards the target

### 4.1.5 Summary of Ray-tracing Analysis

The plot of *CMP depth along borehole vs. Surface Source distance from the borehole* demonstrates surface source locations required to satisfy stationary phase at corresponding CMP depth. In the shallower regions of the CMP gathers there are fewer stationary phase contributions from near offset surface sources, while in deeper regions of the CMP gathers, there is a higher possibility of stationary phase contributions from near and far offset surface sources. The orientation of the borehole in Case II at 65° allows for more stationary phase contributions in deeper regions of the borehole, compared to the orientation in Case I at 75°.

The plot of *CMP depth along borehole vs. CMP Virtual Source-Receiver offset* demonstrates the range of CMP source-receiver offsets which occur at different depths in the borehole. The range of offsets are higher in the mid-depth of the borehole (highest fold) and significantly decrease towards to top and the bottom of the borehole. A high fold is critical for the best image recovery. The geometry of the virtual source survey is a function of the number of downhole receivers and receiver spacing, as the downhole receivers ultimately represent the virtual sources. The orientation of the borehole in Case II (65°) allows for more stationary phase contributions in deeper regions of the borehole, which is desirable. Larger offsets imply that larger volumes of the subsurface can be imaged.

The *Distance-time graph* demonstrates the time separation between the direct wave and the reflected wave, which can be separately identified for the model geometries in both cases. While Case I (borehole dipping at 75° towards the target) provides a desirably large time separation between the direct wave and the reflected wave, Case II (borehole dipping at 65° towards the target), has a shorter time delay due to the orientation of the borehole towards the target, which could make the time separation and distinguishing of the direct ray and reflected ray difficult in further simulations and is undesirable.

Therefore, the ray-tracing analysis suggests that although the model geometry in Case II

(produced with the borehole dipping at 65° towards the target) provides sufficient stationary phase contributions to image the vein, and produces a wider range of offsets and images deeper regions of the borehole, it does not provide a sufficient time separation between the direct and reflected arrivals, which is rectified in Case I (borehole dipping at 75°). Case I provides a desirably large time separation at the expense of not imaging deeper regions of the borehole, while Case II provides a much less time separation as a trade-off to imaging deeper section of the borehole. An ideal borehole geometry would provide both, a sufficient time separation between direct and reflected arrivals and stationary phase contributions leading to better imaging in deeper regions of the borehole.

## 4.2 Finite Difference Modelling

As an additional guite to the field experiments, a synthetic seismogram study is carried out on a simplified 2-D geological model of the barite vein and surrounding bedrock at Collier Point, NL, prior to the actual field study. The exercise is aimed at imaging the steeply dipping barite vein, and to optimize the geometry and the data processing flow of the field experiments.

A simplified 2-D geological model representing the Collier Point barite vein and surrounding arkosic bedrock is created using a graphics program. The 2-D geological model is then used to create a velocity model using scripts based on the finite difference code obtained from the Seismic Unix package supported by the Center for Wave Phenomena (CWP) at the Colorado School of Mines. The velocity model is given values attributed to the arkosic bedrock and barite vein (Table 4.3). The velocity model is then used along with a 2-D finite-difference modelling program to generate synthetic seismic data, and study the effect of changing parameters, trace spacing and implementation issues prior to the actual field experiment, to simulate the real world geometric scenario of interest.

**Finite-difference modelling** is a 'time marching' procedure in which the appropriate scalar equation is solved recursively i.e. it calculates the motion at a point in the grid for a particular time step based on the motion already calculated for previous time steps. Because the method splits the whole area flexibly, it can be used to study complex structures composed by homogeneous or non-homogeneous formations [Wang et al., 2004]. Finite difference models may have difficulties in implementing accurate boundary conditions and may produce undesirable effects such as edge reflections and grid dispersion. The edge reflections from the sides and bottom of the model space can interfere with resulting synthetic seismograms. To minimize the effect of edge reflections, absorbing boundary conditions are set, which demonstrate viscous behavior to absorb the incident energy. Grid dispersion produces a delay between lower and higher signal frequencies as the wave propagates on a grid. It can be minimized by setting the grid spacing parameter (R) to less than 10 percent of the shortest wavelength used. As a result, the model needs to have 10 grids per wavelength for stability, and the limiting wavelength is calculated by dividing the smallest velocity by the largest frequency.

$$\begin{aligned} \text{Grid Spacing Parameter (R)} &= \frac{\text{Minimum Velocity}}{\text{Maximum Frequency}} \times 10\% \\ &= \frac{3000 \text{ m/sec}}{1000 \text{ Hz}} \times 10\% = 0.3 \text{ m} \end{aligned} \tag{4.1}$$

The grid spacing (R) along the model is set to 0.2 m for numerical simplicity, therefore 1 node covers a distance of 0.2 m, and 1 m equals 5 nodes.

### 4.2.1 2D Velocity Model

A 2D geological model of the barite vein and surrounding bedrock was created using the CorelDraw X3 Graphics Suite, and is drawn in 1382 × 500 pixel grid, which scales out to 276.4 m × 100 m in real space. The barite vein is positioned at 103 m (515th node) along

the x-axis, and has a width of 2 m (10 nodes), and an arbitrary depth of 100 m (500 nodes).

The 2D geological model is produced as a greyscale image file, in order to set velocity values corresponding to the colours (black for arkose and white for the barite vein) in Seismic Unix. The model is converted to a velocity file prior to the finite difference modelling by using a program which associates the constant velocities of the dyke and surrounding bedrock to the corresponding black and white colours in the model image (Appendix A). The barite vein is displayed in black and is specified a constant velocity of 3000 m/sec. The surrounding arkosic bedrock displayed in white and is specified a constant velocity of 5000 m/sec. The peak frequency chosen is 500 Hz, resulting in a maximum frequency of 1000 Hz (Table 4.3).

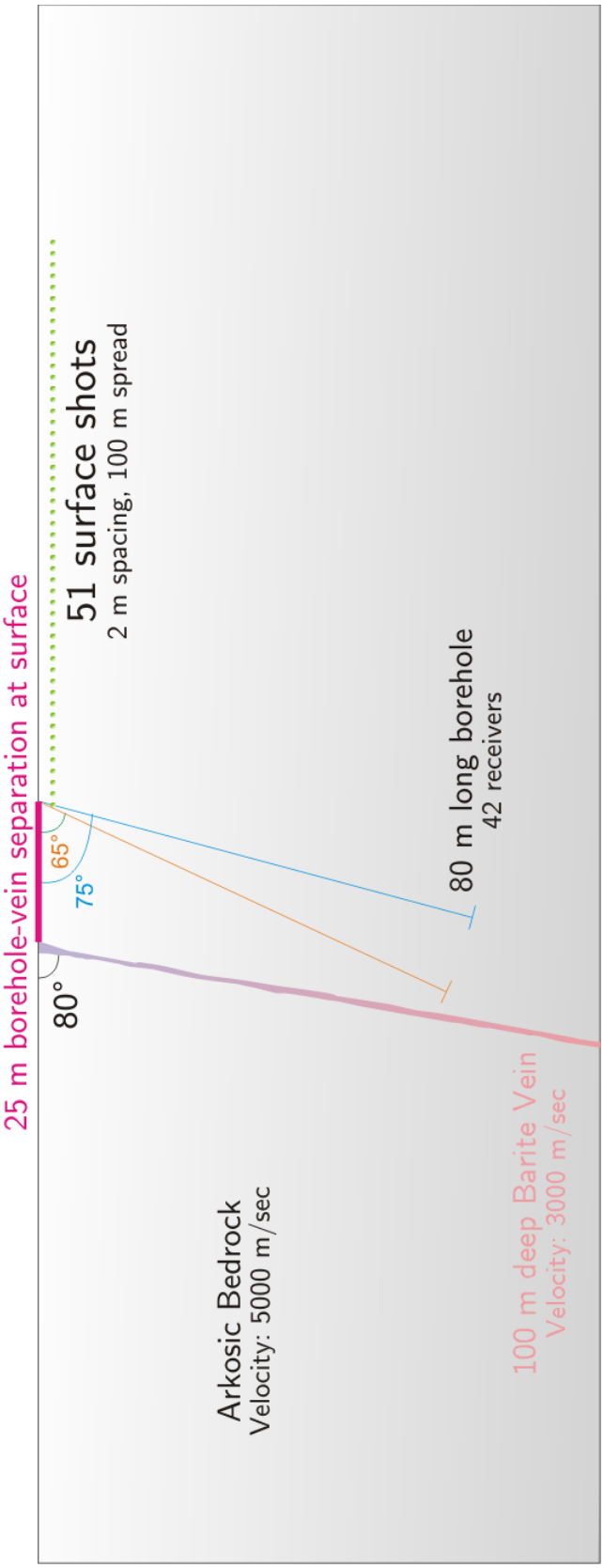


*Fig. 4.6:* Diagram demonstrating the subsurface geometrical relation between drilled boreholes oriented at 75° and 65° towards the target, with respect to a dipping barite vein oriented at 80° from the surface (away from the target)

### 4.2.2 Processing Parameters in Finite Difference Modelling

The borehole to target distance in the simulation is set to 25 m, to simulate the geometry at Collier Point, NL. The initial depth of the virtual sources and receivers is set to 0.6 m. The model parameters chosen in this simulation study is comprised of the target dipping at 80° away from the borehole, and the borehole dipping at 75° (in Case I) and 65° (in Case II) towards the target, for a borehole-target distance of 25 m. The borehole housing the vertical receiver string is positioned at 125 m (625th node) along the x-axis, at a distance of 25 m from the vein, and extends for a depth of 80 m. The borehole is comprised of 42 receivers and corresponding 42 virtual sources. The borehole receiver order is set such that Channel 1 is at the top of the borehole and Channel 42 at the bottom of the borehole. The setup is comprised of 51 shots, spaced 2 metres apart from each other, for a distance of 100 m. The first shot is positioned at 127 m (635th node) along the x-axis and continue in the x-direction with a shot increment of 2 m, resulting in a maximum offset of 100 m. Due to limitations on the length of the source array at the actual field site, the number of shots in the final processing sequence can be edited to **31 shots**, prior to ProMAX processing to produce a **maximum offset of 60m** (Figure 4.6).

*Tab. 4.3:* 2D Model Parameters applied to the Finite-Difference modelling program

| Parameter | Value |
|---|---|
| Total no. of shots generated | 51 |
| No. of shots used in finite difference models | 31 |
| Shot Spacing | 2 |
| No. of Receivers | 42 |
| Receiver Spacing (m) | 2 |
| Peak Frequency (Hz) | 500 |
| Vein Velocity (m/sec) | 3000 |
| Host Velocity (m/sec) | 5000 |
| Borehole Depth | 80 |
| Borehole to target distance | 25 |

*Tab. 4.4:* List of parameters and experimental cases studied using the Finite-Difference modelling program

| Parameter | Case I | Case II |
|---|---|---|
| Dip of target with respect to surface | 100° | 100° |
| Dip of borehole with respect to surface | 75° | 65° |
| Borehole to target distance (m) | 25 | 25 |
| Maximum Source Offset used in finite difference models (m) | 60 | 60 |

*Tab. 4.5:* 2D Grid Parameters applied to the Finite-Difference modelling program

| Parameter | Case I and II |
|---|---|
| Grid Spacing (m) | 0.2 |
| Width | 276.4 m, 1382 nodes |
| Height | 100 m, 500 nodes |
| Borehole Location | 625 m, 125 nodes |

## 4.3 Data Processing

A simplified 2D geological model graphic of the barite vein and surrounding bedrock is created in CorelDraw and exported in PiCture eXchange (.pcx) format, with the features specified in grayscale values. The .pcx file is then translated to a 2D velocity model where the barite vein and surrounding bedrock are specified velocities based on greyscale values depicted in the model graphic (Appendix A).

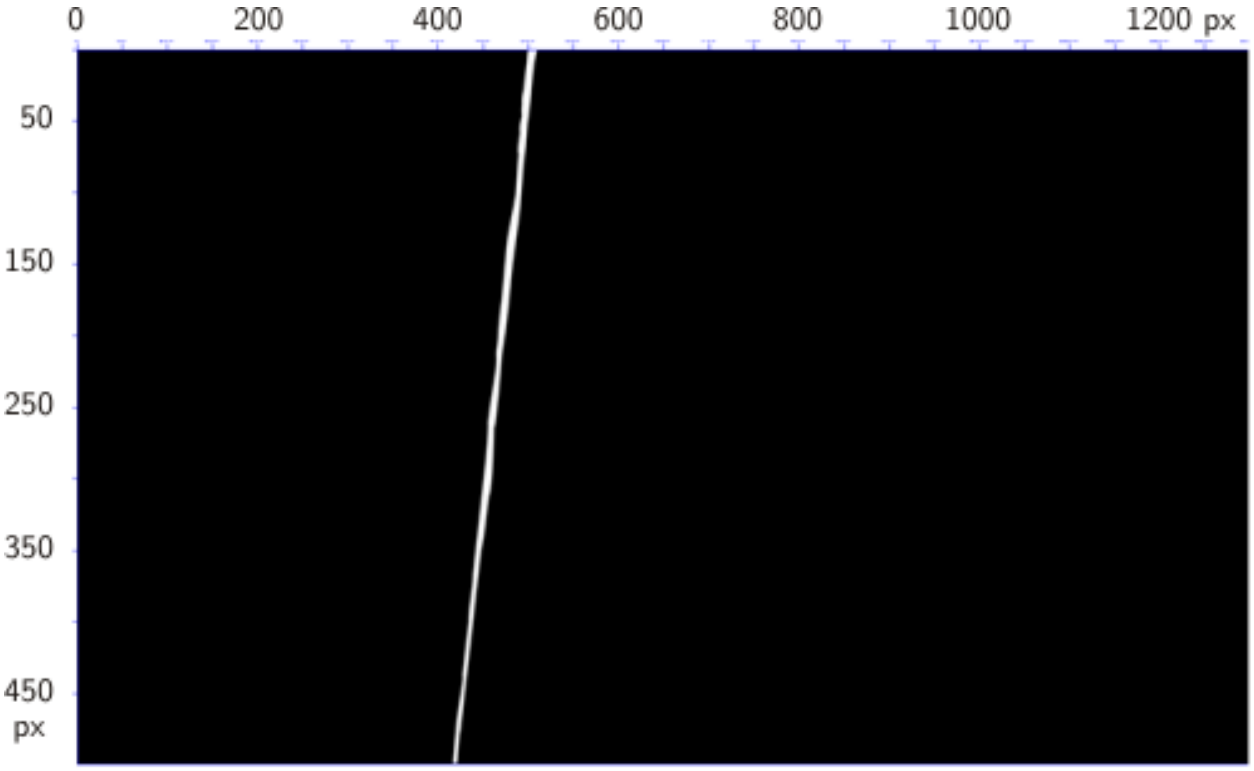


*Fig. 4.7:* 2D model image file produced in Seismic Unix
The geologic features are demonstrated using greyscale values. The barite vein is displayed in white, and the surrounding arkosic host is displayed in black

A 2D finite difference modelling script is used to generate coordinates for a set of 42 receiver locations within the dipping borehole B.1, and generate synthetic shot gathers for each of the 51 shots located on the surface (Appendix B.2). The 51 individual shot files are converted into a single concatenated multi-shot file, and are assigned field file header or

channel numbers (Appendix B.3).


*(a)* Shot 1 - The seismogram represents a VSP from the first surface source location


*(b)* Shot 51 - The seismogram represents a VSP from the last surface source location

*Fig. 4.8:* Shots produced in Seismic Unix using the finite-difference modelling program

The multi-shot file is then read, looping through the range of 51 surface shots and 42 receiver channels, to cross-correlate the 51 shot records with the 42 individual channels within each of the shots to simulate a new virtual source location at the 42 borehole receivers. The virtual sources are created through the cross-correlation of the direct wave of the receiver at the virtual source location with each receiver in the surface shot. This process is repeated for all surface shots with the same virtual source receiver (Appendix B.4). The correlation gathers are generated by sorting the correlated data into common cross-correlated receiver pairs, as demonstrated in Table 4.6.

*Tab. 4.6:* Correlation scheme for creating virtual sources[1]

| Virtual Source | Surface source #1 | + | Surface source #2 | + | Surface source #3 | ... | Surface Source #51 | = | Virtual source gather |
|---|---|---|---|---|---|---|---|---|---|
| 1 | R1×R1 | | R1×R1 | | R1×R1 | | R1×R1 | = | VS1:R1 |
| | R1×R2 | | R1×R2 | | R1×R2 | | R1×R2 | | R2 |
| | R1×R3 | + | R1×R3 | + | R1×R3 | ... | R1×R3 | | R3 |
| | ... | | ... | | ... | | ... | | ... |
| | R1×R48 | | R1×R48 | | R1×R48 | | R1×R48 | | R48 |
| 2 | R2×R1 | | R2×R1 | | R2×R1 | | R2×R1 | = | VS2:R1 |
| | R2×R2 | | R2×R2 | | R2×R2 | | R2×R2 | | R2 |
| | R2×R3 | + | R2×R3 | + | R2×R3 | ... | R2×R3 | | R3 |
| | ... | | ... | | ... | | ... | | ... |
| | R2×R48 | | R2×R48 | | R2×R48 | | R2×R48 | | R48 |
| ... | ... | | ... | | ... | ... | ... | | ... |
| 48 | R48×R1 | | R48×R1 | | R48×R1 | | R48×R1 | = | VS48:R1 |
| | R48×R2 | + | R48×R2 | + | R48×R2 | ... | R48×R2 | | R2 |
| | R48×R3 | | R48×R3 | | R48×R3 | | R48×R3 | | R3 |
| | ... | | ... | | ... | | ... | | ... |
| | R48×R48 | | R48×R48 | | R48×R48 | | R48×R48 | | R48×R48 |

[1] R## represent borehole receiver numbers and correspond to channels 1 through 42 in the VSP data. V## represent virtual source numbers and correspond to the 42 borehole receivers transformed to virtual sources.

The individual cross-correlated shot files are then concatenated by summing each correlation gather to produce one trace for each of the 42 virtual sources. The script for the operation is adapted to concatenate only those cross-correlated shot files having a maximum source offset of 60 m, i.e. it only sums the cross-correlated files generated from surface sources 1 through 31. This is done to reduce the maximum source offset from 100 m to 60 m, which is a more accurate representation of the physical constraints at Collier Point. The shots with longer offset can be used to assess the limitations imposed by physical constraints at the site. The concatenated data is inserted into a single multi-shot file, the name format used with cross-correlated files, which can be sorted in ProMax using the header selev (Appendix B.5).

The concatenated cross-correlated file is converted to .sgy format and exported to the ProMAX 2D Seismic Processing suite for further processing (Appendix D). The VSP data will be redatumed into the borehole using the seismic interferometry method, resulting in virtual shot records with the virtual sources in the borehole, thus minimizing the effect of the overburden and providing a larger range of illumination angles. The surface data is processed by applying a standard common mid-point/depth point (CMP/CDP) flow, and imaged using Kirchoff Depth Migration.

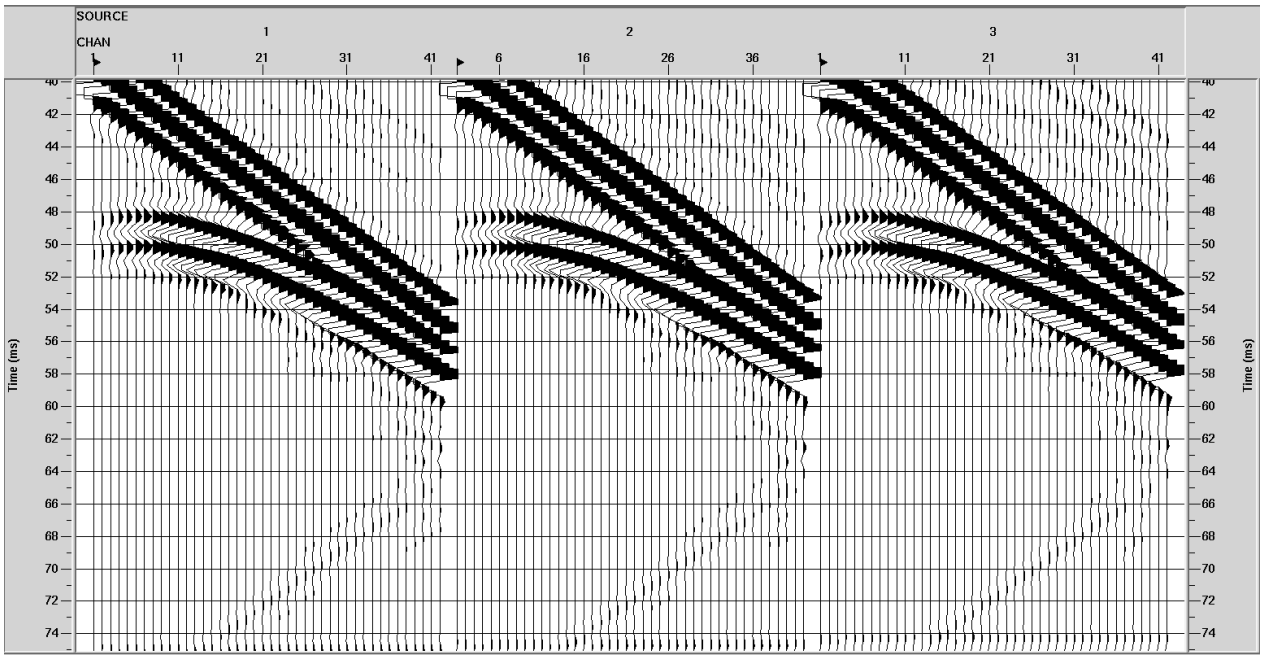


*(a)* Case I, which has the borehole dipping at 75° towards the target

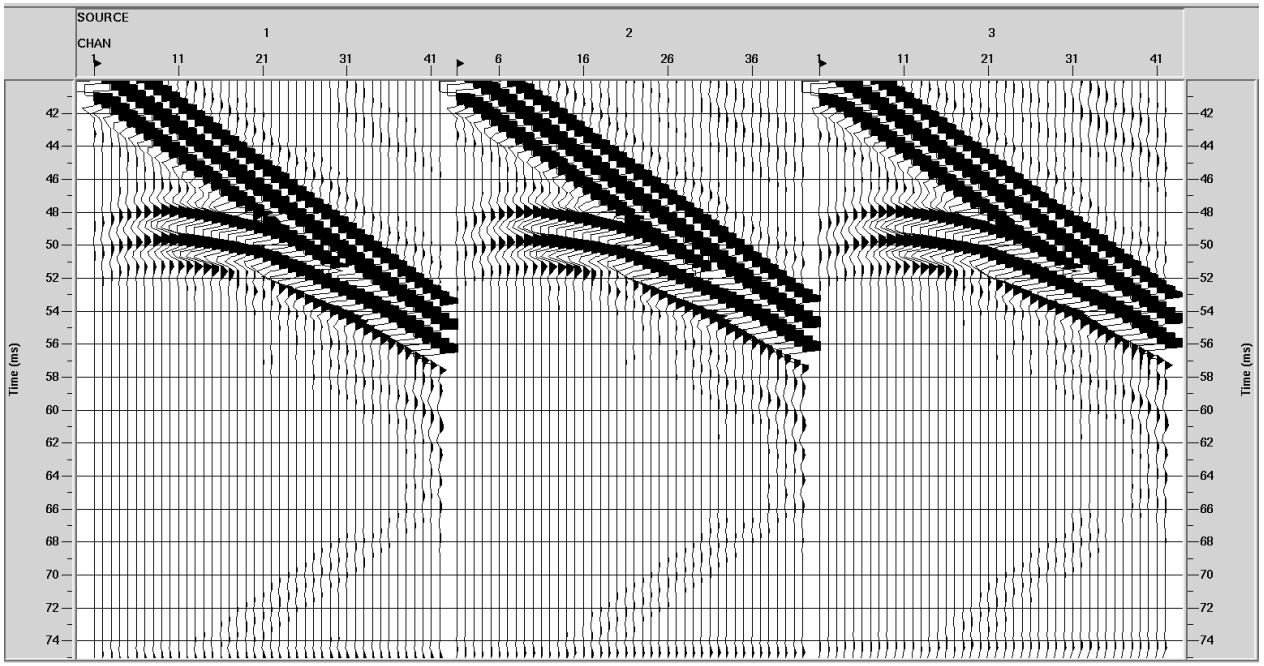


*(b)* Case II, which has the borehole dipping at 65° towards the target

*Fig. 4.9:* Trace display for surface sources 1, 2 and 3 located closest to the borehole

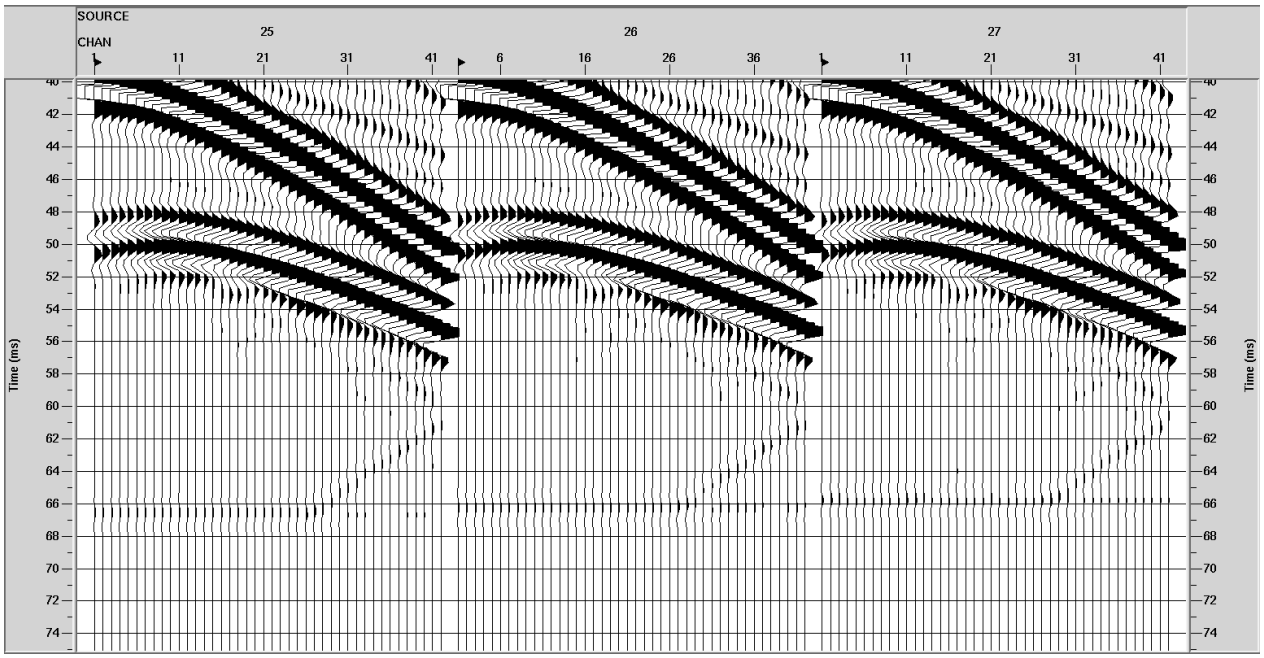


*(a)* Case I, which has the borehole dipping at 75° towards the target

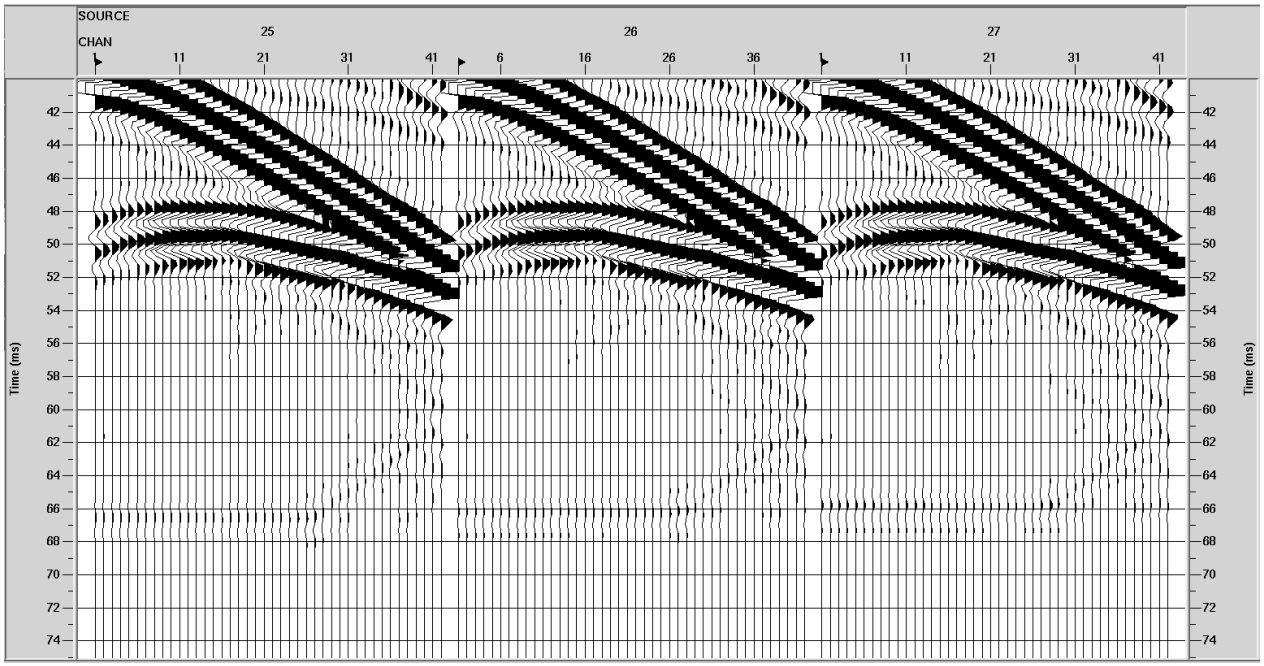


*(b)* Case II, which has the borehole dipping at 65° towards the target

*Fig. 4.10:* Trace display for surface sources 25, 26 and 27

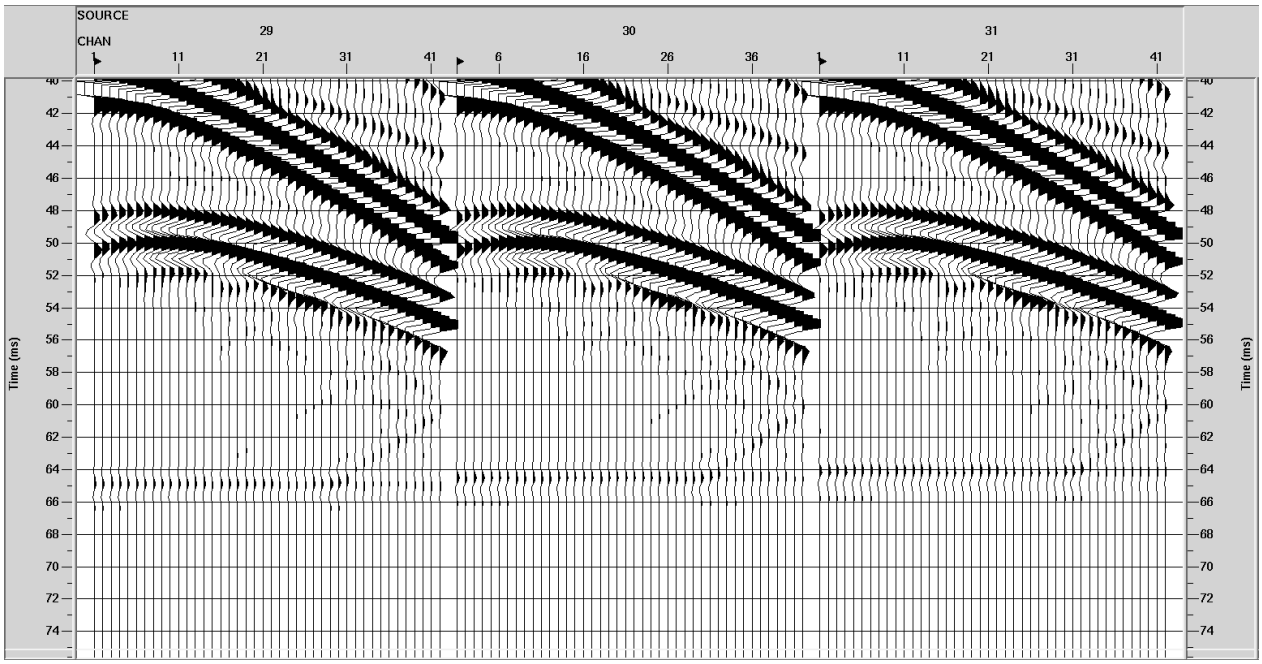


*(a)* Case I, which has the borehole dipping at 75° towards the target

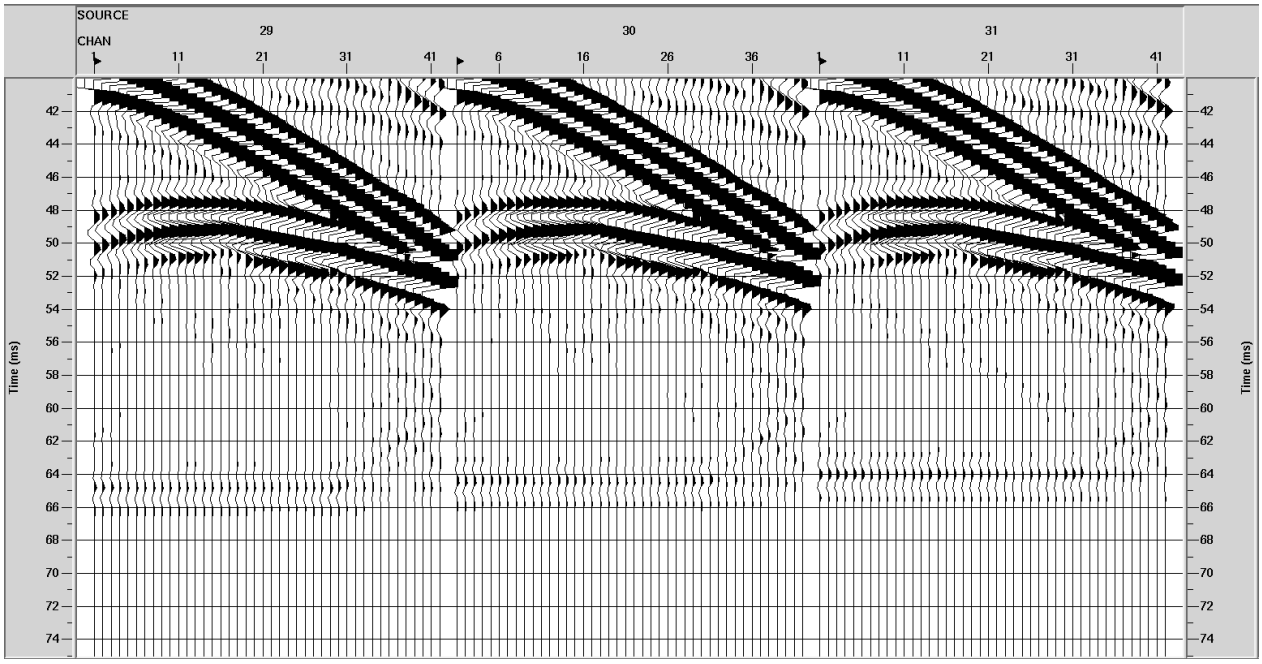


*(b)* Case II, which has the borehole dipping at 65° towards the target

*Fig. 4.11:* Trace display for surface sources 29, 30, 31, which are furthest away from the borehole using a maximum offset of 60 m

### 4.3.1 Virtual Source Gather

The virtual source gather is equivalent to a conventional surface seismic shot gather, where the virtual direct wave is equivalent to the surface seismic direct wave. It was created by sorting the correlation gather according to ascending virtual source location, followed by vertical stacking by virtual source location. The vertical stacking of the correlation gather involves the summation of correlograms associated with the same virtual source. The virtual direct wave is represented in the seismogram as the linear event that crosses the zero-lag at the position of the virtual source. In these samples, the zero lag is at 40 ms. Therefore, the first 40 ms (leads) of the virtual shots were ignored as they consist of acausal data, and only the bottom 40 ms (lags) were examined.

The virtual shots positioned at the top (Figures 4.12a, 4.12b), middle (Figures 4.13a, 4.13b) and bottom (Figures 4.14a, 4.14b) of the borehole were examined in Cases I and II to confirm a strong response from the reflector, and to ensure that arrival times from the reflector is consistent with the model geometry.

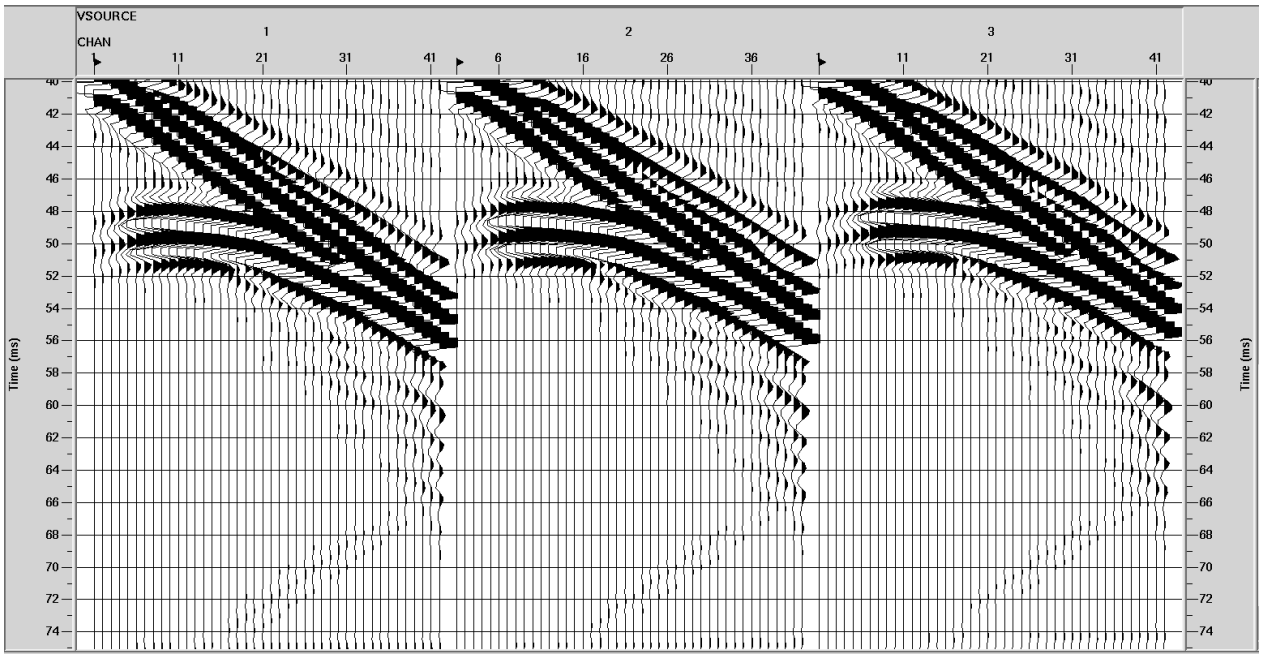


*(a)* Case I, which has the borehole dipping at 75° towards the target

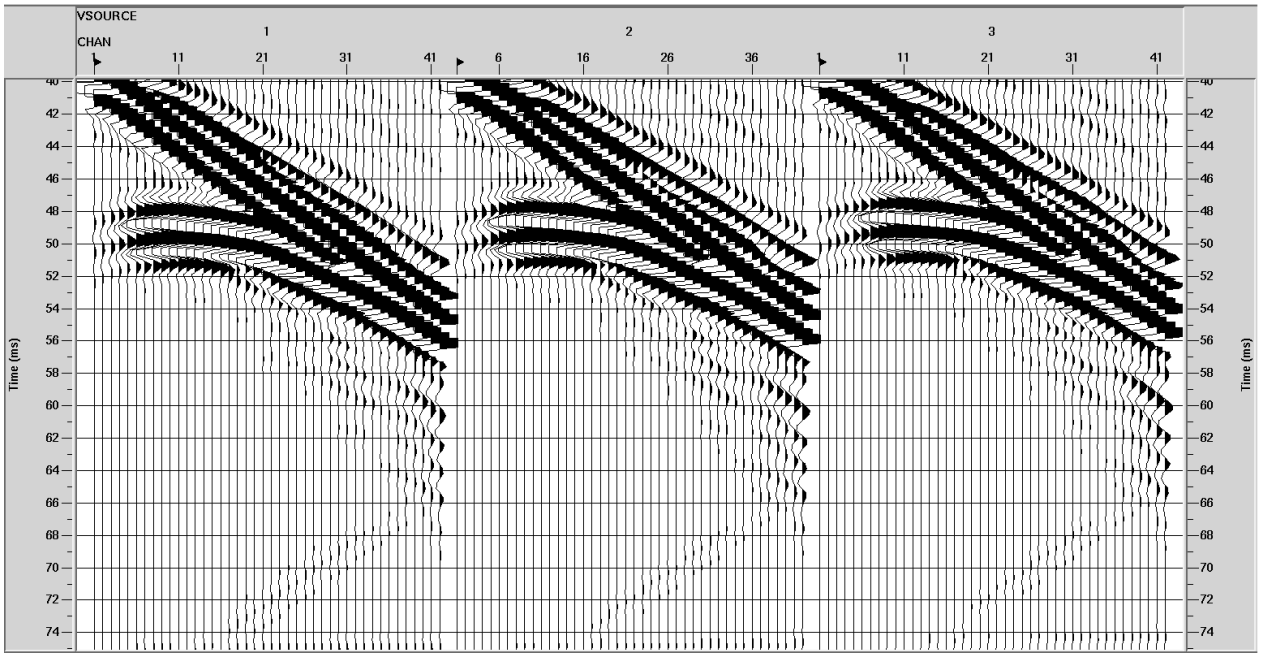


*(b)* Case II, which has the borehole dipping at 65° towards the target

*Fig. 4.12:* Virtual Source Gather for virtual shots 1, 2 and 3 located at the top of the borehole

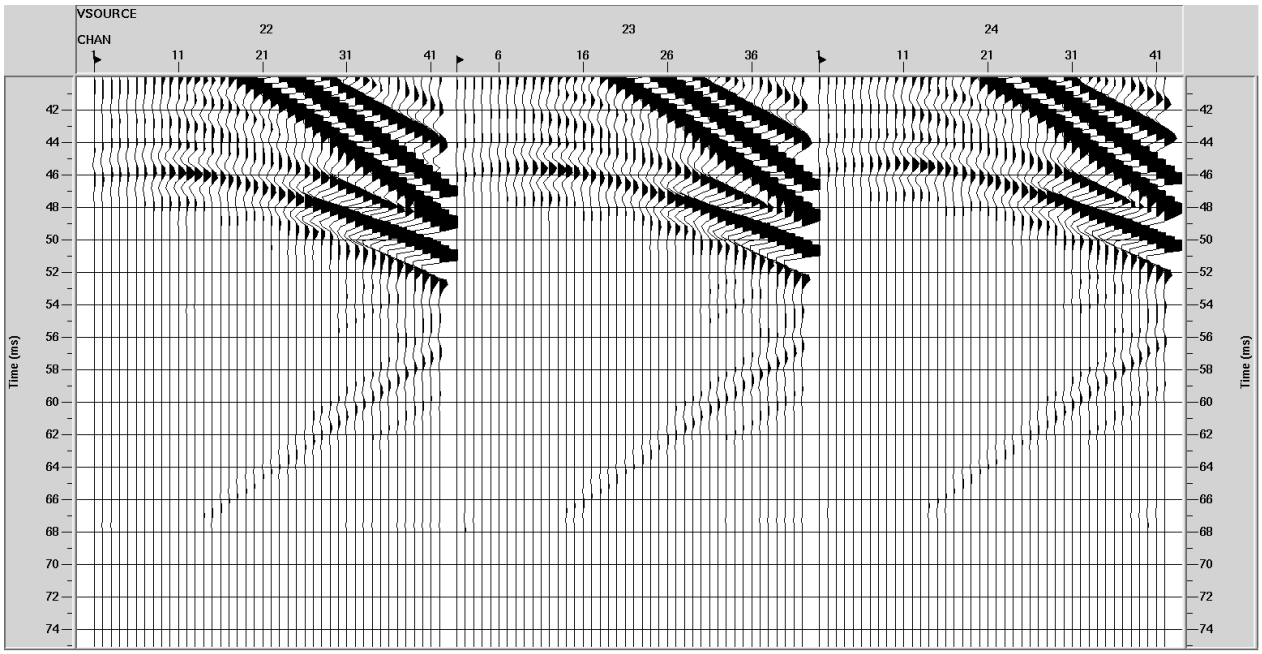


*(a)* Case I, which has the borehole dipping at 75° towards the target

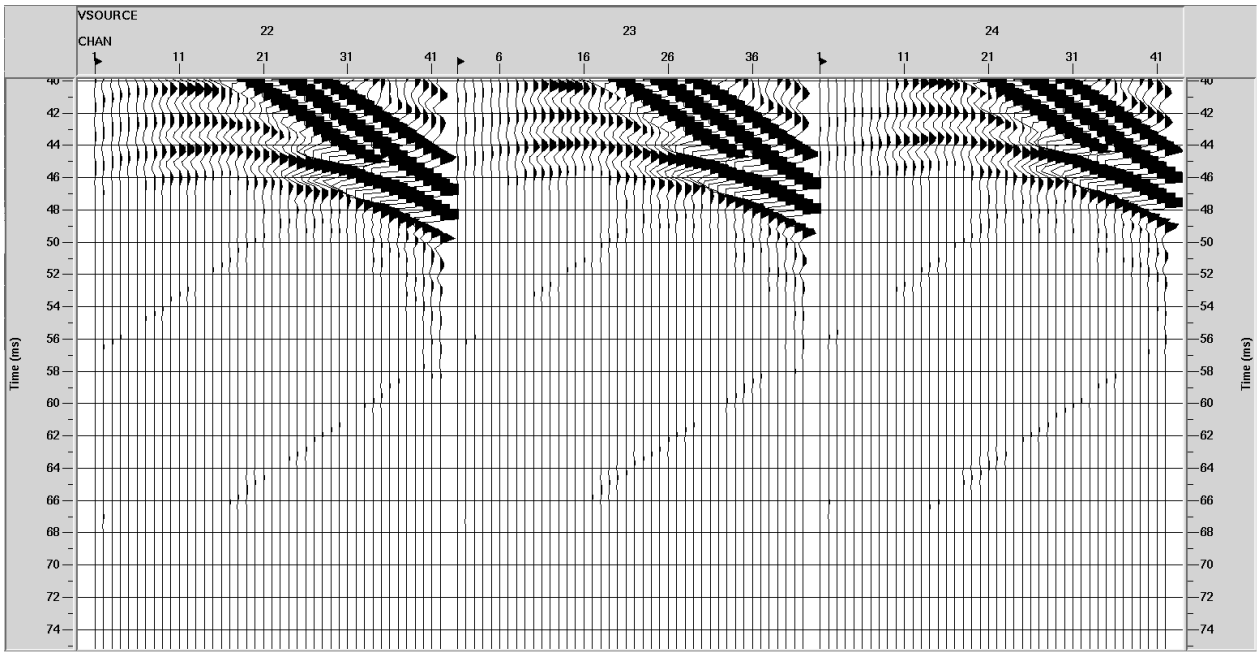


*(b)* Case II, which has the borehole dipping at 65° towards the target

*Fig. 4.13:* Virtual Source Gather for virtual shots 22, 23 and 24 located at the middle of the borehole

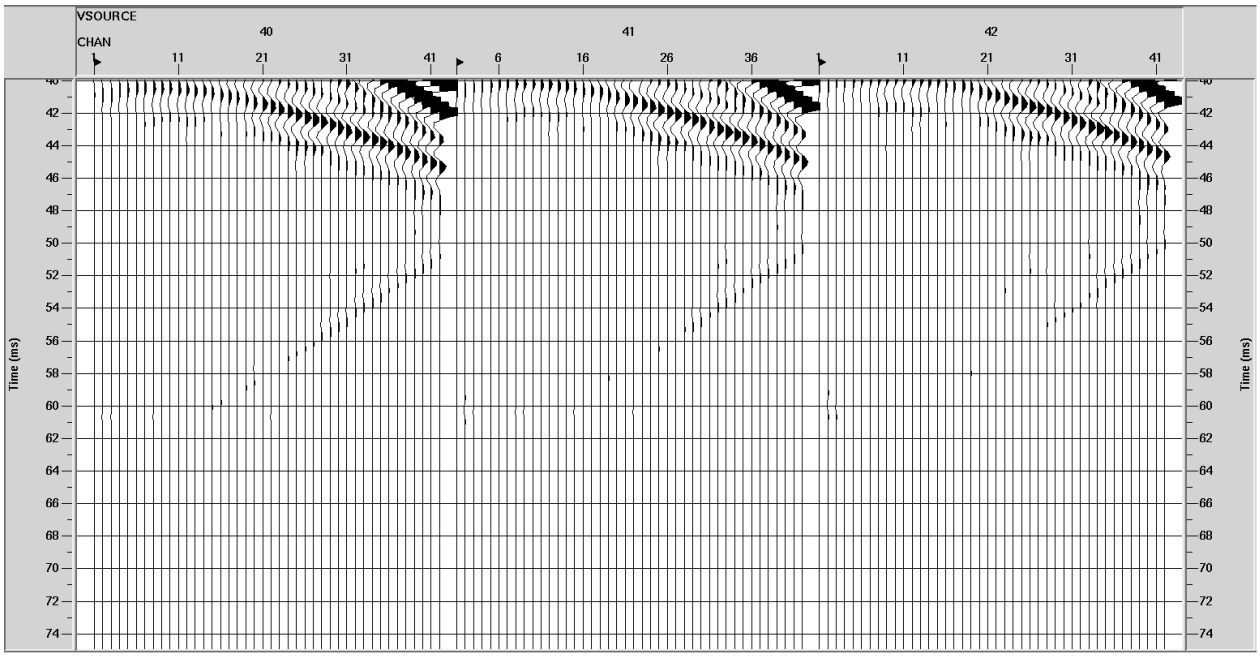


*(a)* Case I, which has the borehole dipping at 75° towards the target

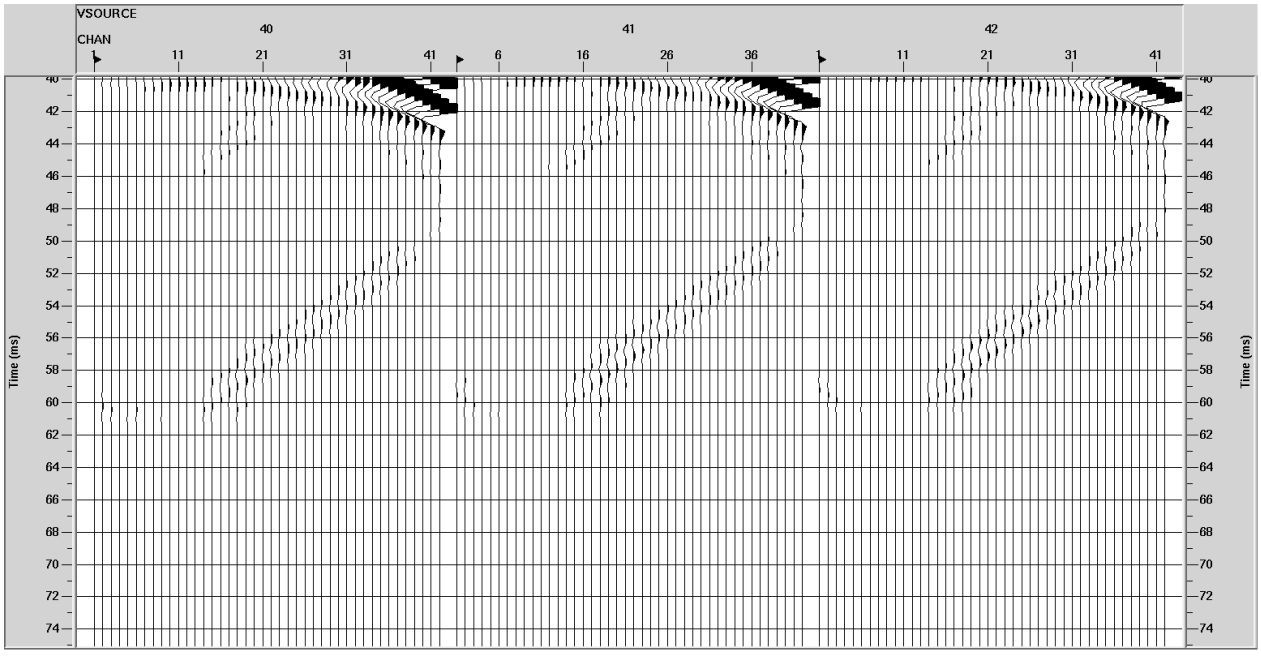


*(b)* Case II, which has the borehole dipping at 65° towards the target

*Fig. 4.14:* Virtual Source Gather for virtual shots 40, 41 and 41 located at the end of the borehole

### 4.3.2 Assignment of Polarities

The transition from the high velocity arkose, low density arkose host and lower velocity, higher density barite vein creates a negative reflection coefficient (Table 3.11). Therefore, the reflection events originally plot as negative polarity events, due to the strong negative reflection coefficient between the interfaces. For the sake of easier viewing and interpretation, the CDP and Kirchoff depth migration profiles are purposefully plotted in *reverse polarity* (and therefore are shown as positive polarity events) to draw the eye of the viewer to the relevant reflection events.

### 4.3.3 CDP Stack

The virtual shot gathers are sorted from the time receiver domain to the common midpoint-offset domain to create a CMP (Common Mid-point Point gather), also known as CDP (Common Depth Point) Gather. The ProMAX program is used to identify the virtual shot and receiver pairs that share a Common Depth Point (CDP), and organize the virtual shot gather as a function of the source and receiver coordinate geometry through a geometry job flow (Appendix D). The point of highest fold is located at the middle of the vein, and the number of source-receiver pairs decreases at the top and bottom depth regions of the borehole. Following the organization of data according to the CDP and receiver pairings using the geometry spreadsheet, it is NMO (Normal Moveout) corrected. The NMO correction was uncomplicated as the model comprises of homogeneous velocity fields. The NMO correction causes the data to become stretched as a function of offset and depth, and the summing of these period-stretched events may cause the stacked data to be smudged. Hence, a stretch mute of 30% is applied in the NMO process, which limits the maximum stretch to 30%. The shots with longer offset of 100 m (Figures 4.16 and 4.18) are used to assess the limitations imposed by physical constraints at the site, which has a maximum possible offset of around 60 m. A static shift is applied to the direct wave arrival times to eliminate the first 40 ms

(leads) containing acausal data and places the zero lag at time zero. The CDP traces are then summed and stacked. This produces a CDP gather of linear reflections which have been summed together constructively to produce the CDP stack.

**Top of Borehole** **Bottom of Borehole**

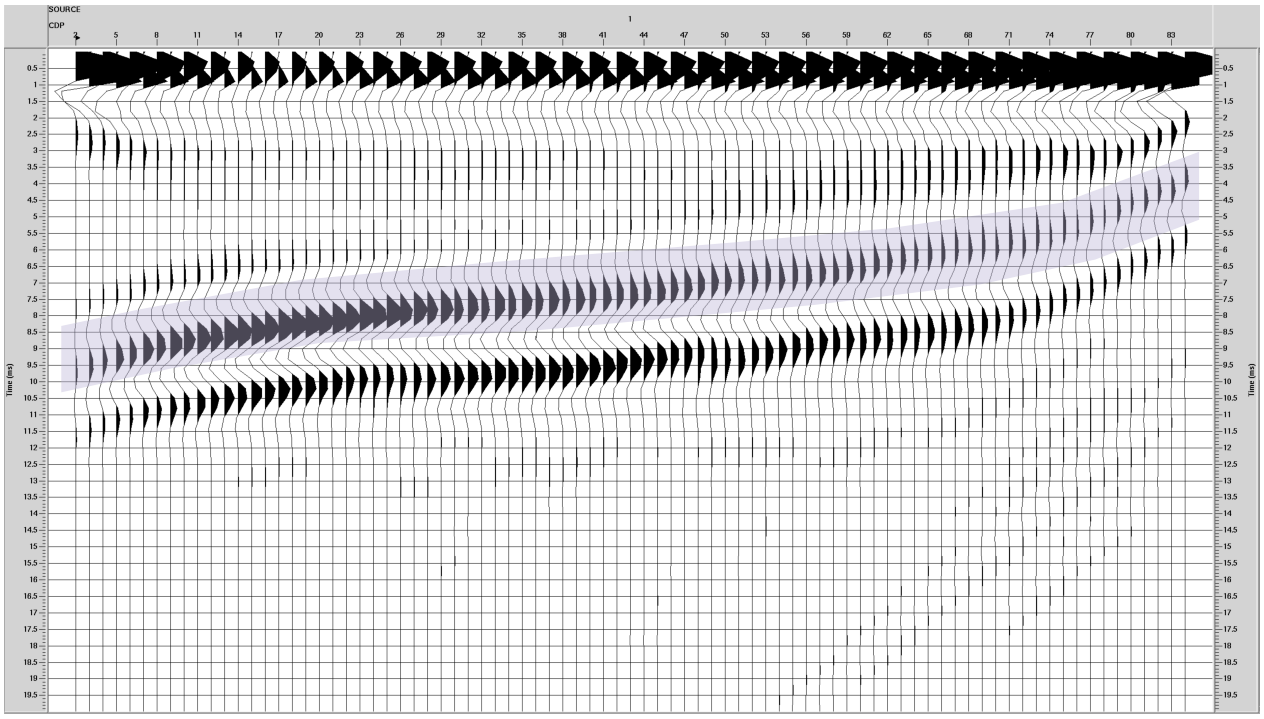


*Fig. 4.15:* CDP Stack of seismic section in Case I, with the borehole dipping at 75° towards the target, and 60 m Offset

Barite reflection is marked in purple. 0.3 gain and plotted in reverse polarity

**Top of Borehole** **Bottom of Borehole**

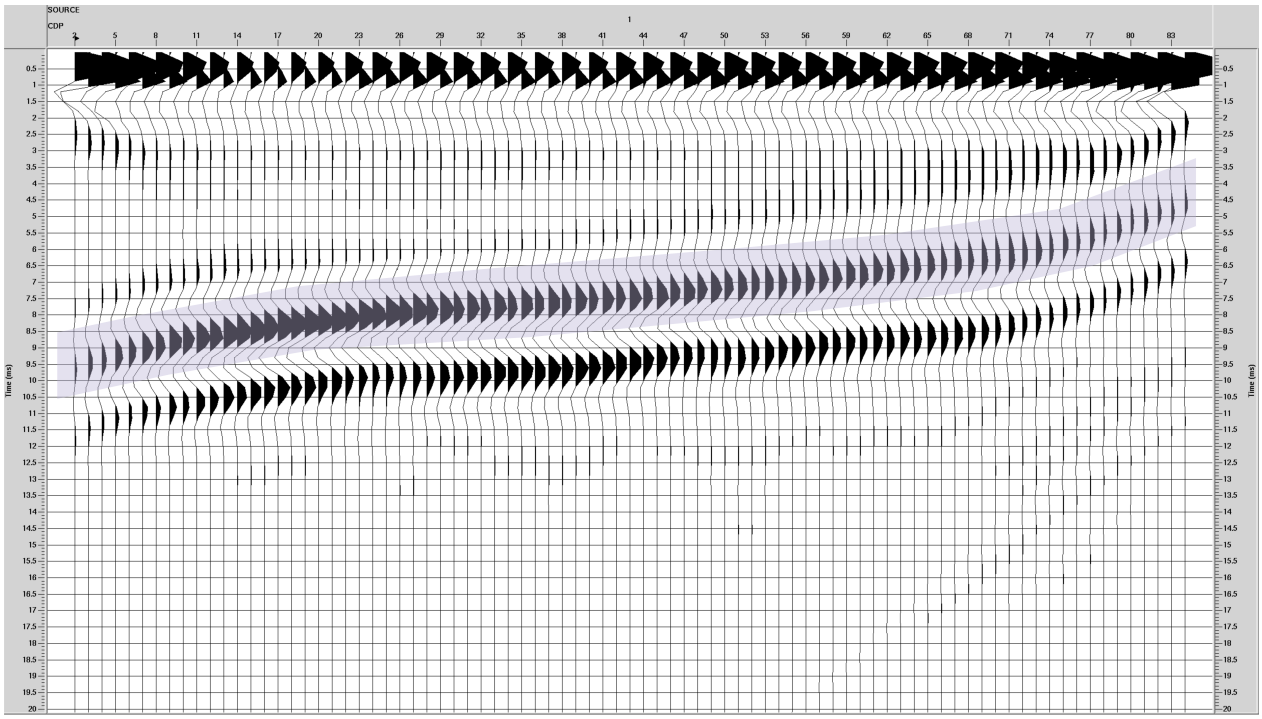


*Fig. 4.16:* CDP Stack of seismic section in Case I, with the borehole dipping at 75° towards the target, and 100 m Offset

Barite reflection is marked in purple. 0.3 gain and plotted in reverse polarity.

**Top of Borehole** **Bottom of Borehole**

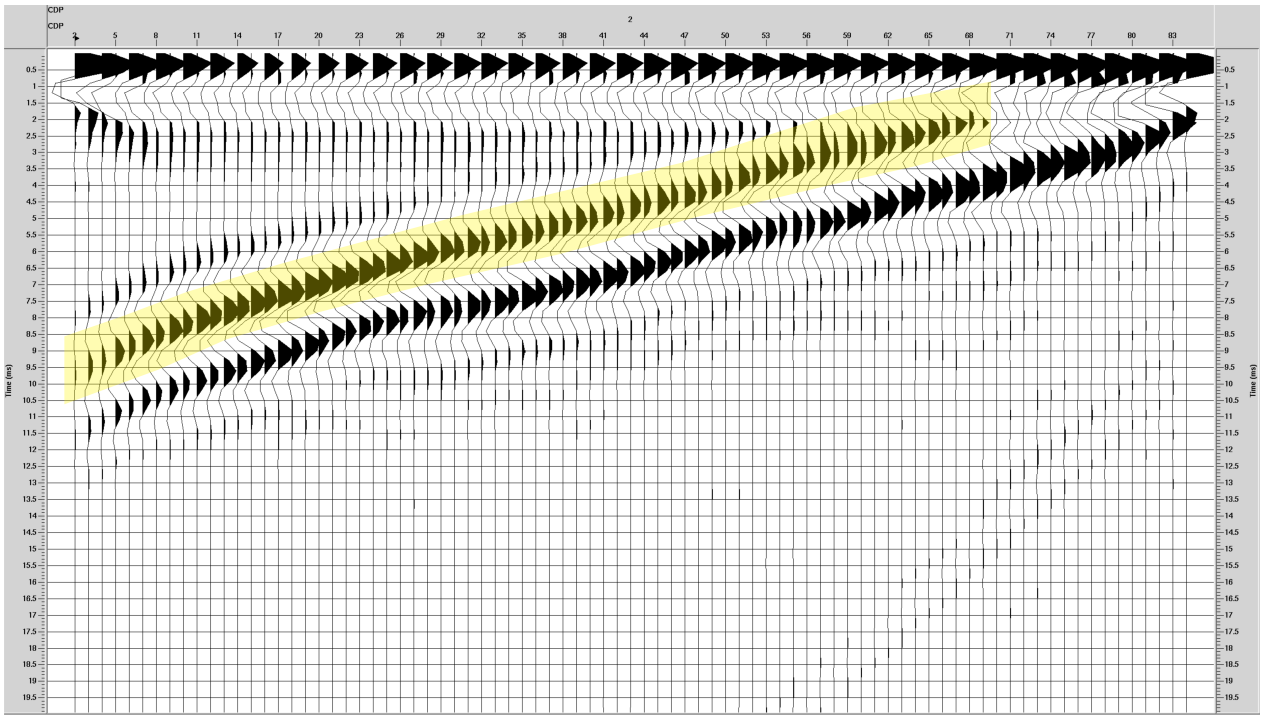


*Fig. 4.17:* CDP stack of seismic section in Case II, with the borehole dipping at 65° towards the target, and 60 m Offset

Barite reflection is marked in yellow. 0.3 gain and plotted in reverse polarity

**Top of Borehole** **Bottom of Borehole**

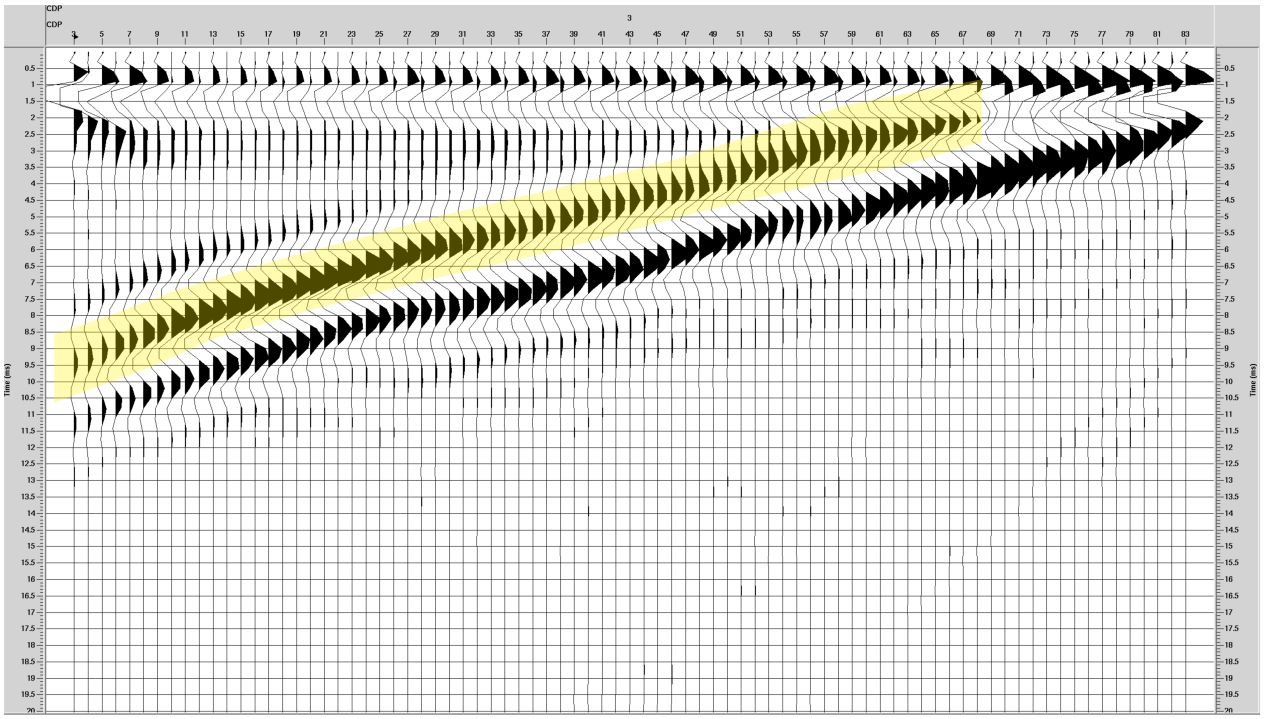

*Fig. 4.18:* CDP stack of seismic section in Case II, with the borehole dipping at 65° towards the target, and 100 m Offset

Barite reflection is marked in yellow. 0.3 gain and plotted in reverse polarity

### 4.3.4 Migration

The stacked seismic section is Kirchhoff time migrated to correct the seismogram in the time-space domain to focus the stacked image. As with the NMO correction, the Kirchhoff migration was uncomplicated due to the model comprising of homogeneous velocity fields, and was implemented by inputting a velocity function in the ProMax program (Appendix D).

**Top of Borehole** **Bottom of Borehole**

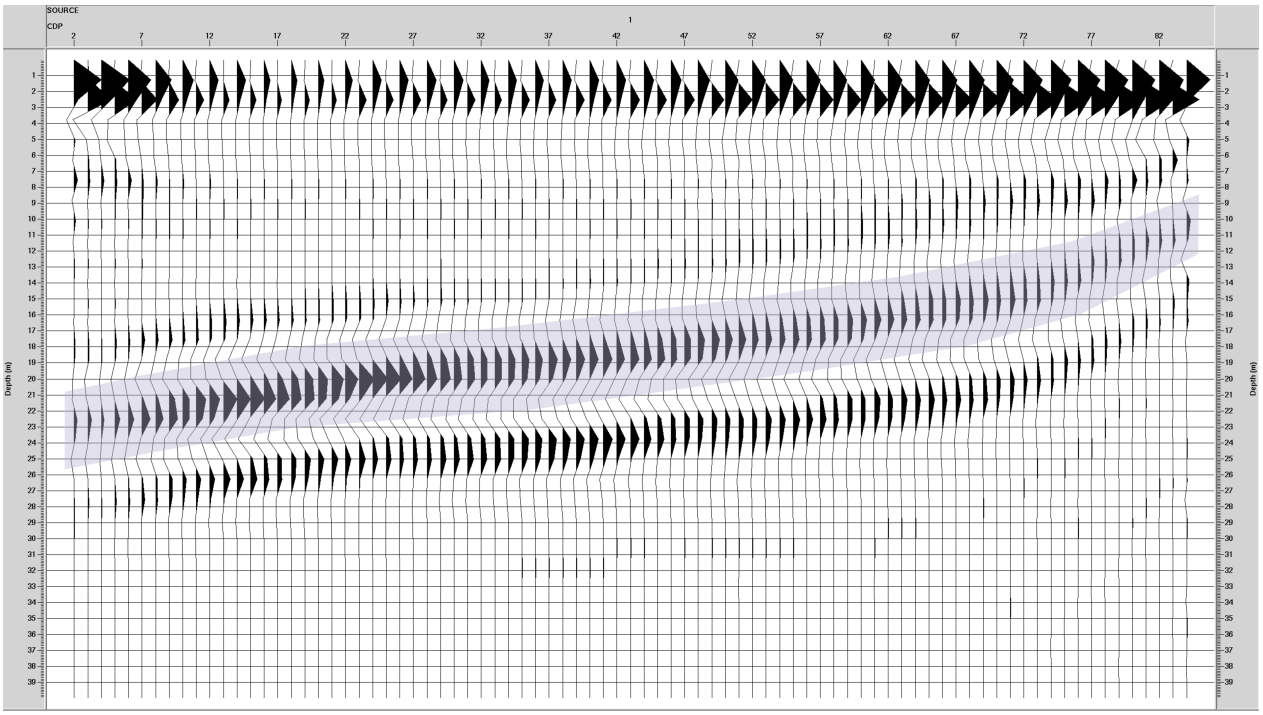


*Fig. 4.19:* Migrated Stack of seismic section in Case I, with the borehole dipping at 75° towards the target, and 60 m Offset

Barite reflection is marked in purple. 0.5 gain and plotted in reverse polarity

**Top of Borehole** **Bottom of Borehole**

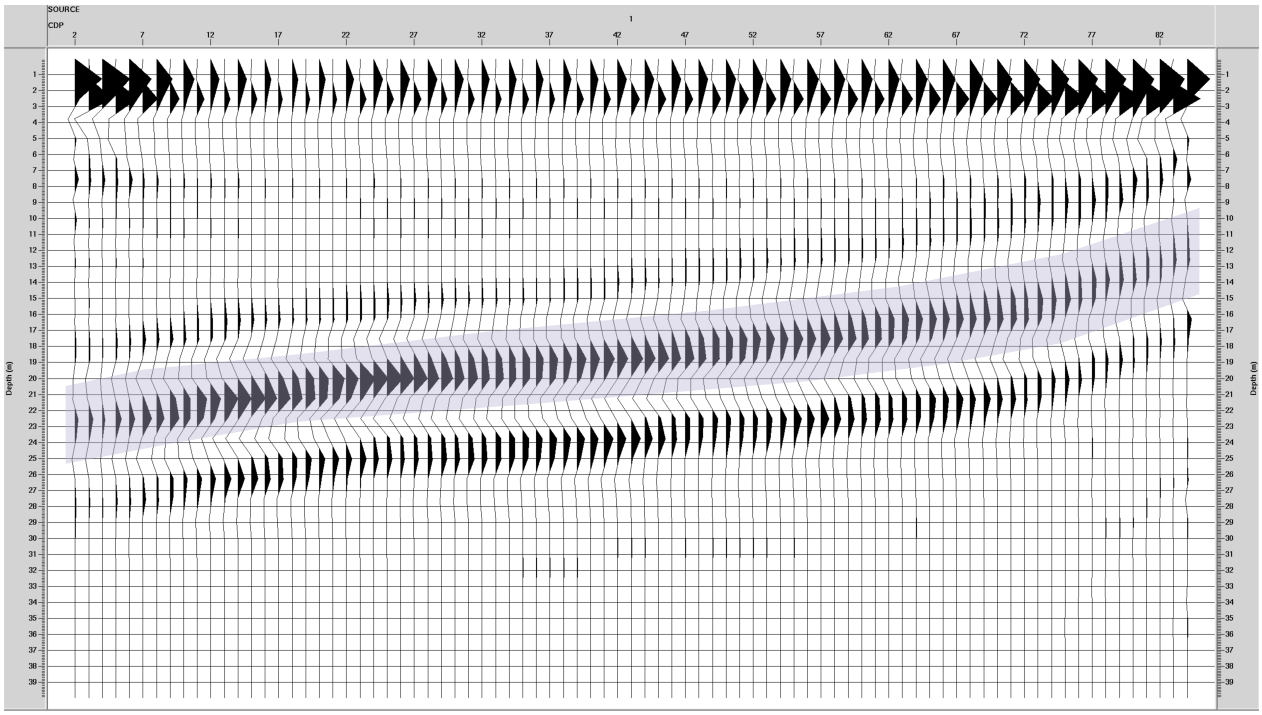


*Fig. 4.20:* Migrated Stack of seismic section in Case I, with the borehole dipping at 75° towards the target, and 100 m Offset

Barite reflection is marked in purple. 0.5 gain and plotted in reverse polarity

**Top of Borehole** **Bottom of Borehole**

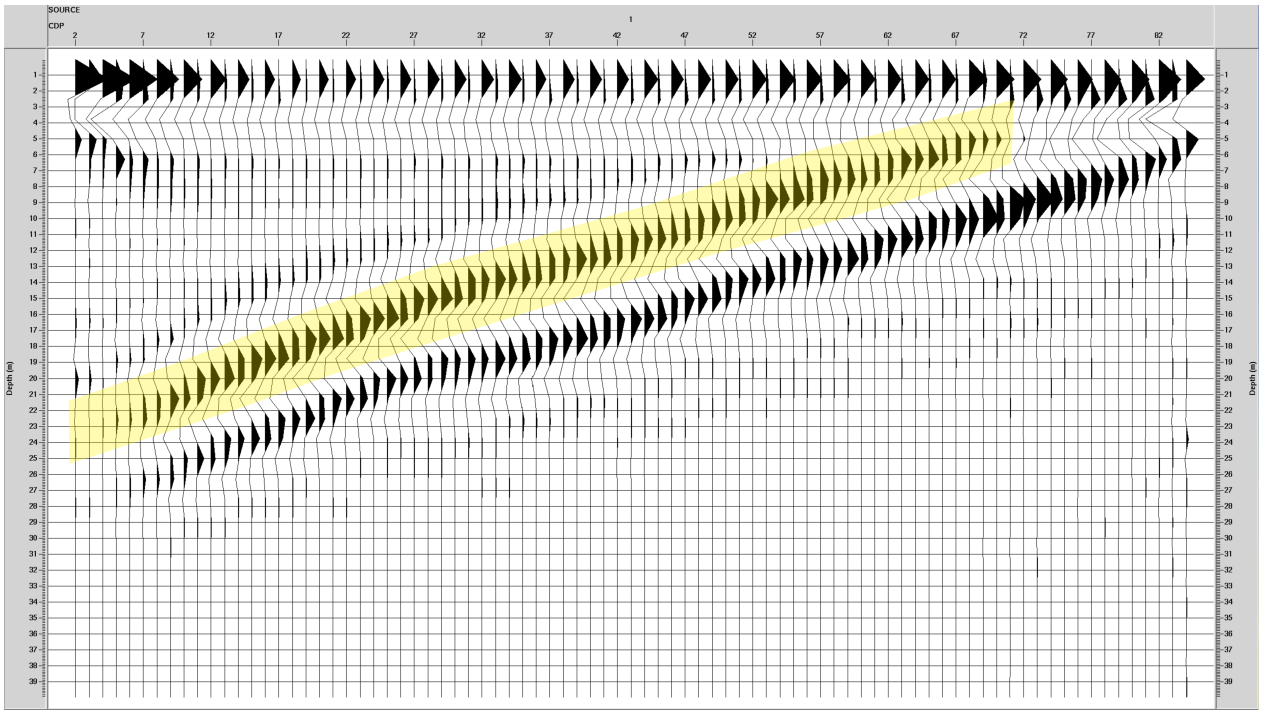


*Fig. 4.21:* Migrated stack of seismic section in Case II, with the borehole dipping at 65° towards the target, and 60 m Offset

Barite reflection is marked in yellow. 0.5 gain and plotted in reverse polarity

**Top of Borehole** **Bottom of Borehole**

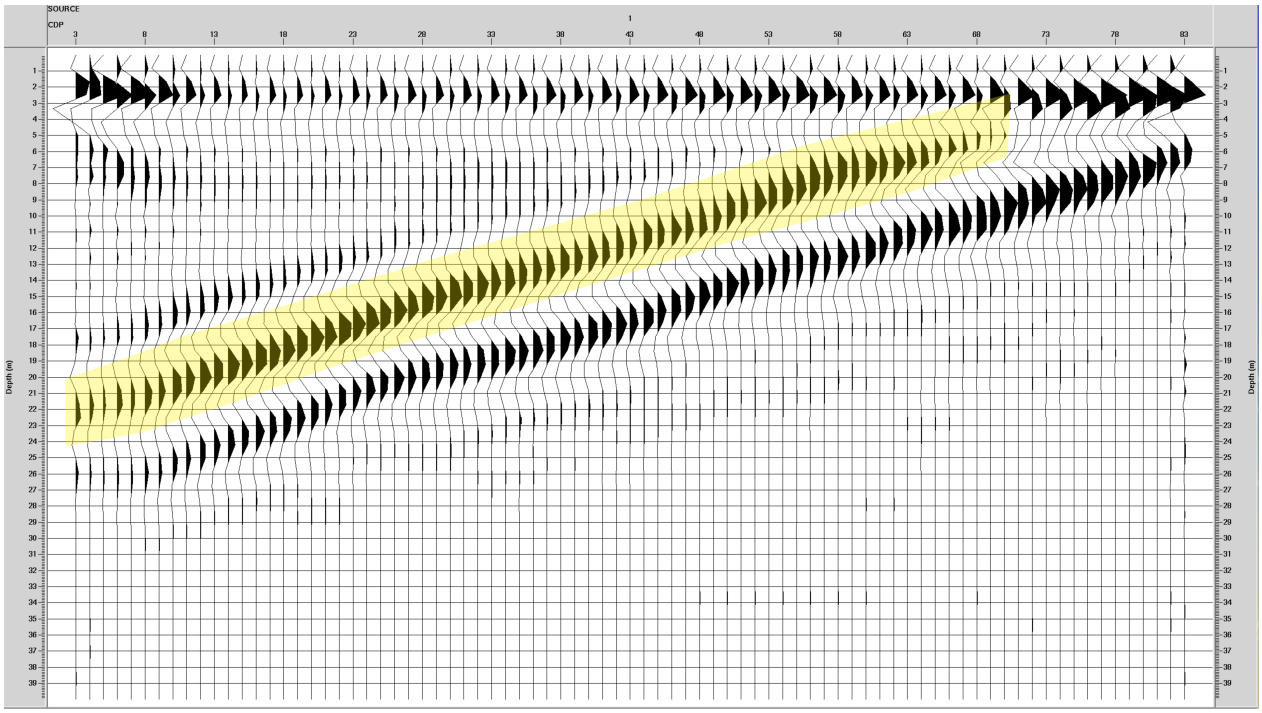


*Fig. 4.22:* Migrated stack of seismic section in Case II, with the borehole dipping at 65° towards the target, and 100 m Offset
Barite reflection is marked in yellow. 0.5 gain and plotted in reverse polarity

### 4.3.5 Analysis of Synthetic Data

The synthetic seismic data model illustrates how the data is expected to occur using standard acquisition and processing techniques in the field, and can hence be analysed to investigate the effectiveness of using varying borehole dip angles of 75° (Case I) and 65° (Case II) towards enhancing the image recovery of the near-vertical barite dyke using the virtual source method. The synthetic data produces two main features, a linear feature at $\approx$ 1 ms and the barite vein which appears as a dipping event at $\approx$ 10 ms. The dipping reflection event has side lobes as a processing artifact as a result of the finite difference modelling. The linear 1 ms feature is also likely a processing artifact.

In both cases it is observed that the resolution and data quality decreases significantly

at the top and bottom of the CDP profiles. This occurs due to fewer stationary phase contributions at the top and bottom of the borehole (as demonstrated in the ray-tracing analysis), which results in incorrect kinematics during the summation of the correlation gathers. In Case II (65°), it is observed that the deeper regions of the vein are mapped with better resolution compared to Case I (75°). This is likely due to the more favourable geometry in Case II which has the receivers placed more closely to the barite vein target, furthermore the ray-tracing analysis also indicates a wider range of offsets and stationary phase contributions in Case II (65°) model (Subsection 4.1.5). It is observed that longer offsets (of 100 m) produce a better seismic image in both cases. It is also noted that Case II (65°) demonstrates less loss in data quality with a decreased offset of 60 m compared to Case I with the same offset length (Figures 4.17 and 4.19), likely as a result of its more advantageous placement of receivers being placed closet to the borehole, which produces a better result.

However, Case II (65°), has a shorter time delay due to the orientation of the borehole towards the target, which could make the time separation and distinguishing of the direct ray and reflected ray difficult in further simulations and is undesirable. Therefore, a 70° dipping geometry was chosen for the borehole experiment as the orientation would likely be most favourable for the structure in deeper regions of the vein to be interpreted accurately.

# Chapter 5

## Interferometry Experiment

## 5.1 Drilling Procedure

The drilling of the borehole was conducted in August 2016. The borehole was inclined at approximately 70° (measured as 73° at the casing) towards the vein for a drilling depth of 84 m. The borehole-barite vein separation at the surface is estimated at 25 m. The drillers encountered a series of 'soft zones' through the drilling exercise, which may be the result of fractures within the subsurface or altered zones. The drillers also encountered pinkish drilling fluids at the certain depths. The pink drilling fluids do not necessarily represent barite zones, and may be associated with drilling through regions of red sandstone.

## 5.2 Walk-Away Seismic Experiment

The walk-away VSP seismic experiment was conducted on November 5th 2016 at the Collier Point Barite property.


*Fig. 5.1:* Drillers creating a borehole at the Collier Point Barite Property

## 5.3 Equipment

The seismic data is recorded on an *Aries Lite* recording system, with a sample rate of 1/4 ms and a record length of 3 seconds. The equipment consisted of a 24 channel hydrophone with a 2 m spacing, which was lowered into a 82 m long borehole. Forty-three shot points carrying 39 grams of explosive charge were laid out at 2 m intervals (Appendix E). The shot points for the dynamite were trenched to solid bedrock in order to generate the highest possible frequencies (Figure 5.3) and the dynamite was placed in 75 cm boreholes. The forty-three shot points were carried out in two series: Shots 1 through 22 were carried out with

Channel 1 at 82 m borehole depth, and the last Channel 24 at 36 m borehole depth. The hydrophone was then raised by 26 metres, such that Shot 23 through Shot 43 were carried out with Channel 1 at 56 m borehole depth, and the last Channel 24 at 10 m borehole depth (Figure 6.2).

*Fig. 5.2:* A receiver on the bottom of hydrophone cable used in the experiment

*Fig. 5.3:* Photo of trench dug for placing shot points during the Collier Point Interferometry Experiment

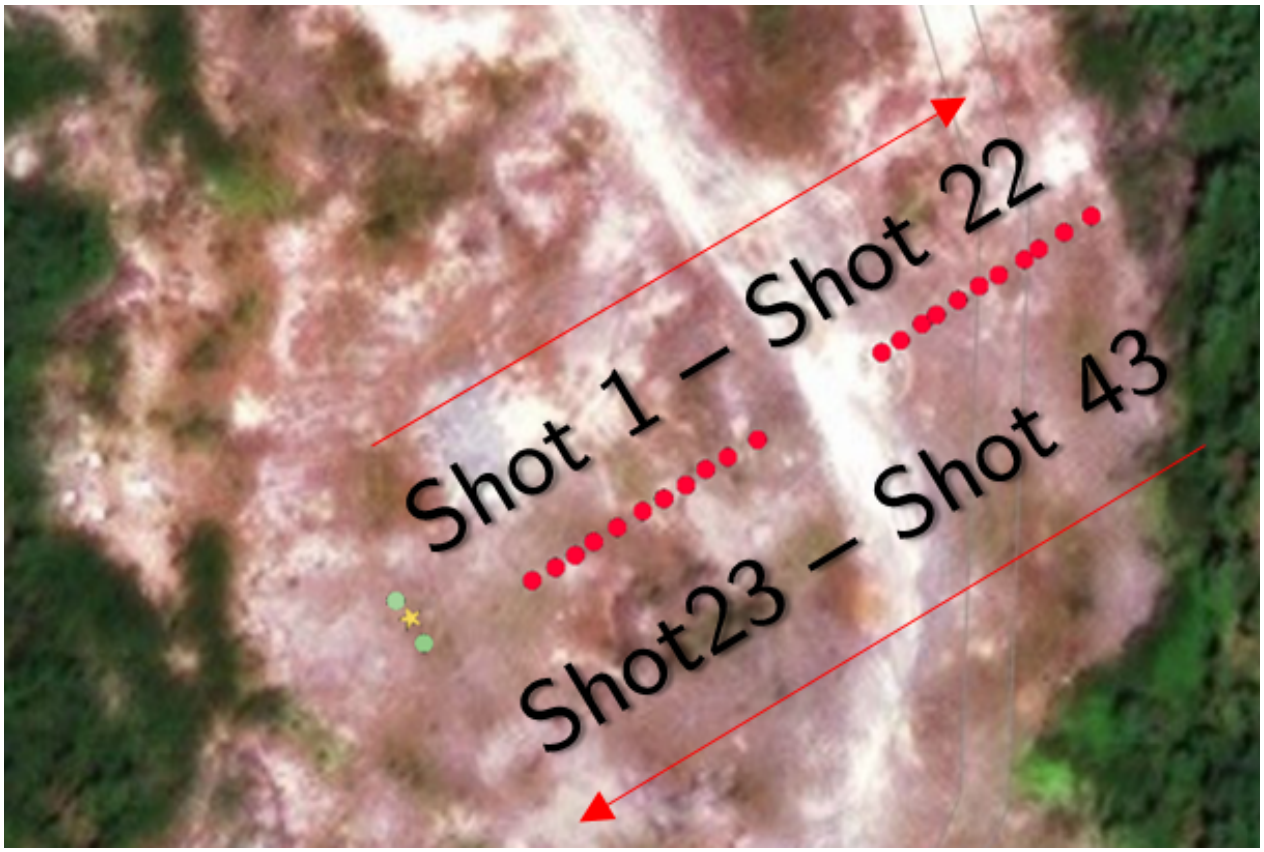


*Fig. 5.4:* Satellite photo of the Collier Point interferometry experiment site demonstrating location of shot points, borehole and shooting directions.
The borehole used in the interferometry experiment is denoted by the yellow star, and the shot points are denoted by the red dots. Shots 1 - 22 were fired in a direction away from the borehole, and shots 23 - 43 were fired in a direction towards the borehole

# Chapter 6

## Seismic Data Processing

The seismic data acquired is pre-processed by strongly filtering the dataset using the ProMAX 2D Seismic Processing suite to remove generated noise and enhance any possible reflection from the barite vein (Section 6.1). Following the pre-processing, cross-correlated files are created in Seismic Unix and the cross-correlated concatenated files are exported back to ProMAX. The VSP data is redatumed into the borehole using the seismic interferometry method, resulting in virtual shot records with the virtual sources in the borehole and a virtual source gather (VSG). The dataset is processed by applying a standard common midpoint (CDP) flow, and imaged using post-stack Kirchoff Depth Migration.

## 6.1 Pre-processing

The main aim of pre-processing prior to the creation of virtual source gathers is to attenuate noise which can be amplified through the dataset during the cross-correlation process, and to enhance possible reflections. Spectral analysis, F-K analysis are a few of the tools that are generally utilized to recognize the interference waves. The pre-processing flow is described in Figure 6.1, and the reasoning for these processes will be explained in following sections.

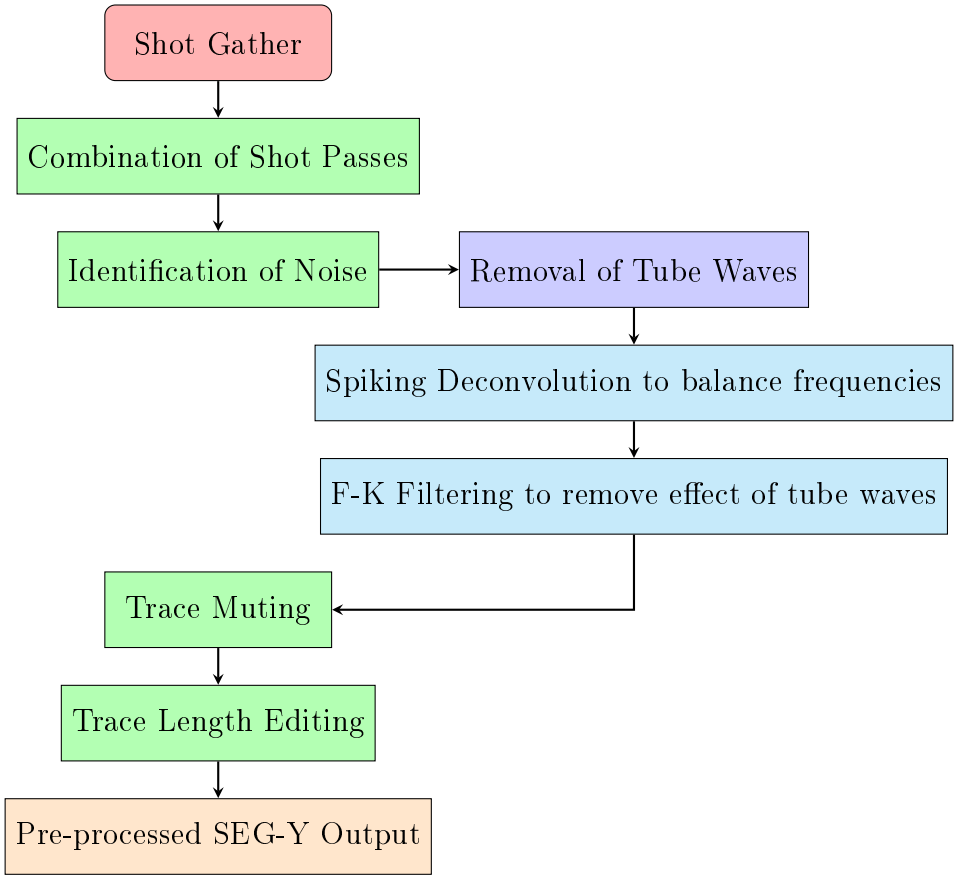


*Fig. 6.1:* Pre-processing Flow

### 6.1.1 Combining separate Vertical Seismic Profiles

The interferometry experiment at the Collier Point Barite Property produced two series of vertical seismic profiles (VSP's): Shot 1 to Shot 22 with Channel 1 at 83 m borehole depth, Channel 24 at 26 m borehole depth; and Shot 23 to Shot 43 with Channel 1 at 56 m borehole depth, Channel 24 at 10 m borehole depth. The two profiles were then summed together at overlapping hydrophone sections (by Dr. S. Deemer). This was done to provide full hydrophone coverage from 10 m borehole depth to 84 m borehole depth, using the 46 m long hydrophone cable (Figure 6.2). Any timing errors were corrected.

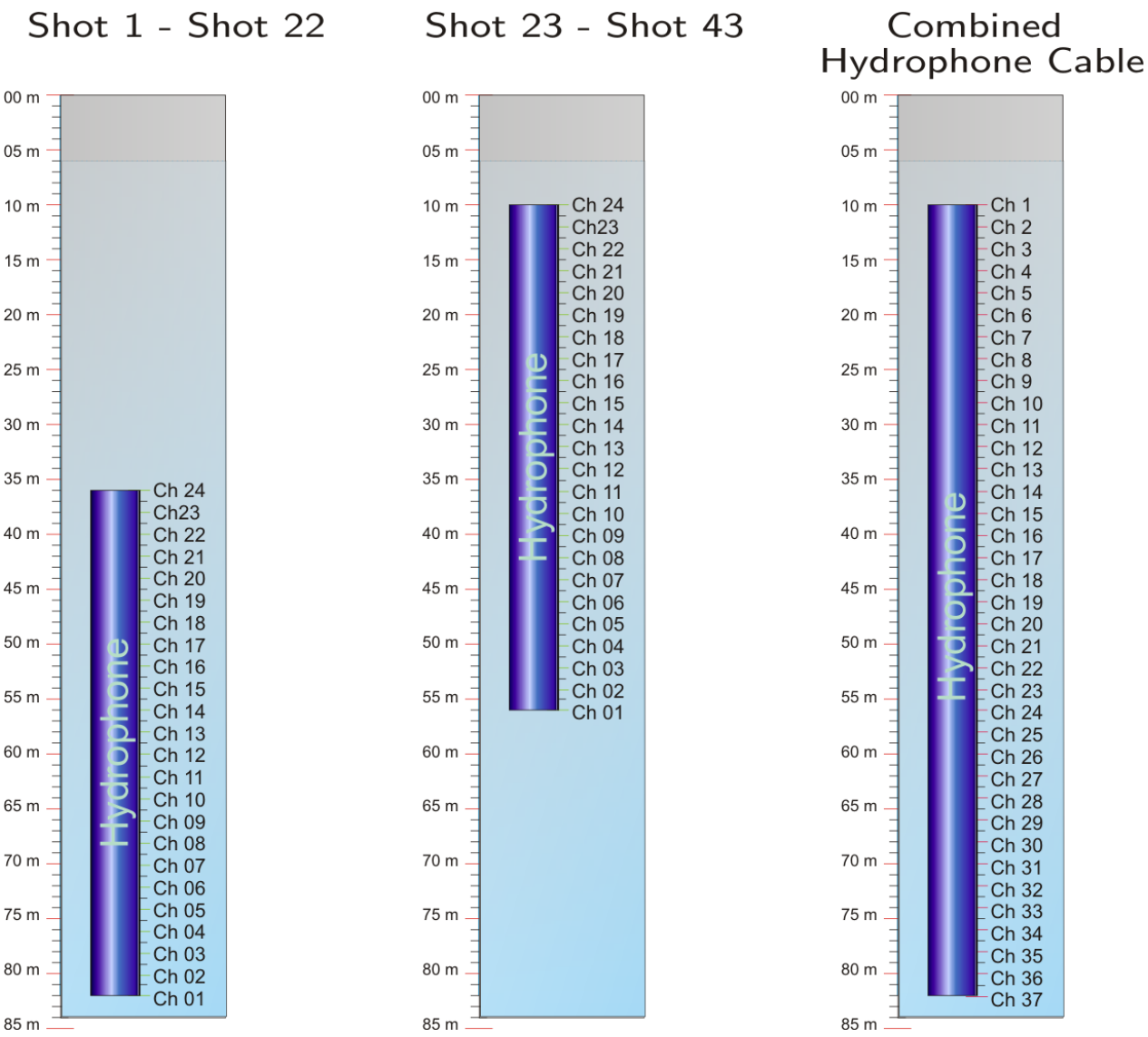


*Fig. 6.2:* Diagram demonstrating position of hydrophone and channels within the borehole Water level in the borehole is at 6 m. For Shots 1 - 22, the Channel 1 was at 82 m and Channel 24 at 36 m borehole depths. For Shots 23 - 43 the hydrophone cable was raised such that Channel 1 was at 56 m and Channel 24 at 10 m borehole depths.

### 6.1.2 Identification of noise in Collier Point Dataset

It is necessary to identify noise, and the sources of noise within the dataset in order to apply the appropriate noise-eliminating techniques and design suitable processing flows. The seismic interferometry method is employed here in the form of a vertical seismic profiling (VSP) technique wherein surface shots are deployed at various offsets from the borehole, and

receivers are positioned at a various depth within the borehole, resulting in the seismic wavefield being recorded in the interior of the Earth as opposed to the surface as in conventional methods. Therefore, Rayleigh and Love waves which propagate at the Earth's surface do not directly interact with the buried receiver. However, the fluid-filled borehole produces a cylindrical discontinuity resulting in guided interfacial waves which travel at the interface between the borehole wall and borehole fluid. These guided interfacial waves are called **tube waves** and are repeated for every seismic shot and represent *high amplitude coherent noise*. Generally speaking, the waves propagate along the axis of the borehole, but do not propagate outward from the borehole as body waves. However, the data demonstrates that the tube waves convert to body waves at interfaces within the borehole (likely stratigraphic) which also reflect the tube waves up and down the borehole.

Tube waves are chiefly generated when the surface Rayleigh wave (produced by the source) moves across the top of the borehole (wellhead) causing it to vibrate vertically. However, in the case of the Collier Point Dataset, the tube waves appear to be generated by compressional body waves (P-waves) upon encountering a strong impedance contrast within the borehole caused by abrupt changes in lithology, fractures, the bottom of the surface casing, or sudden changes in borehole diameter [Hardage, 2000].

Unlike random noise, the tube waves cannot be removed through conventional summation methods because its waveform is consistent through all shots and summation may negatively result in amplification of noise [Hardage, 2000]. Tube wave generation is unavoidable in typical VSP acquistion methods due to impedance contrasts within the borehole wall as a result of abrupt changes in the borehole casing, fractures and lithology changes, which causes a direct P-wave to generate a tube wave at these locations. In some cases, the effect of tube waves may be minimized by reducing ground roll at the wellhead by increasing the distance between the surface source and the wellhead, as the amplitude decreases with increasing propagation distance. However, this method is ineffective at the Collier Point site

as the tube waves appear to be generated due to lithological contrasts or fracturing along the borehole walls.

### Tube waves in Collier Point Dataset

The noise in the Collier Point dataset is primarily in the form of tube waves (Figure 6.4). The tube waves reflect strongly from the bottom of the borehole, and are generated from the P-wave at 20 m, 32 m and a zone between 40-58 m in borehole depths, and travel both up and down the borehole (Figure 6.5, Table 6.1). The tube wave zones are consistent with brittle features around the rock wall as seen in the borehole camera logs (Figure 6.7), where the tube waves are generated in regions with extremely coarse/brittle features or fracturing around the borehole wall (Figure 6.6). The textures noted in the logs correspond to physical changes noted along the borehole walls, i.e. veining, an increase in fracturing, etc. The fracturing may be the result of interaction between the rock and drill bit, with the less ductile rock-types breaking under mechanical stress (Figure 6.6).

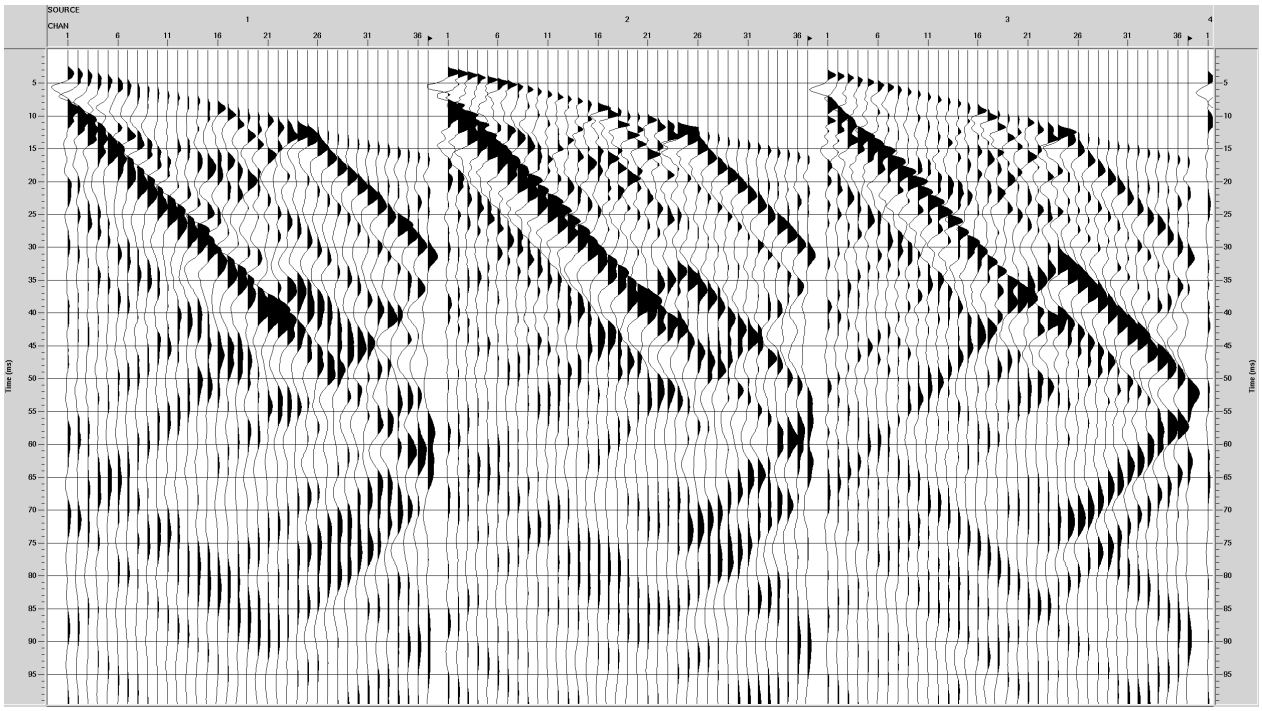


*(a)* Shot 1 - Shot 3 from 0 - 100 ms. 0.2 Gain. Reverse Polarity.

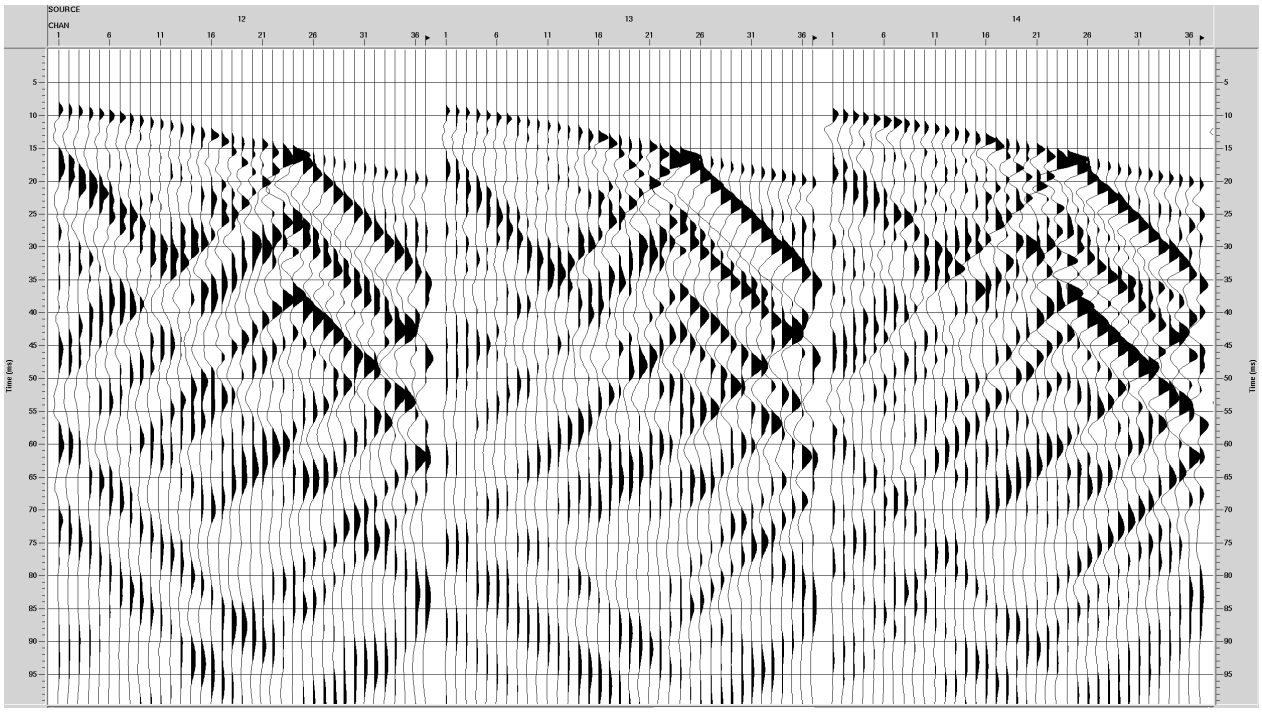


*(b)* Shot 12 - Shot 14 from 0 - 100 ms. 0.2 Gain. Reverse Polarity.

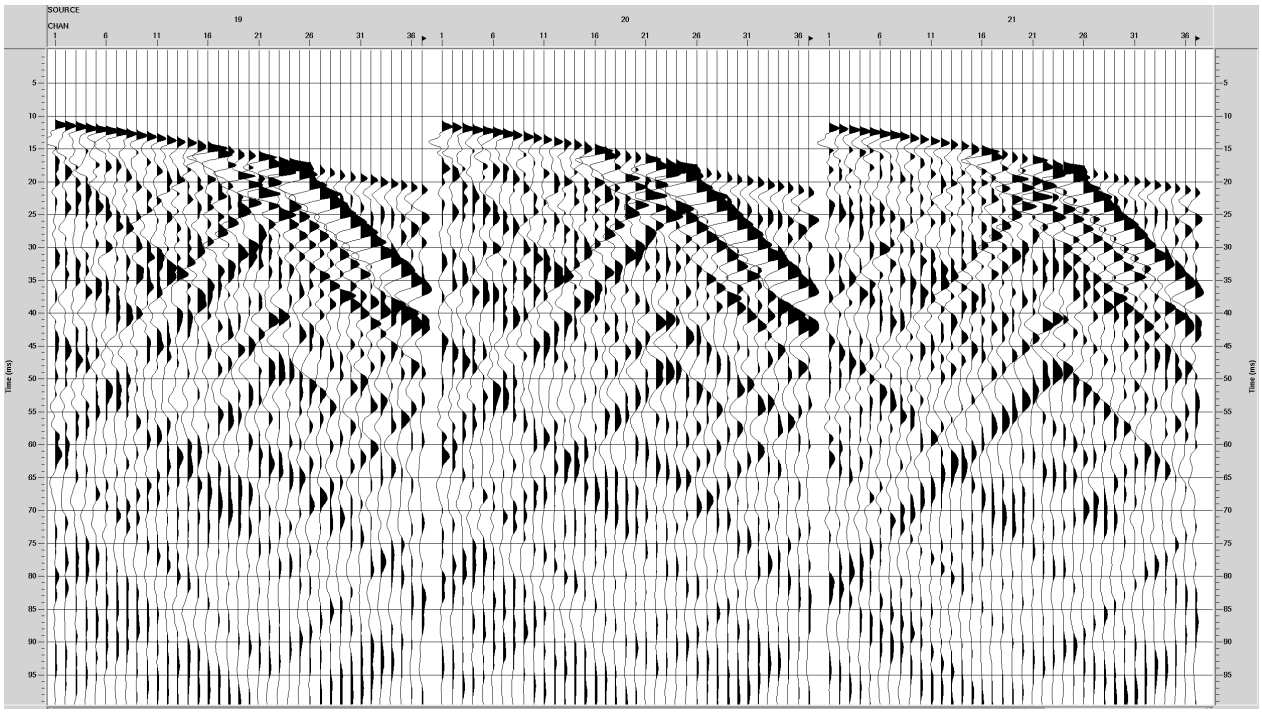


*(c)* Shot 19 - Shot 21 from 0 - 100 ms. 0.2 Gain. Reverse Polarity.

*Fig. 6.4:* Unprocessed and raw seismograms

*Tab. 6.1:* Description & origin of major tube waves in the Collier Point dataset

| Label | Description |
|---|---|
| 1 | Downgoing tube-wave originating at Channel 25 (58 m) |
| 2 | Downgoing tube-wave originating at Channel 17 (42 m) |
| 3 | Late downgoing tube-wave originating at Channel 17 (42 m) |
| 4 | Late downgoing P-wave originating at Channel 6 (20 m) |
| 5 | Downgoing tube-wave originating at the surface |
| 6 | Later downgoing tube-wave originating at the surface |
| 7 | Upgoing tube-wave generated from downgoing P-wave at Channel 17 (42 m) |
| 8 | Upgoing tube-wave originating from downgoing P-wave at Channel 21 (50 m) |
| 9 | Upgoing tube-wave likely generated from downgoing tube-wave |
| 10 | Upgoing tube-wave generated from the bottom of the borehole |
| 11 | Upgoing tube-wave generated from wither the bottom of the borehole, or off downgoing tube-wave 6 |
| 12 | Upgoing P-wave generated from the bottom of the borehole |
| 13 | Upgoing P-wave generated from the bottom of the borehole, or off downgoing tube-wave 6 |
| 14 | Upgoing P-wave generated likely generated from downgoing tube-wave 6 from downgoing tube-wave 6 from the surface |

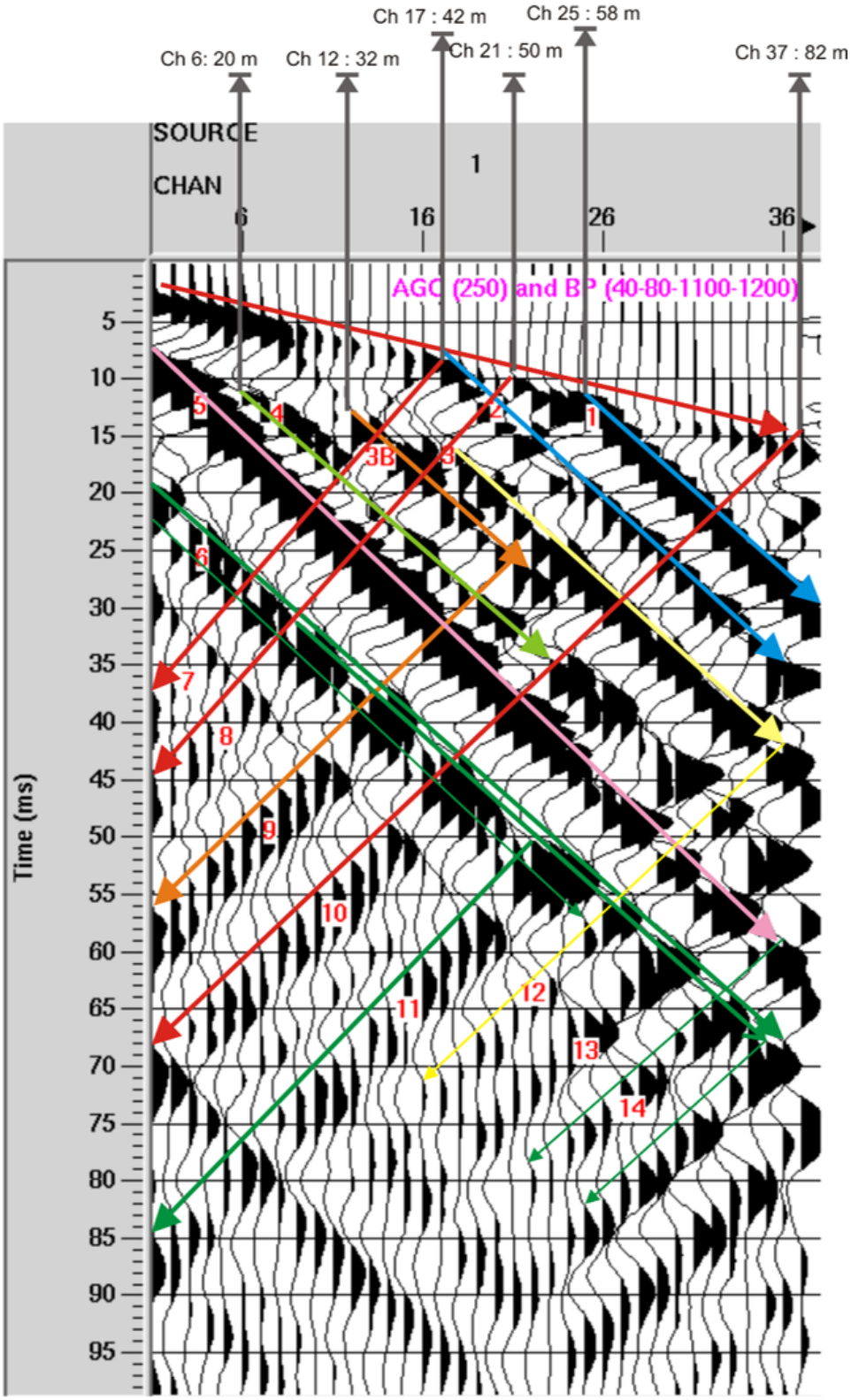


*Fig. 6.5:* Diagram demonstrating tube wave propagation in Shot 1
Note the high contamination of tube waves through the dataset, generating from the P-wave arrival from Channels 17, 21 and 25, and from the bottom of the borehole.

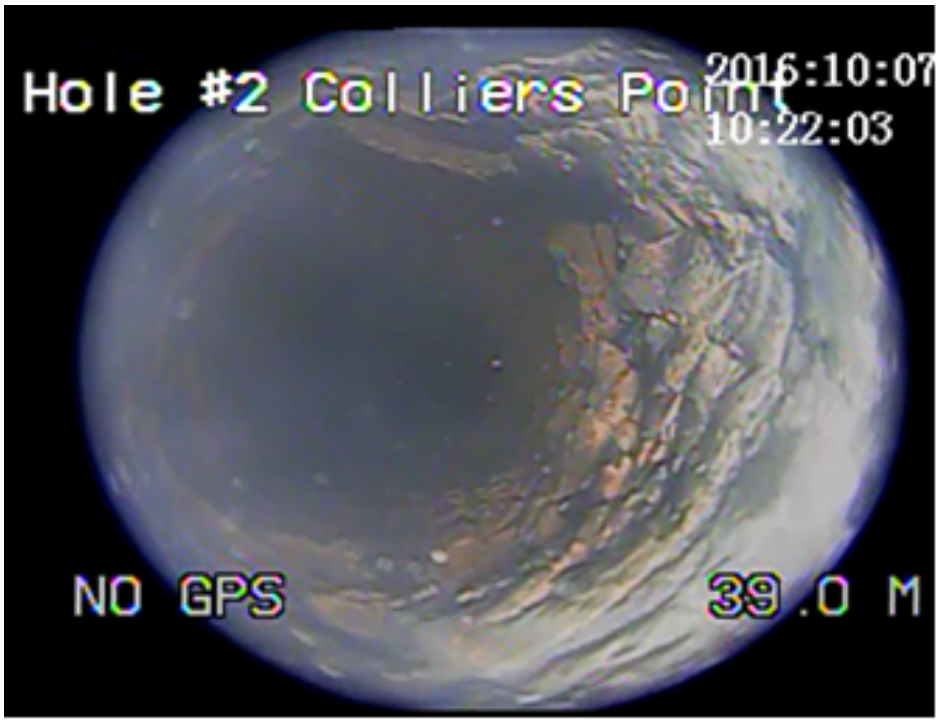


*(a)* 73° inclined borehole used in interferometry experiment

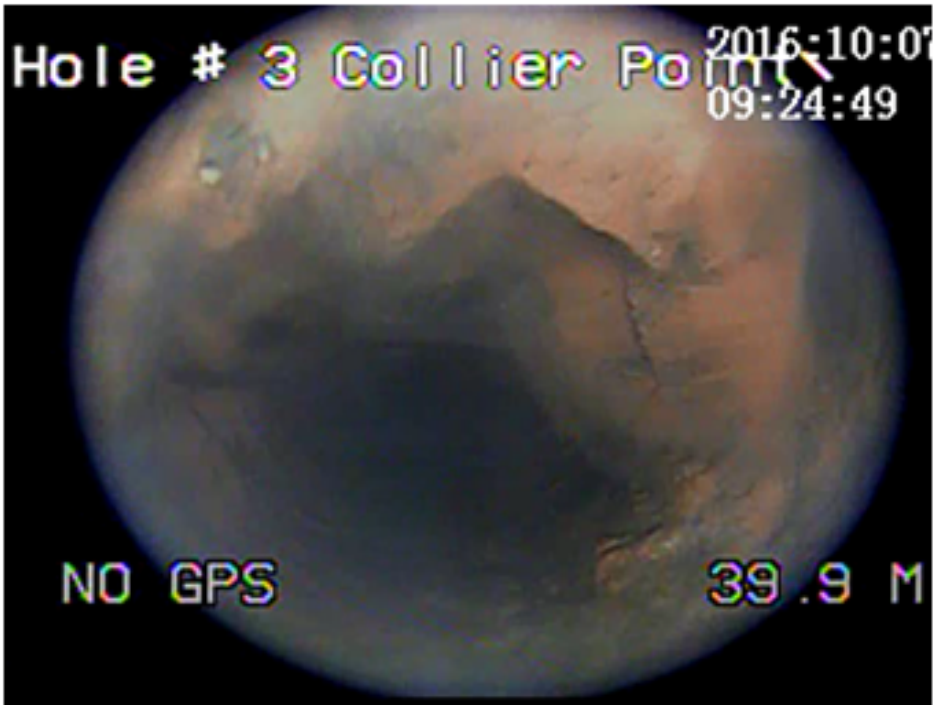


*(b)* Vertical borehole located a few metres away from the inclined borehole

*Fig. 6.6:* Fracturing around borehole walls as captured in borehole cameras

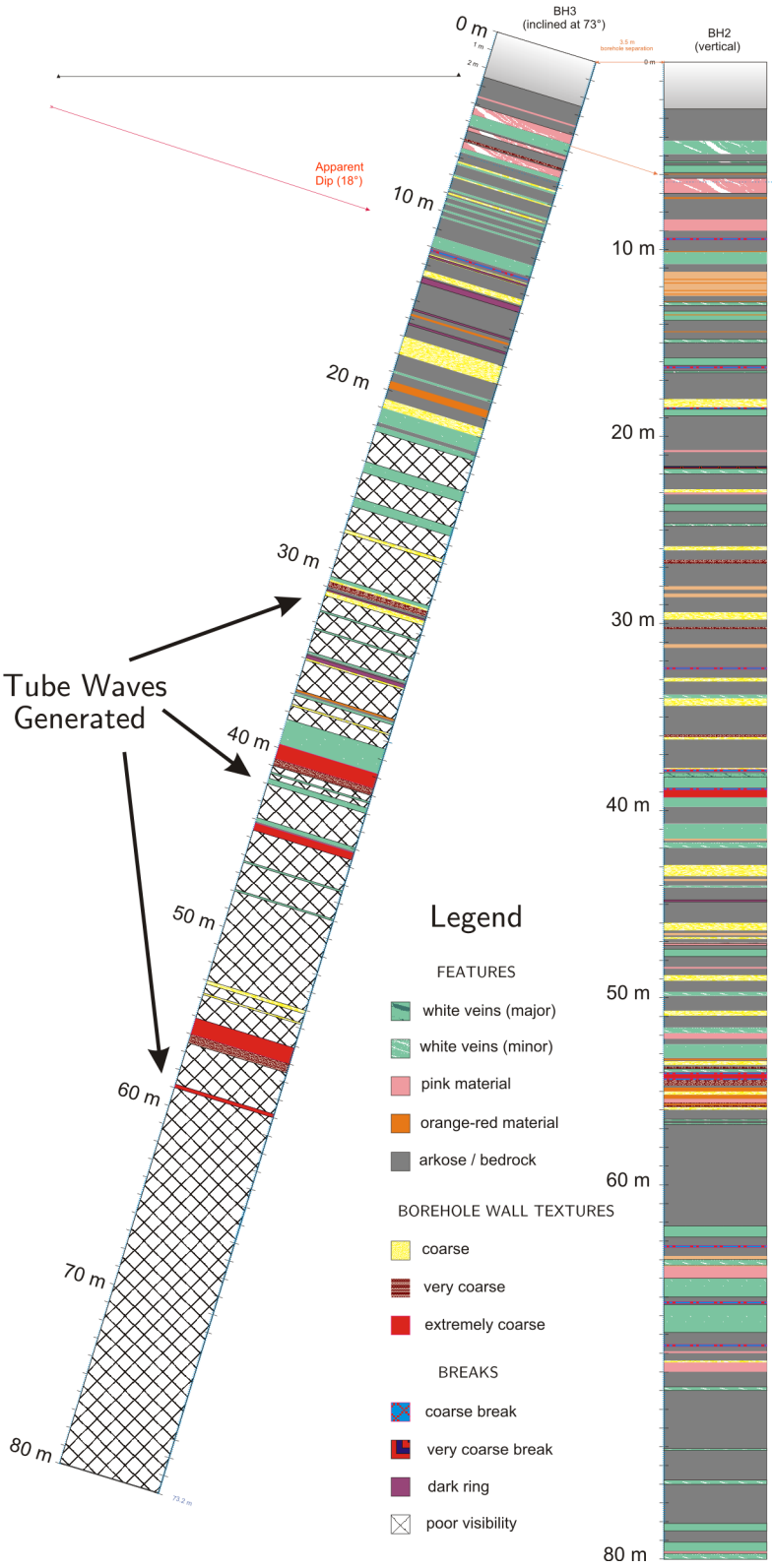


*Fig. 6.7:* Borehole camera log of inclined and vertical borehole at the Collier Point site

### 6.1.3 Deconvolution

A *Spectral Analysis* of the Collier Point dataset is first conducted to characterize the frequency content. The *Direct Wave* is observed to have a peak frequency of $\approx$ 300 Hz with a bandwidth around 1000 Hz (Figure 6.8). It is observed that the dataset is swamped by low-frequency $\approx$ 100 Hz *tube waves* (Figure 6.9) which outweigh the contribution of higher frequencies which are expected with dynamite sources (Figure 6.10).

**Deconvolution** works under the principle that the observed seismic response is comprised of undesirable effects such as attenation and reverberation along with useful signal. The Deconvolution process estimates these undesirable effects as a linear filter. It works under the theory that the recorded seismic signal, S(t) is the product of convolution between the source signal, W(t) and Earth response, R(t). $\eta(t)$ is random noise (Equation 6.1). Therefore, deconvolution of the source wavelet, S(t), from the seismic data results in recovery of the impulse response.

$$S(t) = W(t) * R(t) + \eta(t) \tag{6.1}$$

The two kinds of deconvolution initially considered for the Collier Point dataset were *Predictive Deconvolution* and *Spiking Deconvolution*. **Predictive Deconvolution** is initially considered as a method of attenuating the tube waves due to the 'predictive' nature of the tube waves, bouncing back and forth from the top and bottom of the borehole and from fractured regions, and has been previously used in other datasets with success [Gulati et al., 2001]. However, the method was not suitable for the Collier Point dataset as the autocorrelation of the shots suggested that a wide variation of suitable prediction distances were required from shot to shot (Figure 6.12), which renders predictive deconvolution ineffective.

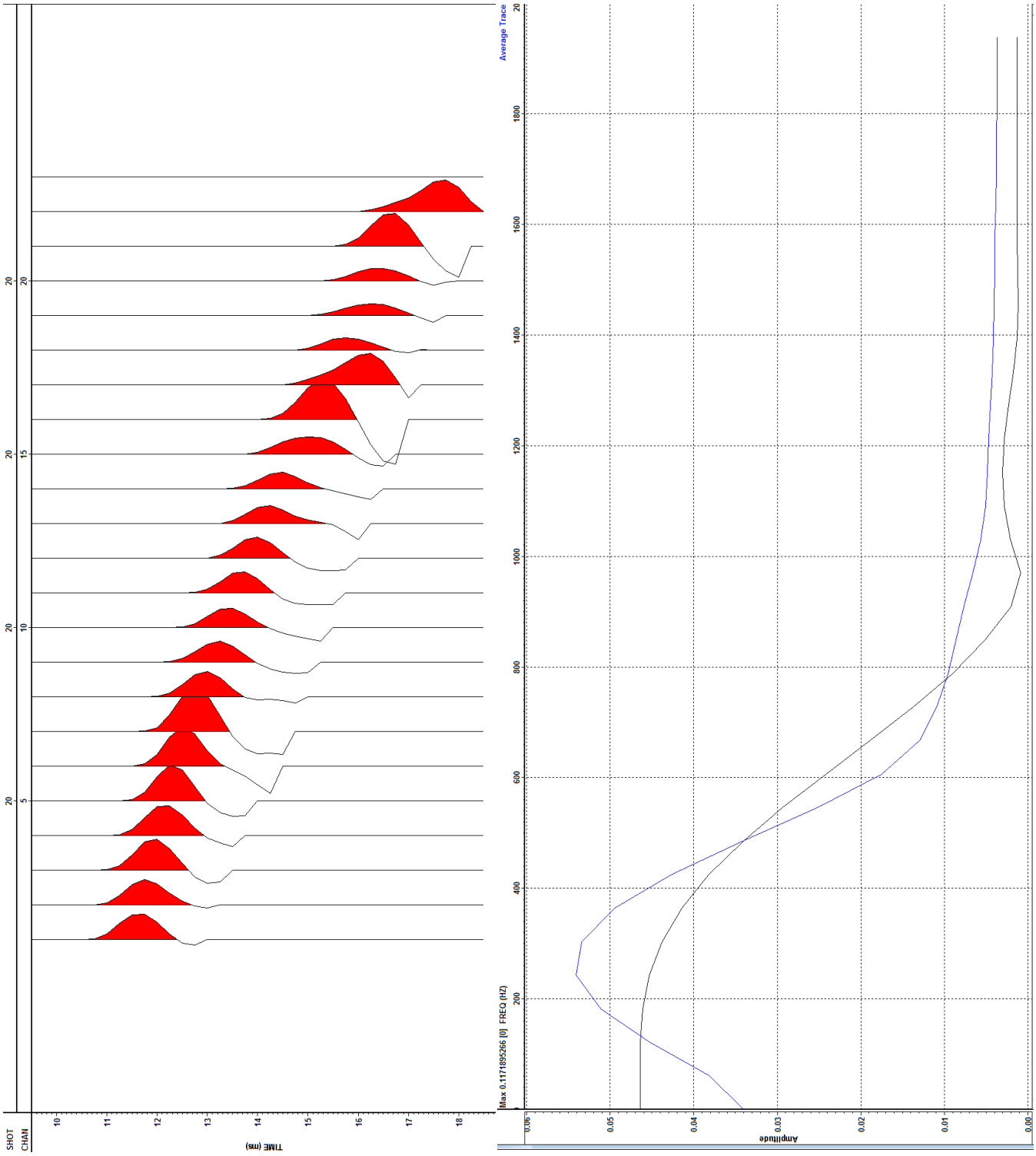


*Fig. 6.8*: Spectral Analysis of Direct Wave in Shot 20 in the Collier Point Dataset

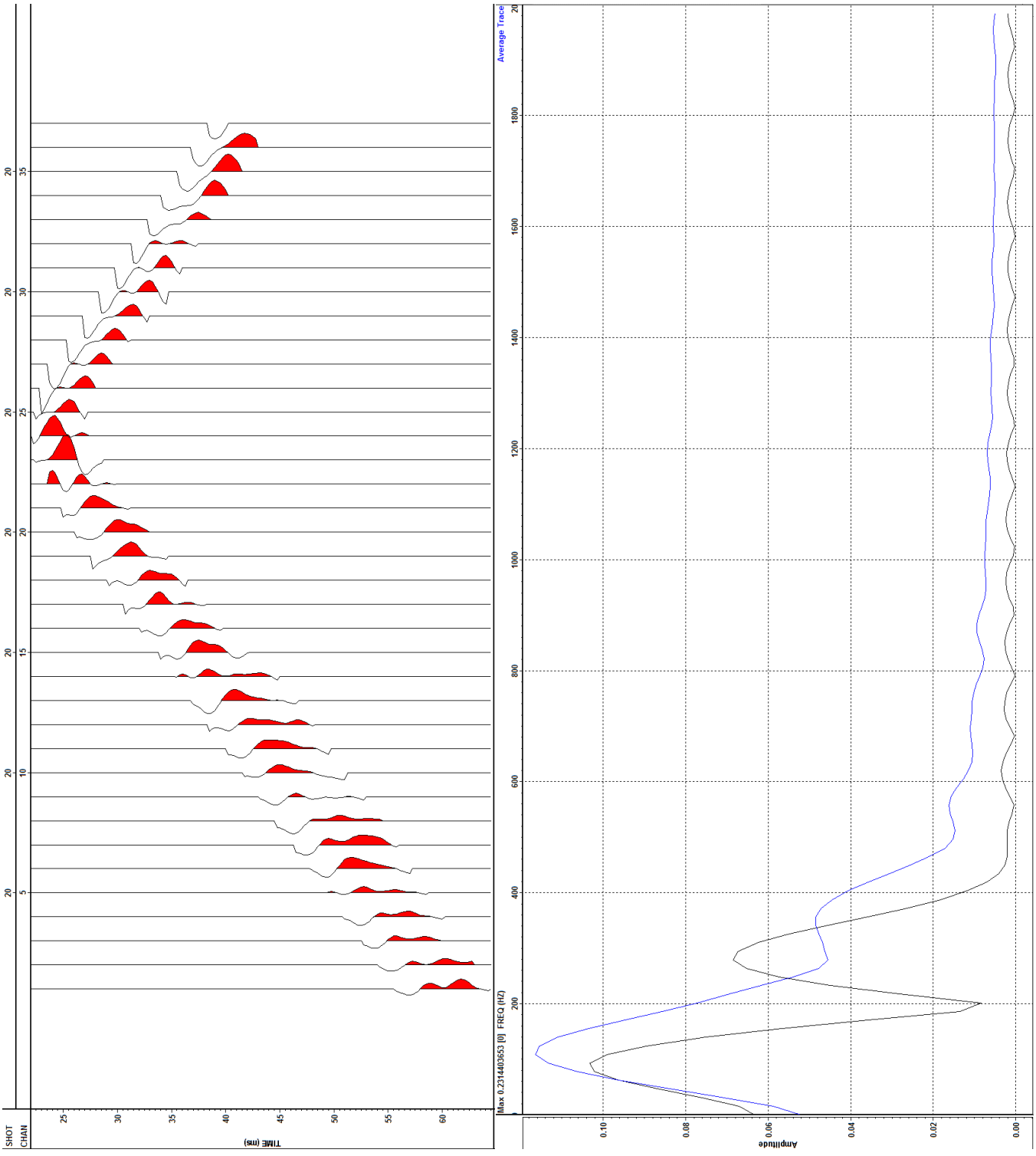


*Fig. 6.9:* Spectral Analysis of a tube wave in Shot 20 in the Collier Point Dataset

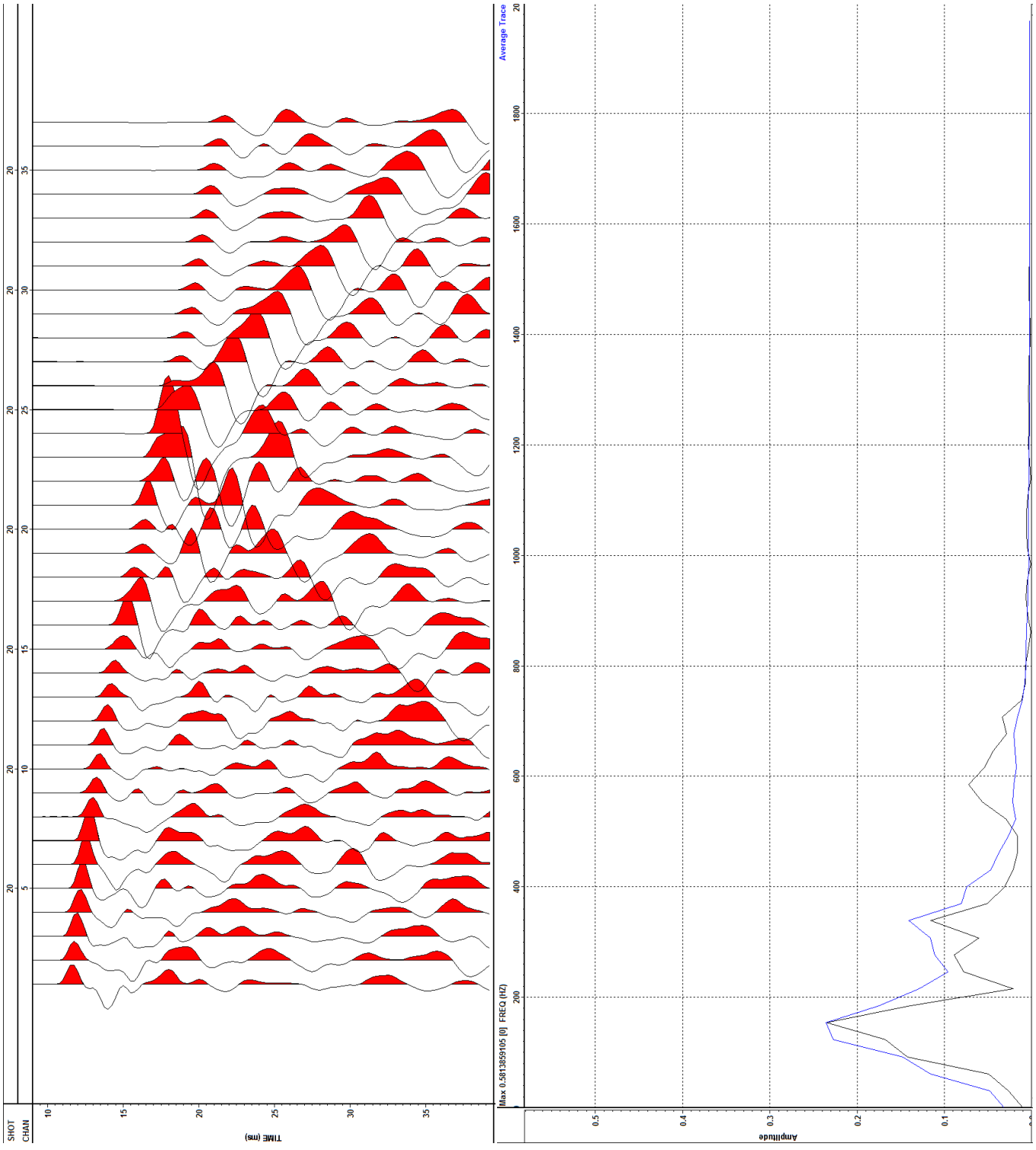


*Fig. 6.10:* Spectral Analysis of Shot 20 in the Collier Point Dataset

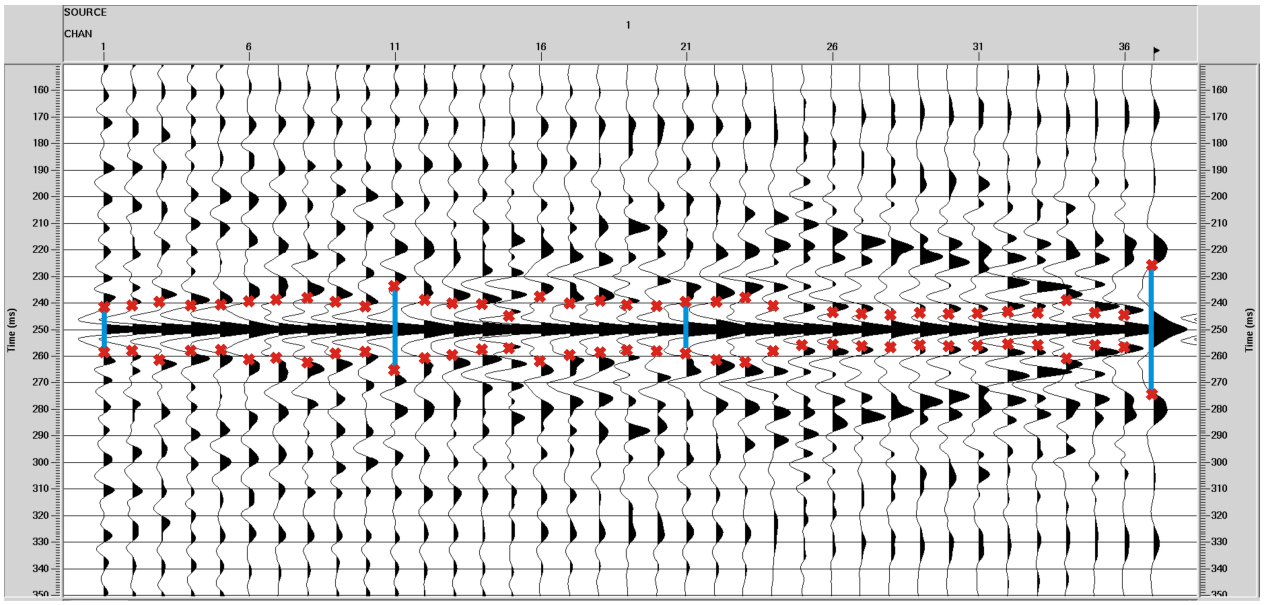


*(a)* Autocorrelation of Shot 1

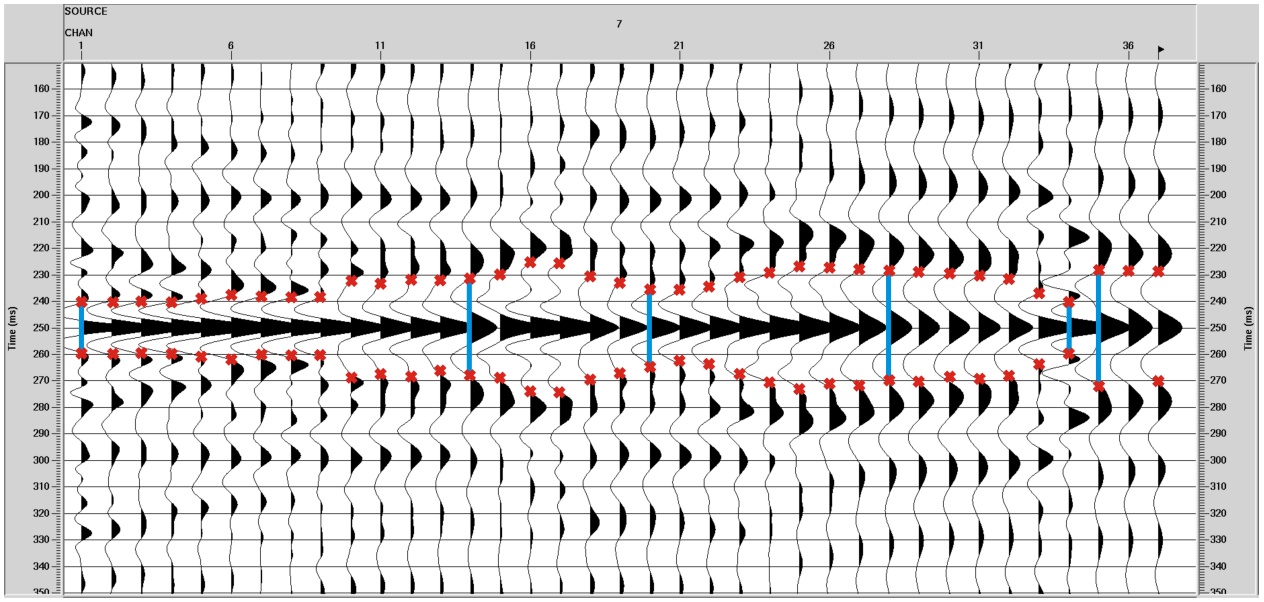


*(b)* Autocorrelation of Shot 7

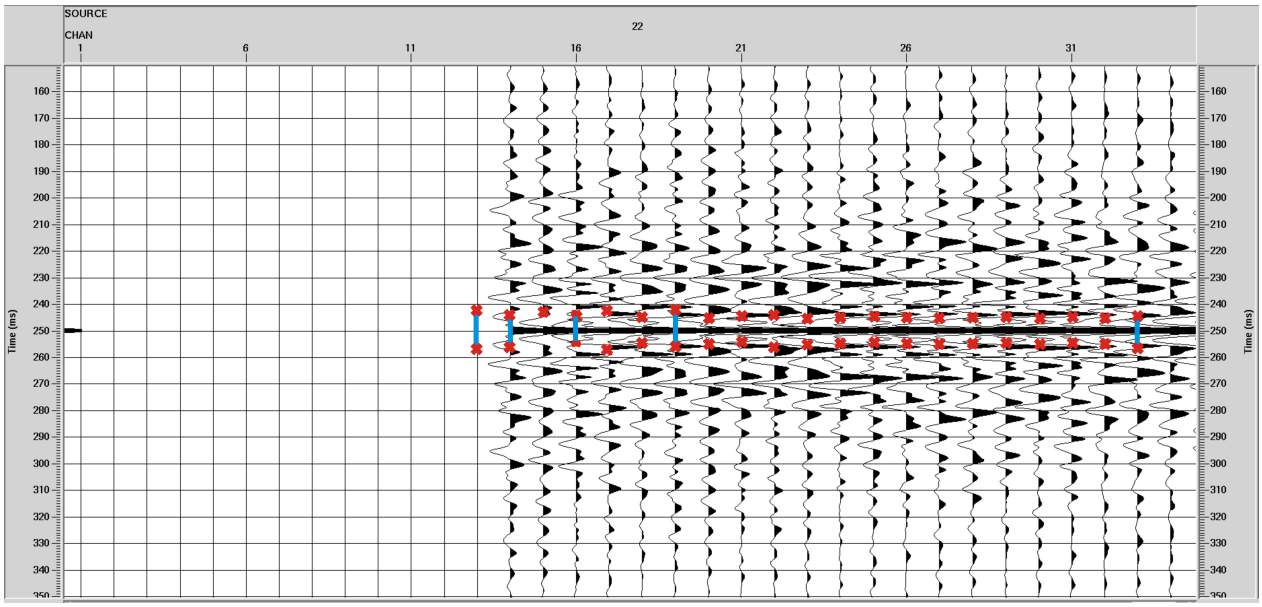


*(c)* Autocorrelation of Shot 22

*Fig. 6.12:* Autocorrelation of shots in the Collier Point Dataset
30% Scaling. Prediction distances are marked by blue bars.

*Spiking Deconvolution* of the data is then considered to broaden and flatten the frequency spectrum due to the low frequency ($\approx$ 100 Hz) tube waves essentially swamping the spectrum and diminishing the effect of higher frequencies as seen in spectral analyses of Shot 1 and Shot 22 (Figures 6.13 and 6.14). **Spiking Deconvolution** is used as a spectral whitening technique to balance the spectrum and bring out the contribution of the higher frequencies in order to effectively image the target. The spiking deconvolution applied in ProMAX is implemented using the *Weiner-Levinson least square algorithm.* After testing various operator lengths, a spiking deconvolution operator length of **60 ms** was found to produce the most desirable result (Figure 6.15) and therefore applied to broaden the spectrum and bring up the higher frequencies in the dataset (Figure 6.16).

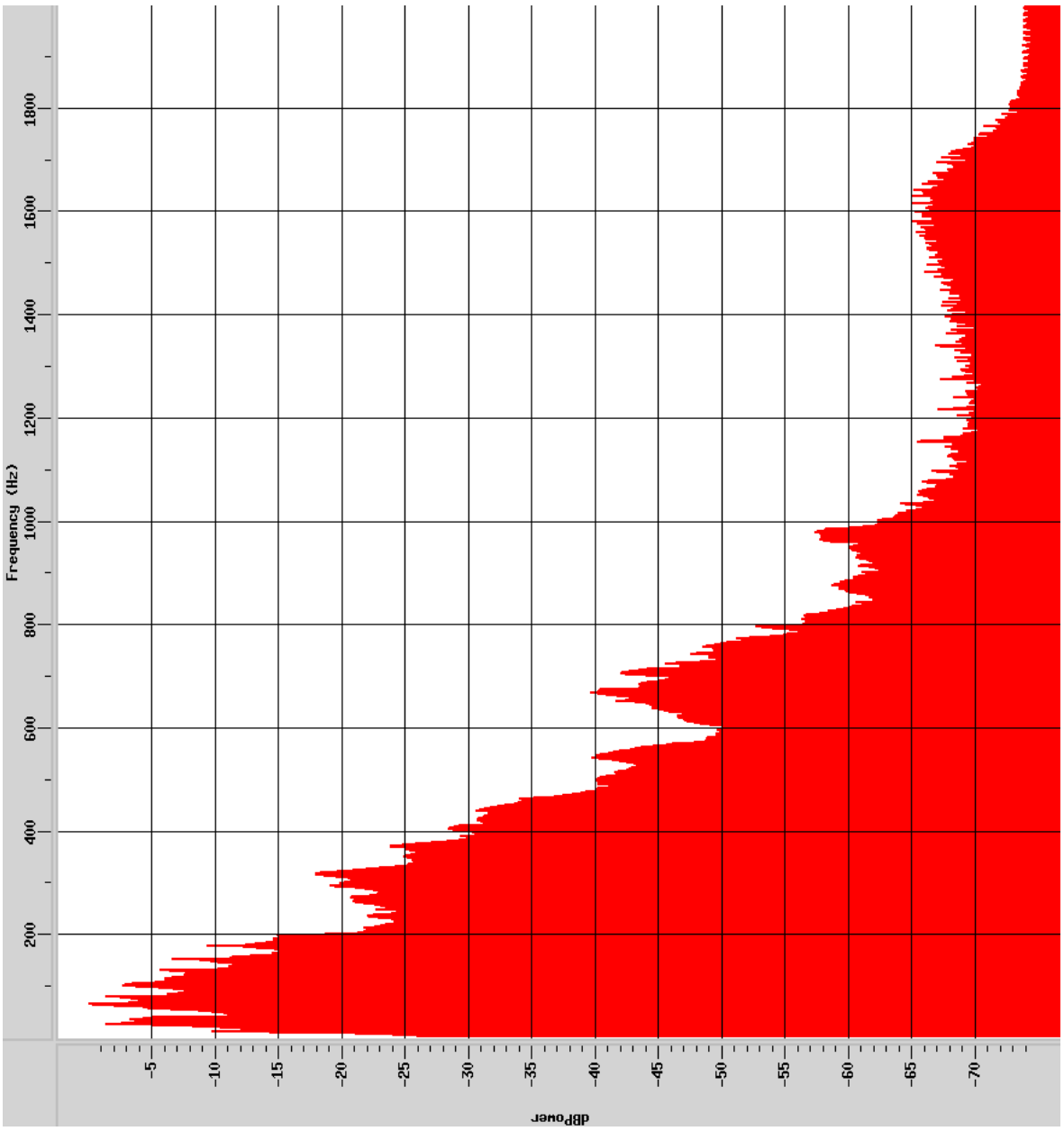


*Fig. 6.13:* Spectral Analysis of Shot 1 before Spiking Deconvolution

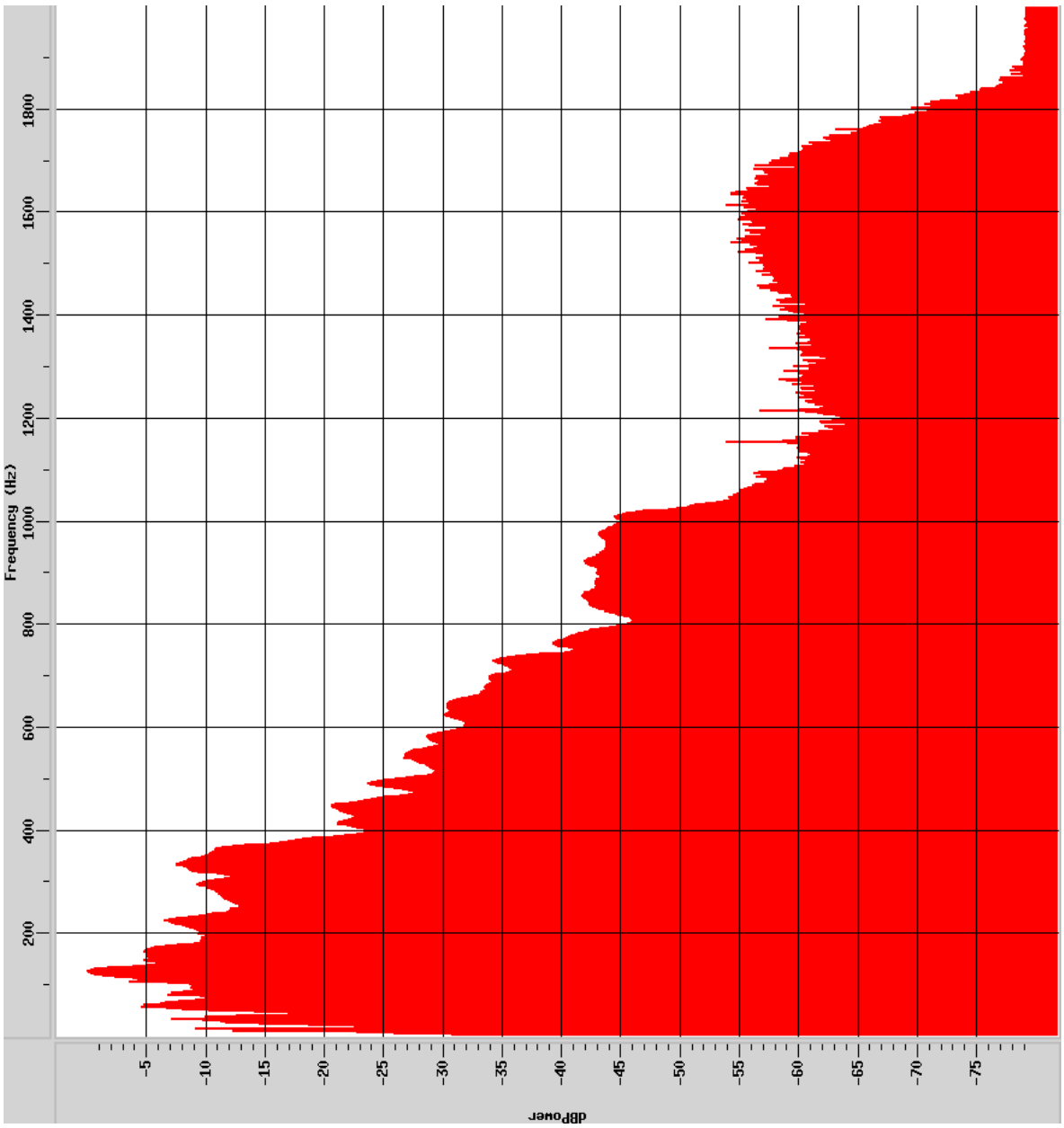


*Fig. 6.14:* Spectral Analysis of Shot 22 before Spiking Deconvolution

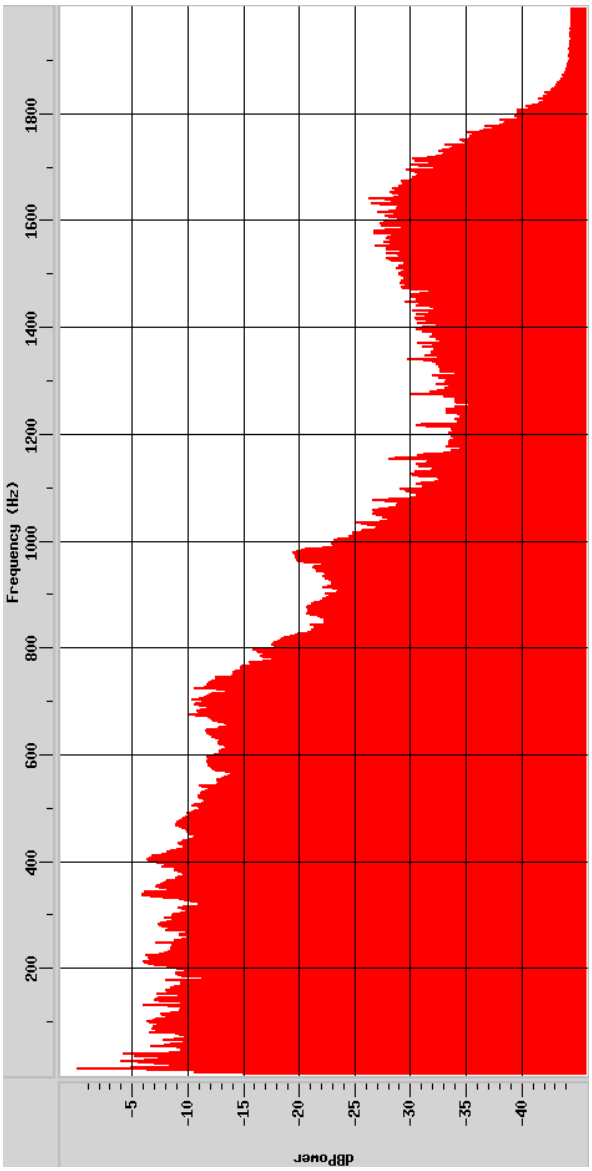


*(a)* Shot 1

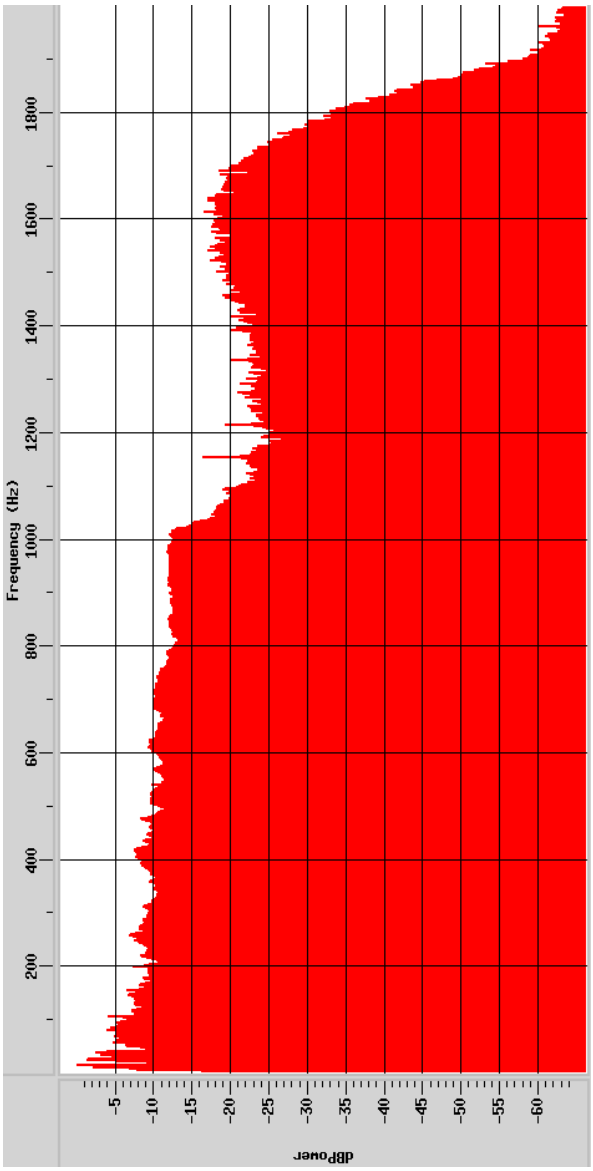


*(b)* Shot 22

*Fig. 6.15:* Spectral Analysis after Spiking Deconvolution (60 ms)

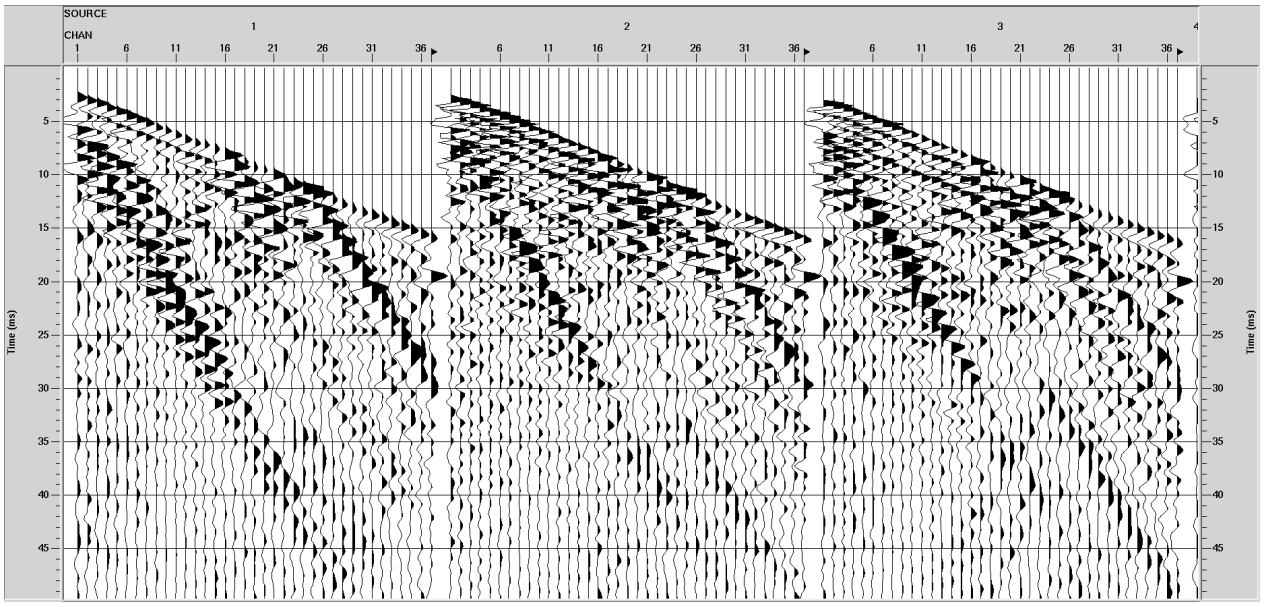


*(a)* Shot 1 - Shot 3

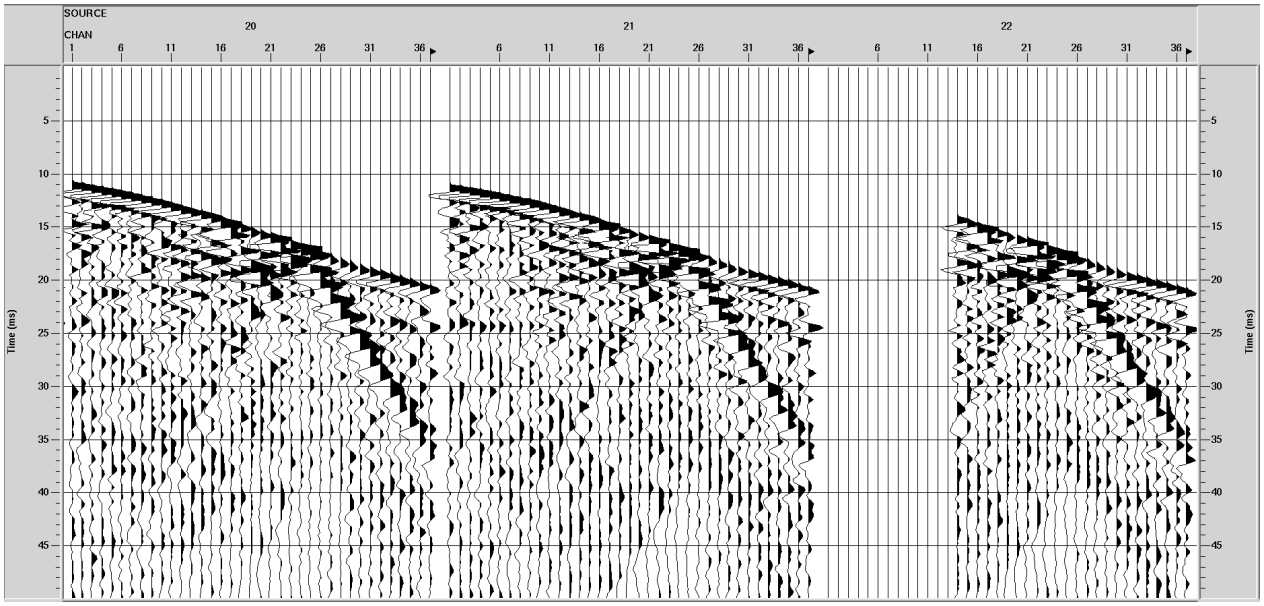


*(b)* Shot 20 - Shot 22

*Fig. 6.16:* Seismic Dataset after Spiking Deconvolution (60 ms)
Reverse Polarity and Gain = 0.3. Note that the tube wave is spatially aliased at higher temporal frequencies.

### 6.1.4 F-K Filtering

Although the **Spiking Deconvolution** doesn't completely remove the contribution of the tube waves, it balances the spectrum, thereby enabling other noise-removal methods (such as F-K filtering) more likely to work well (Figure 6.16). An *F-K (Frequency-Wavenumber analysis* of the dataset for Shot 12 (Figure 6.18) demonstrates how the energy density within a given time interval is contoured on a frequency-versus-wavenumber plot, and can be used to examine the direction and apparent velocity of seismic waves in the dataset. F-K analysis is therefore a tool which enables the design and quality control of F-K filters applied to the seismic data, by isolating unwanted waves such as tube waves.

*F-K velocity filtering* is a processing technique commonly used to remove undesirable energy modes from digitally recorded seismic data [Embree et al., 1963]. It was implemented to attenuate the effect of tube waves, and aliased tube waves which are the primary noise source within the dataset. As velocity is a vector quanity, it works on the premise that the propagation velocities of seismic wave modes differ as a function of - the direction of propagation, and the magnitude of the velocities. As a velocity filter isolates unwanted energy by working on either, or both functions, noise that cannot be easily attenuated in the T-X (Time-Space) domain may be attenuated in the F-K (Frequency-Wavenumber) domain [Hardage, 2000].

In the F-K domain, the velocity, $V$ is expressed in Equation 6.2 where $\omega$ is the angular velocity, $F$ is the frequency, and $K$ is the wave-number.

$$V = \frac{2\pi F}{K} = \frac{\omega}{K} \tag{6.2}$$

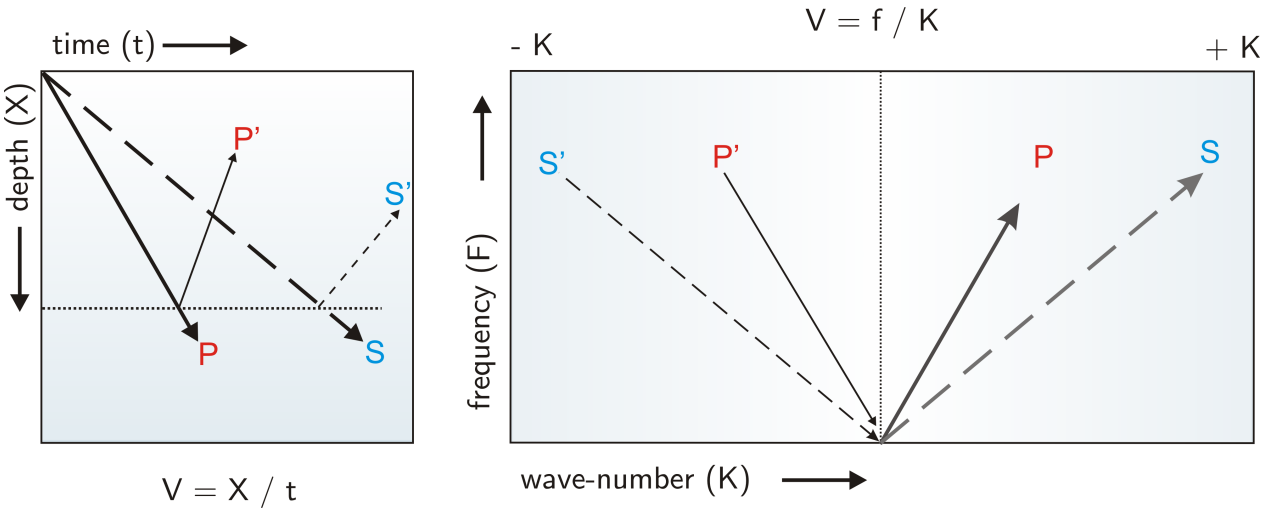


*Fig. 6.17:* Diagram representing downgoing and upgoing P and S-waves in the T-X domain and F-K domain (Adapted from [Hardage, 2000])
The above diagram demonstrates how downgoing P and S-waves in VSP data are transformed into F-K space following a 2D Fourier Transform. The downgoing waves appear in the +K (positive wavenumber) half plane, and upgoing waves in the -K (negative wavenumber) half plane.

VSP wave modes are separated during velocity filtering by transforming the dataset from the T-X (Time-Space) sampled traces to the F-K domain by two-dimensional Fourier Transform, following which the data is converted back to the T-X domain by inverse Fourier Transform.

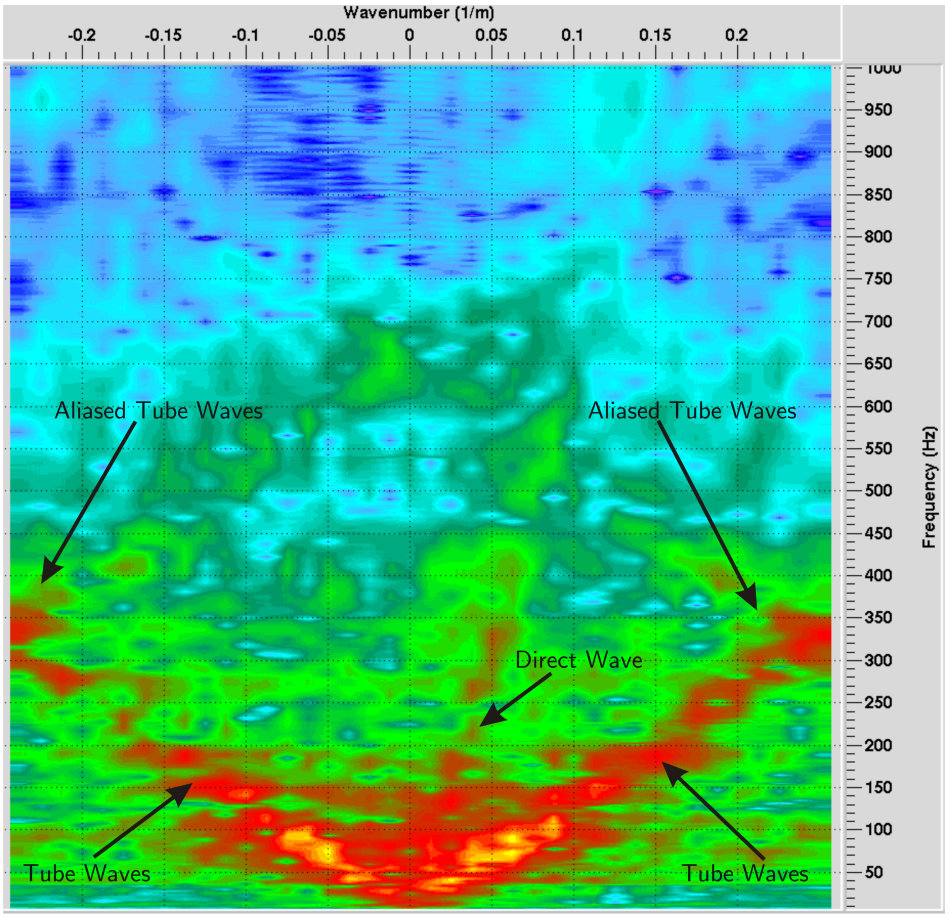


*Fig. 6.18:* F-K Analysis of Shot 12 with waves within the F-K Spectrum labelled

It is observed that the F-K filtering is significantly better in attenuating tube waves when designed to strictly pass (or accept) only the direct wave and region of possible reflections (Figure 6.22), when compared to only blocking (or rejecting) the tube waves and associated aliasing (Figure 6.21). Hence, after testing a series of F-K filters, a **F-K Accept** (Figure 6.20) which passes only the applied polygon region, was chosen over the more commonly used F-K Reject filter (Figure 6.19) which isolates the applies polygon region. The F-K Reject polygon was designed manually on a shot gather by shot gather basis. The dataset is moved to Seismic Unix to create the **correlation gathers** following the application of the Spiking Deconvolution to balance the frequencies and F-K filter to attenuate the effect of the tube waves.

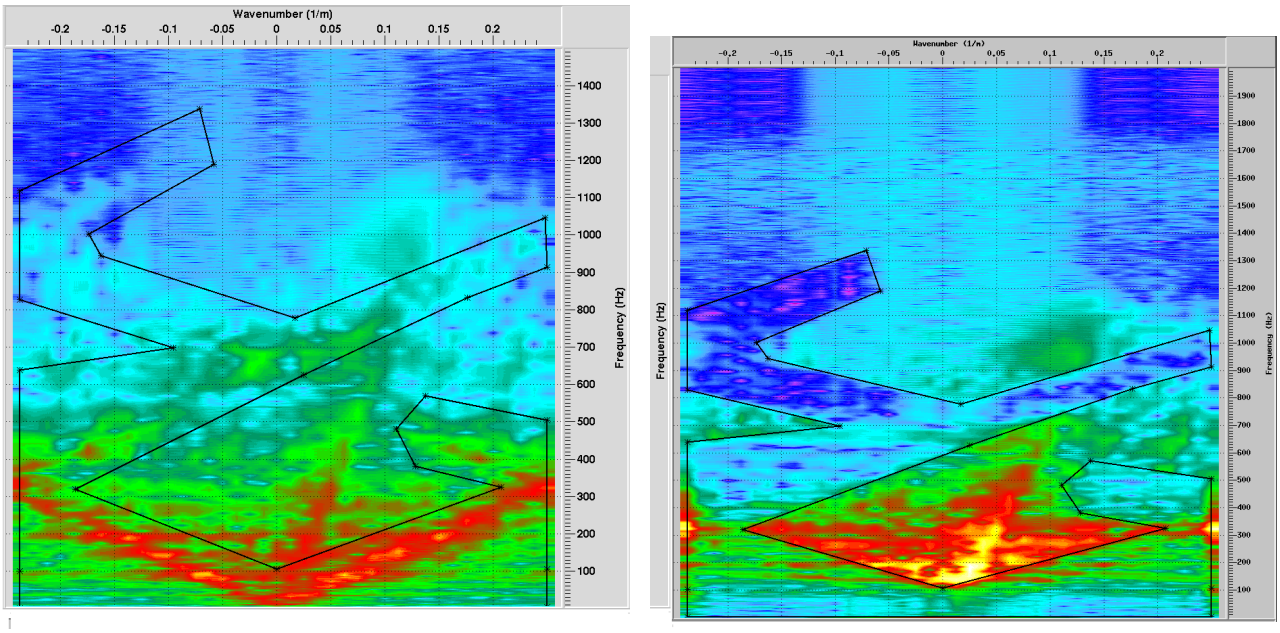


*(a)* F-K reject filter polygon *(b)* Resultant F-K spectrum after filtering

*Fig. 6.19:* F-K Reject Filtering

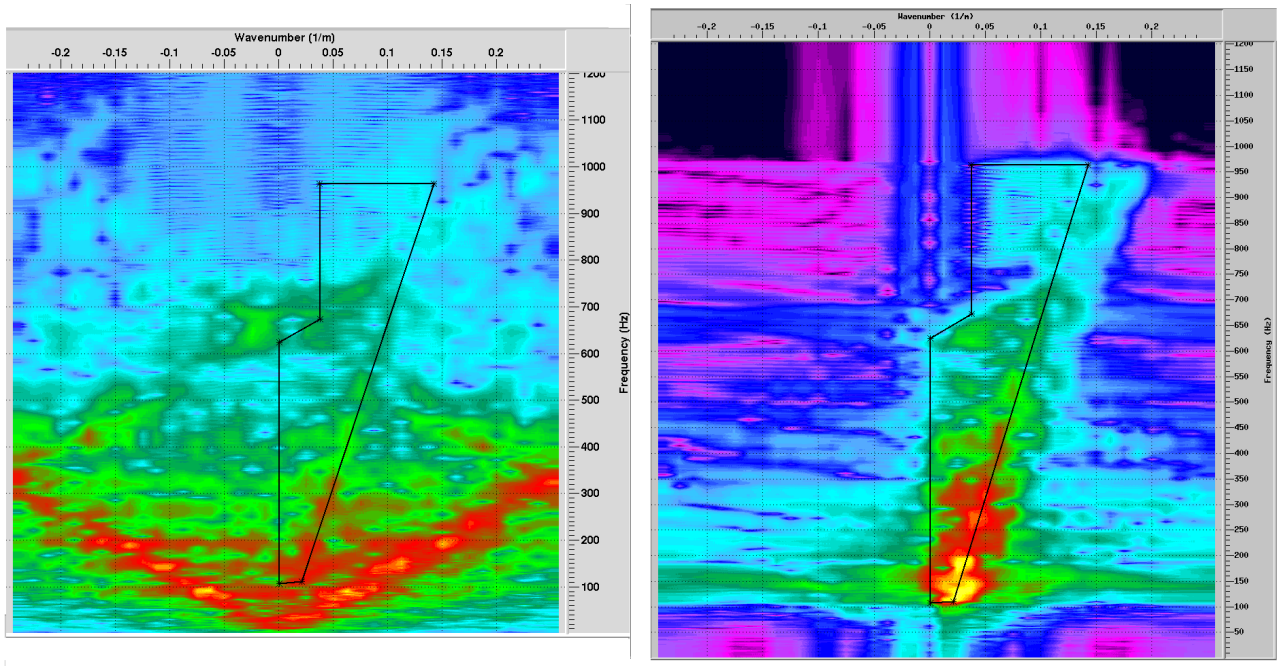


*(a)* F-K accept filter polygon *(b)* Resultant F-K spectrum after filtering

*Fig. 6.20:* F-K Accept Filtering

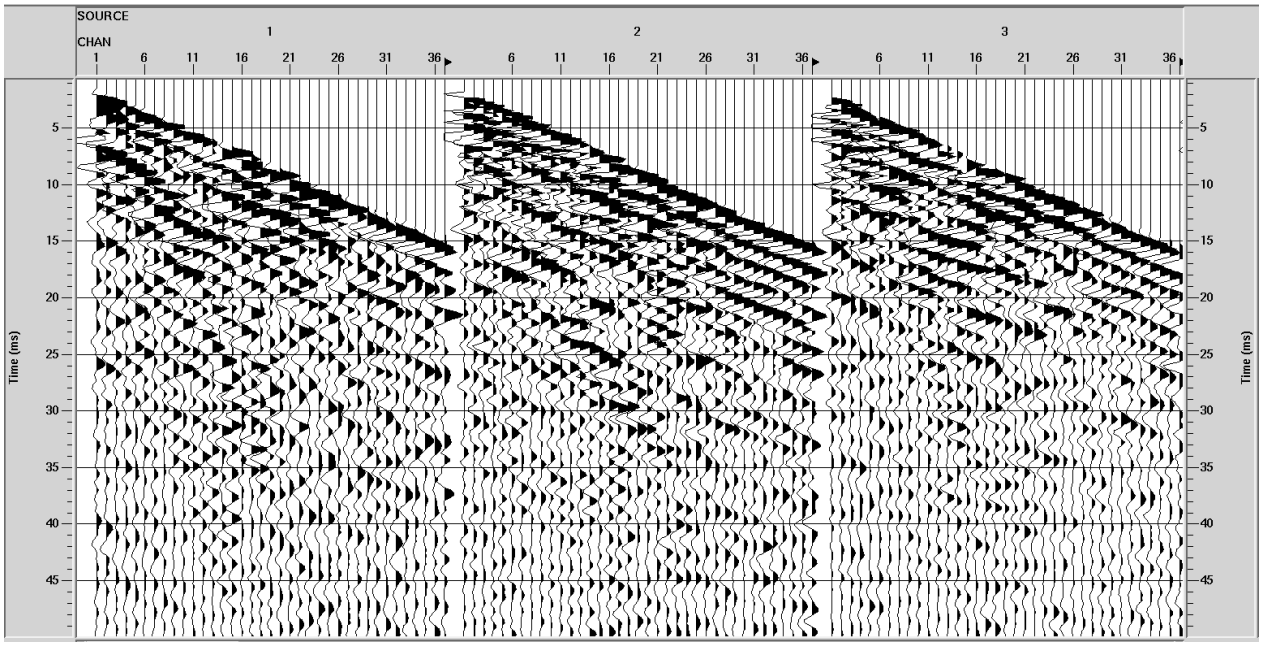


*(a)* Shot 1 - Shot 3

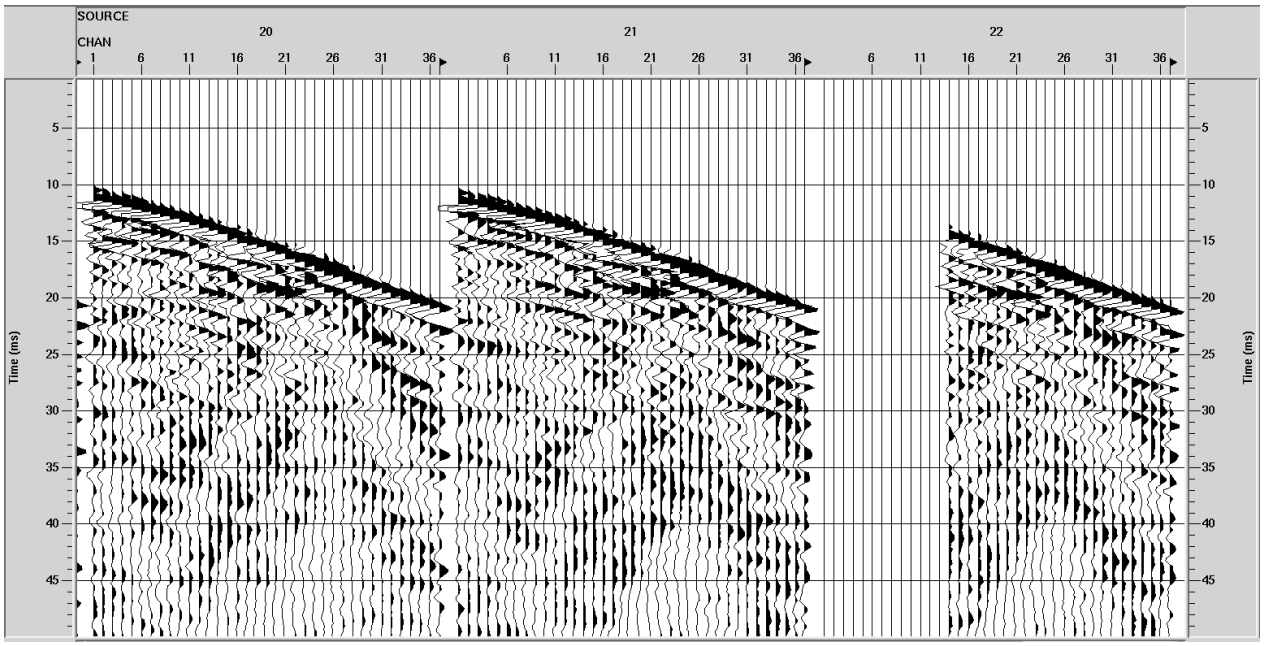


*(b)* Shot 20 - Shot 22

*Fig. 6.21:* Seismic Dataset after F-K Reject Filtering and Spiking Deconvolution (60 ms)
Reverse Polarity and Gain = 0.3

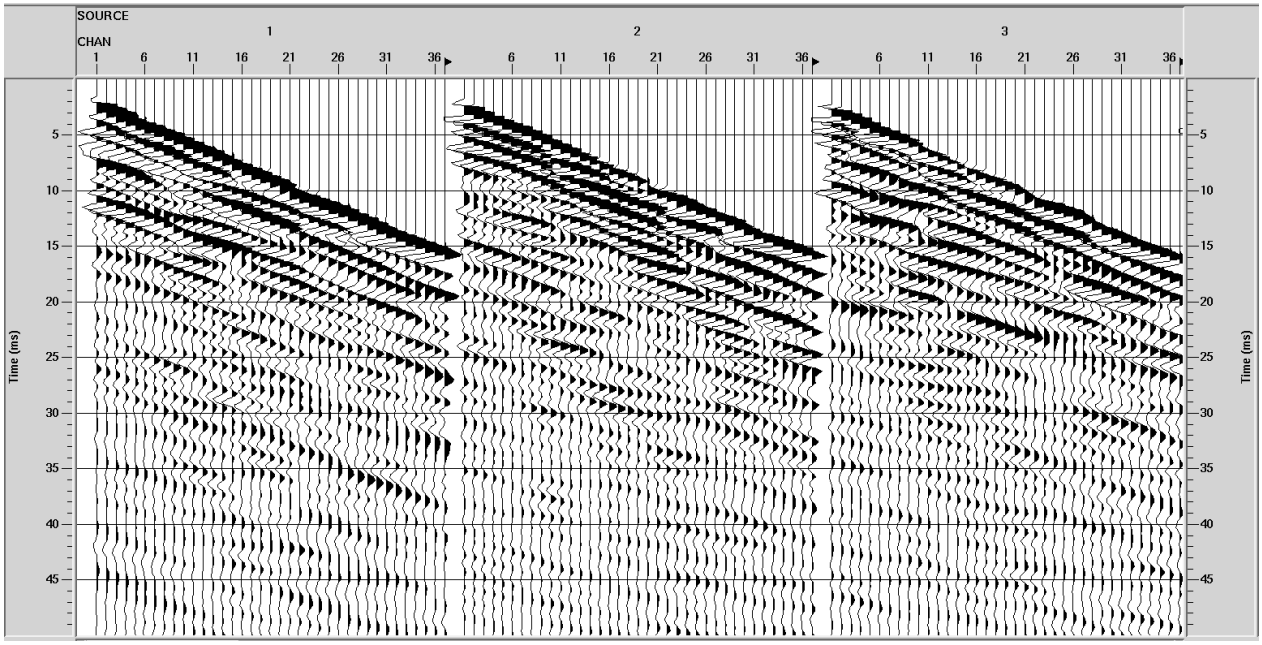


*(a)* Shot 1 - Shot 3

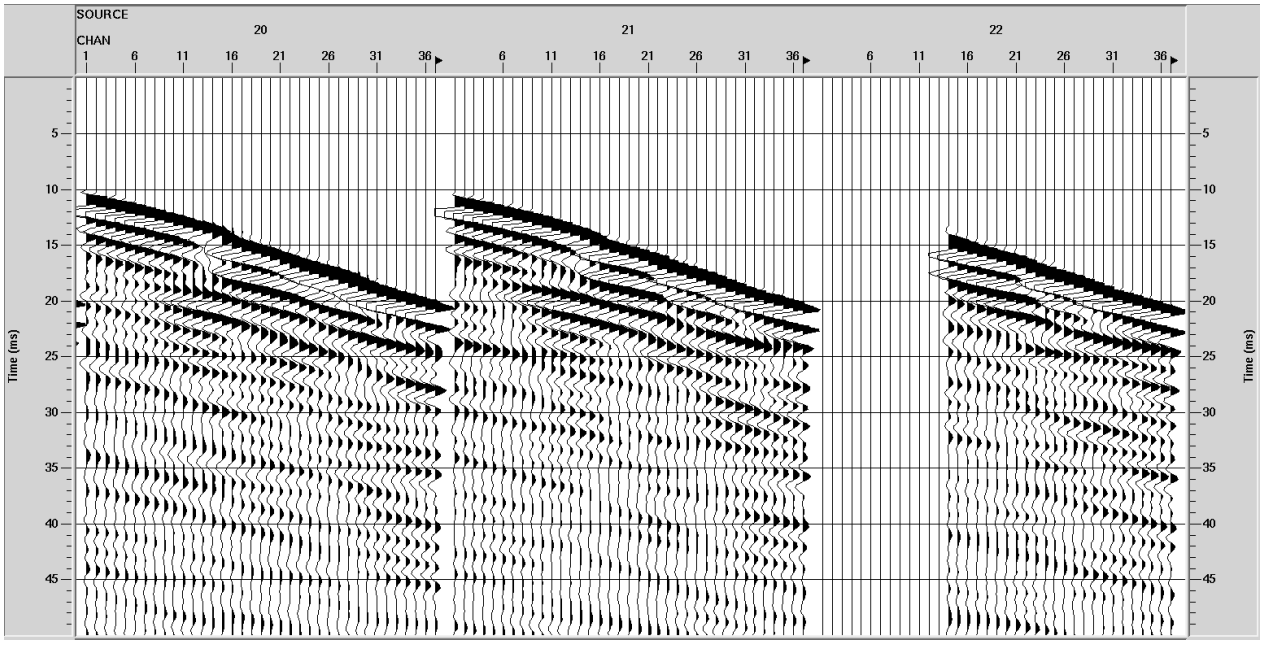


*(b)* Shot 20 - Shot 22

*Fig. 6.22:* Seismic Dataset after F-K Accept Filtering and Spiking Deconvolution (60 ms) Reverse Polarity and Gain = 0.3

## 6.2 Interferometry

Following the pre-processing, the preprocessed data-set in .sgy format was moved to the Seismic Unix interface to commence the interferometry procedure. The interferometry processing flow is described in Figure 6.23, and the reasoning for these processes will be explained in following sections.

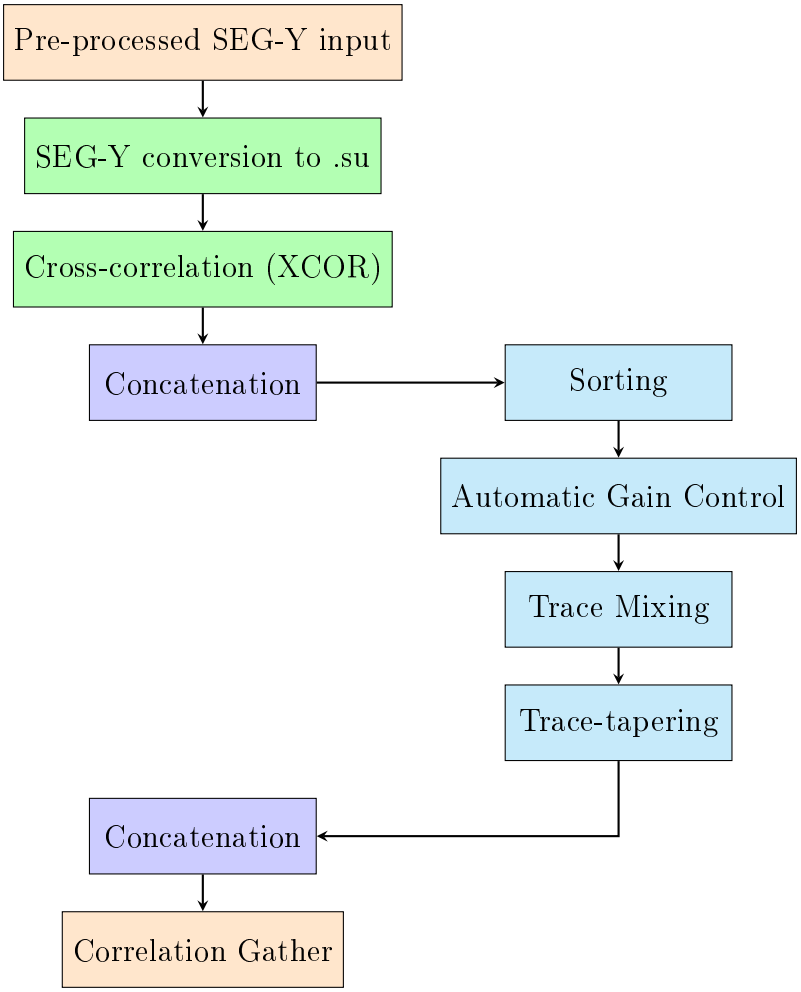


*Fig. 6.23:* Interferometry processing flow

### 6.2.1 Correlation Gather

The cross-correlation gather was created in Seismic Unix using the script XCOR2 (Appendix C.3). The pre-processed Collier Point dataset is converted to .su format in Seismic Unix and read, looping through the range of 21 surface shots and 37 receiver channels. Each of the 21 surface shot records are cross-correlated with the 37 individual receiver channels within each of the shots to create a cross-correlated file. The individual cross-correlated files are then concatenated.

The concatenated cross-correlated file is sorted by Virtual source number, Channel Number, and FFID number such that, each of the 37 Virtual sources have 37 receiver channels within them and each channel has 21 surface shots. The individual channel ensembles are then gained (AGC) to a 40 ms window and are subjected to a **standard weighted mix** (Subsection 6.2.1), and a **linear trace taper** (Subsection 6.2.1). The individual gained, weighted and trace-tapered files are then concatenated to create a **Correlation Gather** (Appendix C).

The correlation gather for Live Source 1 is shown in Figure 6.28. The cross-correlation of two receivers increases the trace length to that of each receiver combined. The intial trace length is 200 ms and the correlated trace-length is doubled to 400 ms. The **zero-lag** is at 200 ms. It represents the initial time at which energy starts to propagate from the virtual source location for any given correlogram, i.e. 'time zero' in the virtual source gather. The *leads* (0 - 199 ms) are the energy seen before zero-lag and do not contain any geological information (acausal data). The *lags* (200 - 400 ms) are the energy seen after zero-lag and contain the virtual source energy (causal data). Cross correlation and summation of the correlation gathers produces the **virtual source gather**.

### Trace Mixing

Trace mixing is implemented to the cross-correlated files as a rapid method of enhancing horizontal signal and diminishing random noise prior to concatenation. The method multiplies lateral trace samples within a trace mixing window of 3 traces by a symmetrical weighting function biased towards the central trace (1, 3, 1), sums the weighted samples and normalizes this accumulated weighted sample by the sum of the weights (Figure 6.27) . The function is carried out using the **sumix** command in Seismic Unix.

### Trace-tapering

The cross-correlated files are trace-tapered following the trace-mixing and prior to concatenation (Figure 6.27). The method tapers down the amplitudes on distant traces in each input ensemble, ensuring that sequential data is gradually reduced instead of being apruptly set to zero, thereby minimizing processing artifacts which occur at the edges of ensembles. The taper length should be simultaneously large enough to minimize artifacts but small enough to not obscure the signal, hence a linear taper of 3 traces is applied to the cross-correlated files. The function is carried out using the **sutaper** command in Seismic Unix.

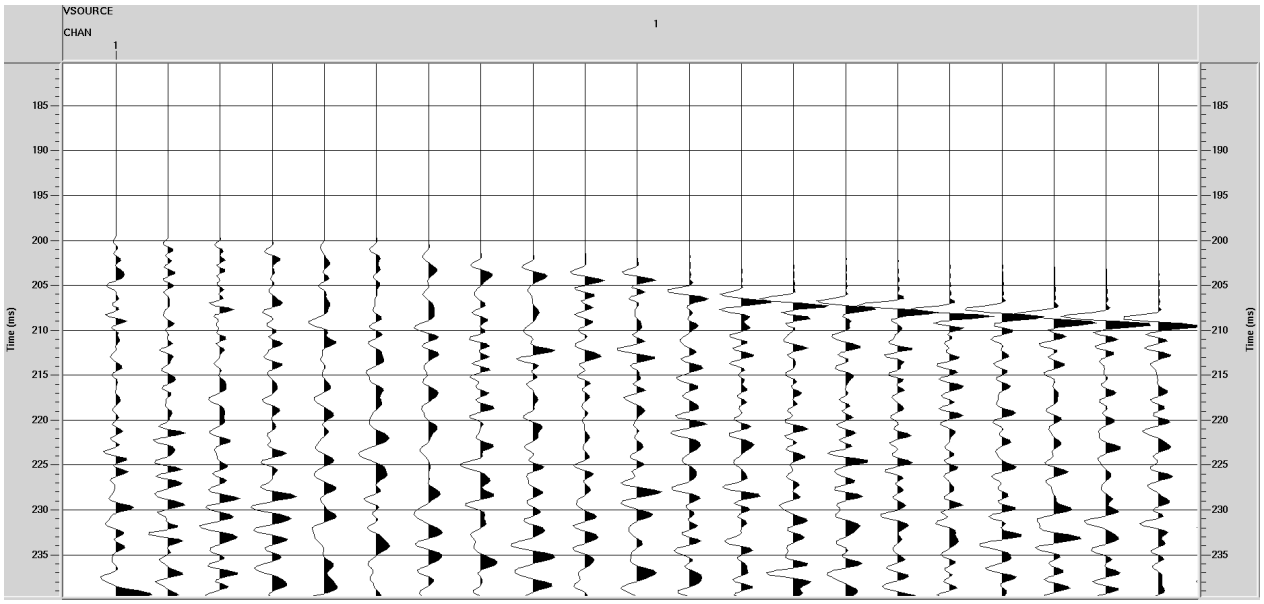


*Fig. 6.24:* Channel without trace-mixing or trace-tapering
Plot demonstrates Channel 1 in Virtual Source 1 prior to summation. No trace-mixing or trace-tapering has been impleneted. Reverse Polarity, 0.5 gain.

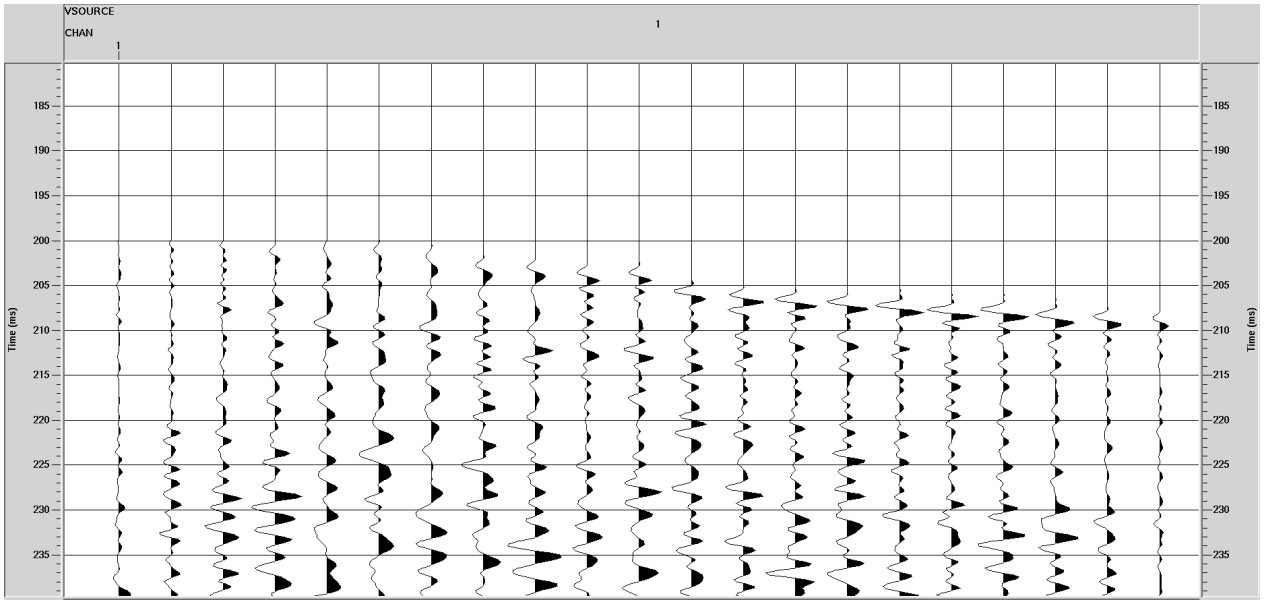


*Fig. 6.25:* Channel after trace-tapering to 3 traces
Plot demonstrates Channel 1 in Virtual Source 1 prior to summation. Trace-tapering upto 3 traces has been implemented. Reverse Polarity, 0.5 gain.

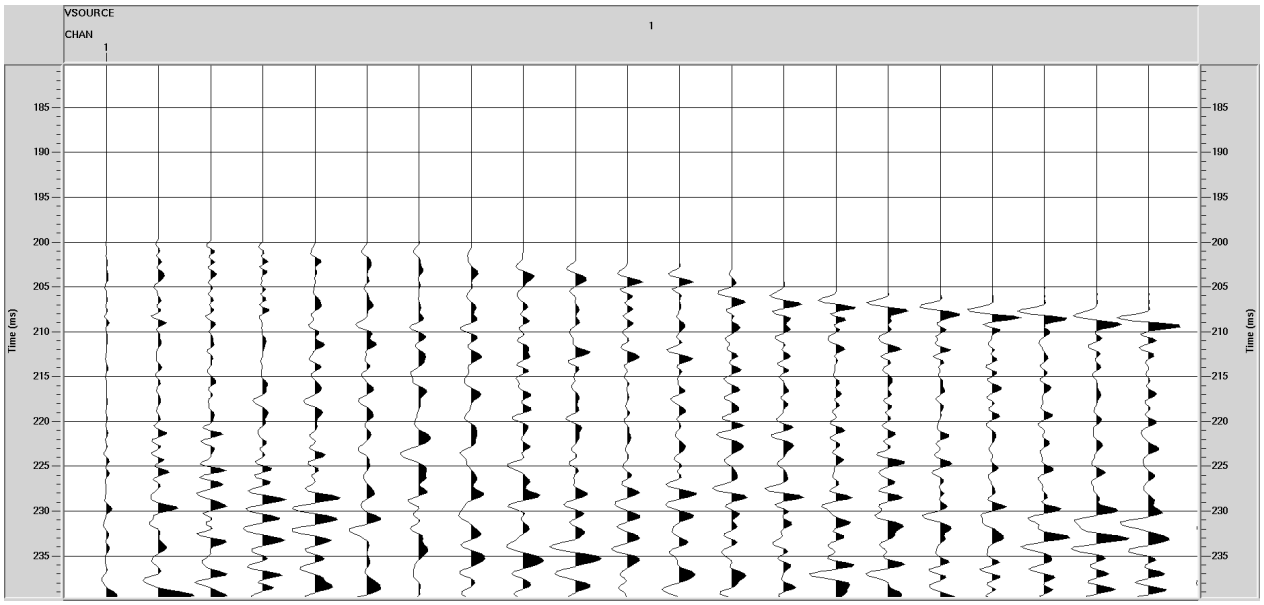


*Fig. 6.26:* Channel after trace-mixing by a standard weighted-mix of 1,3,1
Plot demonstrates Channel 1 in Virtual Source 1 prior to summation. A weighted trace-mix of 1,3,1 has been implemented.. Reverse Polarity, 0.5 gain.

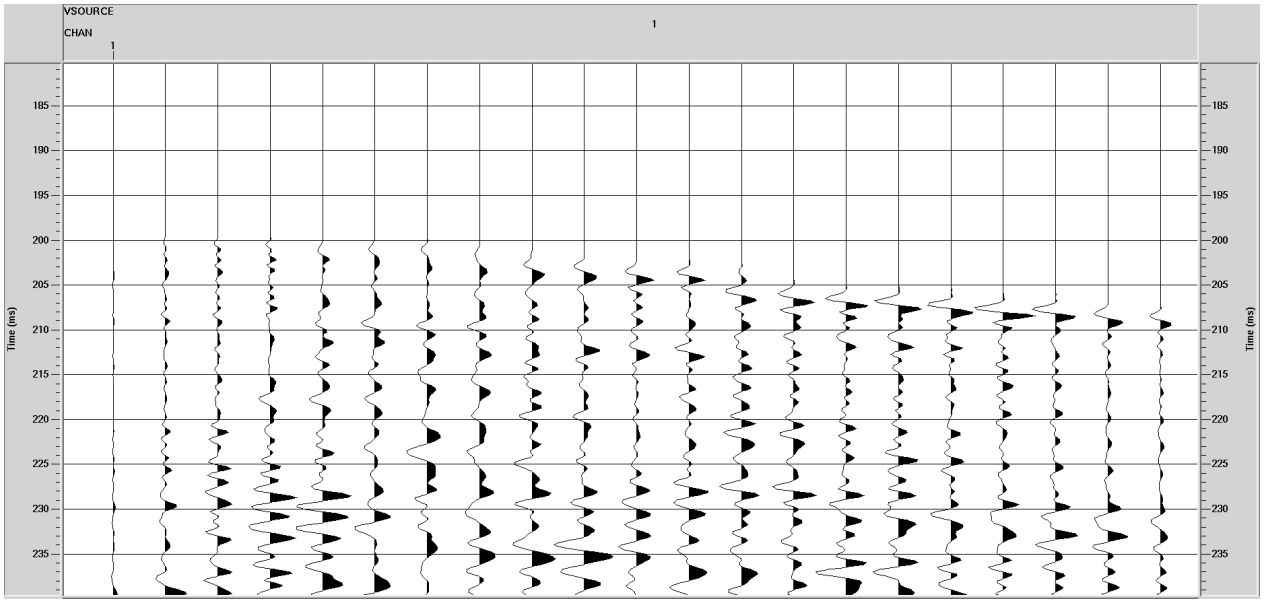


*Fig. 6.27:* Channel after weighted trace-mix of 1,3,1 and trace-tapering to 3 traces
Plot demonstrating Channel 1 in Virtual Source 1 prior to summation. A weighted trace-mix of 1,3,1 and trace-tapering to 3 traces have been implemented. Reverse Polarity, 0.5 gain.

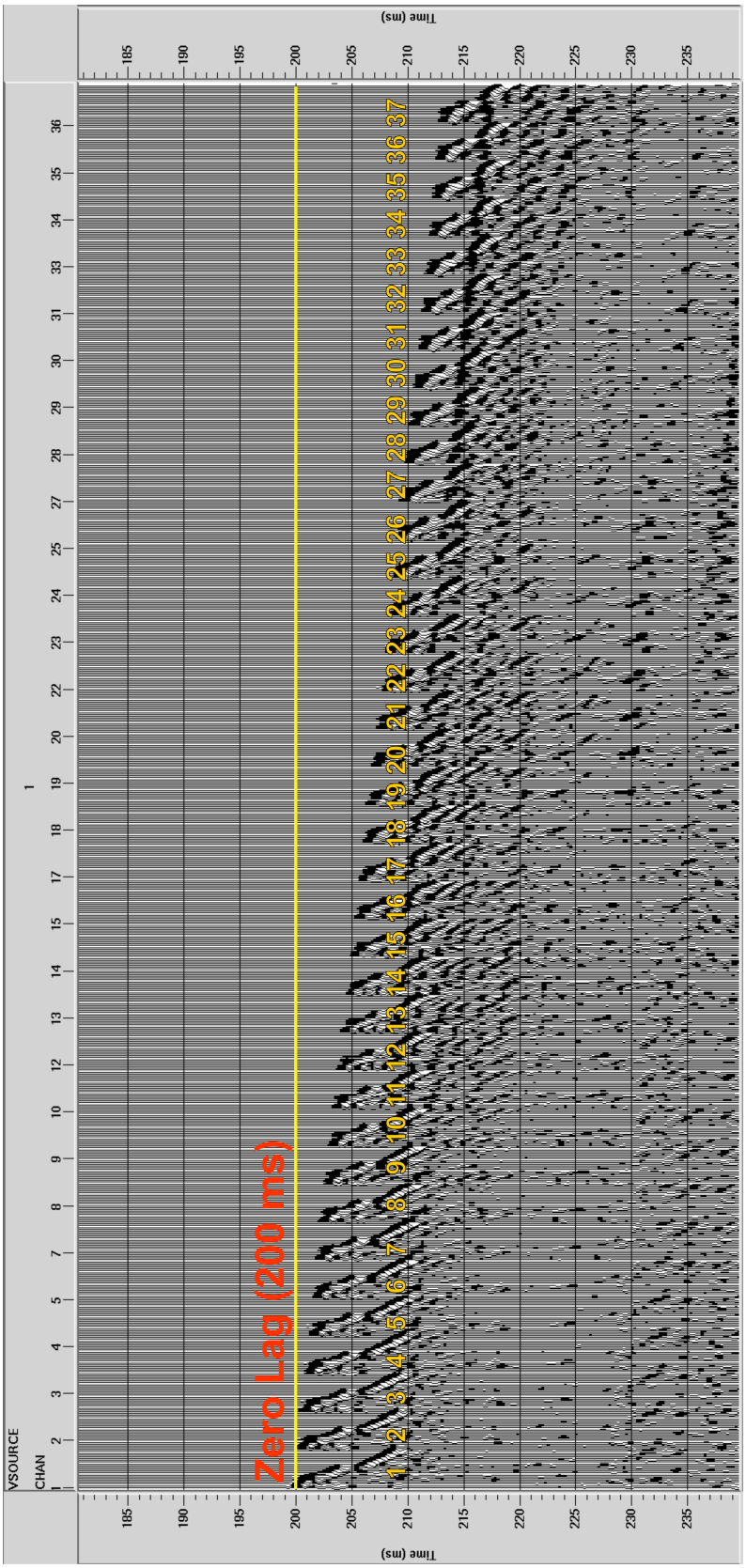


*Fig. 6.28:* Correlation gather for Live Source 1 (before summation)
Correlogram produced for Live Source 1 due to receivers/virtual sources 1 - 37 prior to sorting and summation. Each individual channel (containing 21 traces) from Ch1 - Ch37 in each live source is summed and stacked to create the virtual source gather. Zero lag is at 200 ms.

### 6.2.2 Virtual Source Gather

Following the creation of the **Correlation Gather**, the **Virtual Source Gather** and subsequent CDP gathers are created. The Virtual Source Gather (VSG) creation flow is described in Figure 6.29, and the reasoning for these processes will be explained in following sections.

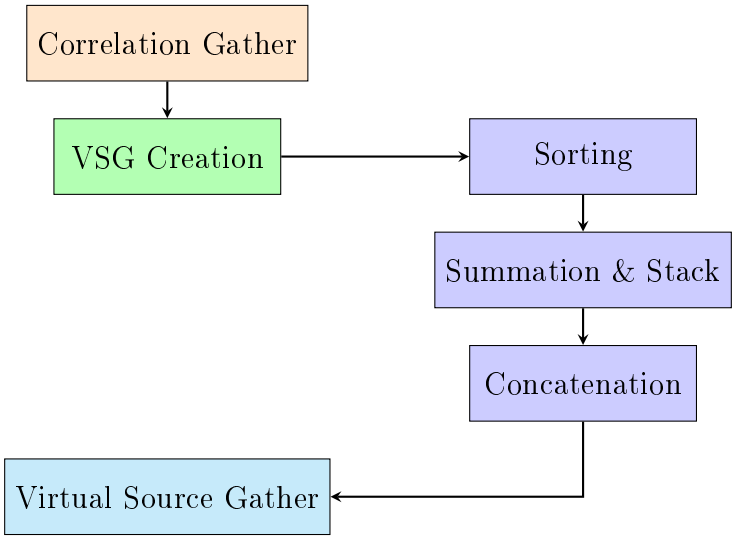


*Fig. 6.29:* VSG creation flow

The virtual source gather is equivalent to a conventional surface seismic shot gather, where the virtual direct wave is equivalent to the surface seismic direct wave, i.e. it is the shot gather that would occur if the source was placed in the borehole. It was created by sorting the correlation gather according to ascending virtual source location, followed by vertical stacking by virtual source location. The vertical stacking of the correlation gather involves the summation of correlograms associated with the same virtual source (Figure 6.30).

To create a virtual source at R1 in the borehole due to contributions from Surface Source 1, the direct arrival at R1 (due to Surface Source 1) is cross-correlated with all of the other 37 traces in the VSP i.e. cross-correlating R1 with every other receiver (1 to 37). This produces a *correlation gather*. The same process is repeated all 21 surface shots, at the same virtual

source receiver (R1). This results in 21 correlation gathers associated with 21 surface source locations (Section 6.2). The 21 correlation gathers are summed to produce a virtual source gather. The rest of the virtual source gathers (at all other virtual source locations 1 – 37) are created in the same way, resulting in 37 virtual source gathers, one for each receiver location. The rightmost column represents virtual Source gather for receiver 1, virtual source gather for receiver 2, etc. ... 37 virtual source gathers in all (Table 6.2).

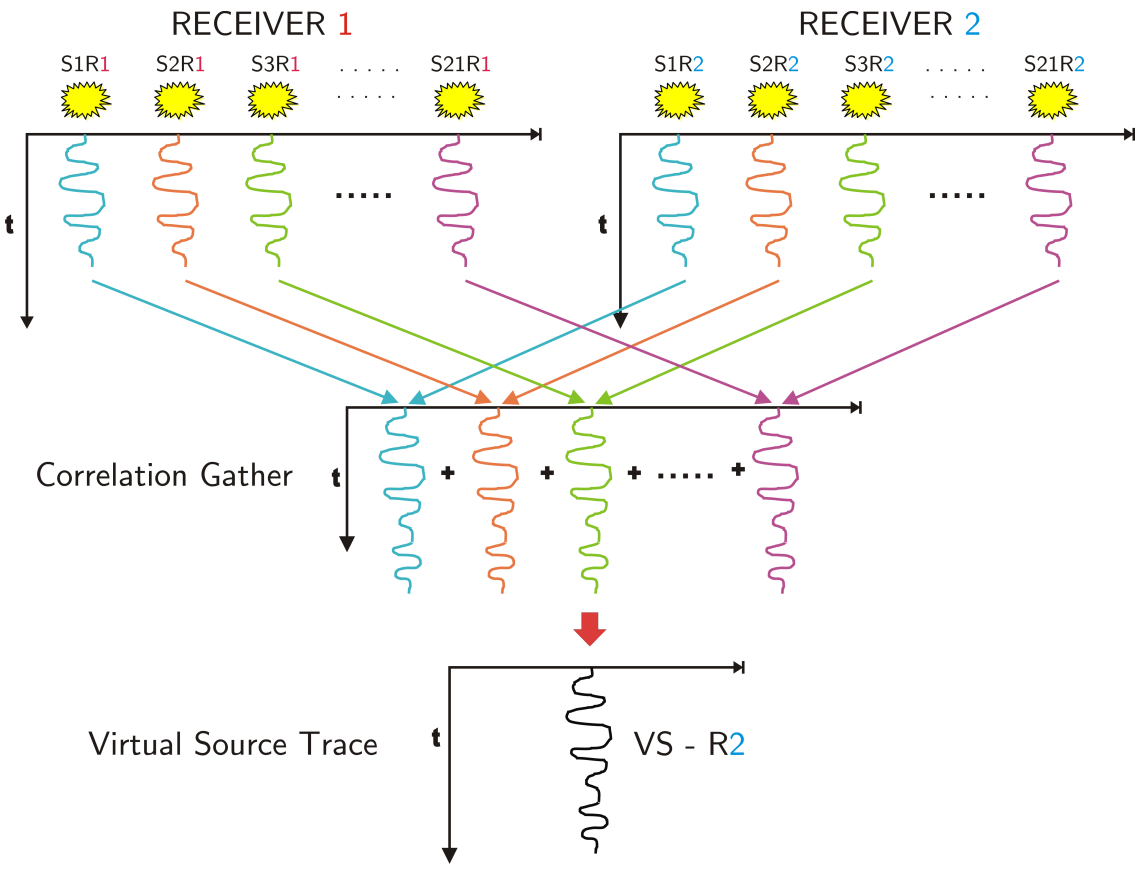


*Fig. 6.30:* Diagram demonstrating Generation of Virtual Source at Receiver 1 recorded at Receiver 2

All receiver contributions for the same surface source are cross-correlated. Trace recorded at Receiver 2 [R2] due to Source 1 [S1] is cross-correlated with the trace recorded at R1 due to S1 (represented by the blue lines). Similarly, trace recorded at R2 due to Source 2 [S2] is cross-correlated with the trace recorded at R1 due to S2 (represented by orange lines). Similar cross-correlated receiver pairs for all other sources from S3 - S21 (represented by green to purple lines) are created to produce a correlation gather. Virtual source trace (VS-R2) represents signal recorded at R2, as if there is a virtual source at R1.

The virtual direct wave is represented in the seismogram as the linear event that crosses

the zero-lag (at 200 ms) at the position of the virtual source. The VSGs were examined to insure reflection detectibility for virtual shots located at the top, middle and bottom of the borehole (Figure 6.32).

An **Automatic Gain Correction** (AGC) of *40 ms* is applied to the dataset prior to the stacking process to equalise the amplitude and boost weaker signals. AGC is an amplitude compensation method which equalises the amplitude. It is based on the following formula (Equation 6.3) where $A$ is the rms square amplitude, $N$ is the number of sampling points in a window of fixed length, and $a$ is the amplitude. The traces are divided in a number of windows. The window slides along the trace and calculates the average amplitude factor, $A$ within the window, and assigns the value to the middle of the window. The window slides down one sample and computes the gain correction until the entire trace has been gained. The scaling function at the gate center, $g(t)$ is given by Equation 6.4.

$$A = \sqrt{\sum_{i-1}^{N} a_i^2} \tag{6.3}$$

$$g(t) = \frac{\text{desired rms}}{\sqrt{\frac{1}{N}\sum_{i-1}^{N} a_i^2}} \tag{6.4}$$

In the processing flow, the AGC is applied prior to the trace-mixing and trace-tapering. If the AGC was applied after, the equalisation of amplitudes would have the negative effect of diminishing the trace-mix and trace-taper operations thereby rendering them ineffective. The AGC applied to the dataset prior to summation of the virtual sources has the effect of dramatically raising weaker signals by balancing amplitudes between traces which brings up the reflection amplitudes, thereby allowing the stacking process to be more effective (Figures 6.31 and 6.32).

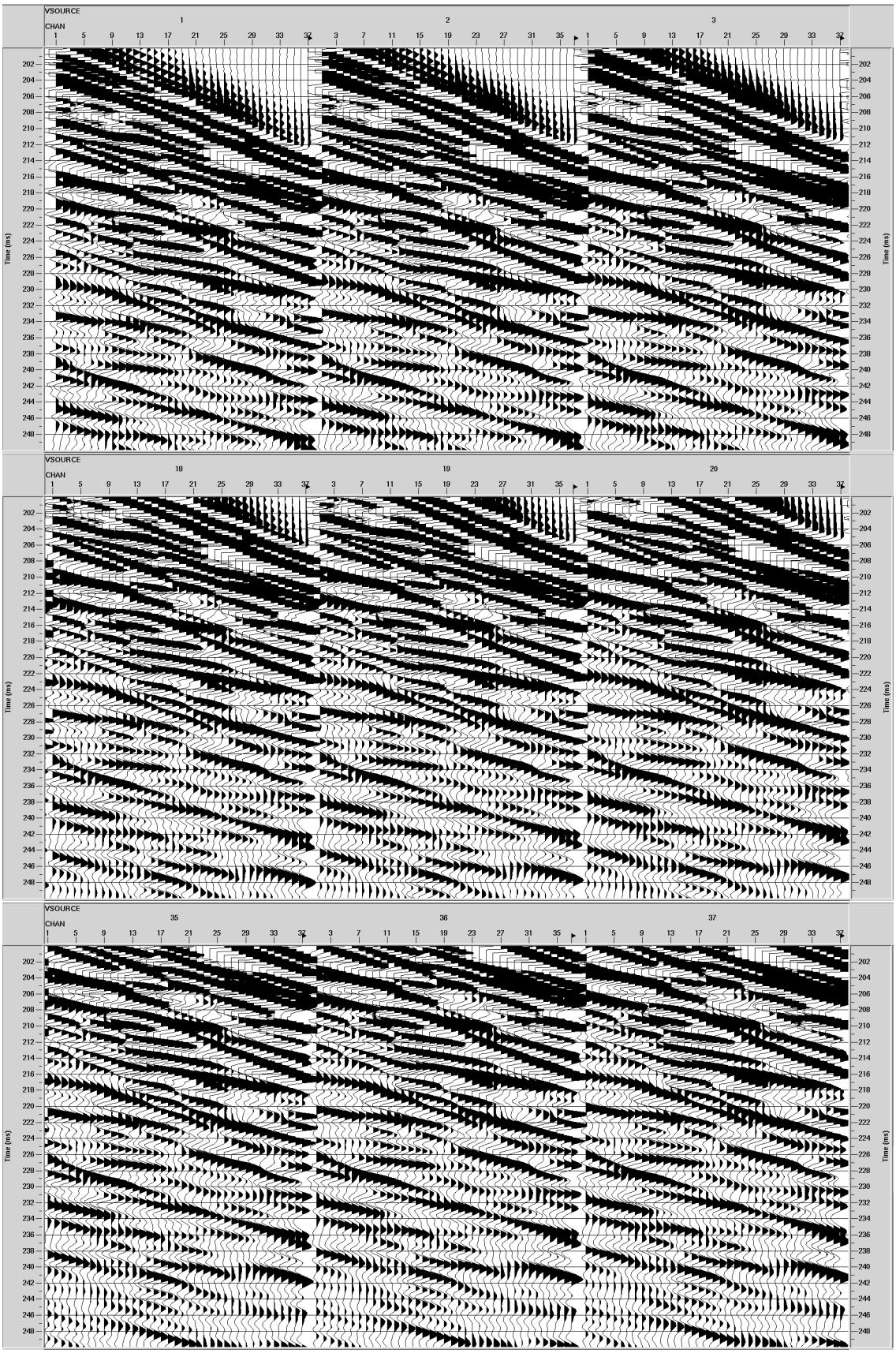


*Fig. 6.31:* Virtual Source Gathers from the Collier Point dataset without AGC (from top to bottom): VSG for virtual sources 1-3 at the top of the borehole, 18-20 towards the middle of the borehole, and 35-37 at the bottom of the borehole. No AGC applied. Zero lag is at 200 ms.

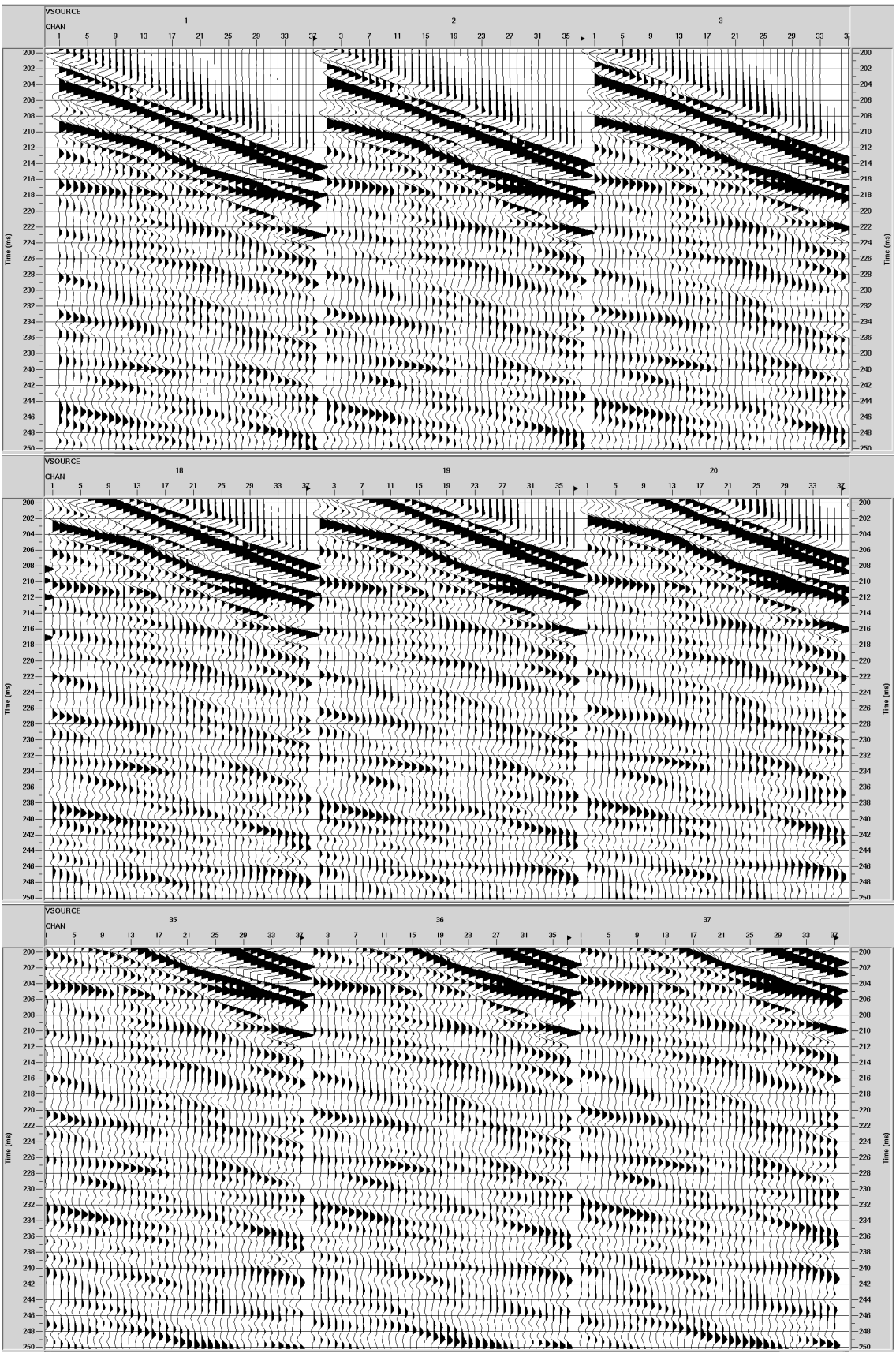


*Fig. 6.32:* Virtual Source Gathers from the Collier Point dataset with AGC (from top to bottom): VSG for virtual sources 1-3 at the top of the borehole, 18-20 towards the middle of the borehole, and 35-37 at the bottom of the borehole. AGC of 40 ms is applied. Zero lag is at 200 ms.

*Tab. 6.2:* Correlation scheme for creating virtual sources in Collier Point Dataset[1]

| Virtual Source | Surface source #1 | + | Surface source #2 | + | Surface source #3 | ... | Surface Source #21 | = | Virtual source gather |
|---|---|---|---|---|---|---|---|---|---|
| 1 | R1×R1 | | R1×R1 | | R1×R1 | | R1×R1 | = | VS1:R1 |
| | R1×R2 | | R1×R2 | | R1×R2 | | R1×R2 | | R2 |
| | R1×R3 | + | R1×R3 | + | R1×R3 | ... | R1×R3 | | R3 |
| | ... | | ... | | ... | | ... | | ... |
| | R1×R37 | | R1×R37 | | R1×R37 | | R1×R37 | | R37 |
| 2 | R2×R1 | | R2×R1 | | R2×R1 | | R2×R1 | = | VS2:R1 |
| | R2×R2 | | R2×R2 | | R2×R2 | | R2×R2 | | R2 |
| | R2×R3 | + | R2×R3 | + | R2×R3 | ... | R2×R3 | | R3 |
| | ... | | ... | | ... | | ... | | ... |
| | R2×R37 | | R2×R37 | | R2×R37 | | R2×R37 | | R37 |
| ... | ... | | ... | | ... | ... | ... | | ... |
| 37 | R37×R1 | | R37×R1 | | R37×R1 | | R37×R1 | = | VS37:R1 |
| | R37×R2 | + | R37×R2 | + | R37×R2 | ... | R37×R2 | | R2 |
| | R37×R3 | | R37×R3 | | R37×R3 | | R37×R3 | | R3 |
| | ... | | ... | | ... | | ... | | ... |
| | R37×R37 | | R37×R37 | | R37×R37 | | R37×R37 | | R37 |

[1]R## represent borehole receiver numbers and correspond to channels 1 through 37 in the VSP data. V## represent virtual source numbers and correspond to the 37 borehole receivers transformed to virtual sources.

## 6.3 Assignment of Polarities

The hydrophone convention is such that compression is plotted as a negative polarity. Therefore, the reflections appear as negative polarity in the pre-processed shot gathers. As cross-correlation is essentially a shift-multiply-add procedure, cross-correlation of two traces with negatives produces a positive polarity correlation. This nulls the effect of the hydrophone convention and results in the dataset following 'general' convention where a positive polarity represents a compression/positive reflection coefficient, in the succeeding CDP Stack and Kirchhoff migrations. It should be noted that a strong negative reflection coefficient exists between the interfaces (Table 3.11), due to which the reflection events originally plot as negatively polarised events. For the sake of easier viewing and interpretation, the CDP and Kirchoff depth migration profiles are purposefully plotted in *reverse polarity* (and therefore are shown as positive polarity) to draw the eye of the viewer to the relevant reflection events.

## 6.4 CDP Stack

A Common Depth Point (CDP) stack is created to vertically stack input ensembles of the traces. The virtual shot gathers are sorted from the time receiver domain to the common midpoint-offset domain to create a CDP (common midpoint gather). The ProMAX program is used to identify the virtual shot and receiver pairs that share a Common Depth Point (CDP), and organize the virtual shot gather as a function of the source and receiver coordinate geometry through a geometry job flow (Appendix D). The geometry is comprised of 73 common depth points over 82 m with a 1 m trace spacing (Appendix F). The point of highest fold is located at the middle of the CDP profile (CDP 37, Appendix F), and the number of source-receiver pairs decreases at the top and bottom depth regions of the borehole.

**Top of Borehole** **Bottom of Borehole**

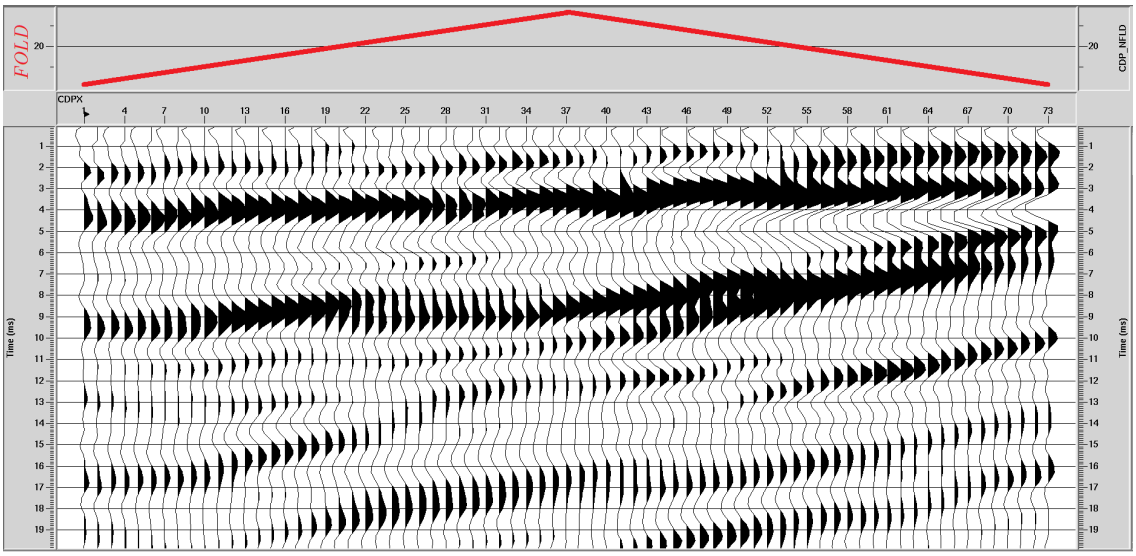


*Fig. 6.33:* CDP Fold
Plot demonstrating fold in stacked CDP section in reverse polarity. Highest fold (37 traces) is located at the central CDP 38, and decreases towards the beginning and end of the CDP profile. Plotted in reverse polarity.

Following the organization of data according to the CDP and receiver pairings using the geometry spreadsheet, it is normal moveout (NMO) corrected to a velocity of 5000 m/sec. The NMO correction causes the data to become stretched as a function of offset and depth, and the summing of these period-stretched events may cause the stacked data to be smudged. Hence, a stretch mute of 30% is applied in the NMO process, which limits the maximum stretch to 30%. A static shift is applied to the direct wave arrival times to eliminate the first 200 ms (leads) containing acausal data and places the zero lag at time zero. The CDP traces are then summed and stacked. This produces a CDP gather of linear reflections which have been summed together constructively to produce the CDP stack.

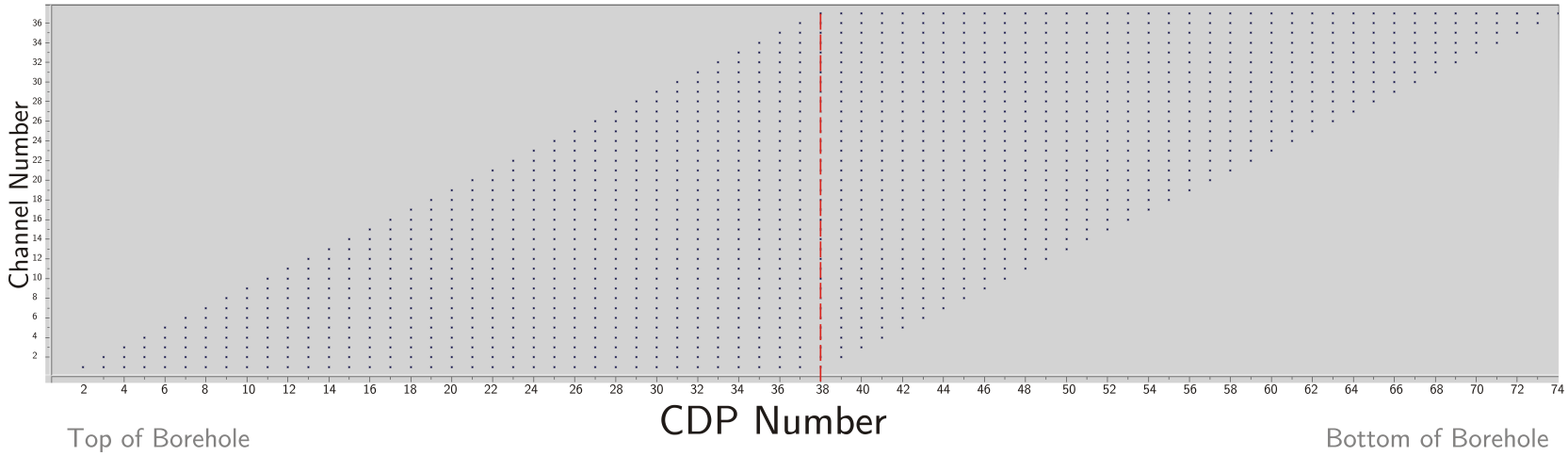


*Fig. 6.34:* CDP Geometry Spread
The spread of CDP number vs. Channel Number demonstrates the number of channels contributing a trace to the imaging of every CDP. The red dashed line represents the point of highest fold (CDP 38). The number of source-receiver pairs decreases towards the top and bottom of the borehole.

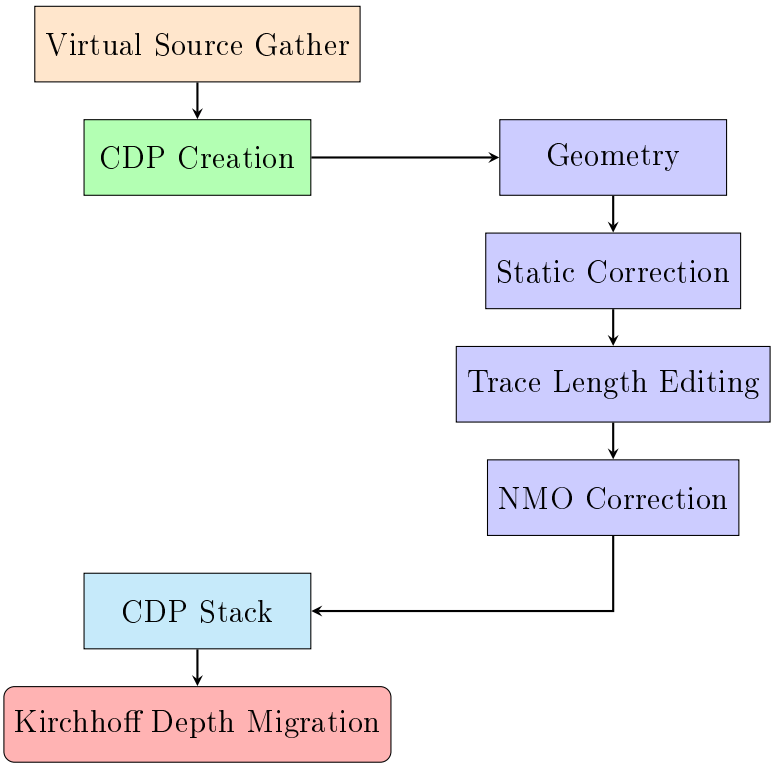


*Fig. 6.35:* CDP and Depth Migration creation flow

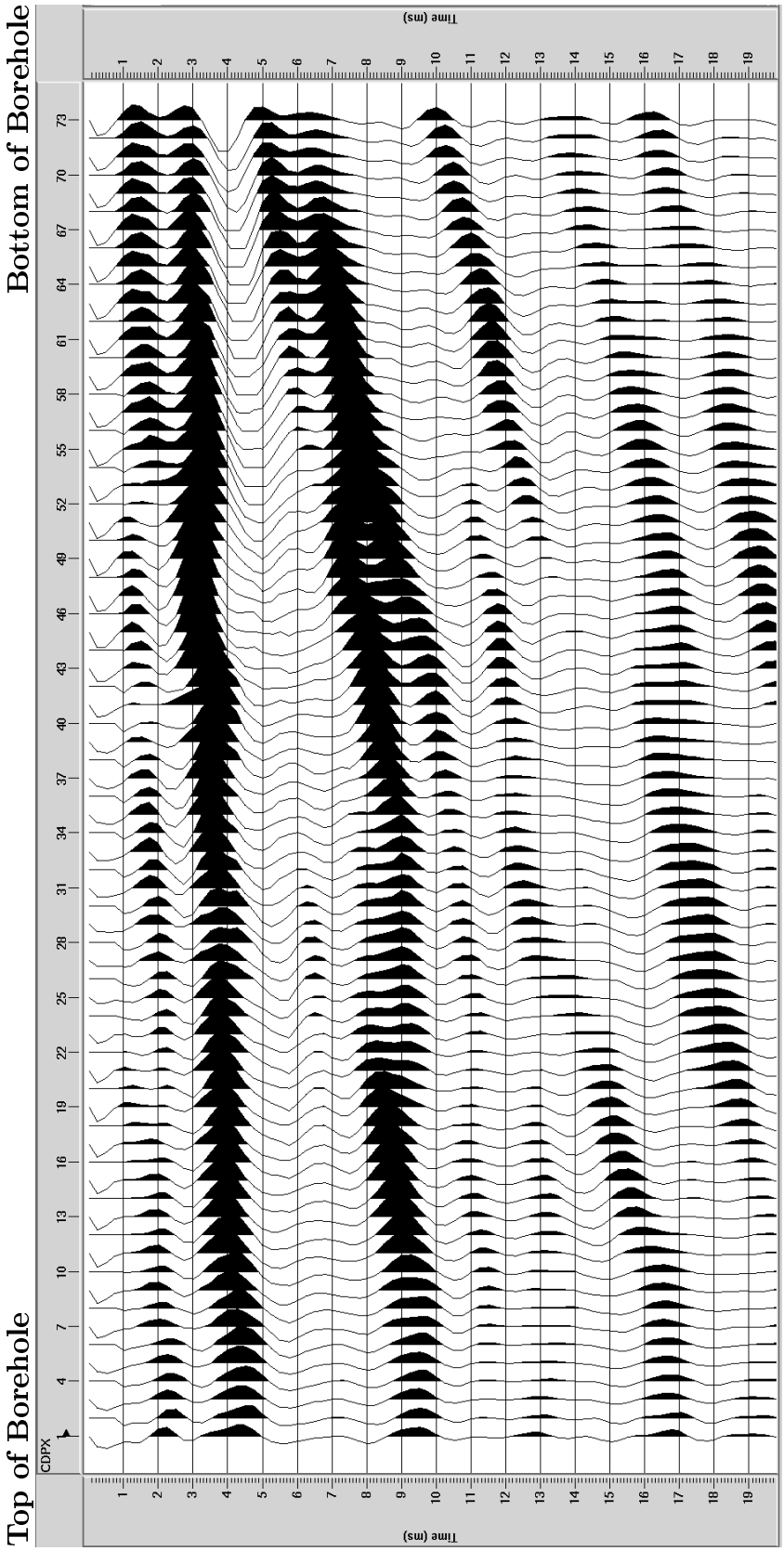


*Fig. 6.36:* CDP Stack for Collier Point Dataset
CDP stack is comprised of 73 CDP points with 1 m spacing in reverse polarity. Dataset is not trace mixed or tapered prior to summation of correlation gathers.

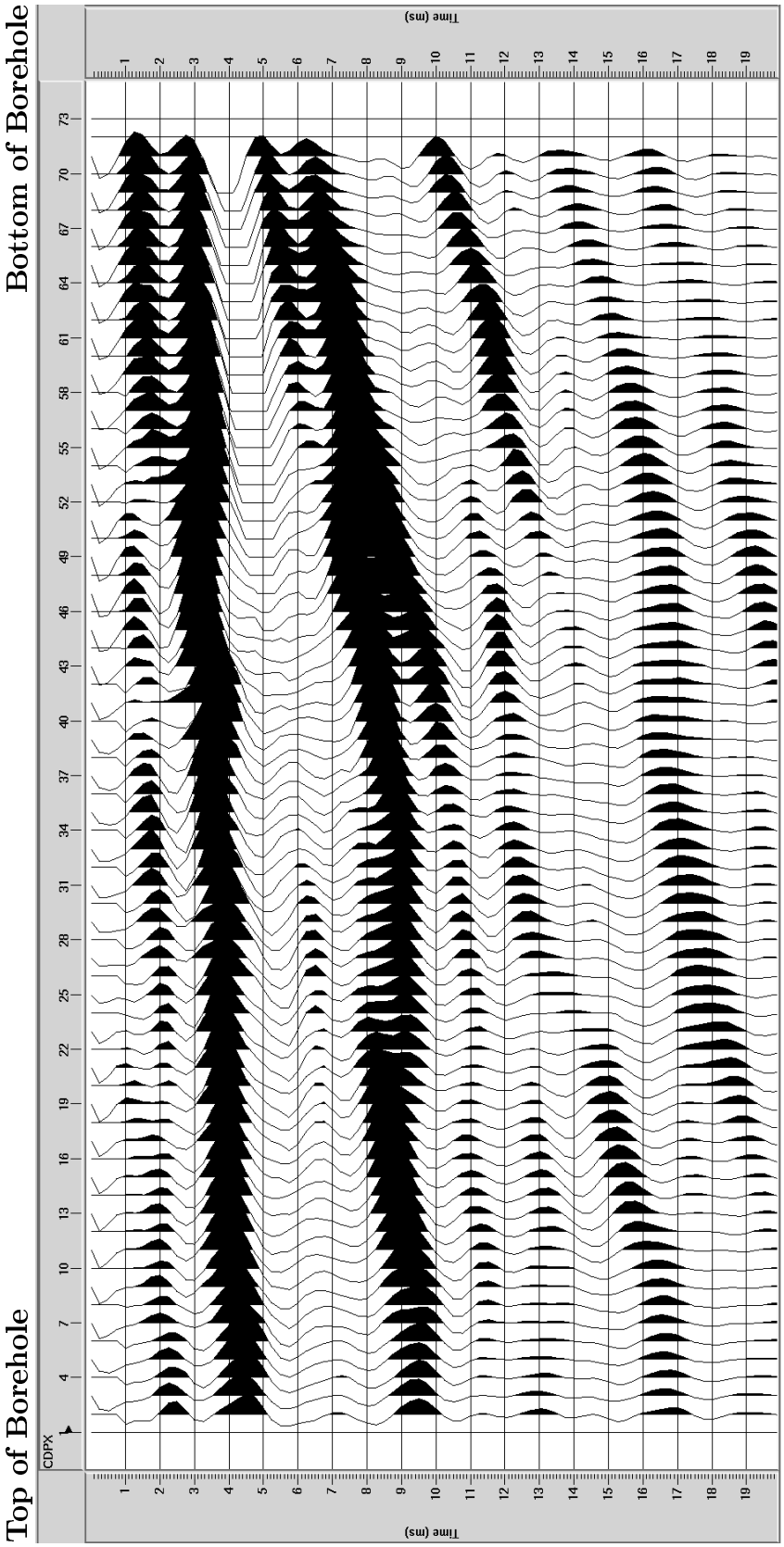


*Fig. 6.37:* CDP Stack for Collier Point Dataset
CDP stack is comprised of 70 CDP points with 1 m spacing in reverse polarity. Dataset is trace-tapered by 10 traces prior to summation of correlation gathers.

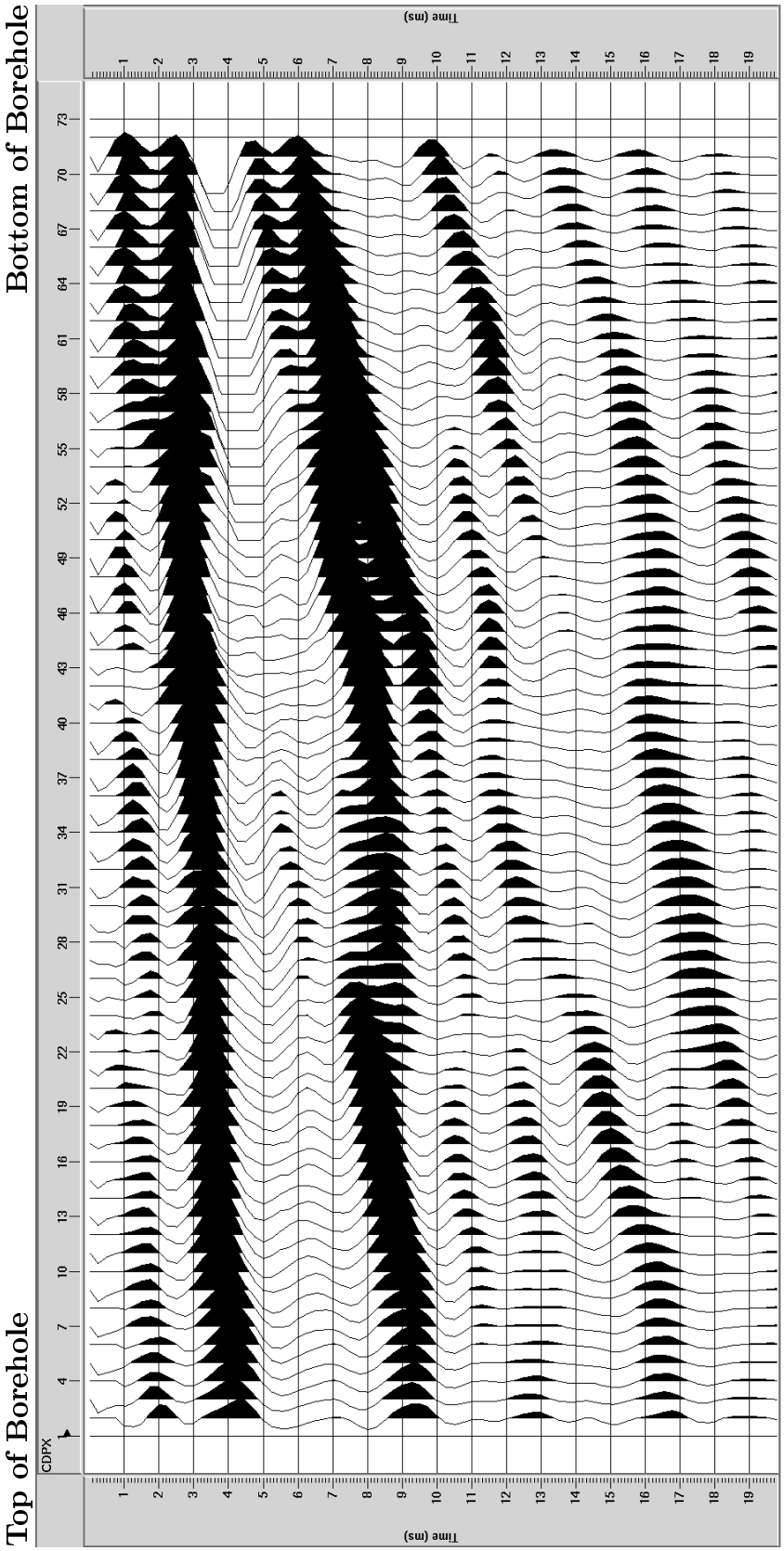


*Fig. 6.38:* CDP Stack for Collier Point Dataset
CDP stack is comprised of 70 CDP points with 1 m spacing in reverse polarity. Dataset is trace-mixed (1, 3, 1) and trace tapered to 10 traces prior to summation of correlation gathers.

## 6.5 Depth Migration

The stacked seismic section is Kirchhoff time migrated to correct the seismogram in the time-space domain to focus the stacked image. As with the NMO correction, the Kirchhoff migration was uncomplicated due to the model comprising of homogeneous velocity fields, and was implemented by inputting a velocity function in the ProMax program (Appendix D).

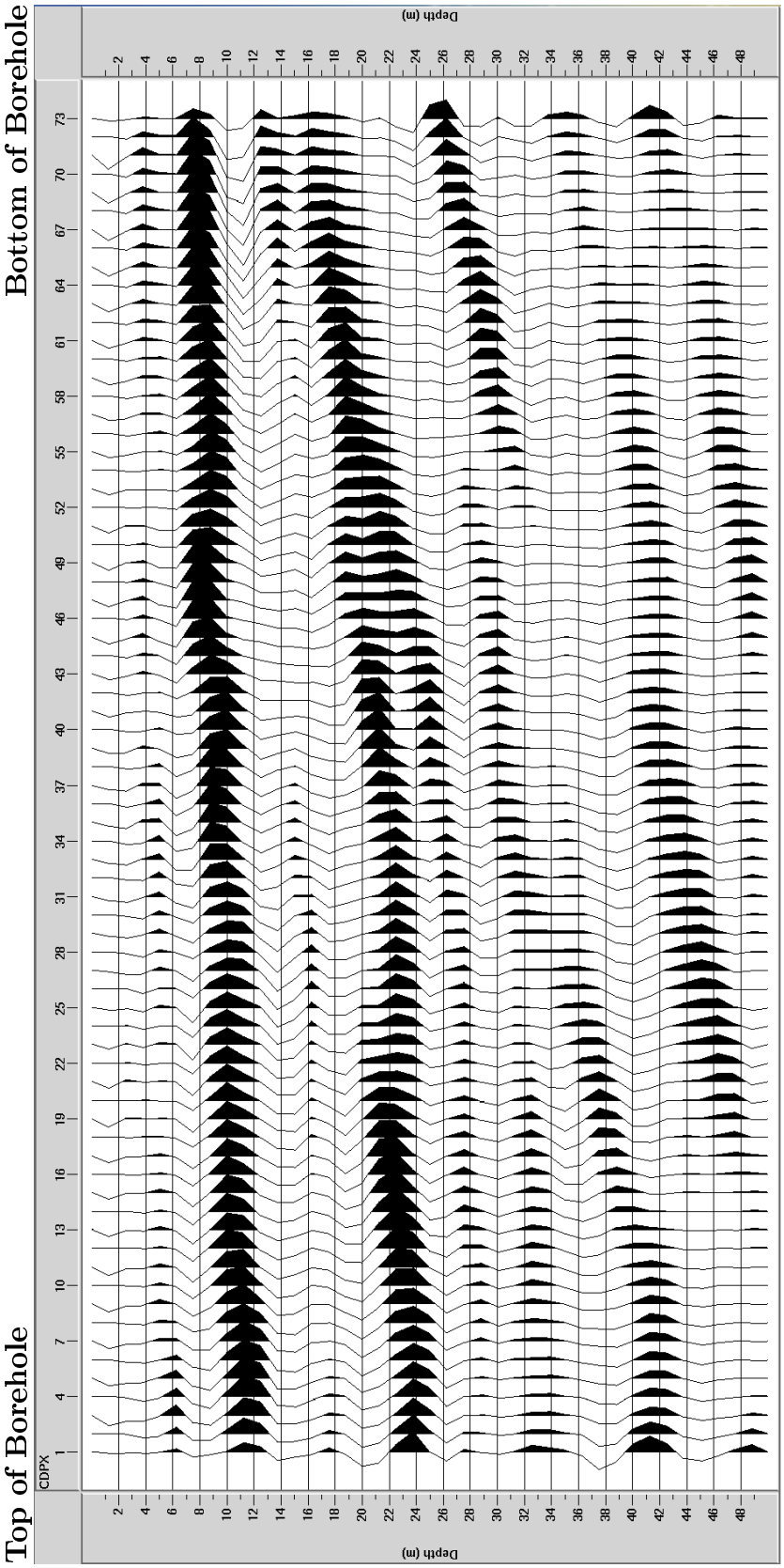


*Fig. 6.39:* Kirchhoff Depth Migrated Stack for Collier Point Dataset
Migrated stack is comprised of 73 CDP points with 1 m spacing in reverse polarity. Dataset is not trace mixed or tapered prior to summation of correlation gathers.

## 6.6 Summary of Processing

**Trace-mixing** or **trace-tapering** of the Collier Point dataset does not appear to result to significant changes or improvement to the dataset. Trace-tapering to 3 traces only results in a very slight change in amplitude in beginning and end CDP's with the lowest fold. Trace-mixing causes very minor enhancement of signal. Higher windows for trace-mixing and trace-tapering are inadvisable due to to low number of available channels (37 channels), resulting in limitations with applicable parameters. Therefore, these methods do not result in significant improvement in data quality for this dataset (Figure 6.40). The processed **CDP Stack** demonstrates two very strong reflection events, which are also visible in the **Kirchhoff Depth Migration**. These reflection events will be identified and discussed in Chapter 7.

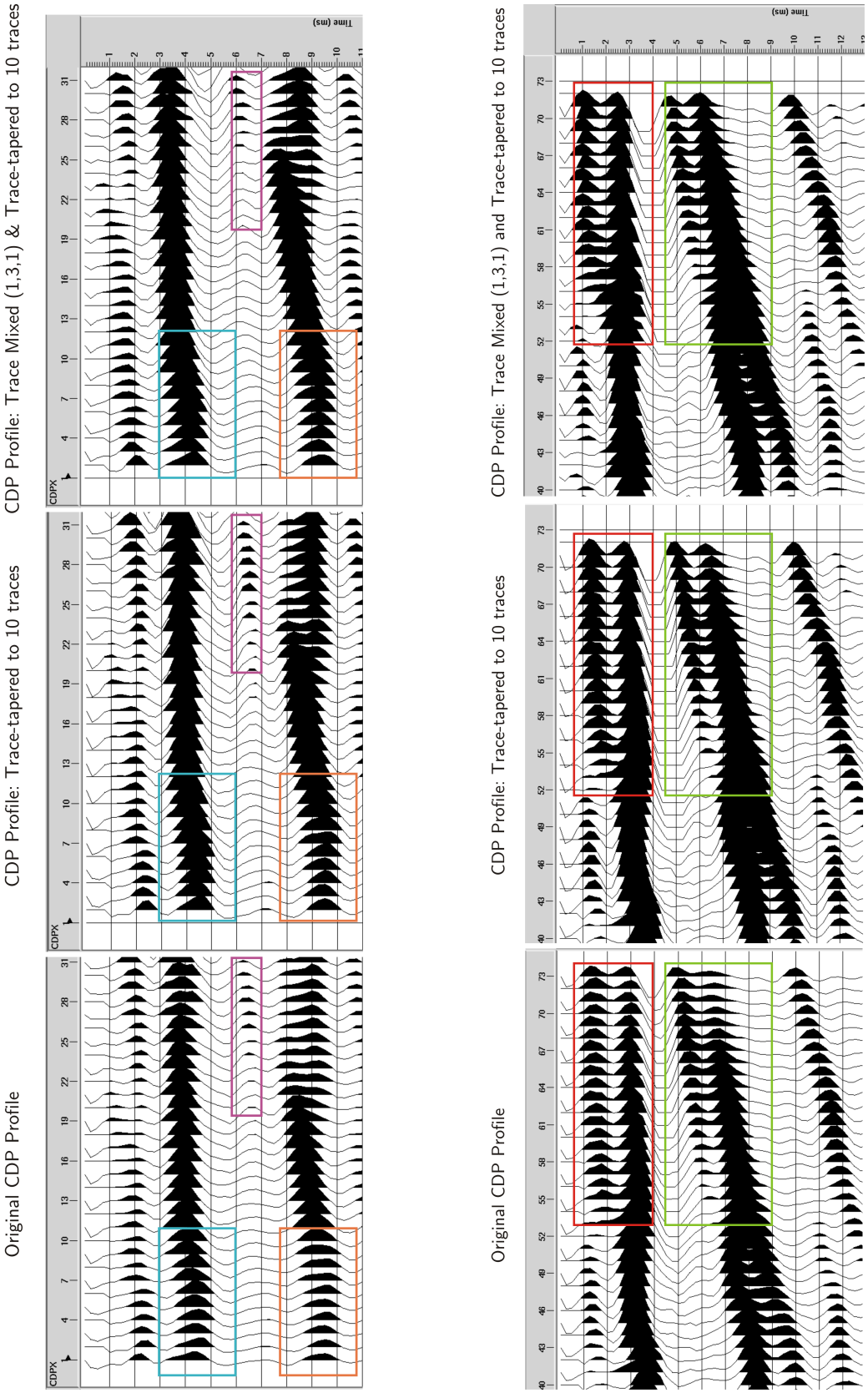


*Fig. 6.40:* Differences in trace-mixing and trace-tapering

# Chapter 7

## Discussion

Following the creation of the CDP stack and migrated seismic section, the dataset is analysed to identify the barite vein target and characterize the vein to build a proposed geological model.

## 7.1 Identification of Vein in Dataset

Assuming that the seismic velocity of the arkose is approximately 5000 m/sec, and the distance between the receivers and barite vein target is 25 m, there should be an $\approx 10$ ms time delay between the direct wave and the reflection (Equation 7.1). The dataset was analysed to pick out possible reflection events. There are two possible reflection events identified in the pre-processed seimogram (before interferometry) (Figure 7.1) -

1. *Reflection Event 1* at $\approx 7$ ms from the direct wave, and

2. *Reflection Event 2* at $\approx 10$ ms from the direct wave

In the virtual source gathers (VSG's) produced after sorting, summation and stacking, stationary-phase events stack in constructively. Hence, by checking the VSG's two reflection events were picked out for examination purposes, which were also identified on pre-processed

seismograms as *Reflection Events 1 and 2* (Figure 7.2). Based on the above reasoning, *Reflection Event 2* is identified as the barite vein, i.e. the event at 18 ms, with an ≈ 10 ms delay from the direct wave in the pre-processed seismogram, and also with an ≈ 10 ms delay in the VSG (Figure 7.3).

$$Time(t) = \frac{\text{Two-way Distance (x)}}{\text{Velocity (v)}} = \frac{25 \text{ m} * 2}{5000 \text{ m/sec}} = 0.010 \text{ sec} = 10 \text{ ms} \tag{7.1}$$

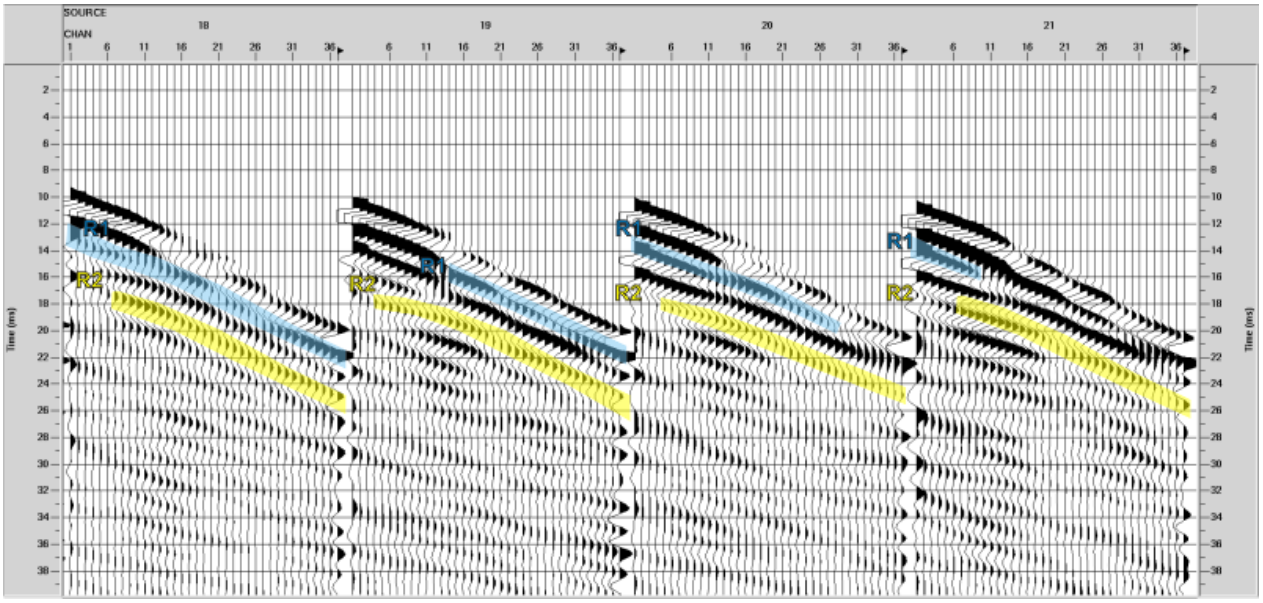


*Fig. 7.1:* Reflection events identified in pre-processed VSP
Possible reflection events in pre-processed seismogram (Reverse polarity). Reflection Event 1 is marked in blue and Reflection Event 2 is marked in yellow.

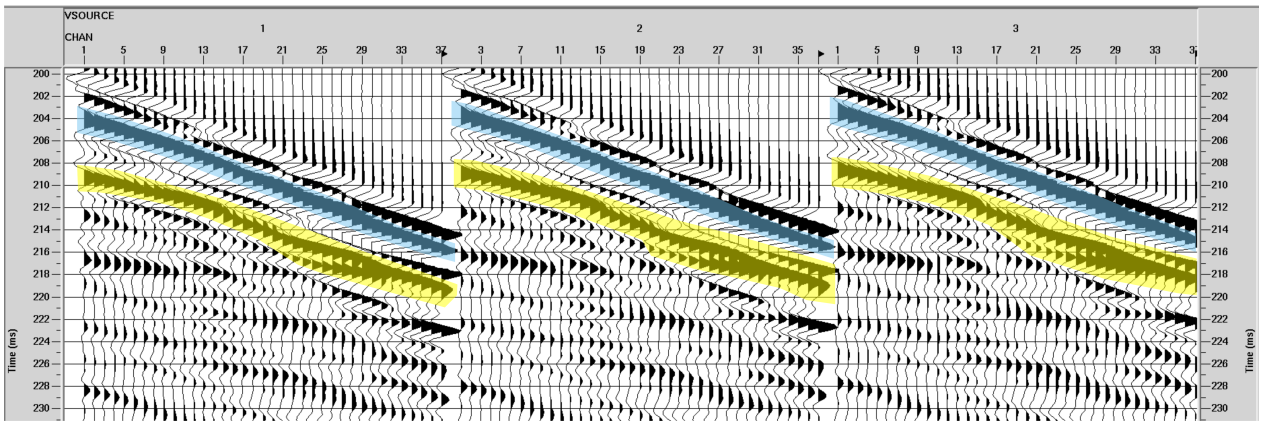


*Fig. 7.2:* Reflection Events identified in Virtual Source Gathers

Possible reflection events in Virtual Source Gathers (Reverse polarity). Reflection Event 1 is marked in blue and Reflection Event 2 is marked in yellow.

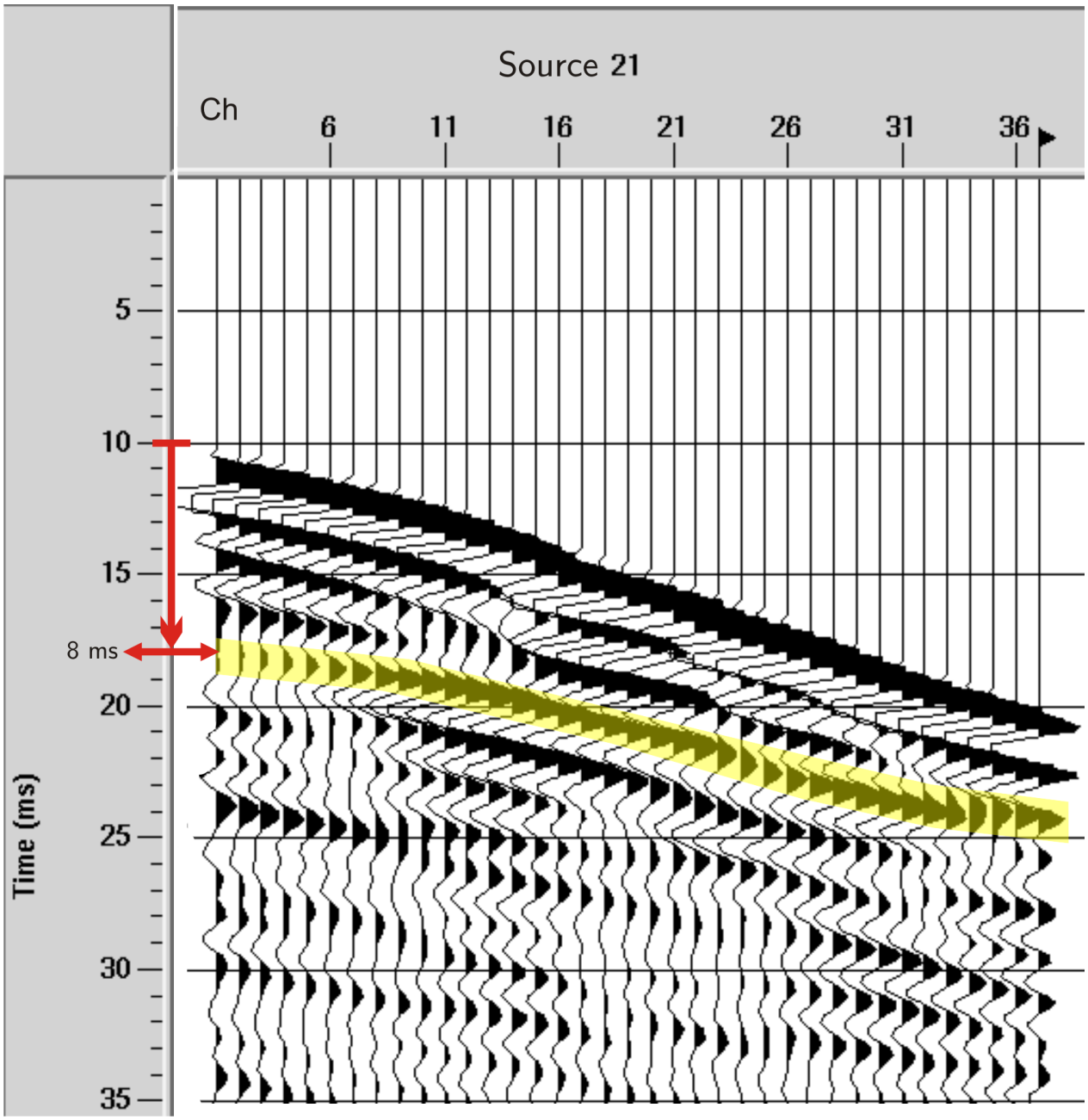


*Fig. 7.3:* Timing of possible barite vein in pre-processed seismogram (before interferometry) Possible barite reflection event is marked in yellow and has an $\approx$ 8 ms delay from the direct wave.

## 7.2 Examination of Reflection Events

The reflection events 1 and 2 observed in the Virtual Source Gathers (VSG's) were also noted in the Common Depth Point (CDP) Stack (Section 6.4). *Reflection Event 2* is identified as the barite vein (Section 7.1) and the origin of *Reflection Event 1* is unknown.

**Top of Borehole** **Bottom of Borehole**

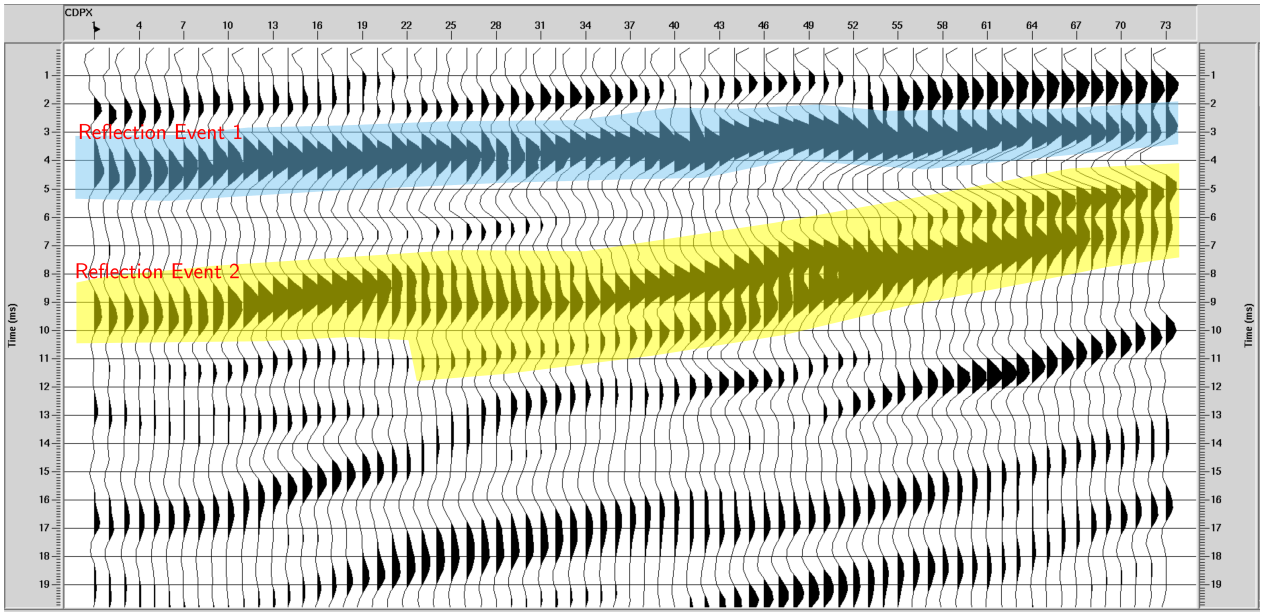


*Fig. 7.4:* Reflection Events viewed in CDP Stack
Possible barite reflection event is marked in yellow and has an ≈ 8 ms delay from the direct wave. Plotted in reverse polarity.

## 7.3 1-D synthetic modelling

The seismic response changes when subjected to different lithological boundaries, layer thicknesses and geometries. For instance, the wavelet in *Reflection Event 2* varies significantly at different CDP depths. 1-D synthetic modelling is conducted using the **synth** and **inver_synth** scripts (Provided by Dr. C. Hurich) to study the response of the wavelet's

amplitude and shape through constructive and destructive interference, thereby inferring a heuristic model for the structure of the barite vein and surrounding rock, and enabling interpretation. The reflection coefficients combined with the interference defines the amplitude response. The **synth** and **inver_synth** scripts work by convolving the *Ricker wavelet* (model seismic wavelet) with the reflection coefficient between two successive rock layers to produce a synthetic seismogram. The **inver_synth** script is modified to test a group of geologic scenarios in one run of the modelling. The synthetic wavelet is chosen to be a *Ricker Wavelet* as it is zero-phase and best matches the seismic data (which is a zero-phase wavelet following the cross-correlation process). The dominant frequency of the Ricker Wavelet is chosen to be 300 Hz (Figure 7.5), as it is the dominant frequency within the Collier Point dataset.

The Collier Point seismic data is partially sub-resolution and the amplitude cannot be calibrated. The synthetics cannot be scaled to the real data in absolute values since seismic data are always relative values once they have been processed. As a result, the script exists purely as a method of matching and comparing the relative amplitudes in the seismic data wavelet with the produced model wavelet.

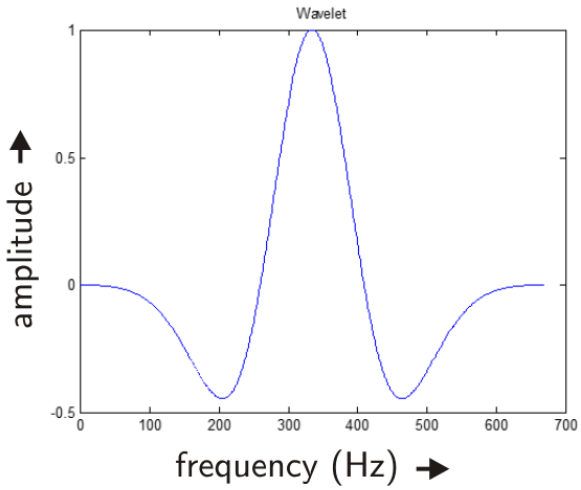


*Fig. 7.5:* Ricker Wavelet using in 1-D modelling
The Ricker Wavelet has a dominant frequency of 300 Hz

### Modelling Parameters

The rock models chosen in the 1-D synthetic modelling program are described in (Table 7.1). The arkose and barite are assigned values corresponding to the laboratory measurements (Table 3.11). The breccia is given values for a low-velocity, low-density 'low breccia' and a higher-velocity, higher-density 'high breccia' (50% mix of arkose and barite each).

*Tab. 7.1:* Properties of rocks used in 1-D synthetic modelling and resulting tuning thickness (or limit of resolution at 300 Hz)

| Modelled Rock | Density ($\rho$) g/cc | Velocity (V) m/sec | Wavelength ($m$) [at 300 Hz] | Tuning Thickness (m) [at 300 Hz] |
|---|---|---|---|---|
| Arkose | 2.69 | 5042 | 16.8 | 4.2 |
| **Barite** | 4.49 | 2477 | 8.2 | **2.1** |
| Low Breccia | 3.5 | 3500 | 11.6 | 2.9 |
| High Breccia | 3.59 | 3760 | 12.5 | 3.1 |

#### 7.3.1 Single Boundary Response

The single boundary response consists of a geometry with an arkose-to-barite and a barite-to-arkose boundary only. In the case of the arkose-to-barite boundary (Figure 7.6) it is observed that the convolution of the Ricker wavelet (7.5) with the arkose-barite reflection coefficient results in a seismic wavelet that produces a negative peak (due to negative reflection coefficient) as it goes from the high velocity arkose to low-velocity barite. Conversely, convolution of the Ricker wavelet with the barite-arkose (positive) reflection coefficient produces a positive peak (Figure 7.7).

Velocity (Samples)

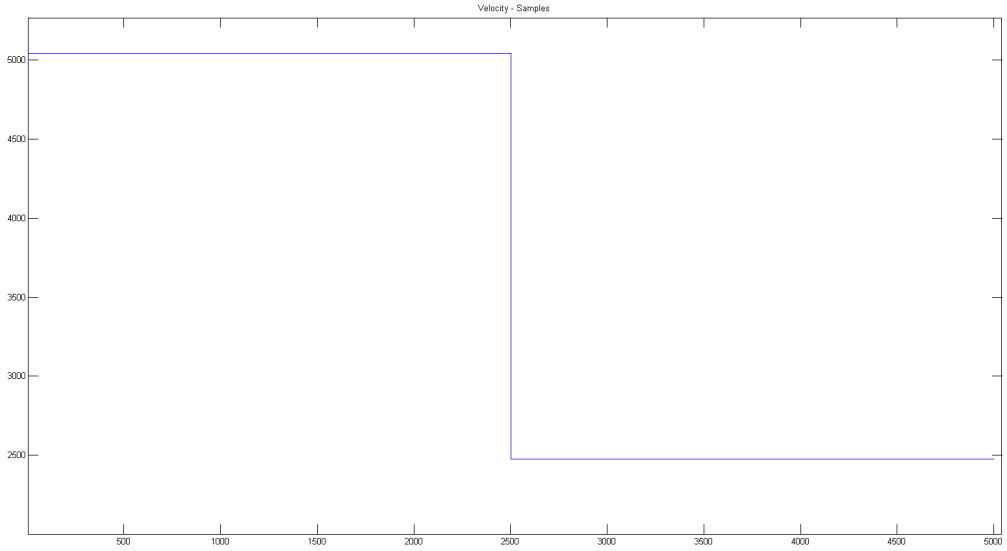


Synthetic Seismogram

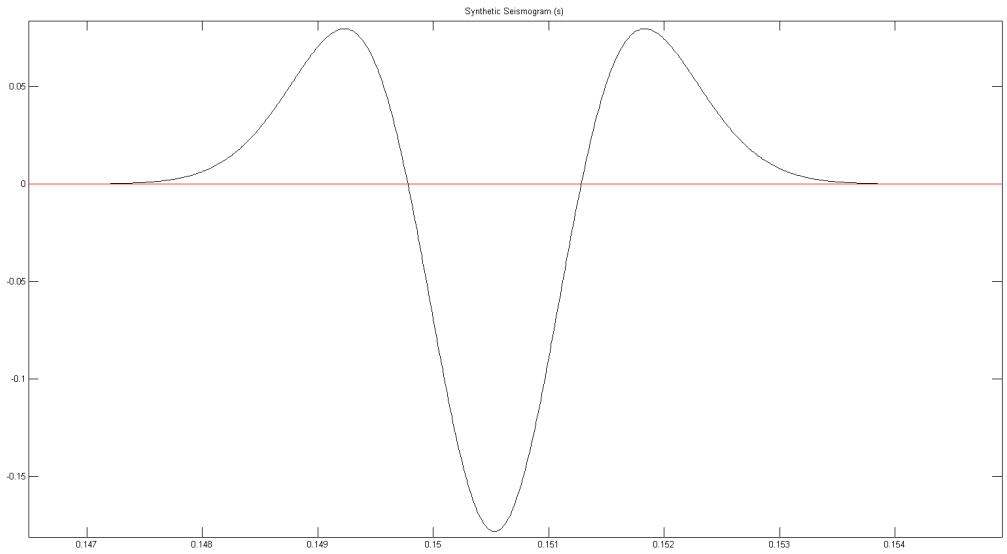


*Fig. 7.6:* Single boundary arkose-barite interface

Velocity (Samples)

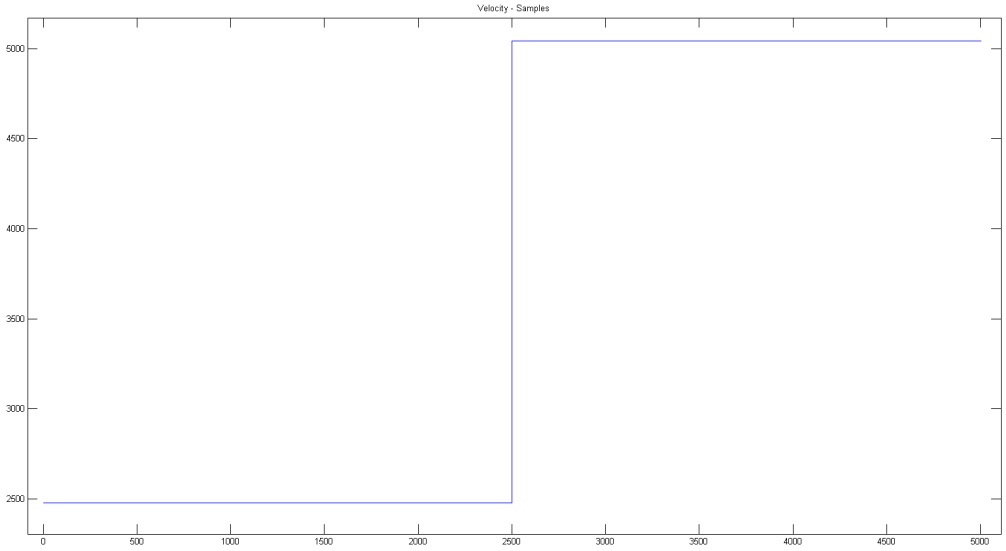


Synthetic Seismogram

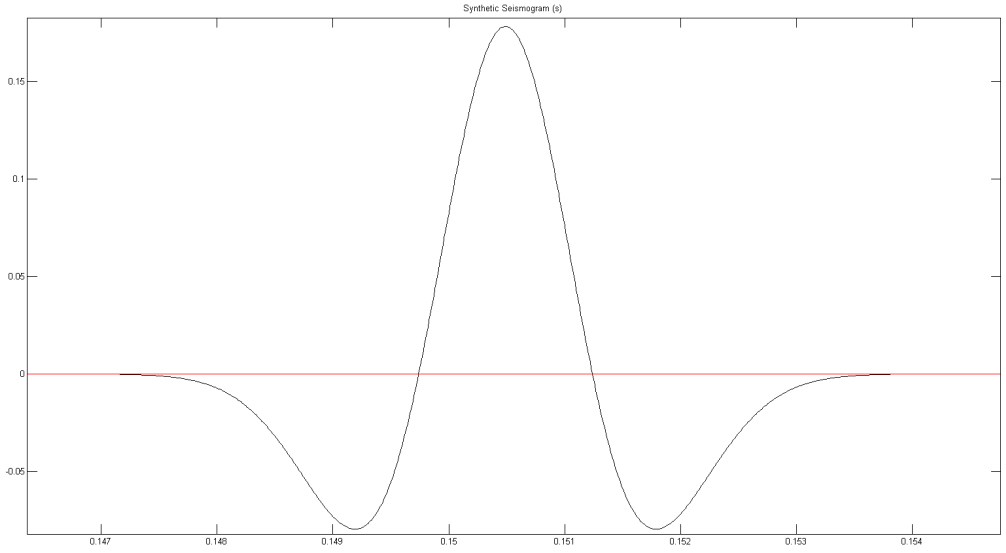


*Fig. 7.7:* Single boundary barite-arkose interface

### 7.3.2 Three-layer response

As discussed in Subsection (3.6.3), the seismic response to the thin barite vein results in both constructive and destructive interference as the seismic wavelet passes through the individual layers which modifies the peak-trough amplitude. The *maximum peak-through amplitude* or amplitude response occurs at **1/4 $\lambda$ thickness** also known as the *tuning thickness* or *limit of resolution*, which is the thinnest layer for which the front and back of the layer can be resolved (Figure 7.8). Therefore, within our dataset, the **highest amplitude response/limit of resolution** is at $\approx$ 1 m for 500 Hz frequency, $\approx$ 6 m for 100 Hz frequency, and similarly at $\approx$ 2 m for an average 300 Hz frequency. It is observed that in layers bounded by reflection coefficients of the opposite sign, layers thinner than **1/4 $\lambda$** will still produce an amplitude response that is higher than predicted by a single boundary (Figure 7.8). To demonstrate this, and determine the minimum thickness registered over the single boundary response in the Collier Point Dataset having an average 300 Hz frequency, the *synth* program is used to characterize the *tuning thickness* of a barite unit enclosed within an arkose unit by generating synthetic seismograms. The barite is given thicknesses as noted in Table 7.2 and the peak-to-trough amplitudes are noted for each layer thickness to create the plot in Figure 7.9.

As noted above, the calculated maximum peak-to-trough amplitude (for 300 Hz frequency) should occur at the **1/4 $\lambda$** thickness or *tuning thickness* for a barite unit at *2.1 m* (Subsection 3.6.3). However, in the graph (Figure 7.9) it is observed that the tuning thickness peaks at $\approx$ *3 m*. The disparity in the calculated tuning thickness (2.1 m) and tuning thickness produced using the *synth* program ($\approx$ 3 m) is likely due to the amplitude contributions from the side lobes of the Ricker Wavelet (Figure 7.5). However, it is still established that the amplitude response decreases with decreasing barite thicknesses ($<$ **1/4 $\lambda$**), and falls off to the single boundary response for larger thicknesses ($>$ **1/4 $\lambda$**). Therefore,

layers thinner than the the **1/4** $\lambda$ thickness, will still produce an amplitude response which is higher than that predicted by the single boundary response.

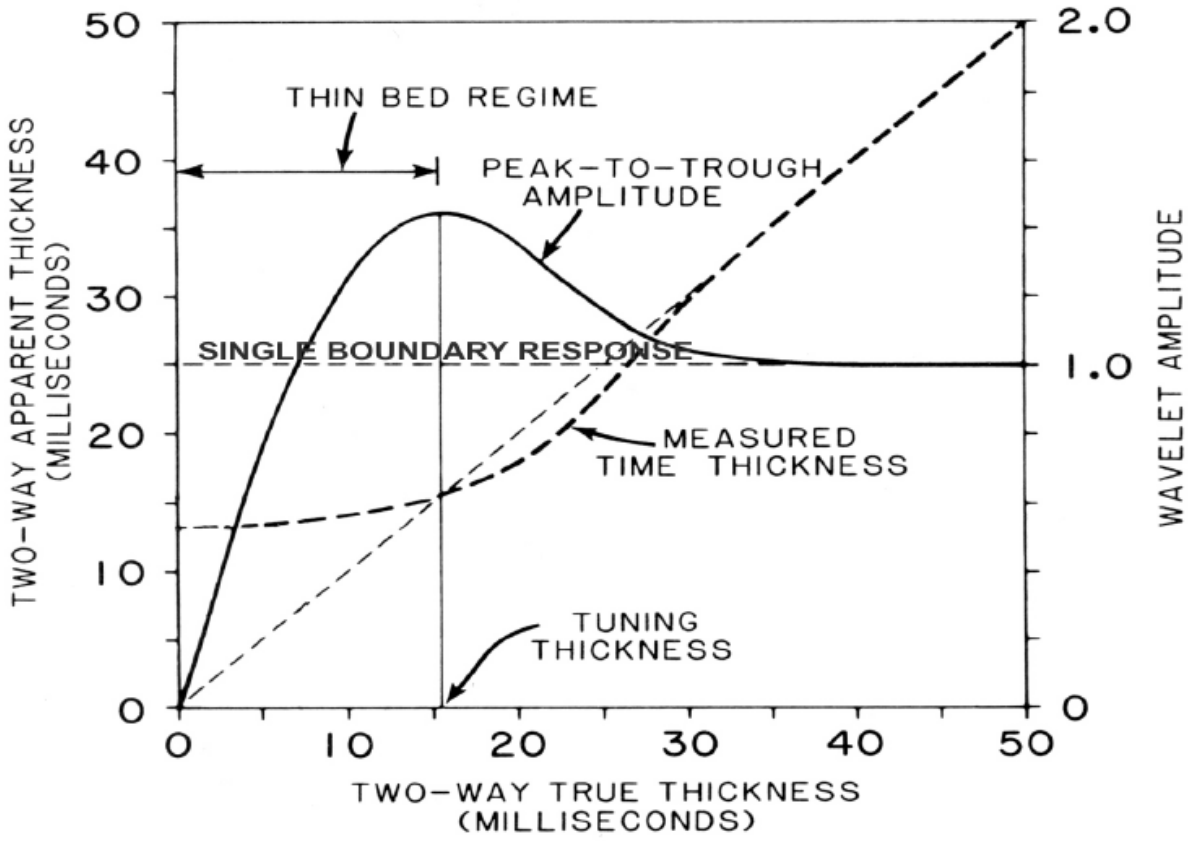


*Fig. 7.8:* Example of tuning when layer is bounded by reflection coefficients of the opposite sign [Hardage, 1987].

*Tab. 7.2:* Layer thicknesses & resulting peak-to-trough amplitudes for 300 Hz Ricker wavelet

| Model | Barite body thickness (m) | Amplitude |
|---|---|---|
| 1 | 0 | 0 |
| 2 | 0.5 | 0.1014 |
| 3 | 0.9 | 0.16431 |
| 4 | 1.3 | 0.2202 |
| 5 | 1.7 | 0.2667 |
| 6 | 2.1 | 0.303 |
| 7 | 2.5 | 0.3275 |
| 8 | 2.9 | 0.3402 |
| 9 | 3.3 | 0.3418 |
| 10 | 3.7 | 0.3344 |
| 11 | 4.1 | 0.3198 |
| 12 | 5.1 | 0.2748 |
| 13 | 6.1 | 0.2484 |
| 14 | 8.1 | 0.2392 |
| 15 | 10.1 | 0.24 |

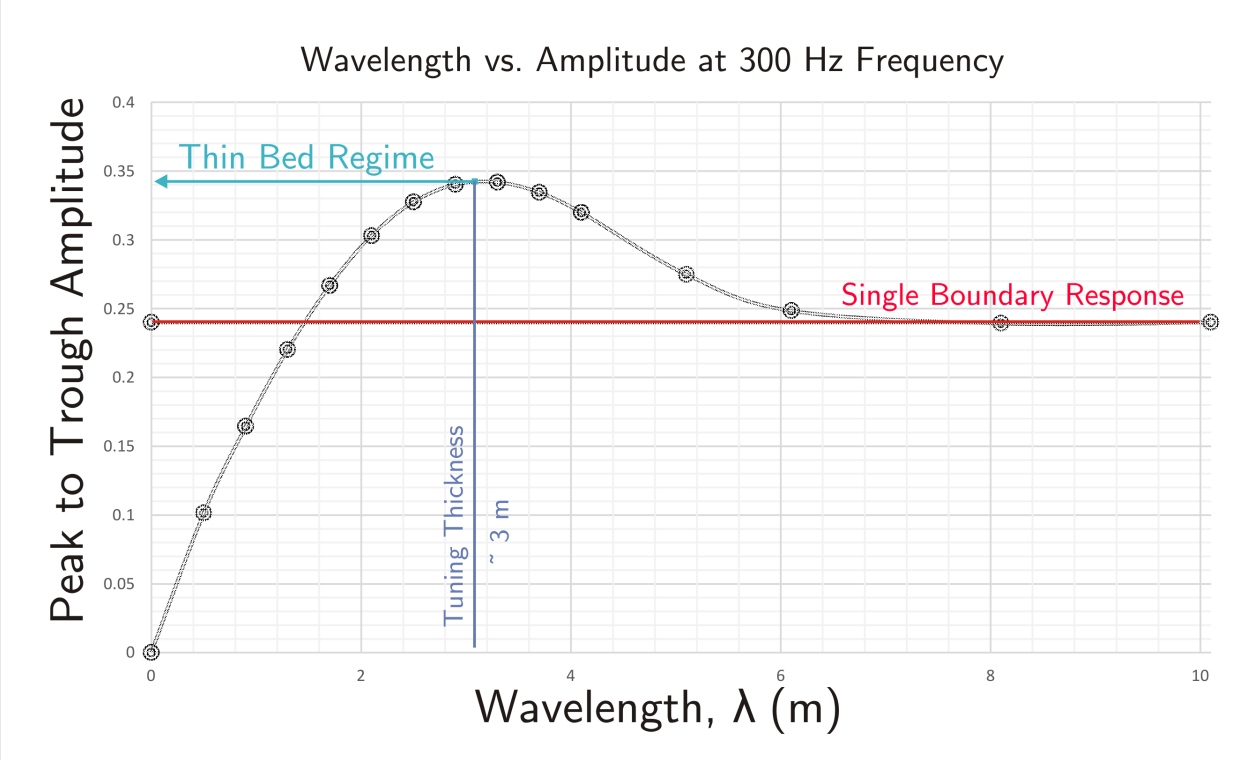


*Fig. 7.9:* Plot of peak-to-trough amplitudes for barite units of varying thicknesses
The maximum peak-to-trough amplitude occurs at the **1/4** $\lambda$ thickness or *tuning thickness*

### 7.3.3 Characterizing Wavelets

As discussed previously, the wavelet response to the barite vein in the Collier Point dataset varies significantly at different CDP depths (Section 7.3). Some of the behaviours observed in the Collier Point dataset are a transition from a singlet to a doublet, and the merging of two single wavelets. A *doublet* or *double wavelet*, in this case study refers to two adjacent positive (or negative) wavelets merging together as seen in Figure 7.10.

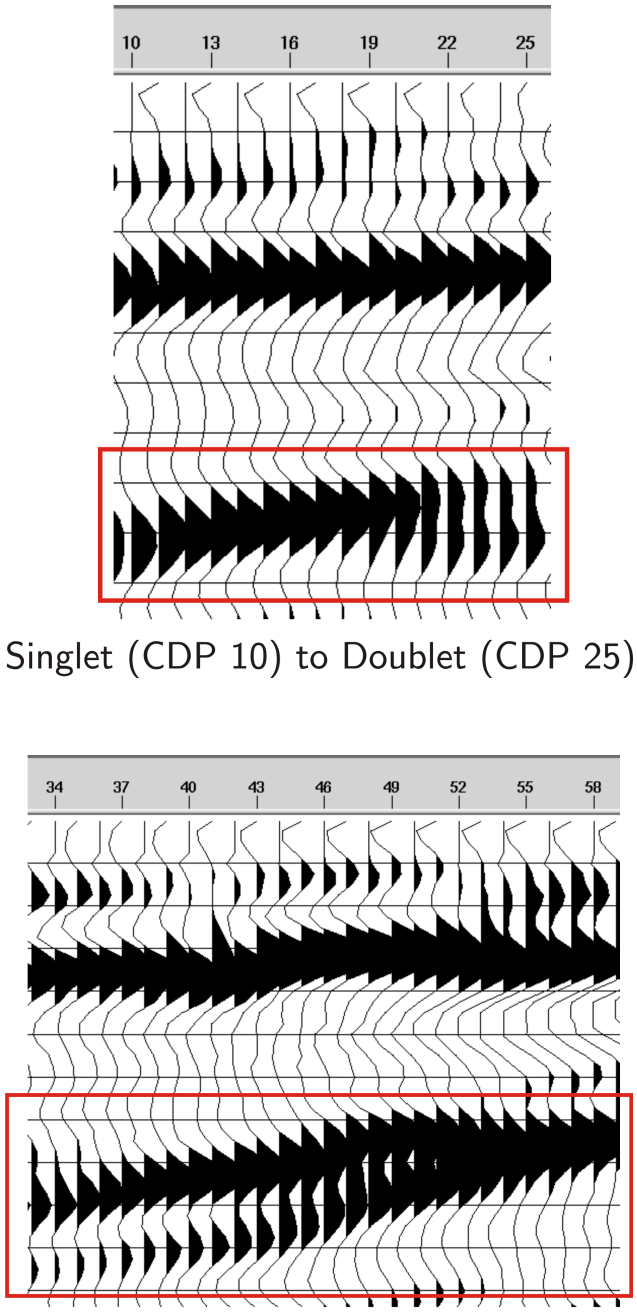


*Fig. 7.10:* Wavelet responses seen in the Collier Point Dataset

The synthetic **three-layer 1D models** (Subsection 7.3.2) of a simple arkose-barite-arkose interface does not result in this wavelet response, instead show a -ve change in amplitude due

to the transition from higher to lower, and similarly, a +ve shift due to the transition from the lower to higher velocities (Figures 7.6 and 7.7). As the *doublet wavelet response* cannot be recreated with a standard three layer 1-D model, a more complex geological model must exist that generates the doublet response. It has been noted that the barite is enclosed in an arkose host in the form of massive and brecciated vein mineralization within a fracture zone comprising of fragmented arkose, breccia and barite (Section 1.2.2). To study the effect of of the breccia zone on the wavelet, synthetic models comprising of a the barite vein surrounded by a breccia zone are created. The modelled breccias are given values outlined in Table 7.1.

### Barite surrounded by breccia

The model consists of a 2 m wide barite unit, directly in contact by 0.5 m of *high* and *low* breccia on both sides and arkose units beyond. The synthetic seismogram too, does not result in the wavelet responses as seen in Figure 7.10 from the Collier Point Dataset, but resembles the high-negative and high-positive waveform as seen in the three-layer response (Figures 7.6 and 7.7), due to the high-negative velocity of the barite unit over-riding intermediate velocity contributions from the thinner breccia units.

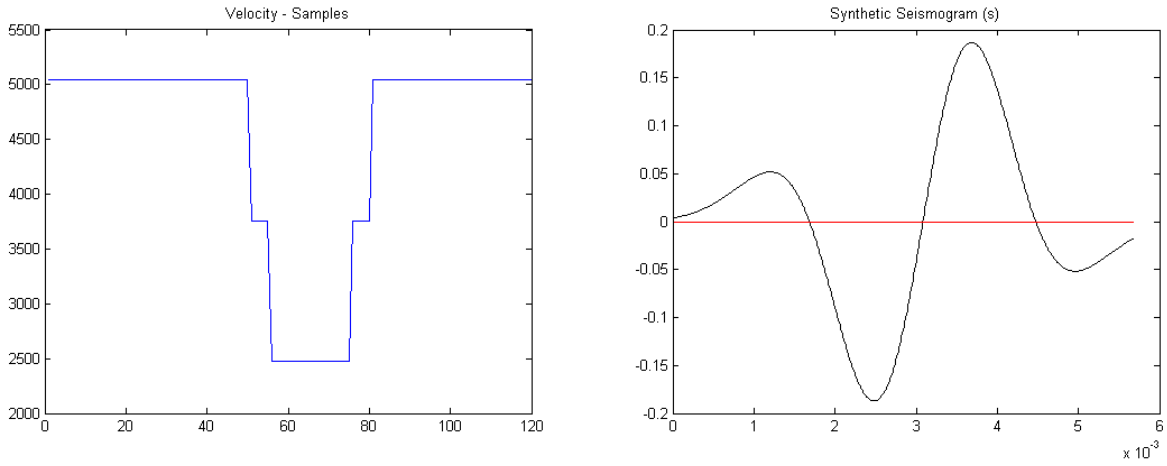


*Fig. 7.11:* Wavelet response for barite surrounded by high breccia
Velocity model (left), Synthetic Seismogram (right)

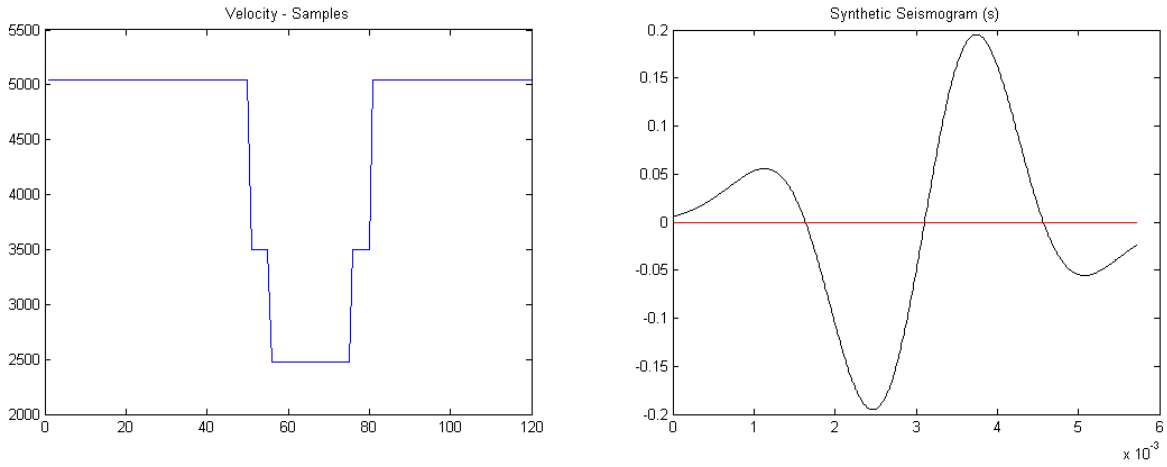


*Fig. 7.12:* Wavelet response for barite surrounded by low breccia
Velocity model (left), Synthetic Seismogram (right)

### Breccia Models

The **inver_synth** script is used to to test a group of geologic scenarios in one run of the modelling. A background log velocity file is created (Table G.1) and imported into the *inver_synth* script, in which two further velocity blocks can be modified - a non-moving velocity body, and a moving velocity body. The *near-vicinity* parameters represent the spaces over which the moving block has moved in a previous step. The breccia model trials that were conducted are demonstrated in Appendix G.

### 7.3.4 Summary of 1-D Modelling

The 1-D modelling and Breccia Models suggest that a *breccia zone* (having a velocity approximately around 3500 m/sec) immediately surrounding the barite vein, instead of a direct transition from arkose to breccia, may possibly result in the *doublet* waveforms as seen in the Collier Point Dataset (Figures 7.13 and 7.15).

The relationship between the data, synthetics and the geology is demonstrated in Figures 7.14 and 7.16, where the synthetic seismograms produced in the the 1-D modelling are scaled and super-imposed on regions in the CDP stack which demonstrate the same

changes in wavelet and a geological interpretation is created for the same. The 1-D modelling demonstrates that the asymmetric lobes produced in the breccia models may be the result of breccia zones having different velocities and densities. It should be noted that the actual velocity of the breccia zones at the Collier Point barite property are unknown and that the chosen low/high breccias are given vales corresponding to a 50/50 mix (*low breccia*) and a higher arkose content breccia (*high breccia*). The geological models produced in the 1-D modelling are *not* unique solutions, but illustrate that a breccia zone likely results in the varying wavelets as seen in the dataset (Figure 7.10), also breccia zones are not limited only through the regions with the doublets in the dataset, as these breccia zones may exist through the entire length of the barite vein.

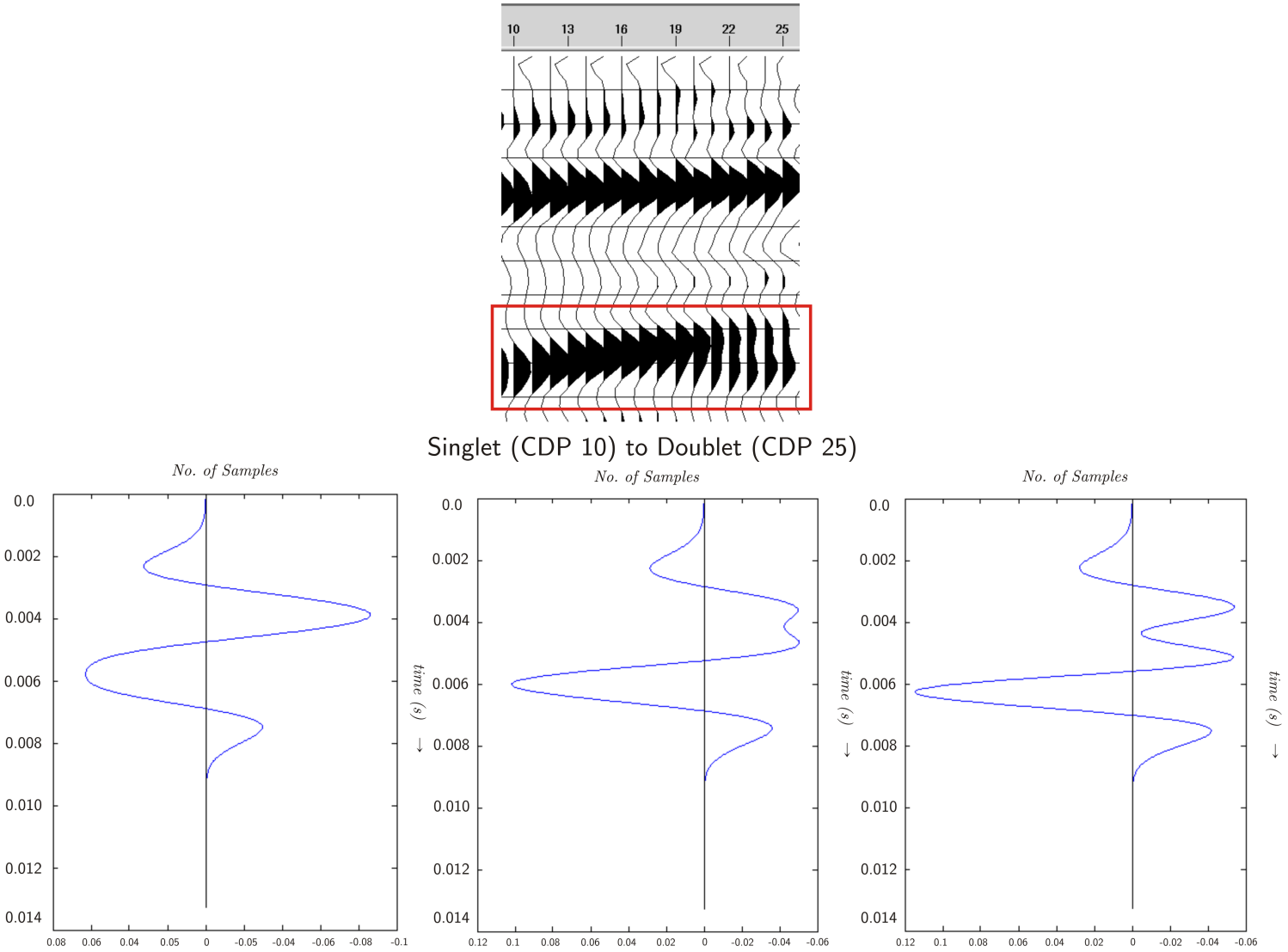


*Fig. 7.13:* Comparison of wavelet responses in Collier Point dataset with Breccia Model 1
Note the conversion of a singlet into a doublet following interactions with a breccia zone. Plotted in Reverse Polarity.

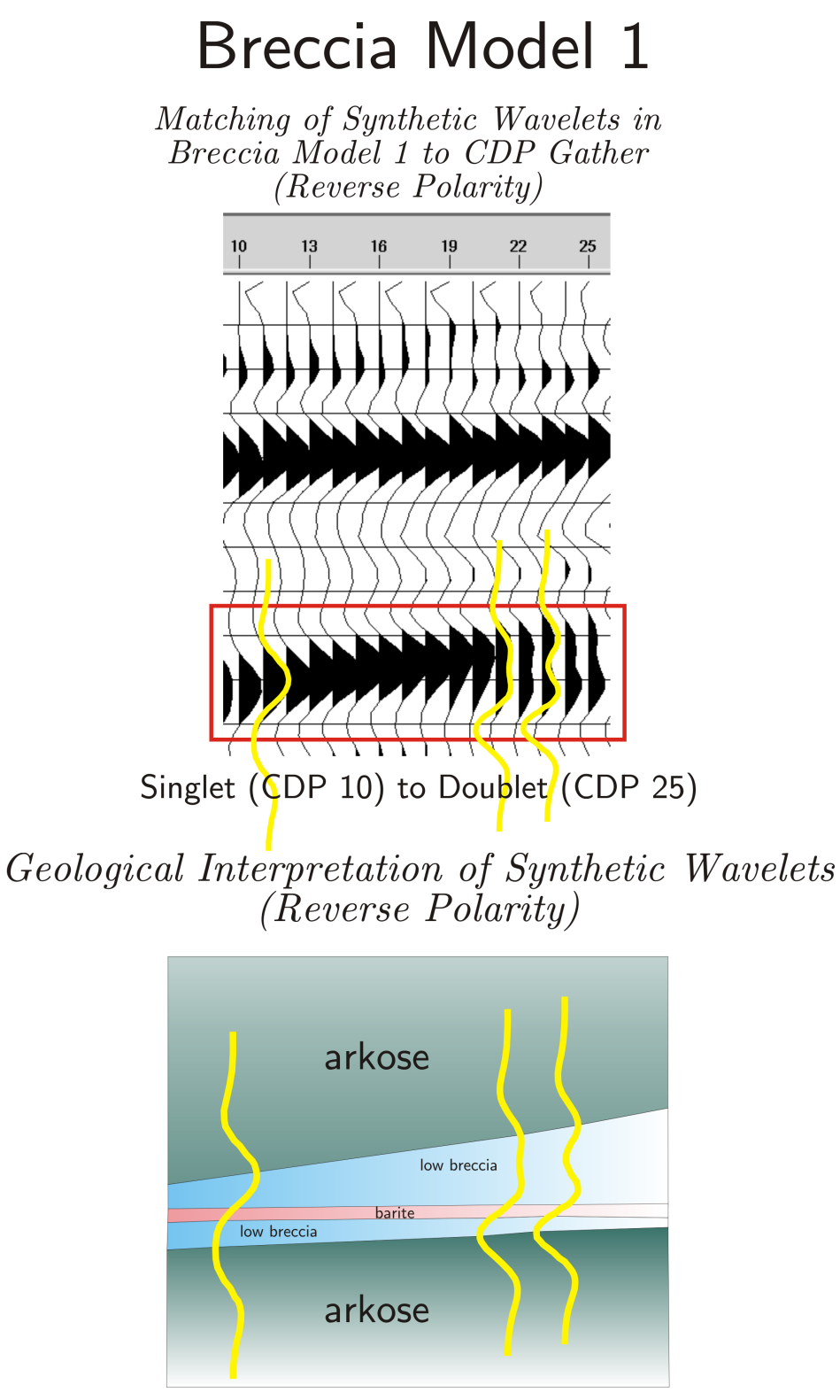


*Fig. 7.14:* Geological interpretation of synthetic wavelets from Breccia Model 1

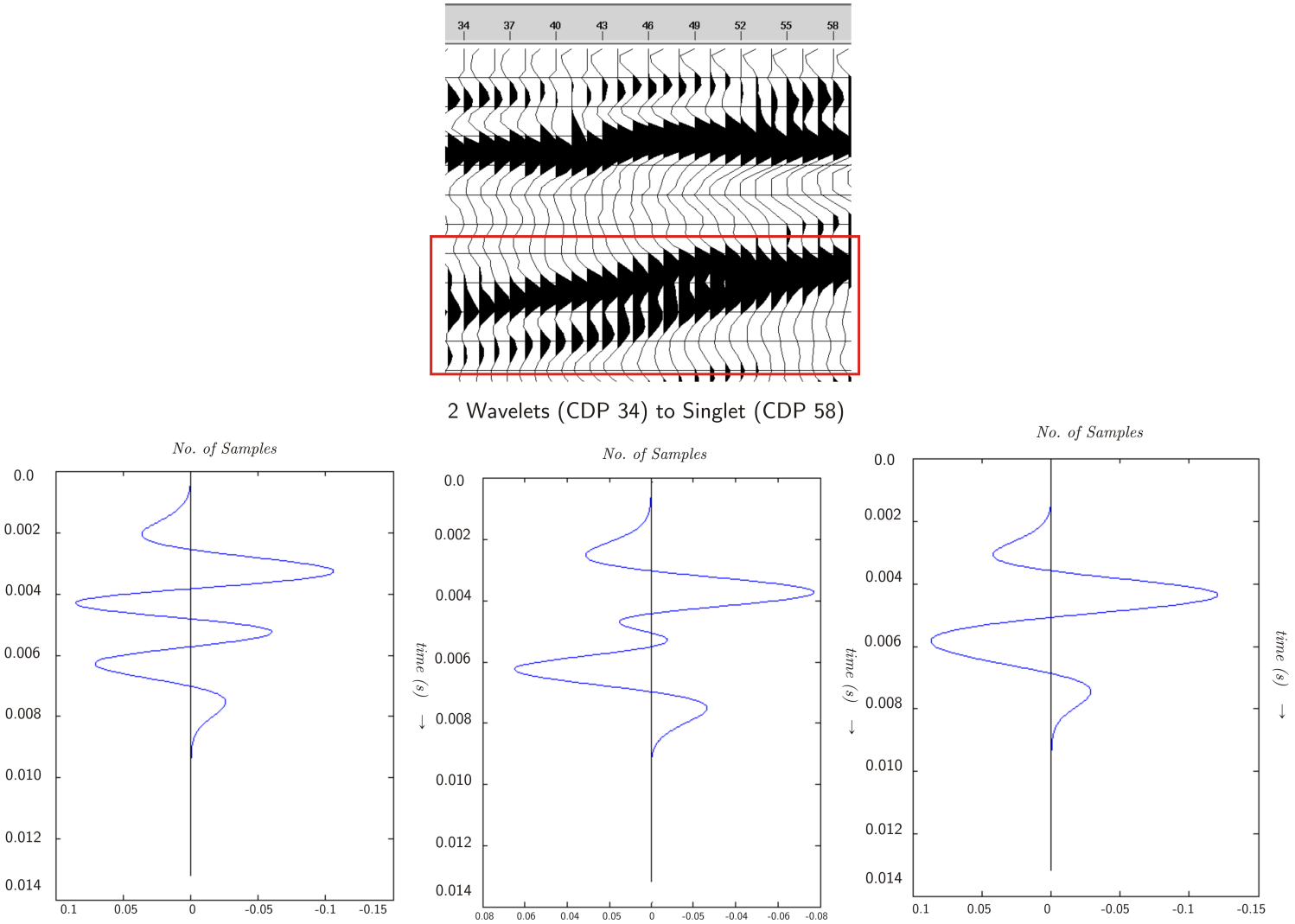


*Fig. 7.15:* Comparison of wavelet responses in Collier Point dataset with Breccia Model 4
Note the conversion of two negative peaks to a single negative peak following interactions with a breccia zone. Plotted in Reverse Polarity.

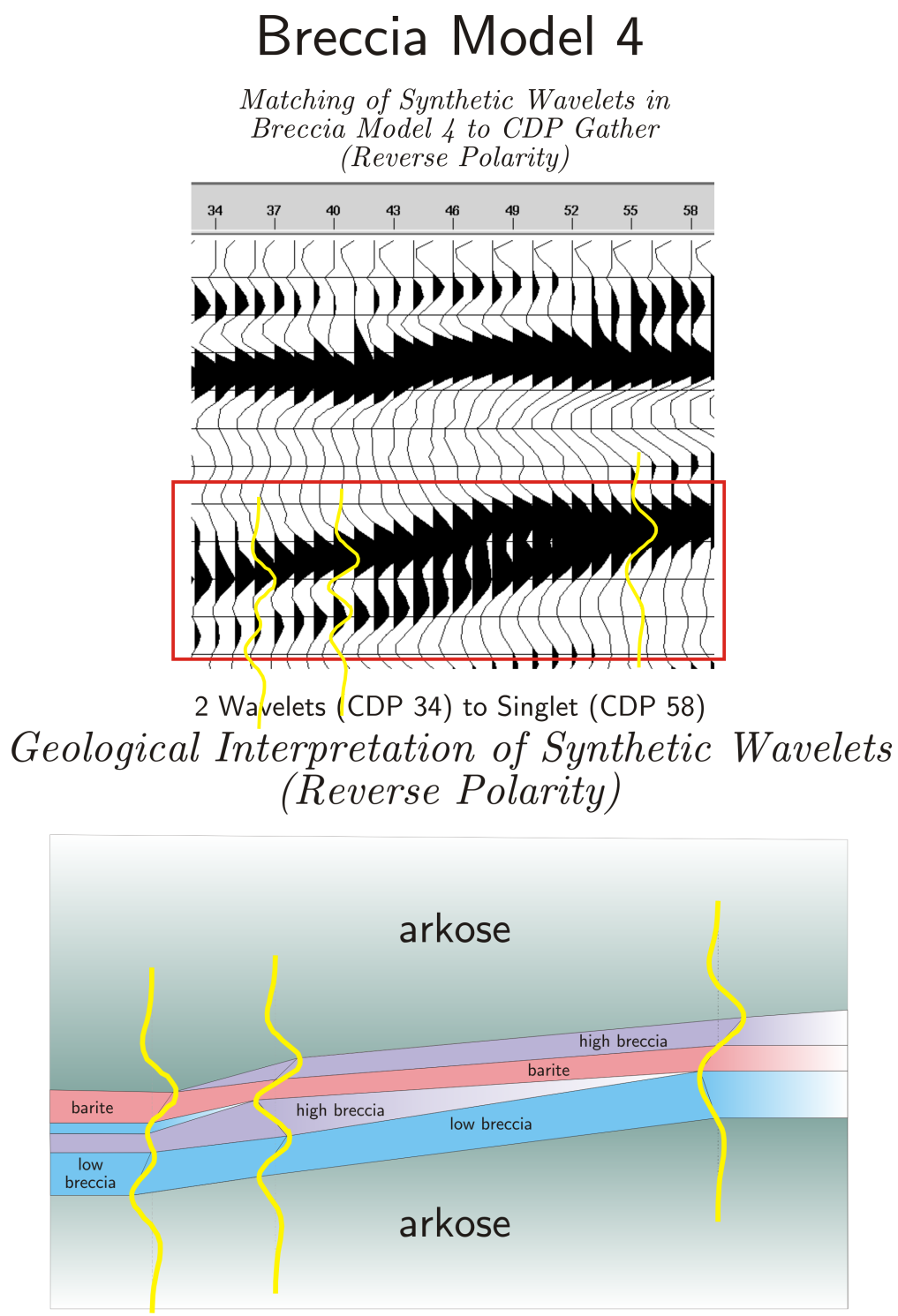


*Fig. 7.16:* Geological interpretation of synthetic wavelets from Breccia Model 4

## 7.4 Proposed Geological Model

Based on the processed dataset (Chapter 6), 1-D and subsequent breccia modelling, a proposed geological model of the Collier Point Dataset was produced. As discussed previously, the Collier Point dataset consists of two strong reflection events, Reflection Events 1 and 2. **Reflection Event 1**, in the Collier Point dataset, appears as a strong event having slightly variable dip and a different structure overall from **Reflection Event 2**, the established barite vein (Figure 7.4).

### 7.4.1 Summary of Reflection Event 1

The origin of Reflection Event 1 is not known to have formed as an artifact during the pre-processing of the raw gathers via the F-K filters and spiking deconvolution (Section 6.1), and is also not known to be formed as an artifact during the interferometry procedure (Section 6.2), as it is visible in the pre-processed gathers prior to interferometry (Figure 7.1). The frequency content of Reflection Event 1 and Reflection Event 2 were analysed and it was noted that both events have a similar *frequency bandwidth* of 200 - 800 Hz (Figures 7.17 and 7.18).

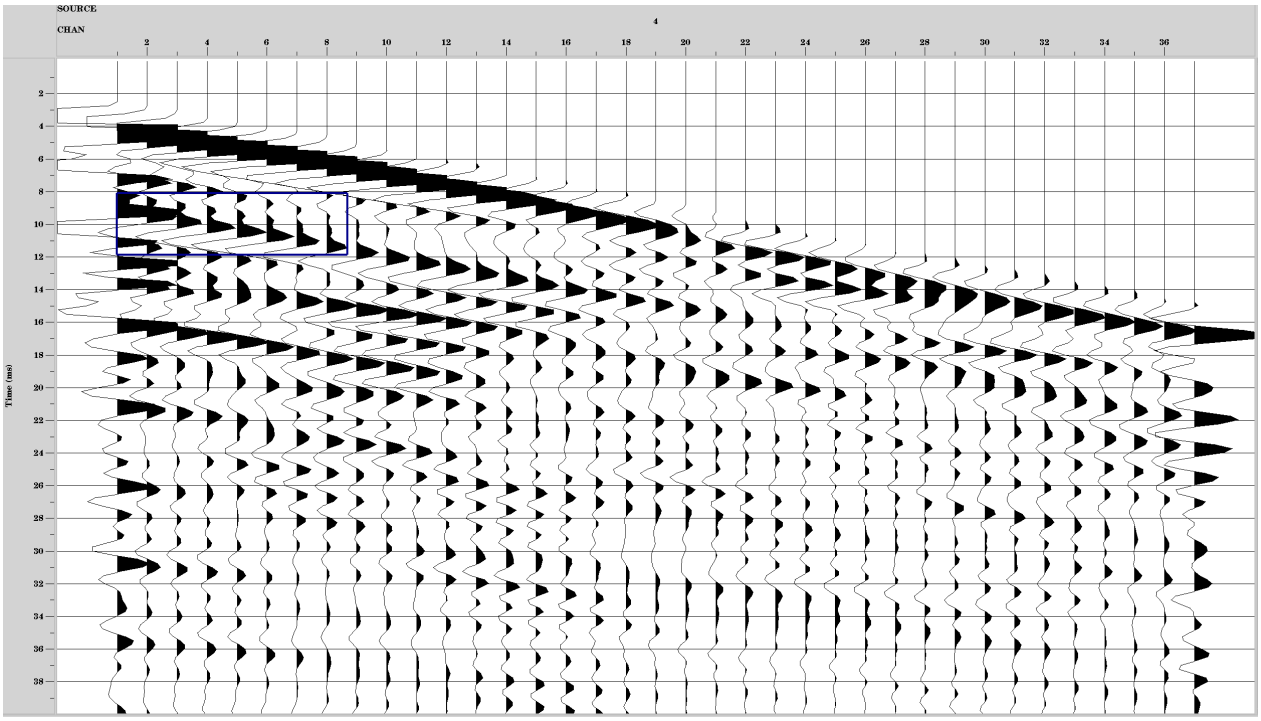


*(a)* Analysis window of Reflection 1 selected - Reverse Polarity

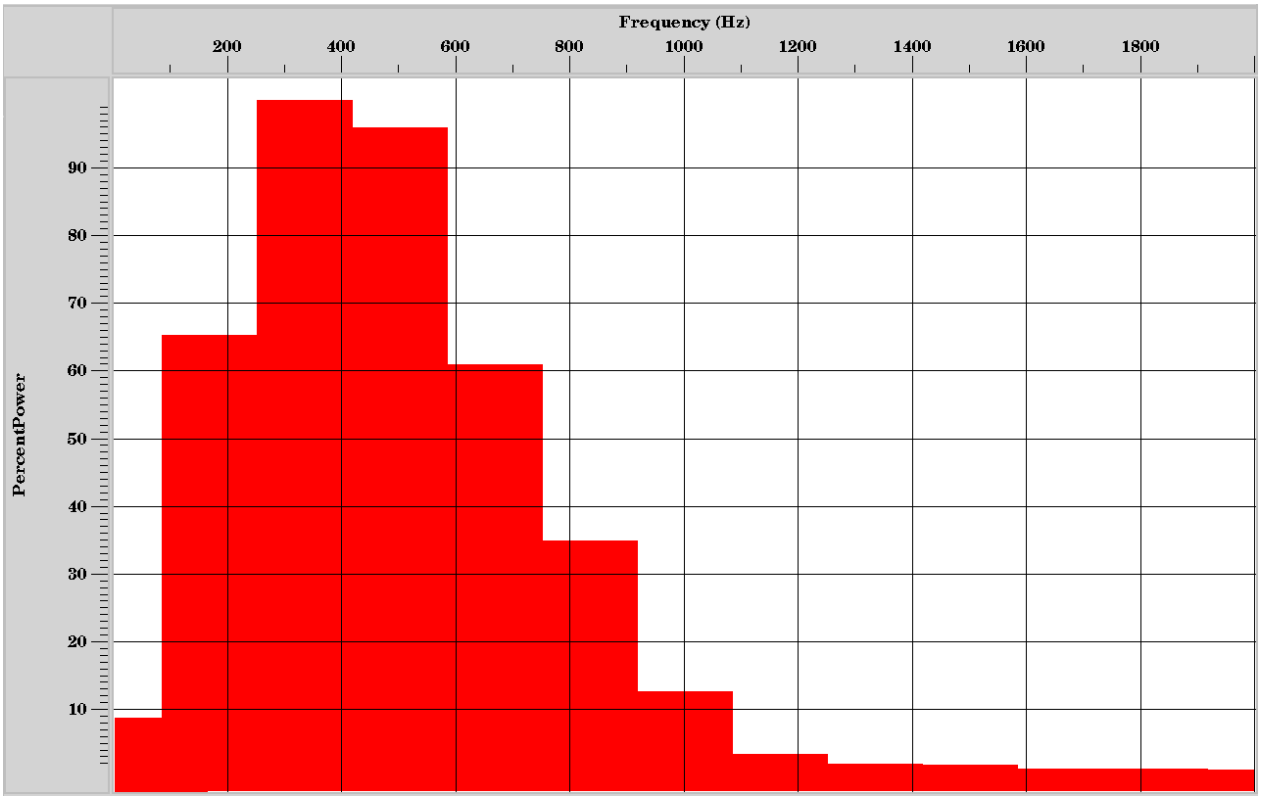


*(b)* Spectral Analysis

*Fig. 7.17:* Frequency content of Reflection Event 1 in Pre-Processed Gather

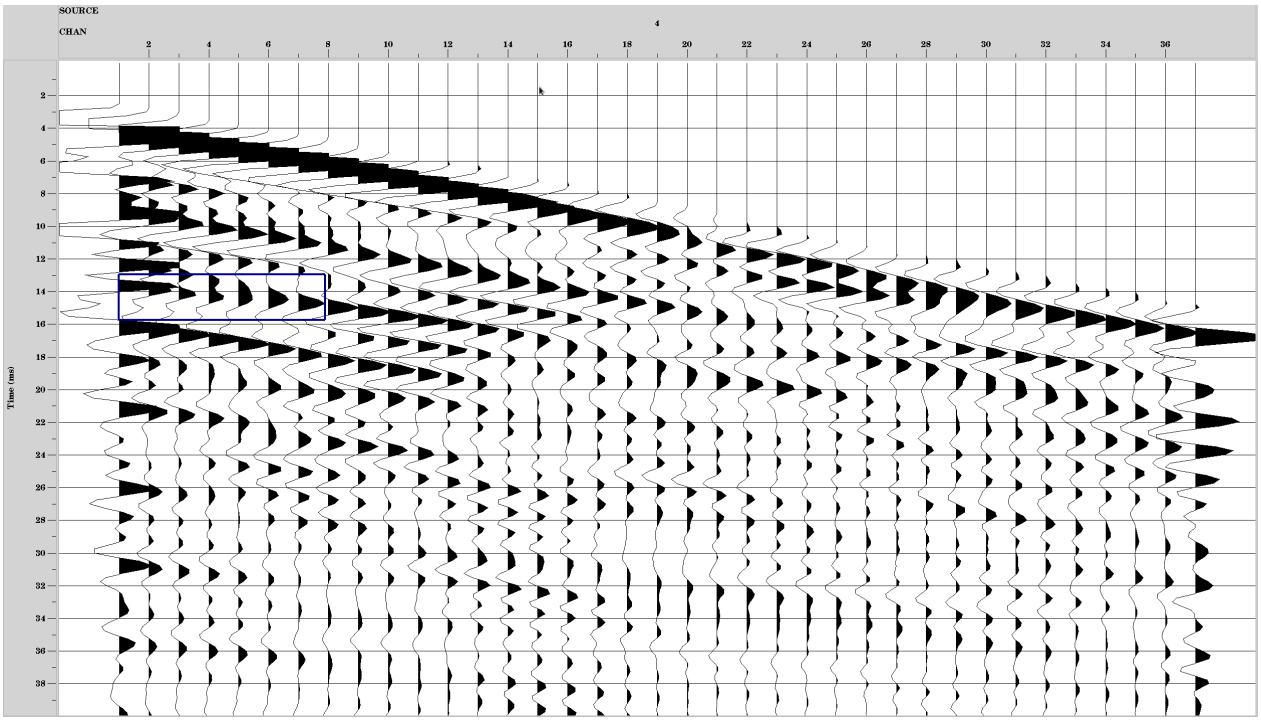


*(a)* Analysis window of Reflection 2 selected - Reverse Polarity

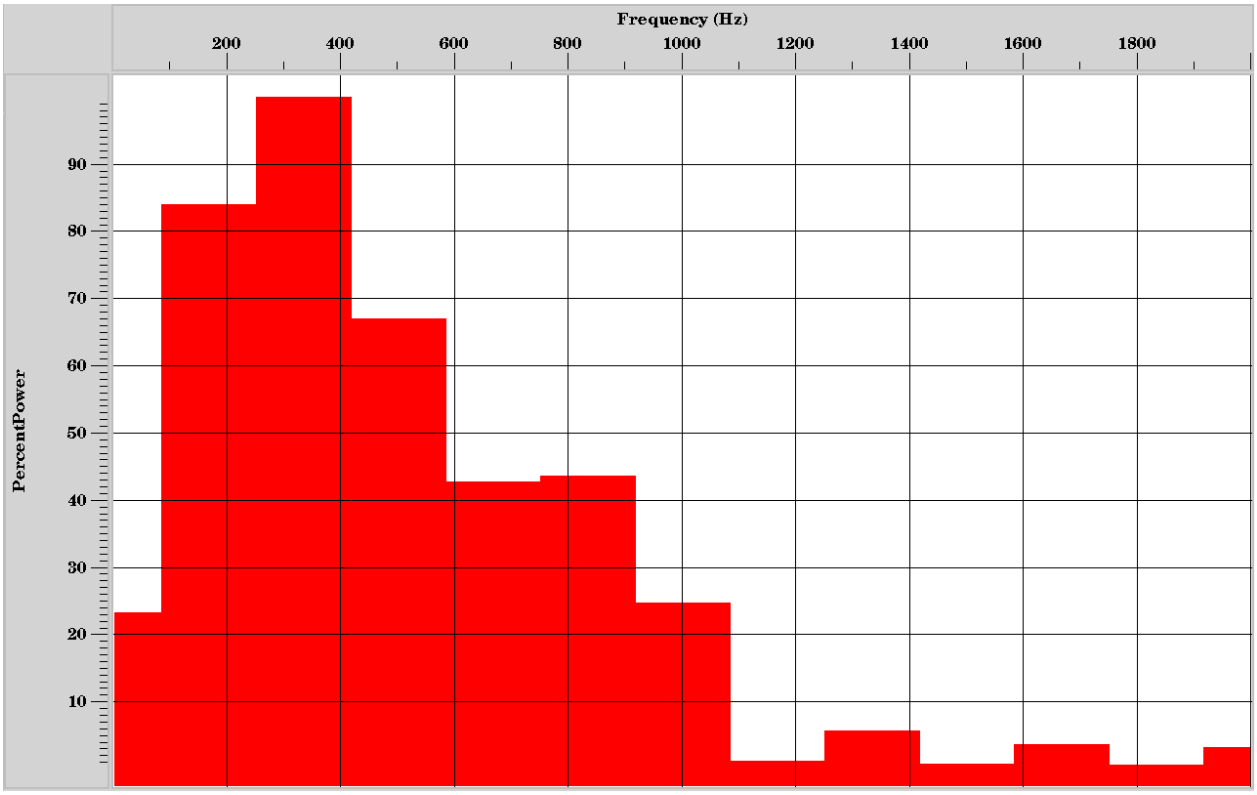


*(b)* Spectral Analysis

*Fig. 7.18:* Frequency content of Reflection Event 2 in Pre-Processed Gather

**Reflection Event 1** occurs to have the same 'breaks' and changes in wavelet at certain depths as demonstrated in **Reflection Event 2** (established barite vein), which lays credence to the theory that the breaks may result due to changes in subsurface lithology which intercept Reflection Event 1 and 2, therefore implying that Reflection Event 1 is a *real* geological event (Figure 7.19). However, it should be noted that prior field studies do not account for any major barite vein discovery in the location or vicinity of Reflection Event 1, apart from Reflection event 2 (the Collier Point barite vein). As a result, any geological interpretation of Reflection Event 1 as a secondary barite vein is inconclusive pending actual field excavations and further on-site studies.

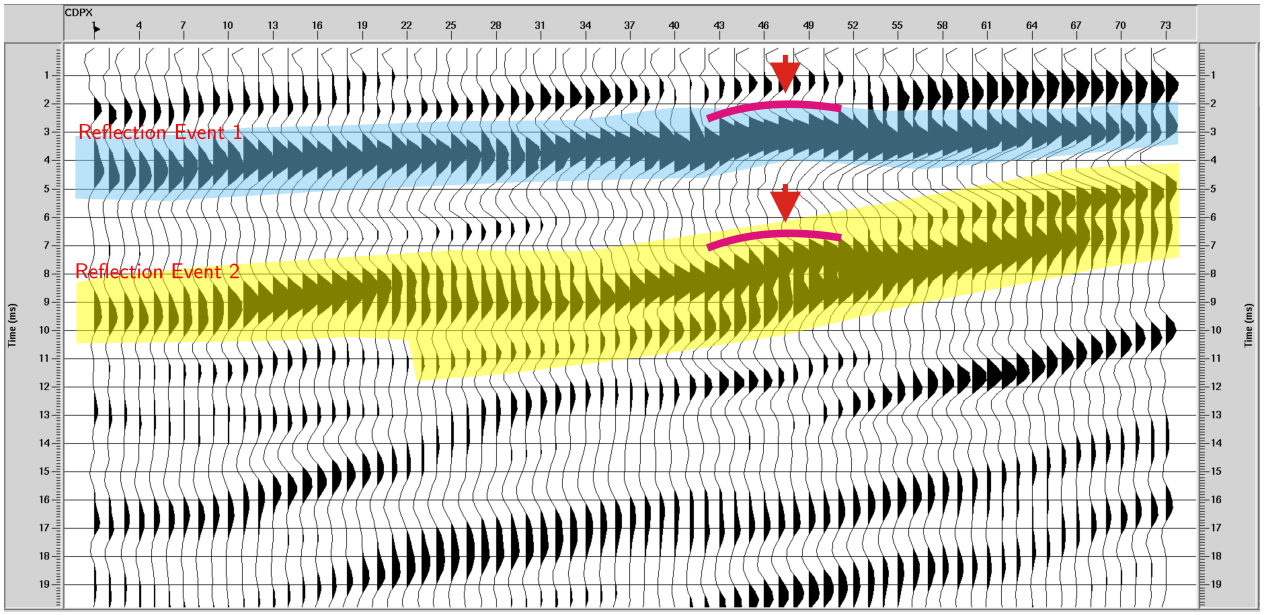


*Fig. 7.19:* Reflection Events and similarities in wavelet at depth
Reflection Event 1 is marked in blue and Reflection Event 2 is marked in yellow.

### 7.4.2 Summary of Reflection Event 2 - the barite vein

**Reflection Event 2** occurs at ≈ 8 ms and is the Collier Point barite vein, which is the subject of this thesis. The structure of the veins in the dataset suggests a series of nearly-vertical dilated veins with fluids seeping into the open fractures which mineralize to barite

and accessory minerals such as calcite. The below figure attempts to describe the subsurface geological model with a simulation of the CDP stack projected perpendicular to the borehole (Figure 7.20). The figure is *not* a true representation of true subsurface geology, as in actual practice, the CDP profile may not be projected precisely orthogonal to the hydrophone cable. The barite vein reflection event is plotted in yellow and the unknown Reflection Event 1 in blue. The soft/rapid drilling zones labelled on the borehole represent regions where the drilling occured very quickly (likely due to fracture zones). The pink drilling fluids do not necessarily represent barite zones, and may be associated with drilling through regions of red sandstone.

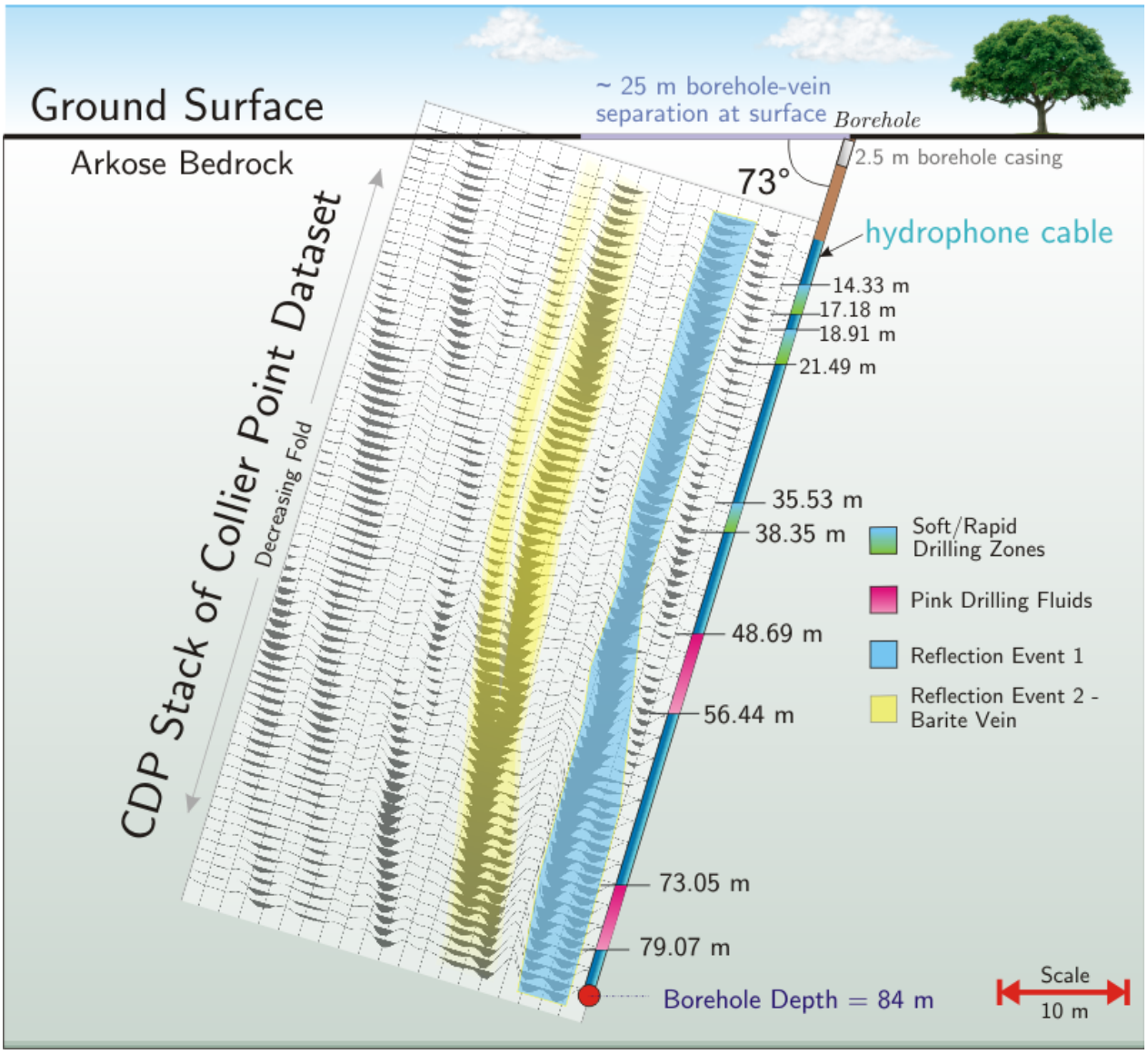


*Fig. 7.20:* Figure demonstrating a simulation of the CDP stack projected perpendicular to the borehole

The figure demonstrates the CDP profile scaled and projected orthogonally on to the borehole. The seismic section is plotted at true distance scale in both dimensions. The figure is not a true representation of true subsurface geology, as the CDP profile may not be projected precisely orthogonally to the hydrophone cable in real life. The barite vein reflection event is plotted in yellow and the unknown Reflection Event 1 in blue.

Prior drilling reports [Hutchings, 1994] suggest the presence of a breccia zone surrounding the barite vein instead of a direct contact from barite to arkose and vice versa. The 1-D modelling (Chapter 7) indicates that interactions between the breccia zones, arkose and

barite may possibly result in the variation of the wavelet (Singlet to doublet, merging of two wavelets, etc.) as seen in the dataset. However, it should be noted that the 1-D models are *non*-unique solutions and breccia zones may exist through the entire length of the barite vein, therefore not limited through the regions with wavelet variations in the dataset. The overall barite vein structure appears to have a structure best described as a series of thin and thick veins '*stepping-over*' and partly overlapping each other. The geological interpretation weakens towards the top and bottom of the borehole due to decreasing CDP *fold*, with the highest fidelity in the middle regions of the borehole.

# Chapter 8

## Conclusion

The purpose of this study is to develop techniques for imaging nearly vertical structures in hard rock exploration, in cases where surface seismic methods are not feasible due to unfavourable source-receiver geometries in relation to the target. This was achieved by using VSP's in combination with the **virtual source method** in seismic interferometry to image a nearly vertical barite vein at the Collier Point Barite property in Eastern Newfoundland, which serves as a well-constrained target for study and technique development. In this method, borehole receivers (in the form of geophones or hydrophones) are lowered down a monitoring well (borehole), and seismic sources are located on the horizontal surface at various offsets from the well. The contributions from surface sources are recorded on the borehole receivers in a walk-away VSP, and the receivers are transformed to virtual borehole sources via seismic interferometry. This transformation of surface sources to virtual borehole sources, uses direct waves that pass through a borehole receiver and are reflected back into adjacent borehole receivers, to simulate a virtual source located at the receiver through which the direct wave passes. This technique theoretically results in the source and receiver being placed in the same borehole, and can hence be considered as equivalent to a conventional situation in which the sources and receivers are placed at the surface (**Chapter 1**).

## 8.1 Summary of the thesis

The acoustic impedance contrast between adjacent lithologies (the geometry and size of the target) is one of the most important factors that determines the strength of the response from a seismic reflector. There must be a sufficiently high impedance contrast between the contrasting lithologies of the host and the target to produce detectable seismic reflections. Velocity and density measurements of the arkose bedrock and barite vein were conducted to yield information about the acoustic impedance and therefore the P-wave reflection coefficient between the arkose and the barite, giving an indication on how strong the reflection from the barite vein may be. It was discovered during testing that the barite is very anisotropic resulting in large variations in measured P-wave velocity. The density and velocity measurements indicated that a *significant* reflection of -0.11 (which is > the minimum requirement of 0.6 to observe a reflection coefficient under ordinary field conditions [Salisbury et al., 1996]) could be expected from the arkose-barite interface, and that the frequency content of the data (100 Hz - 500 Hz) are adequate to allow **1/4** $\lambda$ frequency tuning and detection of the thin barite vein (**Chapter 3**).

The respective dip of the borehole and the target is one of the most important criteria towards imaging the vein, as it directly influences the stationary phase contribution to the wave-field and fidelity of the virtual shots, of which a large number enhances the image recovery of the near-vertical barite dyke. In order to optimize the experiment for the best data recovery, a series of synthetic seismograms were created using finite-difference modelling. The wave-field modelling was guided by ray-tracing analysis to choose a suitable dipping angle for the borehole and to study the constraints imposed by the pre-existing geometry and setup of the experiment at Collier Point, NL (**Chapter 4**).

Following acquisition (**Chapter 5**), the seismic data acquired is pre-processed by strongly filtering the dataset using Spiking Deconvolution and F-K filtering to remove the effect of unwanted tube-waves and enhance any possible reflection from the barite vein (Section 6.1). Following the pre-processing, cross-correlated files are created in Seismic Unix and the cross-correlated concatenated files are exported back to the ProMAX Seismic Processing Suite, where the VSP data is redatumed into the borehole using the seismic interferometry method, resulting in virtual shot records with the virtual sources in the borehole and a virtual source gather (VSG). The dataset is processed by applying a standard common midpoint (CDP) flow, and imaged using Kirchoff Depth Migration (**Chapter 6**).

It is observed that the final dataset comprises two main reflection events: *Reflection Event 1* and *Reflection Event 2*, which is the Collier Point Barite vein (Section 7.1). Reflection Event 1 is the earlier event having slightly variable dip and a different structure overall from the barite vein. The origin of Reflection Event 1 is undetermined, and is not known to have formed as an artifact resulting from the interferometry procedure. Prior drilling reports [Hutchings, 1994] suggest the presence of a breccia zone surrounding the barite vein instead of a direct contact from barite to arkose and vice versa. The 1-D modelling (**Chapter 7**) indicates that interactions between the breccia zones, arkose and barite may result in the variation of the wavelet (Singlet to doublet, merging of two wavelets, etc.) as seen in the dataset for Reflection Event 2 (Collier Point Barite Vein). However, it should be noted that the 1-D models are *non*-unique solutions and breccia zones may exist through the entire length of the barite vein, therefore not limited through the regions with wavelet variations in the dataset. The overall barite vein structure appears to have a structure best described as a series of thin and thick veins '*stepping-over*' and partly overlapping each other. The geological interpretation weakens towards the top and bottom of the borehole due to decreasing CDP *fold* and fewer stationary phase contributions, with the highest fidelity in

the middle regions of the borehole. Overall, the seismic interferometry procedure conducted using the appropriate experiment optimization and processing parameters has resulted in the processed image consistent with descriptions in prior geological reports.

## 8.2 Limitations of Current Work

The acquisition parameters for the interferometry experiment were limited due to pre-existing physical and geological constraints in the form of sloping dug trenches and dense forest cover. The most optimal experimental setup would comprise of a large source-receiver offset and the vein dipping in the direction of the borehole and surface source array (shot locations), which results in maximum stationary phase contributions, and therefore highest-quality imaging of the vein. However, due to these physical constraints, the interferometry experiment at the Collier Point Barite Property was conducted using less than ideal conditions, having a short source-receiver offset and the vein dipping away from the inclined borehole.

Although *Predictive Deconvolution* has previously been used with success to remove the effect of tube-waves from data due to their periodic nature [Gulati et al., 2001], this method was not successful with the Collier Point dataset due to the variability in prediction distances from shot-to-shot, likely as result of variability in the detonation of surface-shot charges (some strong charges and some with loss of energy). An automated trace-by-trace prediction deconvolution (which automatically chooses the second zero crossing) was not implemented due to possible interference from different waves. This necessitated a very strong F-K accept filter for the removal of tube-waves which was implemented from shot-to-shot, and the design of which was time-consuming.

## 8.3 Contribution of this thesis

This thesis has demonstrated that using VSP's in combination with the seismic interferometry procedure has proven to be an appropriate tool towards imaging the thin and nearly-vertical veins, in situations where surface seismic methods are largely inadequate. Presently, there are very few actual field examples implementing seismic inteferometry for this type of imaging. The Collier Point barite vein was chosen as a convenient experimental subject for technique development, as it is thin, nearly vertical, reasonably well constrained and lies within the subsurface. It was noted that the Collier Point barite vein was adequately imaged using these methods, despite being recorded in non-ideal conditions and physical limitations. With the appropriate experiment optimization and processing parameters, VSP's in combination with seismic interferometry can be used to detect and image vertical to near-vertical subsurface bodies of economic importance which may otherwise not be imaged appropriately using surface-seismic methods.

# Bibliography

[Adams and Kerr, 2014] Adams, T. and Kerr, A. (2014). Mineral Commodities of Newfoundland and Labrador: Barite.

[Bakulin and Calvert, 2006] Bakulin, A. and Calvert, R. (2006). The virtual source method: Theory and case study. *Geophysics*, 71(4):SI139.

[Brand, 2010] Brand, E. (2010). *The virtual source method for imaging steeply dipping structures using a walk-away VSP acquisition geometry.* M.sc. thesis, Memorial University of Newfoundland.

[Claerbout, 1968] Claerbout, J. F. (1968). Synthesis of a Layered Medium From Its Acoustic Transmission Response.

[Eaton et al., 1996] Eaton, D. W., Guest, S., Milkereit, B., Bleekker, W., Crick, D., Schmitt, D., and Salisbury, M. (1996). Seismic Imaging of Massive Sulfide Deposits: Part III. Borehole Seismic Imaging of Near-Vertical Structures. *Economic Geology*, 91:835–840.

[Embree et al., 1963] Embree, P., Burg, J. P., and Backus, M. M. (1963). Wide-band velocity filtering; The Pie-Slice process. *Geophysics*, 28(6):948–974.

[Fracflow Consultants Inc., 1998] Fracflow Consultants Inc. (1998). Mine Plan - For The Proposed Barite Mine At Collier Point, Newfoundland. Technical report, St. John's.

[Gulati et al., 2001] Gulati, J. S., Stewart, R. R., and Hoffe, B. H. (2001). Vertical hydrophone cable acquisition and imaging on land. *Geophysics*, 66(4):1190–1194.

[Hale et al., 1992] Hale, D., Ross Hill, N., and Stefani, J. (1992). Imaging salt with turning seismic waves. *Geophysics*, 57(11):1453–1462.

[Hardage, 1987] Hardage, B. A. (1987). Seismic Stratigraphy. In *Handbook of geophysical exploration. Section 1, Seismic exploration ; v. 9*. Geophysical Press, EXPRO Science Publications, London, Amsterdam.

[Hardage, 2000] Hardage, B. A. (2000). Vertical Seismic Profiling : Principles. In Klaus Helbig and Sven Treitel, editors, *Handbook of Geophysical Exploration. Section I, Seismic Exploration ; v. 14*. Pergamon, Amsterdam ; New York, 3rd update edition.

[Howse, 1992] Howse, A. F. (1992). Barite Resources of Newfoundland. Technical report, Geological Survey Branch, Department of Mines and Energy, Government of Newfoundland and Labrador.

[Hurich and Deemer, 2013] Hurich, C. and Deemer, S. (2013). Combined surface and borehole seismic imaging in a hard rock terrain : A field test of seismic interferometry. *Geophysics*, 78(3):P.B103–B110.

[Hutchings, 1982] Hutchings, C. K. (1982). 1982 Summarization Report, Collier Point Fee Simple Mining Grant, Newfoundland for W. Gibbs and S. Jones. Technical report.

[Hutchings, 1994] Hutchings, C. K. (1994). Geological Report: Diamond Drilling Program at Collier Point Barite Property, Licence No. 4482, Assessment Year I. Technical report.

[McCartney, 1967] McCartney, W. D. (1967). Whitbourne map-area, Newfoundland. *Geological Survey Canada Memoir*, (341):135.

[Salisbury et al., 1996] Salisbury, M., Milkereit, B., and Bleeker, W. (1996). Seismic imaging of massive sulfide deposits: Part I. Rock properties. *Economic Geology*, 91(5):821–828.

[Schuster, 2009] Schuster, G. (2009). *Seismic inteferometry*. Cambridge University Press, Cambridge; New York.

[Wang et al., 2004] Wang, R., Jia, X., and Hu, T. (2004). The Precise Finite Difference Method for Seismic Modeling. *Applied Geophysics*, 1(2):69–74.

[Wyllie et al., 1956] Wyllie, M. R. J., Gregory, A. R., and Gardner, L. W. (1956). Elastic wave velocities in heterogeneous and porous media. *Geophysics*, 21(1):41–70.

# Appendices

# Appendix A

## Creation of Velocity Model

### A.1 Preparation of greyscale 2D graphic:

- A background box is drawn, and bodies of interest (such as vein) are superimposed within.
- Outlines are turned off in the graphic to minimize edge effects.
- Greyscale values are set for all bodies according to their velocities.
- CorelDraw file (.cdr) is exported as a PiCture eXchange (.pcx) file, setting the pixel width according to the actual size of the model. Note that the model needs to have 10 grids per wavelength for stability. The limiting wavelength is calculated by dividing the smallest velocity by the largest frequency.
- Note the number of pixels in rows (500 px) and columns (1382 px) to input as model dimensions in the finite difference program.

## A.2 Creation of Velocity Model in Seismic Unix

- The model is produced in greyscale, with the barite vein displayed in black, and the surrounding host rock displayed in white. The .pcx model file (colliermodelpcx.pcx) is converted to an ASCII file (colliermodel.txt) using the following command in Seismic Unix:

```
./convertpcx colliermodelpcx.pcx >colliermodel.txt
```

- The ASCII file is converted to an image file:

```
a2b n1=1 <colliermodel.txt >colliermodel.bin
```

- Plot for quality control:

```
ximage n1=500 legend=1 <colliermodel.bin &
```

- The velocity model file is converted to an image file and plotted for quality control:

```
a2b n1=1 <collier_velfile.txt >collier_velfile.bin
ximage n1=500 legend=1 blockinterp=0 <collier_velfile.bin &
```

# Appendix B

## Seismic Unix Scripts

## B.1 Create receiver locations

The make_rec_input script creates a file of receiver locations (borehole_recs_CP3) for input into sufdmod2a, and is modified by T. Danek.

```
#!/bin/csh -f
set count=0
set countend=42
set dx=-0.84
set dy=1.8
set x=127
set y=0


while ($count < $countend)
  echo $x $y >> borehole_recs_CP3
  set y = `echo "$y + $dy" | bc`
  set x = `echo "$x + $dx" | bc`
```

```
  set count = `expr $count + 1`
end
exit
```

## B.2 Create shot gathers

The fdmodel_dipping program creates the 51 shot gathers, each having 42 channels and collects the coordinates for borehole receiver locations generated using the make_rec_input script. Each shot is written to a separate file.

```
#!/bin/csh -f
set shotnum = 1              #specify the number of the first shot
set shotx = 127              #Location in distance of the first shot.
set total = 51               #number of shots to record
set count = 0

while ($count < $total)
./sufdmod2a <collier_velfile.bin >/dev/null \ #>movie_shot24 | #/dev/null |
dx=0.2 dz=0.2 \
nx=1382 nz=500 \
tmax=.04        \
xs=$shotx \
zs=0.6 \
abs=1,1,1,1 \
#mt=50 |
vsx=borehole_recs_CP3 \
vsfile=shot.$shotnum.500hz.su \
```

```
verbose=1 \
fpeak=500 \

echo $shotnum complete

#Resample the seismogram
suoldtonew <shot.$shotnum.500hz.su |
sufilter f=10,20,800,1200 amps=1,1,.5,0 >shot.$shotnum.500hz_new.su

suresamp nt=133 dt=.0003
<shot.$shotnum.500hz_new.su >CP3.shot$shotnum.500hz.rsmp
rm shot.*.500hz_new.su
rm shot.*.500hz.su
#Set up next shot

set shotnum = `expr $shotnum + 1`
echo new shotnum $shotnum
set count = `expr $count + 1`
echo new count $count
set shotx = `expr $shotx + 2`  #The increment specified here is in meters.
echo new shotx $shotx
end
exit
```

## B.3 Concatenate individual shot files

The concat_fd2 program concatenates the 51 individual shot files produced in fdmodel_dipping into a single multi-shot file (concat_fd2_ALL.su). Since the finite difference routine writes individual files to disk without numbering the field file header or channel the job also numbers these headers.

```
#!/bin/csh -f


set first_file = 1
set last_file = 51


set count = $first_file
while ($count < 52)
echo $count
sushw </home/projects/kriselle_dias/CP2/CP3.shot$count.500hz.rsmp
key=fldr a=$count c=1 >temp
sushw <temp key=tracf a=1 b=1 >temp2
suwind <temp2 key=tracf min=1 max=42 j=1 >temp3
echo finished suwind
sushw <temp3 key=tracf a=1 b=1 >temp4
#suresamp <temp4 nt=500 dt=0.001 >temp5
sufilter <temp4 f=10,50,1200,1300 amps=0.,0.,1.,1. >temp5
cat <temp5 >>/exports/scratch/kriselle_dias/CP3/concat_fd2_ALL.su
#cat $count.su >> $test.su
echo  $count
```

```
set count = `expr $count + 1`

end
suwind key=fldr min=1 max=51
</exports/scratch/kriselle_dias/CP3/concat_fd2_ALL.su >SHOT
suximage perc=98 legend=1 < SHOT

exit
```

## B.4 Concatenate cross-correlated filed with chosen channels

The XCOR2 script reads the concatenated file of all shots (concat_fd2_ALL.su) and cross-correlates with the chosen channel, looping through the range of 51 shots and 42 channels. The output file format is "xc.shotnumber.channel.su".

```
#!/bin/csh -f

# The purpose of this program is to xcorrelate shot records with
# a specified chan within each of the shots to simulate a
# new virtual source location.
# Specify the chan # where the first virtual source will be.
set first_vs = 1
# Specify lastchannel number plus 1
set last_vs = 42
set vs_end = `expr $last_vs + 1`
```

```
set chan = $first_vs
set first_shot = 1
set last_shot = 51
set shotnum = $first_shot
set shotend = `expr $last_shot + 1`
#set check_chan = 1
while ($chan < $vs_end)
while ($shotnum < $shotend)
#make sure this is set to be one more than the
last shot in yourrange.
suwind key=fldr min=$shotnum max=$shotnum
</exports/scratch/kriselle_dias/CP3/concat_fd2_ALL.su >SHOT
echo shot $shotnum
suwind key=tracf min=$chan max=$chan <SHOT >TRACE
echo chan $chan

suxcor <SHOT sufile=TRACE >

/exports/scratch/kriselle_dias/CP3/XCOR_CP2/xc.$shotnum.$chan.su

echo finished
/exports/scratch/kriselle_dias/CP3/XCOR_CP2/xc.$shotnum.$chan.su
set shotnum = `expr $shotnum + 1`
end

set shotnum = $first_shot #make sure this is set
```

```
equal to the first shot in your input range.
set chan = `expr $chan + 1`
echo newchan $chan
end
exit
```

## B.5 Concatenate individual shot files to a multi-shot file

The concat_fd_xc_vs script concatenates a series of individual shot files into a single multi-shot file, the name format is that used with cross-correlated files. This has been updated to put all the data into one file which can be then sorted in ProMAX with header selev. First and last 'files' refer to the original sources and 'vs' refers to what were originally channels.

```
#!/bin/csh -f
set first_file = 1
set last_file = 31
set file_inc = 1
set first_vs = 1
set last_vs = 42
set incr_vs = 1
set vs = $first_vs
set vs_end = `expr $last_vs + 1`
set count = $first_file
set count_end = `expr $last_file + $file_inc`

while ($vs < $vs_end)
    while ($count < $count_end)
```

```
    if (-e /exports/scratch/kriselle_dias/CP3/XCOR_CP3/xc.$count.$vs.su)
then
        sushw key=selev a=$vs
</exports/scratch/kriselle_dias/CP3/XCOR_CP3/xc.$count.$vs.su |
sushw key=d1 a=0 >intermediate
sufilter <intermediate f=10,50,1200,1300 amps=0.,0.,1.,1. >intermediate2
        cat intermediate2 >>
/exports/scratch/kriselle_dias/CP3/concat_fd_xc_vs_ALL.su

    endif
    echo $count
    set count = `expr $count + $file_inc`

    end
echo vs $vs done
set count = $first_file
set vs = `expr $vs + $incr_vs`
end
exit
```

## B.6 Sort, trace-mix & trace taper cross-correlated files to create correlation gather

The SUWIND_MIX_TAPER_CAT script sorts the cross-correlated files such that the FFIDs are sorted within the channels, and the channels are sorted within the virtual sources. It applies an AGC, a standard weighted mix, linearly trace-tapers to the channel ensembles, and concatenates the cross-correlated files to create a correlation gather.

```
#!/bin/csh -f
set count1=1
set count2=1

susort <concat_june.su >CP_sorted.su selev tracf fldr

while ($count1 < 38)
    echo selevx $count1
    suwind <CP_sorted.su key=selev min=$count1 max=$count1 >temp

        while ($count2 < 38)
        echo tracfx $count2
        suwind <temp key=tracf min=$count2 max=$count2 >temp2

            #while ($count3 < 22)
            suwind <temp2 key=fldr min=1 max=21 j=1 >temp3

            sugain <temp3 agc=1 wagc=0.04 >temp3a
```

```
            sumix <temp3a mix=1,3,1 >temp3b
            echo finished sumix

            sutaper <temp3b ntr=21 tr1=3 tr2=3 min=0.3 >temp4
            echo finished sutaper

            cat <temp4 >>concat_MIX131_taper3.su
            echo finished cat


        set count2 = `expr $count2 + 1`
        end
        set count2=1
set count1 = `expr $count1 + 1`
echo $count1 test last
end
exit
```

# Appendix C

## Synthetic Modelling

## C.1 Shots produced using Finite Difference Modelling Program

The *fdmodel_ dipping* script is executed in Seismic Unix to generate the synthetic shot gathers for the dipping borehole simulation (B.2). The simulated study comprises of 51 surface sources spaced 2 m apart at a depth of 0.6 m. The 42 receivers which are spaced 2 m apart, are placed in a dipping borehole, with their coordinates accessed in a separate file (B.1). A total of 51 shot gathers are produced for a maximum source offset of 100 m. The first shot (shotx) is positioned at 127 m along the x-axis. The peak frequency is set to 500 Hz. Shot 1 is closest to the borehole and Shot 51 is furthest away from the borehole. The script utilizes the parameters specified in Table 4.3 and Table 4.5.

## C.2 Concatenating the shot records

The *concat_fd* script is executed in Seismic Unix and concatenates the 51 individual shot files into a large multi-shot (Appendix B). Since the finite difference routine writes individual files to the disk without numbering the field, file header, or channel, the script also numbers

these headers.

## C.3 Cross-correlation of shot records

The *XCOR2* script is implemented in Seismic Unix to cross-correlate the 51 shot records with the 42 individual channels within each of the shots to simulate a new virtual source location at the 42 borehole receivers. The virtual sources are created through the cross-correlation of the direct wave of the receiver at the virtual source location with each receiver in the surface shot. This process is repeated for all surface shots with the same virtual source receiver. The correlation gathers are generated by sorting the correlated data into common cross-correlated receiver pairs, as demonstrated in Table 4.6.

## C.4 Concatenation of cross-correlated shot records

The *concat_fd_xc_vs* script concatenates the individual cross-correlated shot files by summing each correlation gather to produce one trace for each of the 42 virtual sources. The script is adapted to concatenate only those cross-correlated shot files having a maximum source offset of 60 m, i.e. it only sums the cross-correlated files generated from surface sources 1 through 31. This is done to reduce the maximum source offset from 100 m to 60 m. The concatenated data is inserted into a single multi-shot file, the name format used with cross-correlated files, which can be sorted in ProMax using the header selev.

# Appendix D

## ProMAX Processing Steps

The .su Seismic Unix file was converted to .sgy and exported for processing to the ProMAX 2D Seismic Processing suite.

```
segyhdrs <concat_fd_xc_vs_ALL.su
segywrite endian=0 <concat_fd_xc_vs_ALL.su tape=cp2_concatall.sgy
```

Zero lag is at 40 ms.

## D.1 Create dataset to be sorted in ProMax

This job flow converts the concatenated, cross-correlated .sgy file (cp2_concatall.sgy) into a ProMAX dataset (vsource_raw), defines the trace header VSOURCE and displays it. The primary header selected is 'Live Source Number' and the secondary header selected is the 'Channel Number'. This produces a dataset of 31 traces, each having 42 channels.

*Job flow name: Display_SEGY*

```
SEGY-Input
Standard Fixed Trace Length
Invert normal byte order correction - No
Type of Storage to Use - Disk
```

```
Select files using a pattern? - No
Enter DISK file path name - /exports/scratch/kriselle_dias/CP2/cp2_concatall.sgy
Is this STACKED data? No
  MAX traces per ensemble - 42

Trace Header Math
Select mode - Fixed Equation Mode
  Define trace header equation(s) - VSOURCE=SOU_ELEV

Disk Data Output
Output Dataset Filename - vsource_raw
New, or Existing, File? - New
Record length to output - 0.0
Trace sample format - 32 bit
Skip primary disk storage? - No

Trace Display
Primary trace LABELING header entry - Live source number
Secondary trace LABELING header entry - Recording channel number
```

## D.2 Create a virtual stack

This job flow creates a virtual stack (vs_stack_60m) from the concantenated, cross-correlated ProMAX dataset (vsource_raw).

*Job flow name: vs_stack*

```
Disk Data Input
```

```
Select dataset - vsource_raw
Propagate input file history - Yes
Trace read option - Sort
Interactive Data Access? - No
  Select primary trace header entry - VSOURCE=SOU_ELEV
  Select secondary trace header entry - Recording channel number
  Select tertiary trace header entry - Live source number (usr-defined)
  Sort order list for dataset - *:*:*/
  Presort in memory or on disk? - Memory
Read the data multiple times? - No
Process trace headers only? - No
Override input data's sample interval? No

Ensemble Stack/Combine
Type of operation - Stack Only
  How are trace headers determined? First
  Secondary key bin size - 1.0
Maximum traces per output ensemble - 42
Select PRIMARY Trace Order Header Word - VSOURCE=SOU_ELEV
Average the X and Y coordinates of primary key? - No
Select SECONDARY Trace Order Header Word - Ascending
Suppress FOLD normalization? - No
Print results? - Yes


Disk Data Output
```

```
Output Dataset Filename - vs_stack_60m
New, or Existing, File? - New
Record length to output - 0.0
Trace sample format - 32 bit
Skip primary disk storage? No
```

## D.3 Specify Geometry for Creating a new CDP Stack

The 2D Land Geometry Spreadsheet is run first and specifies the new geometry for the 42 borehole receivers which are transformed to virtual sources via seismic interferometry, prior to creating a CDP stack.

*2D Land Geometry Spreadsheet*

**Setup**

```
Assign midpoints method (Required) -
Matching pattern numbers using first live chan and station
Station Intervals
  Nominal Receiver Station Interval - 2.0
  Nominal Source Station Interval - 2.0
  Nominal Survey Azimuth - -1.0
Station Range
  First Live Station Number - 1
  Last Live Station Number - 42
Base Source station co-ordinates upon a match between source
and receiver station numbers? - Yes
Source Type - Surface seismic source
```

Units - Meters

| Mark Block | Station | X | Y | Elev | Static |
|---|---|---|---|---|---|
| 1 | 1 | 0.0 | 0.0 | 0.0 | 0.0 |
| 2 | 2 | 2.0 | ,, | ,, | ,, |
| ... | ... | ... | ,, | ,, | ,, |
| 42 | 42 | 82 | ,, | ,, | ,, |

## Sources

| Mark Block | Source | Station | X | Y | Z | FFID | Offset | Skid | Pattern | Num Chn | Shot Fold | 1st Live Sta | 1st Live Chan | Gap Chan Dlt | Gap Size Dlt | Static |
|---|---|---|---|---|---|---|---|---|---|---|---|---|---|---|---|---|
| 1 | 1 | 1 | 0.0 | 0.0 | 0.0 | 1 | 0.0 | 0.0 | 1 | 42 | 42 | 1 | 1 | 0 | 0 | 0.0 |
| 2 | 2 | 2 | 2.0 | 0.0 | 0.0 | 2 | 0.0 | 0.0 | 1 | 42 | 42 | 1 | 1 | 0 | 0 | 0.0 |
| ... | ... | ... | ... | 0.0 | 0.0 | | 0.0 | 0.0 | 1 | | 42 | 1 | 1 | 0 | 0 | 0.0 |
| 42 | 42 | 42 | 84 | 0.0 | 0.0 | 42 | 0.0 | 0.0 | 1 | 42 | 42 | 1 | 1 | 0 | 0 | 0.0 |

## Patterns

| Mark Block | Pattern | Min Chan | Max/Gap Chan | Chan Inc | Rcvr MinChan | Rcvr Max Chan | Rcvr Inc | Error |
|---|---|---|---|---|---|---|---|---|
| 1 | 1 | 1 | 42 | 1 | 1 | 42 | 1 | |
| 2 | | | | | | | | |
| ... | | | | | | | | |
| 42 | | | | | | | | |

The following job flow applies the source-receiver geometry specified in the spreadsheet to the virtual source stack and creates a new dataset (vsource_geometry), prior to creation of a CDP stack.

*Job flow name: geometry*

```
Disk Data Input
Select dataset - vsource_stack
Propagate input file history - Yes
Trace read option - Sort
Interactive Data Access? - No
  Select primary trace header entry - VSOURCE=SOU_ELEV
  Select secondary trace header entry - Recording channel number
  Select tertiary trace header entry - No trace header selected
  Sort order list for dataset - *:*/
  Presort in memory or on disk? - Memory
Read the data multiple times? - No
Process trace headers only? - No
Override input data's sample interval? No

Trace Header Math
Select mode - Fixed equation mode
  DEFINE trace header equation(s) - FFID=INT(VSOURCE)

Inline Geom Header Load
Primary header to match database - FFID
Secondary header to match database - None
Match by valid trace number? - No
```

```
Drop traces with NULL CDP headers? No
Drop traces with NULL receiver headers? - No
Verbose diagnostics? - No

Disk Data Output
Output Dataset Filename - vsource_geometry
New, or Existing, File? - New
Record length to output - 0.0
Trace sample format - 32 bit
Skip primary disk storage? No
```

## D.4 Create a NMO-corrected CDP stack

The following job flow creates a CDP stack from the virtual source stack (vsource_geometry) and carries out a NMO correction for a NMO velocity of 5000 m/sec, to generate a NMO-corrected CDP stack (cdpstack_60m). The zero lag is at 80 ms. The job flow also corrects the trace length to 40 m, removing acausal contributions to the stack.

*Job flow name: CDP_stack*

```
Disk Data Input
Select dataset - vsource_geometry
Propagate input file history - Yes
Trace read option - Sort
Interactive Data Access - No
  Select primary trace header entry - CDP bin number
  Select secondary trace header entry - Signed source-receiver offset
  Select tertiary trace header entry - No trace header selected
```

```
  Select order list for dataset - *:0-200/
  Presort in memory or on disk - Memory
Read the data multiple times? - No
Process trace headers only? - No
Override input data's sample interval? - No



Hand Statics
Interpolate statics between specified locations? - Yes
Are tgese STATICS or VELOCITIES? - STATICS
What about previous statics? - Add to previous statics
Primary statics location header word - VSOURCE=SOU_ELEV
Secondary statics location header word - Recording channel number
SPECIFY hand statics to be applied - 1:1:-40 / 1:42:-40 / 84:1:-40 / 84:42:-40 /

Trace Length
New trace length - 40.0

Normal Moveout Correction
Direction for NMO correction - FORWARD
  Stretch mute percentage - 30.0
  Apply any remaining static during NMO? - No
  Disable check for previously applied NMO? - No
Get 3D dip velocities? - No
Apply partial NMO? - No
Apply P-Sv converted-wave NMO? - No
```

```
Long offset correction? - None
Get velocities from the database? - No
  SPECIFY NMO velocity function(s) - 1:0-5000,40-5000/84:0-5000,40-5000/

CDP/Ensemble Stack
Sort order of input ensembles - CDP
METHOD for trace summing - Mean
Root power scalar for stack normalization - 0.5
Apply final datum statics after stack? - No
Has NMO been applied? - Yes

Disk Data Output
Output Dataset Filename - cdpstack_60m
New, or Existing, File? - New
Record length to output - 0.0
Trace sample format - 32 bit
Skip primary disk storage? No
```

## D.5 Perform Kirchoff Depth Migration

The following job flow performs a Kirchoff Depth Migration on the CDP stacked seismic section.

*Job flow name: Kirch_Depth_Migration*

```
Disk Data Input
Select dataset - cdpstack
Propagate input file history - Yes
```

```
Trace read option - Get all
Read the data multiple times? - No
Process trace headers only? - No
Override input data's sample interval? - No

Kirchoff Depth Mig.
CDP interval (feet or meters) - 2.0
Maximum frequency to migrate (in Hz) - 1000
Depth sampling interval of output data - 0.0
Maximum depth to migrate - 40.0
Migration aperture (feet or meters) - 0.0
Maximum dip to migrate - 20.0
Avoid spatial aliasing? - Yes
Method for producing the Green's function - Implicit Eikonal solver
Accuracy factor - 1.0
Get interval velocities from database? - No
Interval velocities in depth for migration - 1:0-5000,40-5000/84:0-5000,40-5000/
  Minimum acceptable velocity - 5000.0
  Maximum acceptable velocity - 5000.0
Change maximum memory usage? - No
Change the default tapering? - No
Re-apply trace mutes in depth? - No
Re-kill dead traces? - No

Disk Data Output
Output Dataset Filename - cdpstack_depth_migr
```

```
New, or Existing, File? - New

Record length to output - 0.0

Trace sample format - 32 bit

Skip primary disk storage? No
```

# Appendix E

## Interferometry Logs

Recording System: Aries

No. of channels: 24

Channel Spacing: 2 m

Sample Rate: 1/4 ms

Record Length: 3.0

Spread Type: 24 channel hydrophone

*Tab. E.1:* Collier Point Interferometry Logs

| Shot Num | FFID | Shot Station | Chan at Depth | Chan at Depth | Time | Charge |
|---|---|---|---|---|---|---|
| 1 | 171 | 1E | Ch 1 at 82 m | Ch 24 at 36 m | 11:51 | 39 g |
| 2 | 172 | 2E | Ch 1 at 82 m | Ch 24 at 36 m | 11:58 | 39 g |
| 3 | 173 | 3E | Ch 1 at 82 m | Ch 24 at 36 m | 12:05 | 39 g |
| 4 | 174 | 4E | Ch 1 at 82 m | Ch 24 at 36 m | 12:10 | 39 g |
| 5 | 175 | 5E | Ch 1 at 82 m | Ch 24 at 36 m | 12:14 | 39 g |
| 6 | 176 | 6E | Ch 1 at 82 m | Ch 24 at 36 m | 12:18 | 39 g |
| 7 | 177 | 7E | Ch 1 at 82 m | Ch 24 at 36 m | 12:23 | 39 g |
| 8 | 178 | 8E | Ch 1 at 82 m | Ch 24 at 36 m | 12:27 | 39 g |
| 9 | 179 | 9E | Ch 1 at 82 m | Ch 24 at 36 m | 12:32 | 39 g |

*Tab. E.1:* Collier Point Interferometry Logs

| Shot Num | FFID | Shot Station | Chan at Depth | Chan at Depth | Time | Charge |
|---|---|---|---|---|---|---|
| 10 | 180 | 10E | Ch 1 at 82 m | Ch 24 at 36 m | 12:39 | 39 g |
| 11 | 181 | 11E | Ch 1 at 82 m | Ch 24 at 36 m | 12:48 | 39 g |
| 12 | 182 | 13E | Ch 1 at 82 m | Ch 24 at 36 m | 13:00 | 39 g |
| 13 | 183 | 14E | Ch 1 at 82 m | Ch 24 at 36 m | 13:06 | 39 g |
| 14 | 184 | 15W | Ch 1 at 82 m | Ch 24 at 36 m | 13:18 | 39 g |
| 15 | 185 | 16E | Ch 1 at 82 m | Ch 24 at 36 m | 13:30 | 39 g |
| 16 | 186 | 17E | Ch 1 at 82 m | Ch 24 at 36 m | 13:37 | 39 g |
| 17 | 187 | 18E | Ch 1 at 82 m | Ch 24 at 36 m | 13:43 | 39 g |
| 18 | 188 | 19E | Ch 1 at 82 m | Ch 24 at 36 m | 13:51 | 39 g |
| 19 | 189 | 20E | Ch 1 at 82 m | Ch 24 at 36 m | 13:56 | 39 g |
| 20 | 190 | 21E | Ch 1 at 82 m | Ch 24 at 36 m | 14:03 | 39 g |
| 21 | 191 | 22E | Ch 1 at 82 m | Ch 24 at 36 m | 14:11 | 39 g |
| 22 | 192 | 23E | Ch 1 at 82 m | Ch 24 at 36 m | 14:18 | 39 g |
| 23 | 193 | 22W | Ch 1 at 56 m | Ch 24 at 10 m | 14:45 | 39 g |
| 24 | 194 | 21W | Ch 1 at 56 m | Ch 24 at 10 m | 14:50 | 39 g |
| 25 | 195 | 20W | Ch 1 at 56 m | Ch 24 at 10 m | 14:57 | 39 g |
| 26 | 196 | 19W | Ch 1 at 56 m | Ch 24 at 10 m | 15:03 | 39 g |
| 27 | 197 | 18W | Ch 1 at 56 m | Ch 24 at 10 m | 15:08 | 39 g |
| 28 | 198 | 17W | Ch 1 at 56 m | Ch 24 at 10 m | 15:13 | 39 g |
| 29 | 199 | 16W | Ch 1 at 56 m | Ch 24 at 10 m | 15:19 | 39 g |
| 30 | 200 | 15W | Ch 1 at 56 m | Ch 24 at 10 m | 15:24 | 39 g |
| 31 | 201 | 14W | Ch 1 at 56 m | Ch 24 at 10 m | 15:29 | 39 g |
| 32 | 202 | 13W | Ch 1 at 56 m | Ch 24 at 10 m | 15:35 | 39 g |

*Tab. E.1:* Collier Point Interferometry Logs

| Shot Num | FFID | Shot Station | Chan at Depth | Chan at Depth | Time | Charge |
|---|---|---|---|---|---|---|
| 33 | 203 | 11W | Ch 1 at 56 m | Ch 24 at 10 m | 15:41 | 39 g |
| 34 | 204 | 10W | Ch 1 at 56 m | Ch 24 at 10 m | 15:46 | 39 g |
| Misfire | 205 | 9W | Ch 1 at 56 m | Ch 24 at 10 m | - | 39 g |
| 35 | 206 | 9W | Ch 1 at 56 m | Ch 24 at 10 m | 15:51 | 39 g |
| 36 | 207 | 8W | Ch 1 at 56 m | Ch 24 at 10 m | 15:55 | 39 g |
| 37 | 208 | 7W | Ch 1 at 56 m | Ch 24 at 10 m | 15:58 | 39 g |
| 38 | 209 | 6W | Ch 1 at 56 m | Ch 24 at 10 m | 16:02 | 39 g |
| 49 | 210 | 5W | Ch 1 at 56 m | Ch 24 at 10 m | 16:06 | 39 g |
| 40 | 211 | 4W | Ch 1 at 56 m | Ch 24 at 10 m | 16:11 | 39 g |
| 41 | 212 | 3W | Ch 1 at 56 m | Ch 24 at 10 m | 16:17 | 39 g |
| 42 | 213 | 2W | Ch 1 at 56 m | Ch 24 at 10 m | 16:22 | 39 g |
| 43 | 214 | 1W | Ch 1 at 56 m | Ch 24 at 10 m | 16:27 | 39 g |

# Appendix F

## CDP Geometry

*Tab. F.1:* CDP Numbers with corresponding borehole depths and no. of traces in CDP bin

| CDP | Depth along borehole (m) | CDP Fold |
|---|---|---|
| 1 | 10 | 1 |
| 2 | 11 | 2 |
| 3 | 12 | 3 |
| 4 | 13 | 4 |
| 5 | 14 | 5 |
| 6 | 15 | 6 |
| 7 | 16 | 7 |
| 8 | 17 | 8 |
| 9 | 18 | 9 |
| 10 | 19 | 10 |
| 11 | 20 | 11 |
| 12 | 21 | 12 |
| 13 | 22 | 13 |
| 14 | 23 | 14 |
| 15 | 24 | 15 |

*Tab. F.1:* CDP Numbers with corresponding borehole depths and no. of traces in CDP bin

| CDP | Depth along borehole (m) | CDP Fold |
|---|---|---|
| 16 | 25 | 16 |
| 17 | 26 | 17 |
| 18 | 27 | 18 |
| 19 | 28 | 19 |
| 20 | 29 | 20 |
| 21 | 30 | 21 |
| 22 | 31 | 22 |
| 23 | 32 | 23 |
| 24 | 33 | 24 |
| 25 | 34 | 25 |
| 26 | 35 | 26 |
| 27 | 36 | 27 |
| 28 | 37 | 28 |
| 29 | 38 | 29 |
| 30 | 39 | 30 |
| 31 | 40 | 31 |
| 32 | 41 | 32 |
| 33 | 42 | 33 |
| 34 | 43 | 34 |
| 35 | 44 | 35 |
| 36 | 45 | 36 |
| 37 | 46 | **37** |
| 38 | 47 | 36 |

*Tab. F.1:* CDP Numbers with corresponding borehole depths and no. of traces in CDP bin

| CDP | Depth along borehole (m) | CDP Fold |
|---|---|---|
| 39 | 48 | 35 |
| 40 | 49 | 34 |
| 41 | 50 | 33 |
| 42 | 51 | 32 |
| 43 | 52 | 31 |
| 44 | 53 | 30 |
| 45 | 54 | 29 |
| 46 | 55 | 28 |
| 47 | 56 | 27 |
| 48 | 57 | 26 |
| 49 | 58 | 25 |
| 50 | 59 | 24 |
| 51 | 60 | 23 |
| 52 | 61 | 22 |
| 53 | 62 | 21 |
| 54 | 63 | 20 |
| 55 | 64 | 19 |
| 56 | 65 | 18 |
| 57 | 66 | 17 |
| 58 | 67 | 16 |
| 59 | 68 | 15 |
| 60 | 69 | 14 |
| 61 | 70 | 13 |

*Tab. F.1:* CDP Numbers with corresponding borehole depths and no. of traces in CDP bin

| CDP | Depth along borehole (m) | CDP Fold |
|---|---|---|
| 62 | 71 | 12 |
| 63 | 72 | 11 |
| 64 | 73 | 10 |
| 65 | 74 | 9 |
| 66 | 75 | 8 |
| 67 | 76 | 7 |
| 68 | 77 | 6 |
| 69 | 78 | 5 |
| 70 | 79 | 4 |
| 71 | 80 | 3 |
| 72 | 81 | 2 |
| 73 | 82 | 1 |

# Appendix G

## 1-D Modelling Trials

*Tab. G.1:* Log files used in Breccia Modelling

| **Log 1** | **Log 2** | **Log 3** | **Log 4** |
|---|---|---|---|
| logbreccia | logbreccia2 | logarkosebrecbarite | logarosebrecbarite2 |
| 0.1 - 7.9 m arkose | 0.1 - 7.9 m arkose | 0.1 - 7.9 m arkose | 0.1 - 7.9 m arkose |
| 8 - 14 m low breccia | 8 - 14 m high breccia | 8 - 12 m low breccia | 8 - 15 m low breccia |
| 14.1 - 29.9 m arkose | 14.1 - 29.9 m arkose | 12.1 - 14 m barite | 15.1 - 16.9 m barite |
| | | 14.1 - 18.9 m low breccia | 17 - 24 m low breccia |
| | | 19 - 29.9 m arkose | 24.1 - 29.9 m arkose |

**Breccia Model 1** (Figure G.1) consists of a 1 m thick barite body moving through a 6 m region of low breccia, surrounded by arkose on both sides. The near vicinity parameters are set to low breccia. The moving barite body produces a change in the synthetic wavelet from a single negative peak to a doublet, as it moves from left to right (increasing breccia on the left of barite unit, and decreasing breccia on the right). Therefore, the interactions of the arkose and breccias having varying thicknesses which surround the barite unit likely results in the wavelet changes as seen in the Collier Point Dataset (Figure 7.10).

**Breccia Model 2** (Figure G.2) consists of nearly the same parameters as *Breccia Model 1*, except that the low breccia has been replaced by high breccia (having a higher velocity)

in the background log file and near vicinity parameters. It is noted that the produced synthetic wavelet does not demonstrate transformation to a doublet through the running of the program, as seen in *Breccia Model 1*, but resembles that seen in the three-layer response (Subsection 7.3.2) and barite surrounded by breccia (Subsection 7.3.3). This is likely due to the higher velocity of the breccia units (3760 m/sec) being closer to the arkose units (5042 m/sec), causing it to be interpreted similarly, and therefore negating the effect of the breccia zone.

**Breccia Model 3** (Figure G.3) consists of a 1 m thick barite body moving through a 6 m region of high breccia, surrounded by arkose on both sides. The near vicinity parameters are set to low breccia. The moving barite body produces a change in the produced synthetic wavelet from a single negative peak to an asymmetric doublet, as it moves from left to right (increasing breccia on the left of barite unit, and decreasing breccia on the right), and a transition from high breccia to low breccia. Therefore, interactions of the arkose and breccia unit having increasing thickness, and which surround the barite unit result in the wavelet changes from singlet to doublet, also seen in *Breccia Model 1*. Furthermore, transition from high breccia to low breccia results in the assymetric lobes of the double wavelet.

**Breccia Model 4** (Figure G.4) consists of a 1 m thick barite body moving through a 6 m region of low breccia, surrounded by arkose on both sides. The near vicinity parameters are set to high breccia. The produced synthetic wavelet progresses from two negative peaks to a single negative peak in the first two scenarios (Produced by the moving barite body). The first scenario consists of an arkose - barite - low breccia - high breccia - low breccia - arkose contact and results in the produced seismogram having two negative peaks, likely due to the negative velocities of the barite and low breccia zones. The second scenario consists of a high breccia - barite - high breccia - low breccia - arkose contact, which results in a single high negative peak, likely due to the strong negative velocity from the barite unit. The consequent scenarios then produce the same waveform as seen in *Breccia Model 2* where

high negative value of the barite units negating the effect of the narrow breccia zone, causing it to be interpreted similarly to a three-layer model.

**Breccia Model 5** (Figure G.4) consists of a 1 m barite unit moving though a 7 m region of low breccia, 2 m barite, 7 m region of low breccia and bounded by arkose on both ends. The near vicinity parameters are set to high breccia. The first, second and third scenarios comprise of a two negative peak due to the barite units, and a near doublet due to to interactions between the barite, breccia zone and arkose. In the fourth scenario, the single negative peak changes to an assymetic doublet (as seen in Figure G.3) due to interactions between the arkose, increased breccia zone and barite.

Breccia Model 1

*Background log file* logbreccia

*Non-moving body* Low Breccia - Depth: 10 m, Thickness: 1 m

*Moving Body* Barite - Depth: 8 m, Thickness 1 m

*Parameters in near vicinity of bodies* - Low Breccia - Velocity: 3500 m/sec, Density: 3.5 m/sec

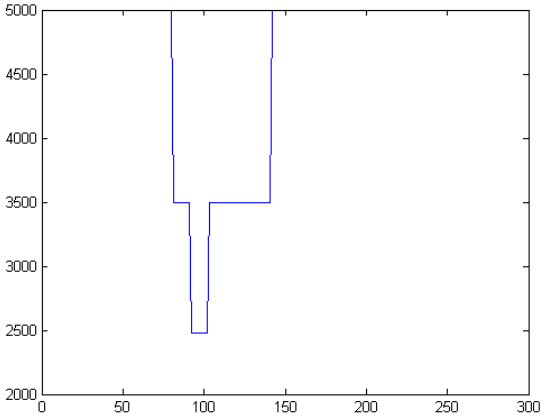
5000
4500
4000
3500
3000
2500
2000
0
50
100
150
200
250
300

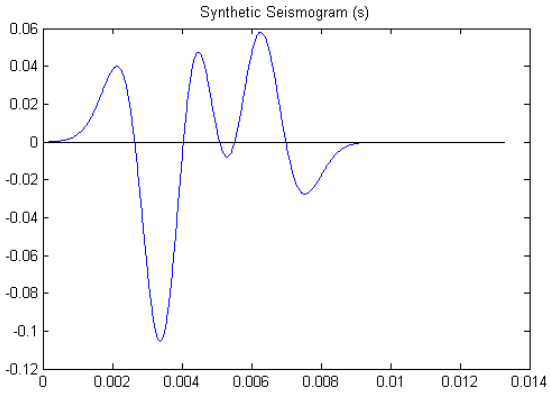
Synthetic Seismogram (s)
0.06
0.04
0.02
0
-0.02
-0.04
-0.06
-0.08
-0.1
-0.12
0
0.002
0.004
0.006
0.008
0.01
0.012
0.014

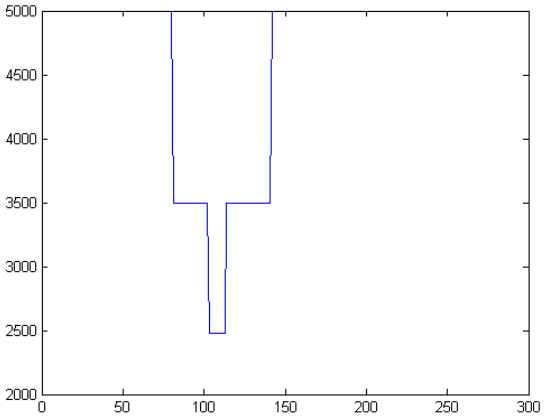
5000
4500
4000
3500
3000
2500
2000
0
50
100
150
200
250
300

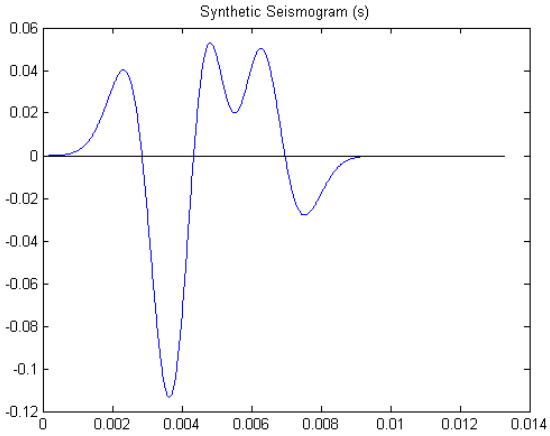
Synthetic Seismogram (s)
0.06
0.04
0.02
0
-0.02
-0.04
-0.06
-0.08
-0.1
-0.12
0
0.002
0.004
0.006
0.008
0.01
0.012
0.014

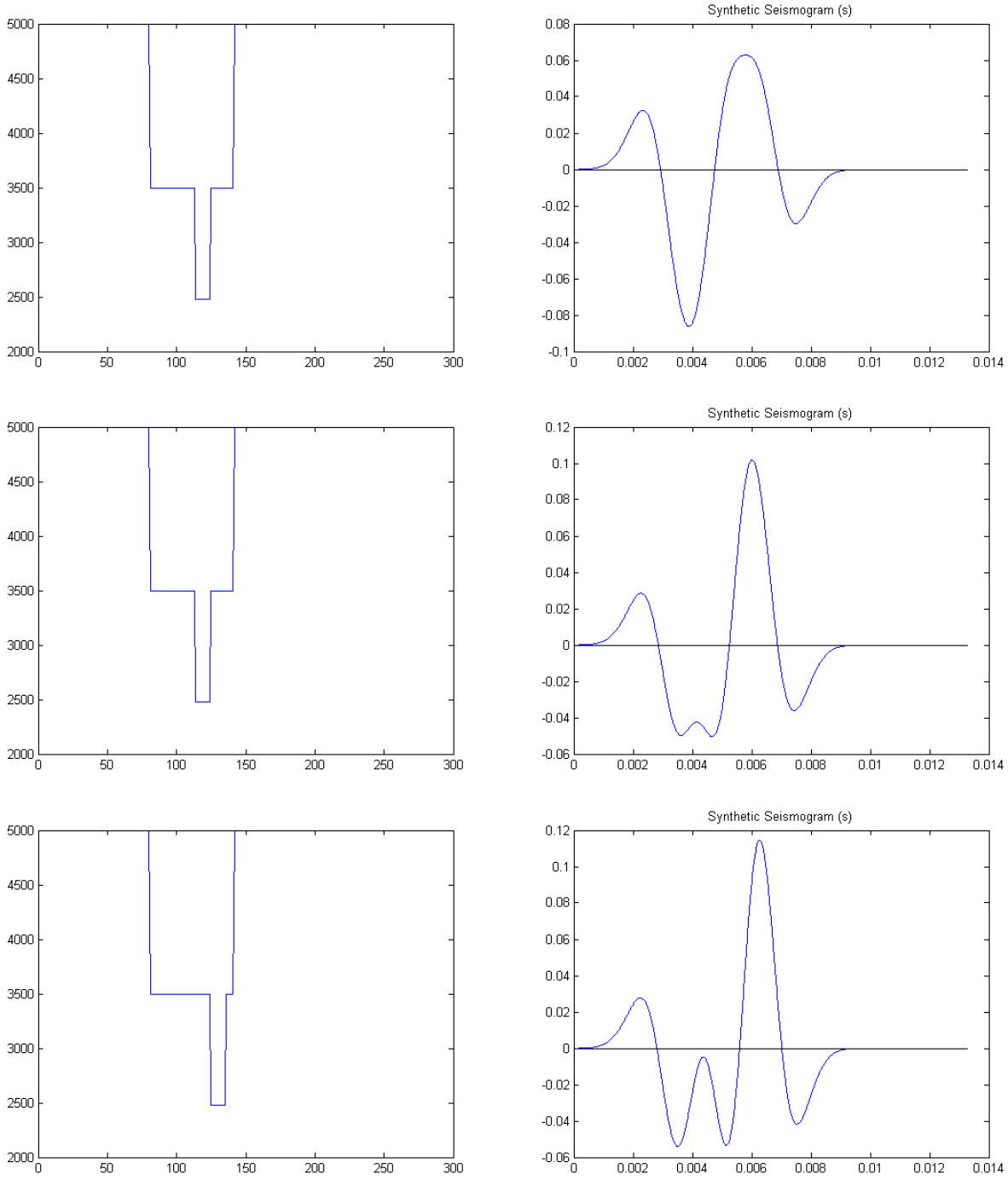


*Fig. G.1:* Scenarios produced for Breccia Model 1
Velocity model (left), Synthetic Seismogram (right) for each scenario produced due to the moving barite block

Breccia Model 2

*Background log file* logbreccia2

*Non-moving body* High Breccia - Depth: 10 m, Thickness: 1 m

*Moving Body* Barite - Depth: 8 m, Thickness 1 m

*Parameters in near vicinity of bodies* - Velocity: 3760 m/sec, Density: 3.59 m/sec

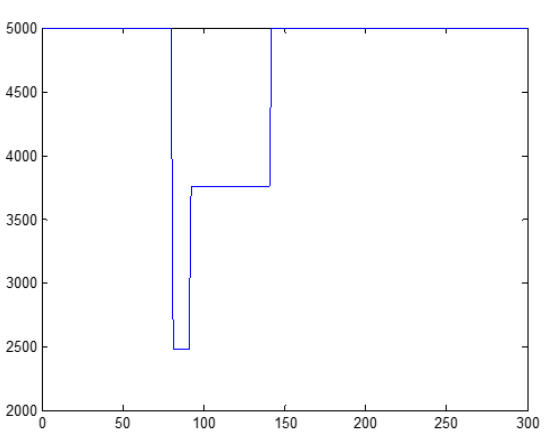


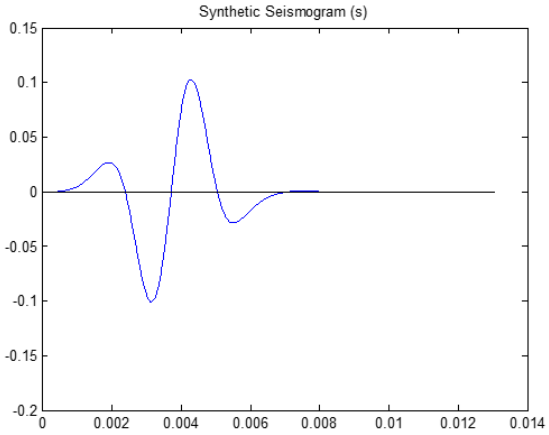


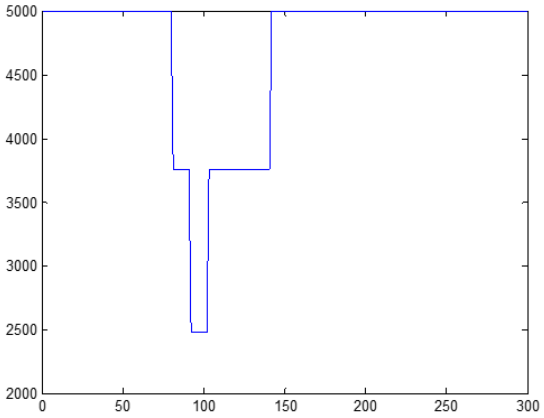


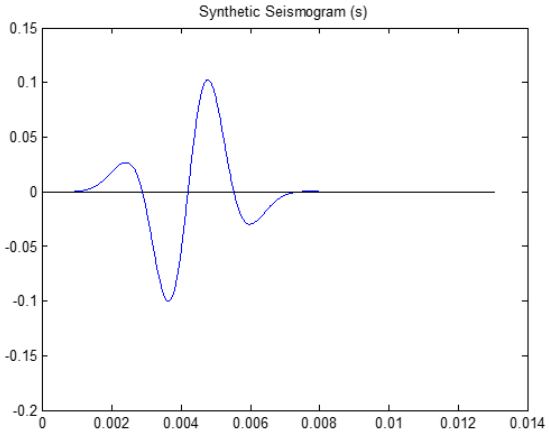

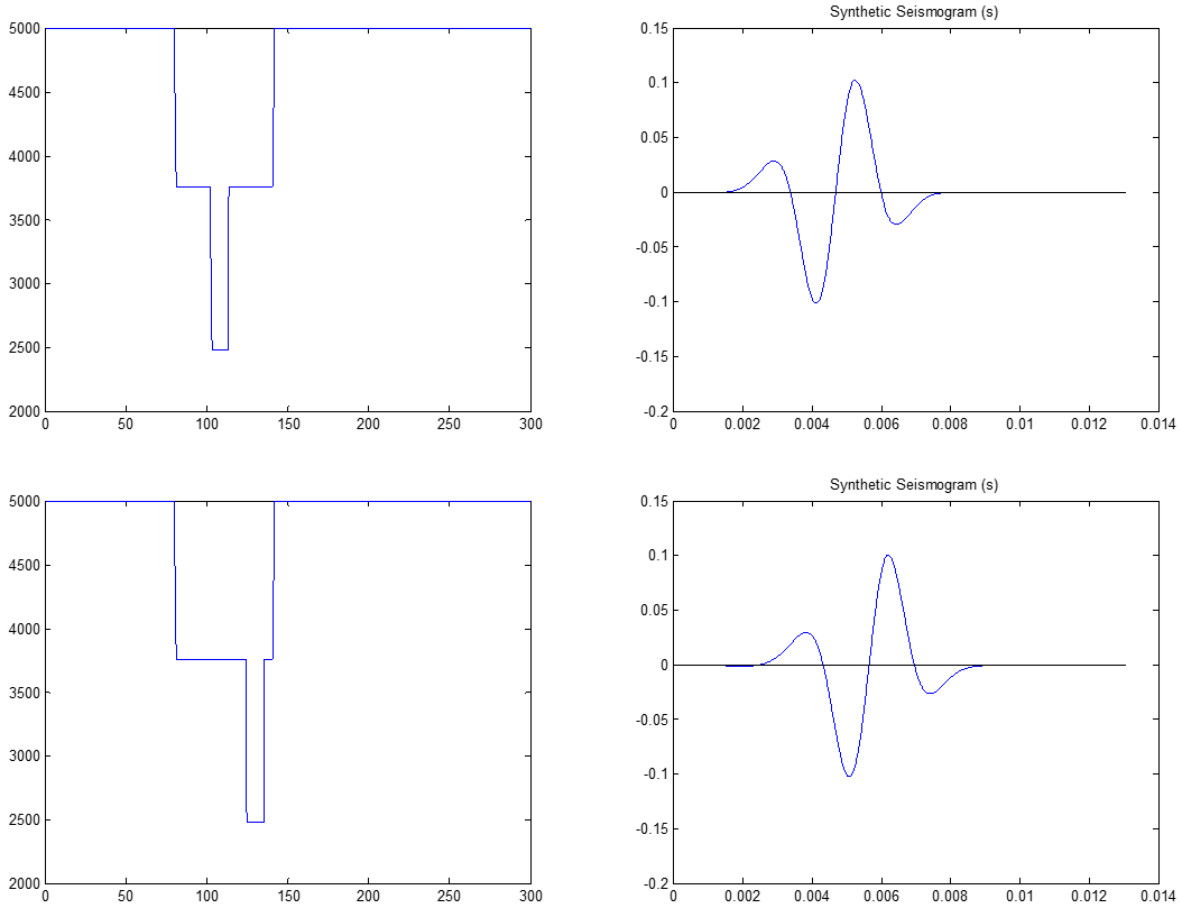


*Fig. G.2:* Scenarios produced for Breccia Model 2
Velocity model (left), Synthetic Seismogram (right) for each scenario produced due to the moving barite block

Breccia Model 3

*Background log file* logbreccia2

*Non-moving body* Low Breccia - Depth: 10 m, Thickness: 1 m

*Moving Body* Barite - Depth: 8 m, Thickness 1 m

*Parameters in near vicinity of bodies* - Velocity: 3500 m/sec, Density: 3.5 m/sec

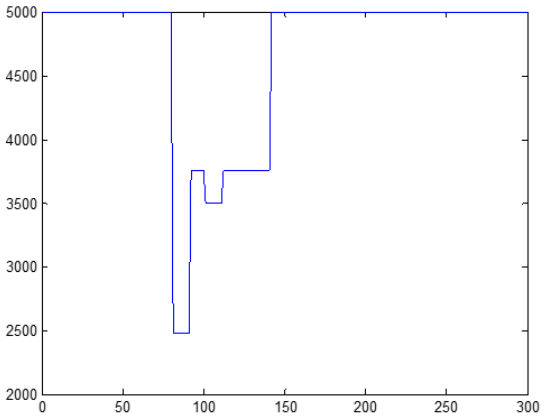


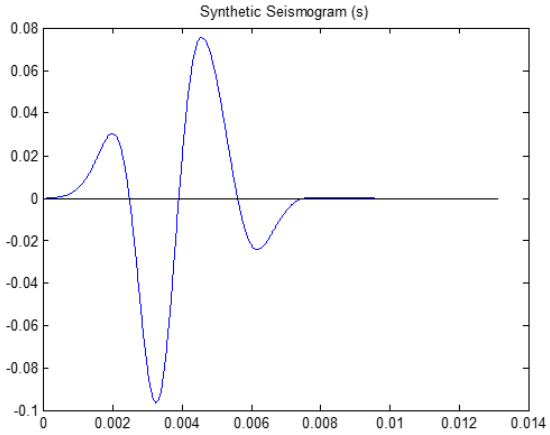


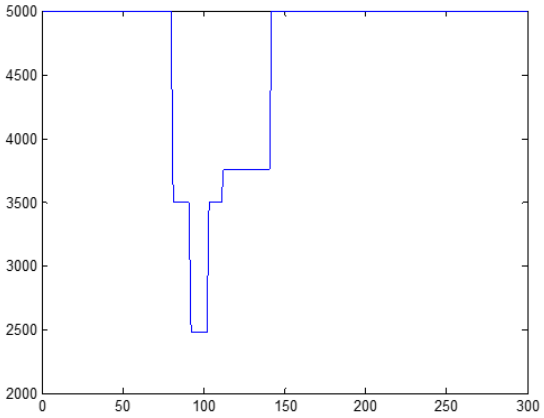


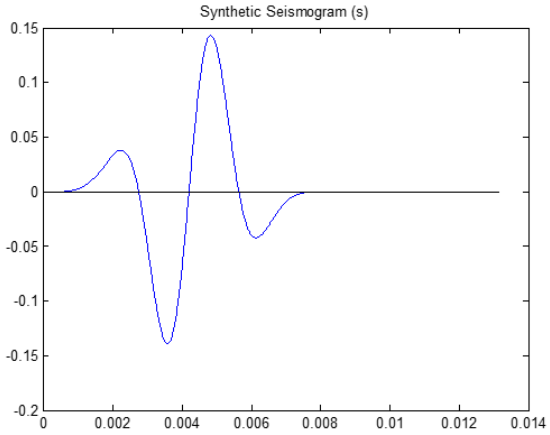

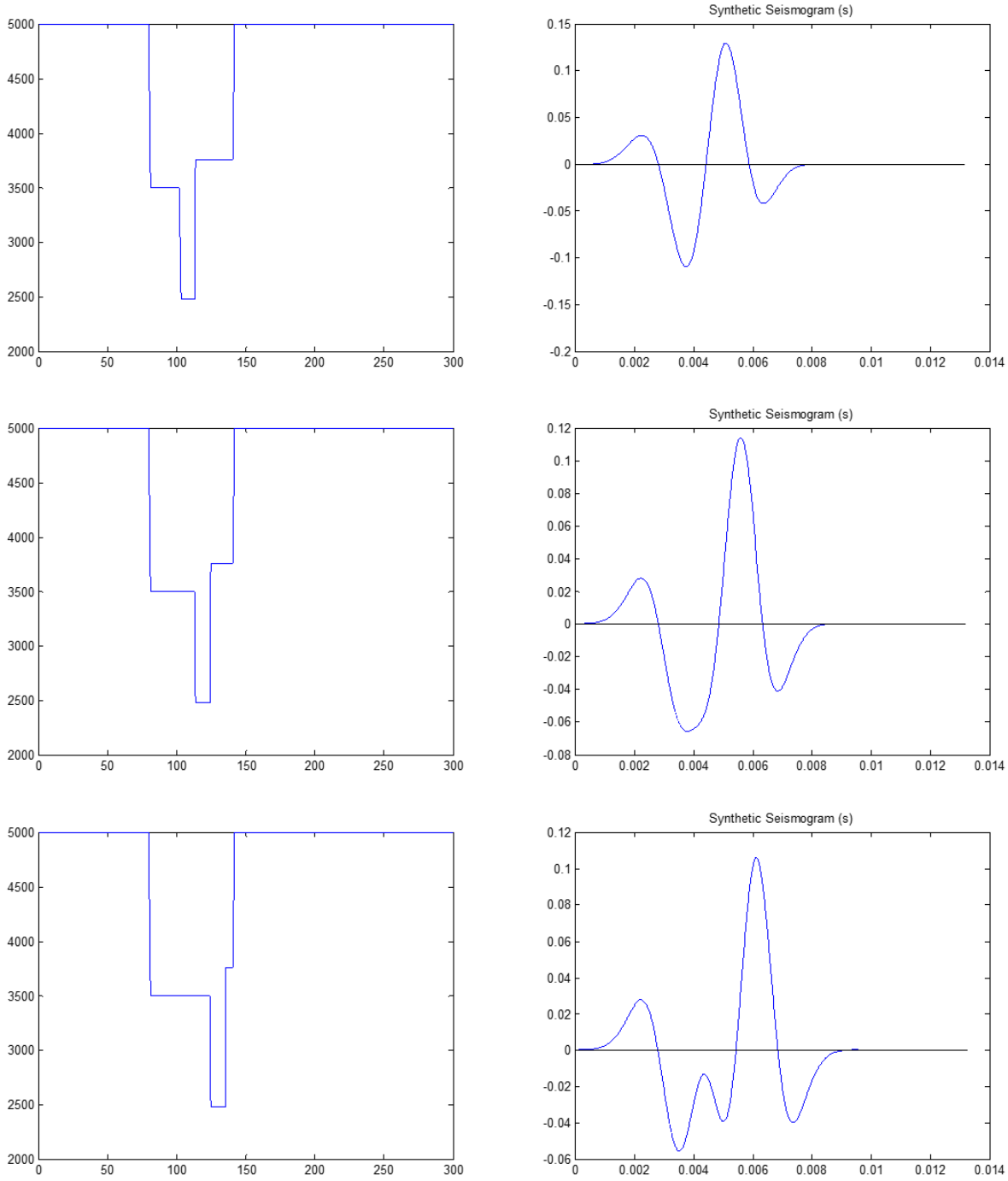


*Fig. G.3:* Scenarios produced for Breccia Model 3
Velocity model (left), Synthetic Seismogram (right) for each scenario produced due to the moving barite block

Breccia Model 4

*Background log file* logbreccia

*Non-moving body* High Breccia - Depth: 10 m, Thickness: 1 m

*Moving Body* Barite - Depth: 8 m, Thickness 1 m

*Parameters in near vicinity of bodies* - Velocity: 3760 m/sec, Density: 3.59 m/sec

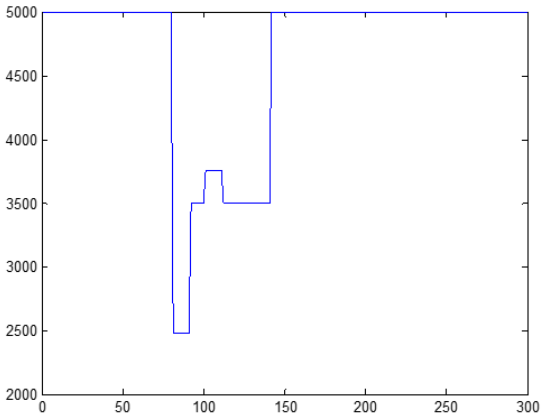


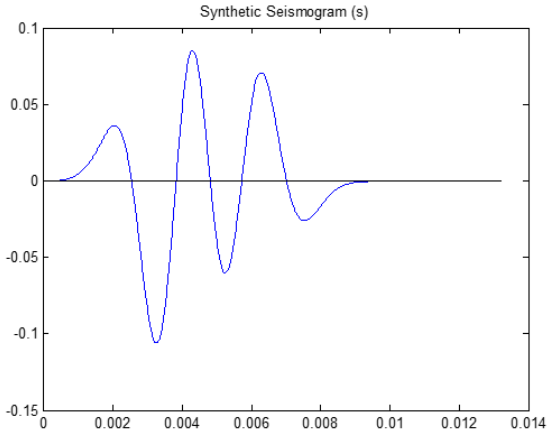


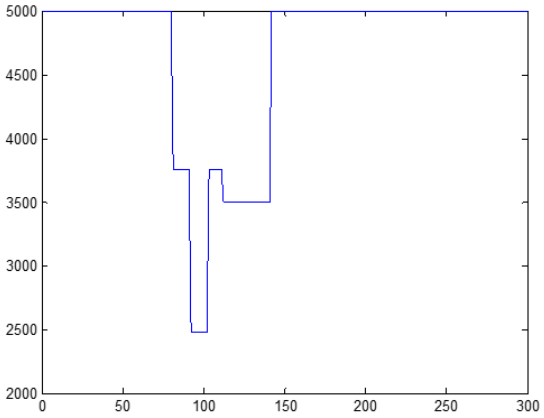


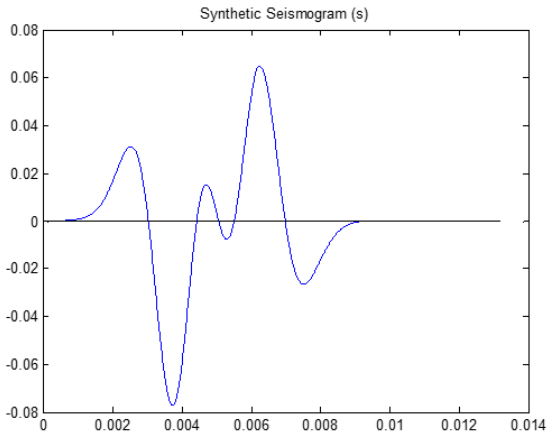

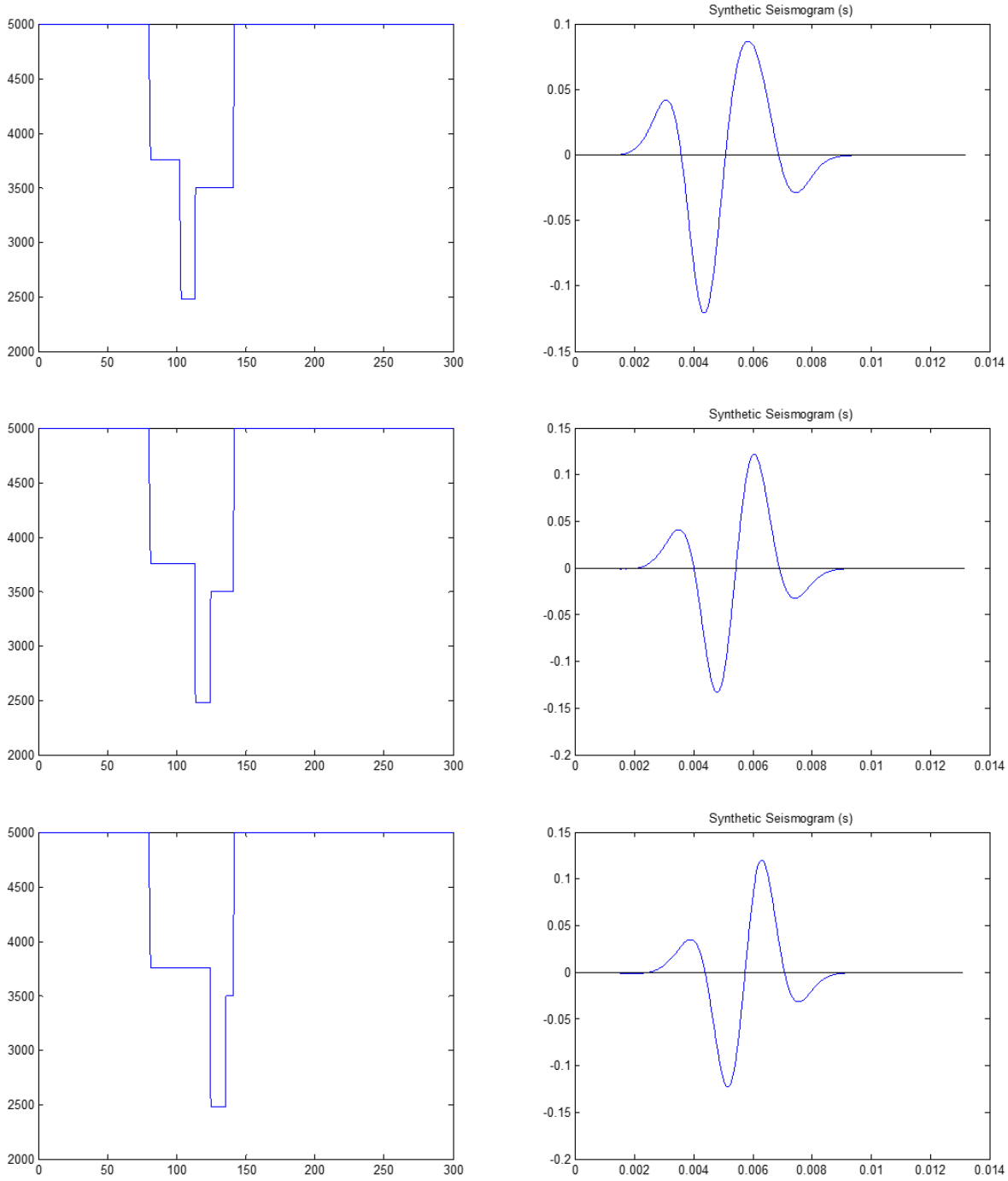


*Fig. G.4:* Scenarios produced for Breccia Model 4
Velocity model (left), Synthetic Seismogram (right) for each scenario produced due to the moving barite block

Breccia Model 5

*Background log file* logarkosebrecbarite2

*Non-moving body* High Breccia - Depth: 10 m, Thickness: 1 m

*Moving Body* Barite - Depth: 8 m, Thickness 1 m

*Parameters in near vicinity of bodies* - Velocity: 3760 m/sec, Density: 3.59 m/sec

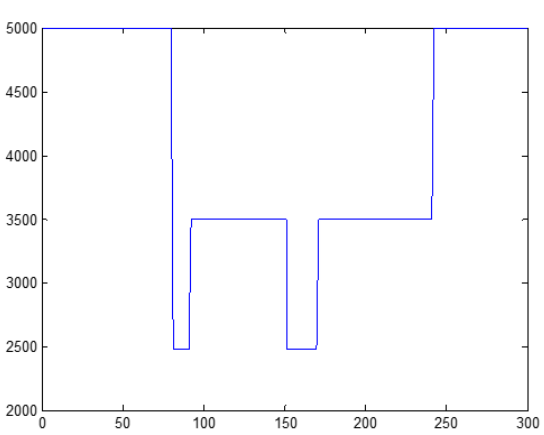


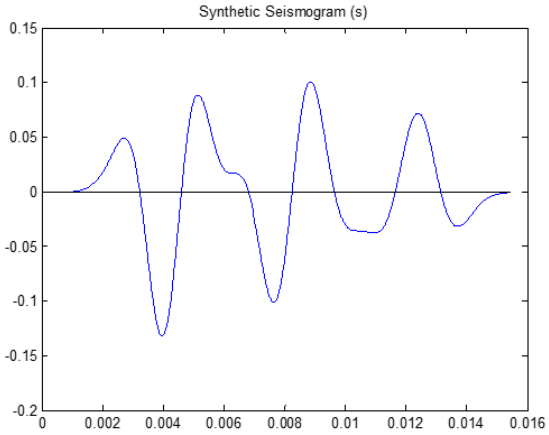


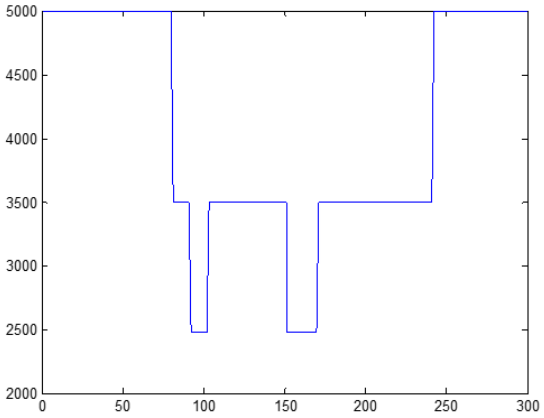


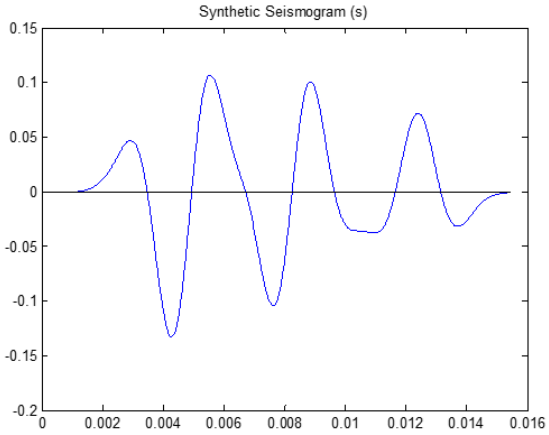

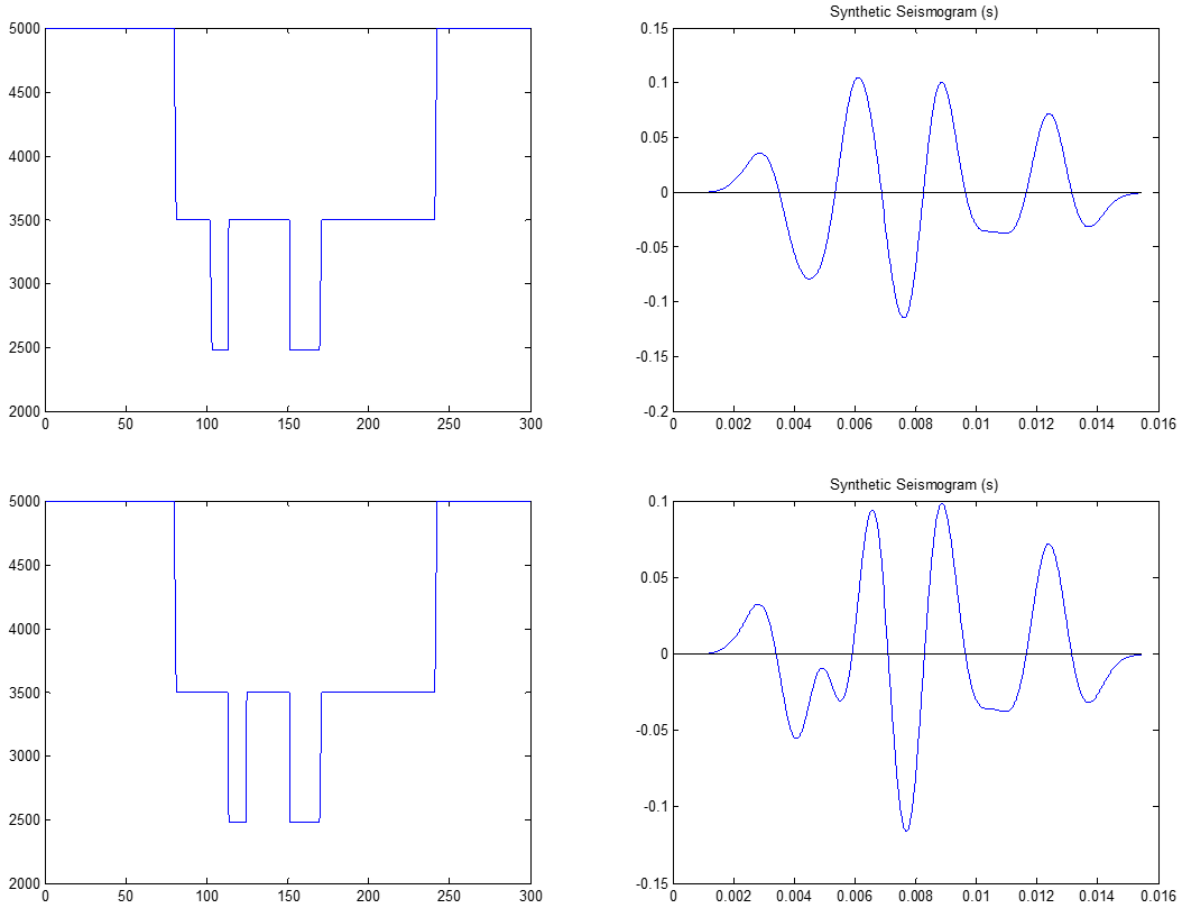


*Fig. G.5:* Scenarios produced for Breccia Model 5
Velocity model (left), Synthetic Seismogram (right) for each scenario produced due to the moving barite block